Durham E-Theses

Reactive scattering of Rydberg atoms

Flynn, Emma L.

How to cite:

Flynn, Emma L. (2008) *Reactive scattering of Rydberg atoms*, Durham theses, Durham University. Available at Durham E-Theses Online: http://etheses.dur.ac.uk/2503/

Durham University

A Thesis Entitled

Reactive Scattering of Rydberg Atoms

Submitted by

Emma L. Flynn MChem (Hons)

0 6 OCT 2008

Department of Chemistry

A Candidate for the Degree of Doctor of Philosophy

2008

Statement of Copyright

Declaration

The work described in this thesis was carried out in the Department of Chemistry at Durham University between October 2004 and October 2007. All the work was carried out by the author, unless otherwise stated, and has not previously been submitted for a degree at this or any other university.

Aspects of this work have been presented at:

- Spectroscopy and Dynamics group conference, University of East Anglia, December 2007, poster presentation.

- Durham University, Department of Chemistry Final Year Postgraduate Symposium, Durham 2007, oral and poster presentation.

- Spectroscopy and Dynamics group conference, University of Oxford, December 2006, oral presentation by Alexander Trottier.

- MOLEC XVI, European Conference of Dynamics of Molecular Systems, Trento, Italy, September 2006.

- 15th Annual Northern Universities Meeting on Chemical Physics, University of York, July 2006, poster presentation.

- Royal Society Discussion Meeting, Physics, Chemistry, and Astronomy of H3+, Royal Society, London, January 2006, poster presentation.

- Spectroscopy and Dynamics group conference, Durham University, December 2005, poster presentation.

- 14th Annual Northern Universities Meeting on Chemical Physics, University of Leeds, June 2005, oral presentation by Stuart Greaves.

- Spectroscopy and Dynamics group conference 2004, University of Leicester, poster presentation.

Acknowledgments

Firstly I would like to thank my wonderful supervisor, Eckart Wrede, for all his help and guidance; he has the patience of a saint and has certainly needed that over the past three years! My thanks also go to Stuart Greaves, who welcomed me into the group and taught me so much in the first year of my Ph.D. Over the last two years it has been a pleasure to work with Alex Trottier, his guidance and help have been invaluable to this project. Additionally, I would like to thank Emma, Anna, David and Oliver who all brought so much fun to the lab.

Much of this research would not have been possible without the aid of the expertise of several people in the department. I would like to say a huge thank-you to the mechanical and electronics workshops and the glass blowers who have always managed to save the day. I would also like to thank Photek for their help in setting up and fine tuning the detection system, the EPSRC and Durham University chemistry department for funding this project.

Finally, I would like to thank all of my friends and family who have been there along the way, in particular my parents, Helen and Jamie, without whom I would never have got this far.

Abstract

A state-of-the-art crossed molecular beam experiment to study the dynamics of bimolecular reactions of electronically highly excited atoms and molecules has been developed. This was primarily designed to investigate the reaction of highly excited Rydberg hydrogen atoms with D_2 molecules. This reaction is of special interest as it can be compared to the ion-molecule reaction $H^+ + D_2$, using the free electron model and this reaction acts as a benchmark to theoreticians in the quest to understand more complex reactions.

The equipment has been calibrated and tested using the well known photodissociation of HI. The initial reactive scattering ion images for $H^* + D_2$ reaction have been recorded. It was hoped that it would be possible to extract state-to-state differential cross sections; however, to date sufficient resolution has not been achieved, and reasons for this are explored in this study.

An overview of the suitability of the prototype molecular wire 1, 4-bis(phenylethynyl)benzene is also included. In this study UV spectra resolving the torsional motion of the benzene rings have been produced using the technique of cavity ring-down spectroscopy.

Contents

List of Figures

List of Tables

Chapter 1: Literature Review

1.1 Introduction

Reactive scattering experiments aim to gain a truly fundamental understanding of chemical reactivity by analysing the angular, kinetic energy, vibrational and rotational distributions of the products of reactive collisions. When compared with theoretical predictions these observations result in an unparalleled insight into the motion of the atoms during the collision. The level of detail obtained is far greater than that gained from analysing the thermodynamics or kinetics of a reaction and as such provides a more stringent test on the accuracy of theoretical models and calculations.

The simplest chemical reaction is the hydrogen exchange reaction. As such, this reaction has been the prototype for many experimental and theoretical studies and is now considered to be well understood [1].

$$H + H_2 \rightarrow H_2 + H$$

Equation 1

The ion-molecule analogue is understood to a far lesser extent due to the less attractive experimental and theoretical conditions required [2]:

$$H^+ + H_2 \rightarrow H_2 + H^+$$
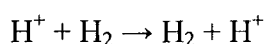
Equation 2

In this chapter some of the key concepts for this study are introduced and previous experiments in this field are reviewed. In the proceeding chapter specific experimental technique development of molecular beam experiments and ion imaging detection are detailed.

1.2 Motivation

The $H^+ + D_2$ ion-molecule reaction is of great scientific interest. The study of this reaction is important as it acts as a benchmark to theoreticians in the quest to understand more complex ion-molecule reactions. Furthermore the reaction between H^+ and D_2 is important in its own right; the large abundance of hydrogen in the universe and the astrophysical importance of H_3^+, which is the intermediate in the $H^+ + H_2$ reaction, makes the reaction of great interest to astrophysicists and astrochemists [3].

The presence of H_3^+ has been discovered in molecular clouds [4], the diffuse interstellar medium [5] and the galatic centre [6], as well as in the planetary atmospheres of Saturn, Jupiter and Uranus [7]. In interstellar space H_3^+ acts as the basis for a large array of ion-molecule reactions, by initiating the chains of reactions that lead to the production of many complex molecular species observed in the interstellar medium [8], and as such is responsible for most of the molecules present in interstellar space. The presence of the IR spectral lines corresponding to H_3^+ in an otherwise almost empty part of the spectrum allows for H_3^+ to be imaged with ground-based telescopes making it an important probe of planetary atmospheres [9].

In plasma chemistry, ion-molecule reactions of hydrogen species are of particular astrophysical interest due to the large abundance of hydrogen and its isotopes [10]. The reaction shown below is both a major source of HD in diffuse interstellar clouds and a method of HD formation in the early universe [11] [12].

$$D^+ + H_2 \rightarrow HD + H^+$$
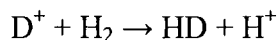
Equation 3

In order to overcome the experimental challenges of the ion-molecule reaction, the ion can be replaced by a Rydberg atom (see *section 1.2*). The energetic similarities of the two species and the unique properties of Rydberg atoms permits the

generalisation of the Rydberg atom scattering experimental results to the ion-molecule reaction [13].

Rydberg atoms play an important part in the chemistry of both laboratory and astrophysical plasmas. They are formed mainly in the outer, cooler regions of plasmas by the recombination of electrons and positive ions [14] [15]. The large relative abundance of hydrogen and its isotopes means that the reactive scattering of $H^* + D_2$ is one of the most common Rydberg reactions in astrophysical plasmas.

1.3 Rydberg atoms

A Rydberg atom is an atom in which at least one electron has a very high principal quantum number, n. Reactive collisions of Rydberg atoms with neutral species are very different to those of their ground-state counterparts [16]. This is due to the large radius of orbit of the highly excited Rydberg electron. The radius of orbit is proportional to n^2 and the binding energy is proportional to n^{-2} as shown in Figure 1.
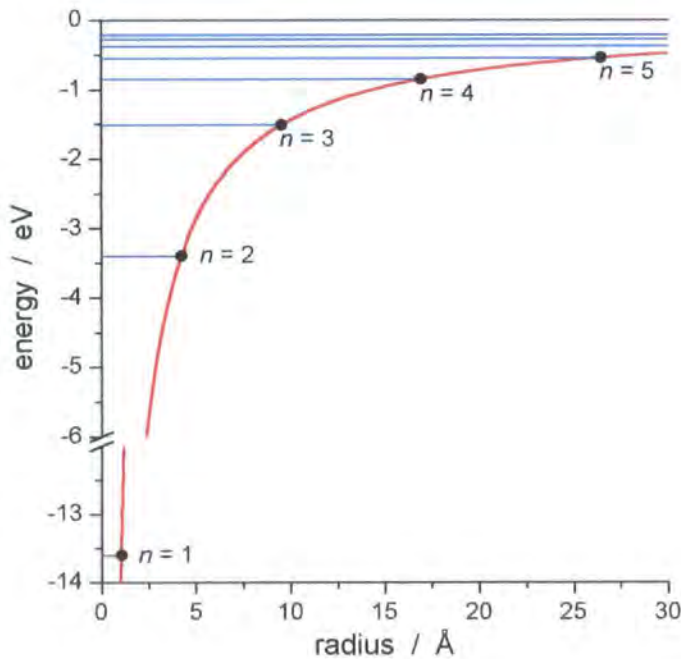
Figure 1: Coulomb potential for electron in hydrogen together with the first few energy levels.

Application of the Bohr model allows this radius to be calculated, along with the root-mean-squared velocity, period of motion and binding energy of the electron. This is shown for $n = 1$ and $n = 30$ in Table 1:

Table 1: Comparison of properties for ground state hydrogen with Rydberg hydrogen atoms [16].

Property	n-Dependence	$n = 1$	$n = 30$
Mean radius, r_n	$n^2 a_0$	5.3×10^{-11} m $(= a_0)$	4.8×10^{-8} m
Root-mean-square velocity of the Rydberg electron, v_n	v_0 / n	2.2×10^6 m s^{-1} $(=v_0)$	7.3×10^4 m s^{-1}
period of the electronic motion, τ_n	$n^3 \tau_1$	1.5×10^{-16} s $(=\tau_1)$	4.1×10^{-12} s
Binding energy, E_n	R / n^2	13.6 eV $(= R)$	15 meV

As the principal quantum number increases, the velocity at which a Rydberg electron orbits the ionic core decreases. Table 1 shows the classical orbital velocity for a hydrogen Rydberg electron with $n = 30$. Its velocity is of the same order of magnitude as the relative velocities of reactants in low energy molecular collisions (in this experiment the relative velocity of the hydrogen is 11270 ms^{-1}) [17]. The Born-Oppenheimer approximation, which assumes that the electrons move rapidly relative to nuclei, does not hold in this case [13].

1.3.1 The independent collider model

The large radius of orbit of electrons in Rydberg atoms has implications for the reactive scattering of Rydberg atoms. The dynamics of Rydberg atom collisions with atoms and molecules are qualitatively different from those involving ground state or low-lying excited state species. For highly excited Rydberg atoms the radius of electron orbit is in the order of hundreds of Angstroms and so is far larger than the effective range of interaction between a charged atom and a neutral species, which is only a few tens of Angstroms. The Rydberg atom is too large to interact with a neutral atom or molecule as a single target, therefore the neutral colliding species can be considered as interacting with the core and electron of the Rydberg atom separately [18].

The independent collider, or free electron model, was first suggested by Fermi to explain spectral line shifts of high-n potassium Rydberg atoms [19], induced by the presence of inert gases at 1 atm [20]. The model simply views the Rydberg atom as two separate quasifree particles, a singly charged ionic core and a companion electron. No connection between the two is made other than that they are travelling at the same speed in the beam. The collision can then consist of either of two separate events: a collision of the ion or the electron with the neutral target. Neither is affected by the presence of the companion particle [16]. In the case of a collision with the ion, the collisions are described by ion-molecule scattering theory, and in the case of a collision with the electron, the collisions are described by electron-molecule scattering theory [21].
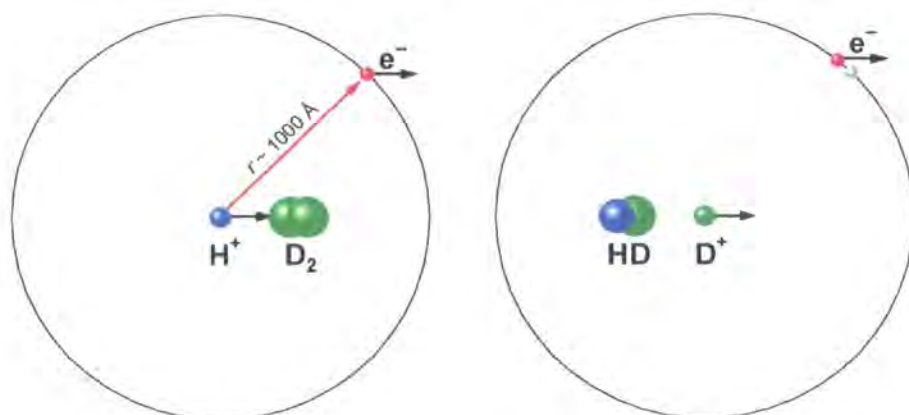
Figure 2: Schematic diagram of a collision of an ion core of a Rydberg atom with a molecule, whereby the electron acts as a spectator.

The independent collider model has been the subject of many experimental studies focussing on different types of collisions [22]. The most studied Rydberg atom-molecule collisions are shown in the list below, where the Rydberg atom and molecule are denoted A* and BC, respectively, with an initial quantum number n, and an angular momentum quantum number l for the A*. The atomic product principal quantum numbers and angular momentum numbers are denoted n' and l' respectively. The current experiment will investigate the reactive collision (Equation 4.10)

$$A^* \ (n,l) + BC \rightarrow A + BC^+ + e^- \qquad \textit{Penning Ionisation} \qquad (4.1)$$

$$A^* \ (n,l) + BC \rightarrow ABC^+ + e^- \qquad \textit{Associative Ionisation} \qquad (4.2)$$

$$A^* \ (n,l) + BC \rightarrow AB^+ + C + e^- \qquad \textit{Reactive Ionisation} \qquad (4.3)$$

$$A^* \ (n,l) + BC \rightarrow A + B^+ + C + e^- \qquad \textit{Dissociative Ionisation} \qquad (4.4)$$

$$A^* \ (n,l) + BC \rightarrow A^+ + BC + e^- \qquad \textit{Collisional ionisation} \qquad (4.5)$$

$$A^* \ (n,l) + BC \rightarrow A^+ + BC^- \qquad \textit{Electron transfer} \qquad (4.6)$$

$$A^* \ (n,l) + BC \rightarrow A^+ + B^- + C \qquad \textit{Dissociative electron transfer} \ (4.7)$$

$$A^* \ (n,l) + BC \rightarrow A^* \ (n, \ l') + BC \qquad \textit{l changing} \qquad (4.8)$$

$$A^* \ (n,l) + BC \rightarrow A^* \ (n' \ l) + BC \qquad \textit{n changing} \qquad (4.9)$$

$$A^* \ (n,l) + BC \rightarrow AB + C^* \ (n', \ 'l) \qquad \textit{reactive collision} \qquad (4.10)$$
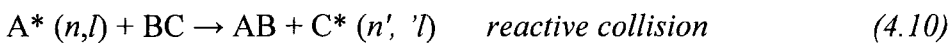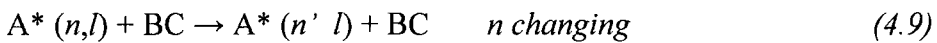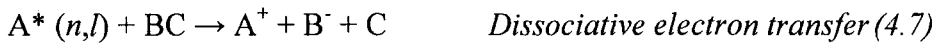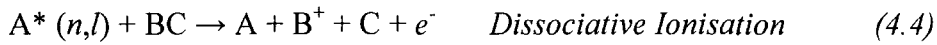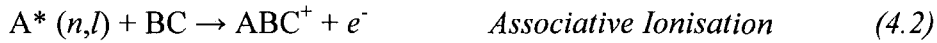
Equation 4

The majority of the evidence in support of the independent collider model has arisen from theoretical and experimental investigations of collisional ionisation reactions *4.5*. These reactions involve high-energy collisions between the Rydberg electron and a neutral target atom or molecule.

Many experiments have confirmed the validity of the free electron model for a wide range of Rydberg scattering phenomena [13]. Koch [23] and Wang *et al.* [24] confirmed that the collision destruction cross-sections for hydrogen and deuterium Rydberg atoms at high translational energies (2.5-40 keVu^{-1}) are equal to the sum of the electronic and ionic cross-sections. Dunning also found agreement with the independent collider model for molecular collisions at low energies (~ 4 μeV), where Rydberg atoms at low velocities were used as a source of low energy electrons [25]. Kocher and Smith investigated collisions where the ion-core was scattered as if the Rydberg electron were absent [26]. The cross-sections of low energy collisions between lithium atoms in high Rydberg states

and various target gases were shown to be in good quantitative agreement with those calculated for ion-core collisions. They were also found to be virtually independent of the principal quantum number, n, of the Rydberg electron, as predicted by the independent collider model. Delpech *et al.* [27] studied excitation exchange in collisions of helium Rydberg atoms with ground-state helium, see reaction in Equation 5.

$$^3\text{He } (n = 9) + {}^4\text{He } (n = 1) \rightarrow {}^3\text{He } (n = 1) + {}^4\text{He } (n = 9)$$
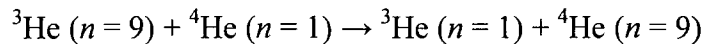
Equation 5

This reaction can be thought of as a charge-transfer reaction between an ion and an atom. The Rydberg electron was found to act as a spectator during this type of reaction. Further evidence in support of the free electron model was presented by Davis *et al.* [13], in their study of inelastic collisions of H^* atoms ($n = 30\text{-}50$) with non-polar molecules (N_2 and O_2) at a collision energy of 1.84 eV. Great similarity was observed between the experimental inelastic collisions and those calculated through ion-molecule theory; additionally a lack of n-dependence again suggested that the quasi-free electron acted as a spectator.

However, as early as 1986, Watel *et al.* [28] reported discrepancies from the free electron model for some collisional ionisation reactions with atoms in low lying Rydberg states ($n = 14$, 15, or 16). The authors later went on to show that He atoms in well defined low-Rydberg states interacting with SF_6 (see Equation 6) (alternatively with NO_2) are not explained by the free electron model [29].

$$\text{He* } (n = 14, {}^1\text{P}) + SF_6 \rightarrow \text{He}^+ + SF_6^-$$
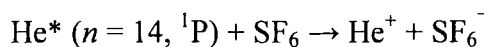
Equation 6

Through study of the behaviour of the Rydberg atom's outer electron, again in ionisational collisions for He ($12 \leq n \leq 15$) on Xe and N_2 Renwick demonstrated that although the colliding partners are unaffected by the spectator, the spectator may be affected by the details of the collision [18].

1.4 Molecular collisions

Molecular collisions are governed by the same basic physical laws as macroscopic collisions, for example, the laws of conservation of energy and momentum. Individual collisions are characterised by an impact parameter, b, the relative velocities of the colliding species, v_{rel}, and the scattering angle, θ. In scattering experiments the relative velocities of the colliding species can be controlled, for example by using crossed molecular beams of reactants with specific energies, where the scattering angle is typically one of the variables to be measured. However, there is no way of controlling the impact parameter for practical reasons as macroscopic beams are used, and ultimately due the uncertainty principle. Thus, collisions involving all values of b will occur as depicted in Figure 3.
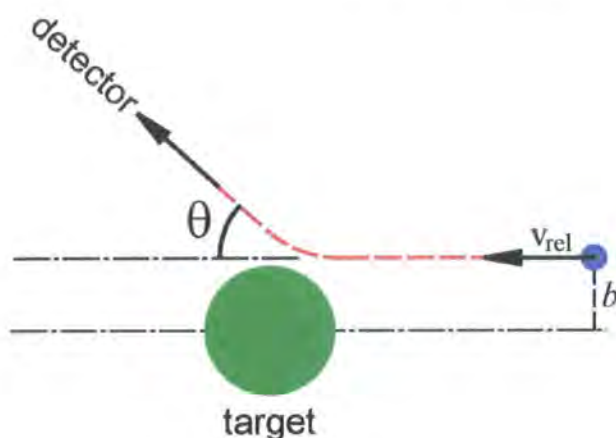
Figure 3: Schematic diagram of a collision between two particles.

1.4.1 The reactive cross section

The study of reactive collisions is complicated by the presence of unreactive inelastic and elastic scattering events. During elastic collisions kinetic energy is conserved and is merely transferred from one species to another. However, inelastic collisions involve the transfer of energy between translational and internal (electronic, vibrational and rotational) degrees of freedom, and kinetic energy is not conserved. The opacity function, $P(b)$, takes into account these unreactive scattering events and defines the probability of a reaction at a specific impact parameter (see Figure 4). The cylindrical symmetry of scattering processes

about the relative velocity vector allows the reactive cross section, σ_r, to be defined by Equation 7.

$$\sigma_r = \int\limits_0^\infty P(b) 2\pi b \, db$$

This is the effective area that the target molecule presents to the incident species that leads to a reaction. It can be measured for specific reactant and product states to produce a state-to-state reaction cross-section.
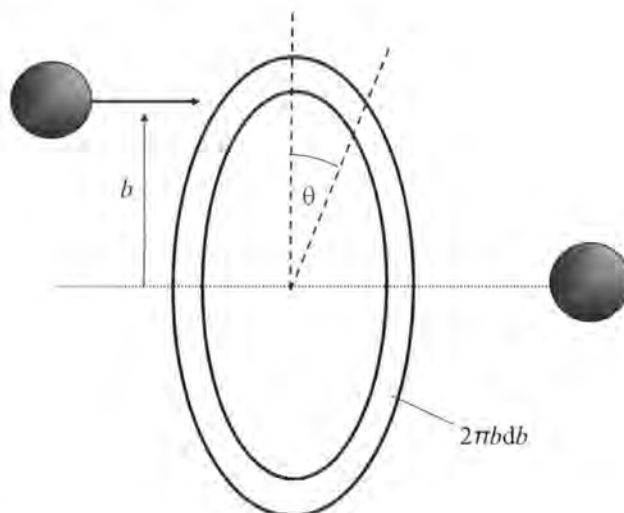
Figure 4: The dartboard averaging over impact parameter. The circumference of a circle b is $2\pi b$ and thus $2\pi b \, db$ is the area of the "dartboard" ring with radius b and thickness db. Adapted from ref [30].

1.4.2 The differential cross section

When two molecules collide the products are scattered in a variety of directions relative to the direction of approach. The differential cross section characterises the angular dependence of the scattering process and is sensitive to properties which are not easily obtainable from experimental study, such as the opacity function. Therefore the differential cross section is one of the most detailed measurable properties of a chemical reaction that can be used to comparatively study the accuracy of theoretical predictions.

$$\sigma_t = \int_0^{2\pi} \int_0^{\pi} \frac{d\sigma_r}{d\omega} \sin\theta \, d\theta \, d\phi$$

The differential cross section is denoted dσ/dω, and is a function of the scattering angles, θ and φ (see Figure 5) and has units of area per solid angle.
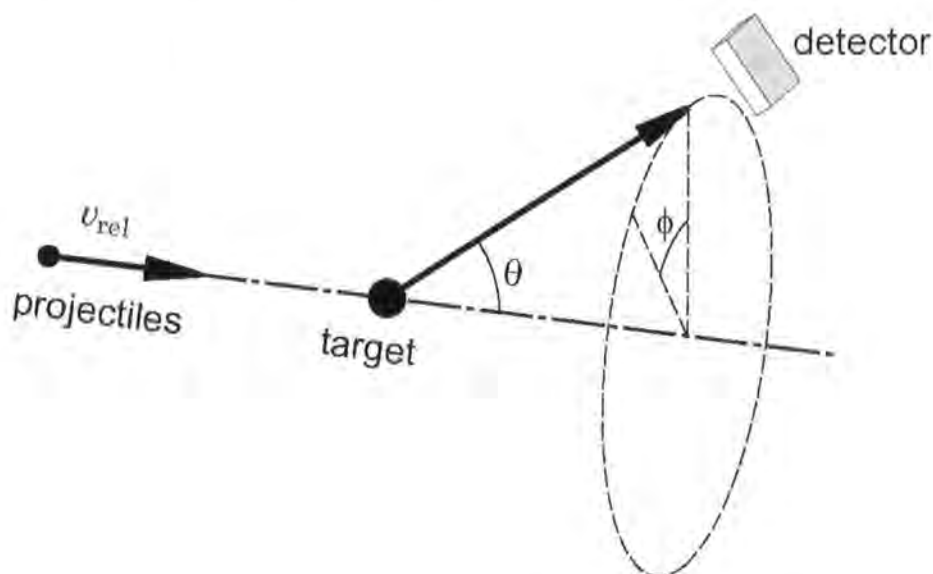
Figure 5: Schematic diagram that depicts the different angles in which products can scatter.

1.5 Experimental studies

In the following section experimental studies of the neutral hydrogen exchange reaction, the ion-molecule analogue and also the Rydberg-molecule reaction are detailed. In experimental studies a hydrogen species is often replaced with a deuterium isotopologue for ease of product detection.

1.5.1 Early experiments: Neutral reaction

The following gives an overview of study on the neutral analogue to the ion molecule reaction, (Equation 1). The general development of crossed molecular beams experiments is discussed in the following chapter (*section 2.2*).

In 1972 Gedded *et al.* researched collisions between deuterium atoms and hydrogen molecules in a crossed beam experiment [31]. They determined both the angular distribution and HD mean velocity as a function of angle and deduced the relative differential reactive scattering cross section in centre of mass coordinates. This was the first experiment to yield a total differential cross section for this reaction. Gotting *et al.* presented results of the first molecular beam scattering experiment on the D + H_2 reaction with both angular and velocity resolution at a collision energy of 1.5 eV using a rotatable time-of-flight mass spectrometer [32]. However, the resolution in this experiment was limited by the broad speed distribution of reactant atoms formed in an arc discharge source. Buntin *et al.* used a pulsed beam technique to provide sufficient resolution to separate the product vibrational states in the reactive differential cross section for the first time [33].

Welge and co-workers preformed a series of experiments at a variety of collision energies, which produced fully rovibrational state resolved differential cross sections for the H + D_2 ($v = 0, j = 0$) reaction [17] [34] [35] [36]. The detail and quality from these experiments allowed a critical assessment of various theoretical predictions. As the experiment in this study is loosely based on the the experiment by Welge and co-workers, the experimental technique employed by the group is overviewed here. A pulsed molecular beam of ortho-D_2, in its rovibrational ground state ($j = 0, v = 0$) crossed H-atoms, generated from the photodissociation of HI in a second molecular beam. Following the collisions, the velocity distribution of the nascent D-atoms was measured using the Rydberg atom time-of-flight technique. Nascent D atoms were excited in a two-photon process into Rydberg atoms:

$$D \ (1s) + hv_1 \ (121.6 \ nm) \rightarrow D \ (2p)$$

$$D \ (2p) + \ hv_2 \ (365 \ nm) \rightarrow D^* \ (n \approx 40)$$
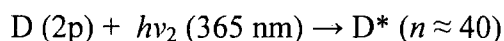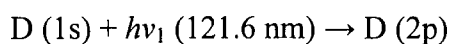
After excitation the D^* atoms continue to drift at their post collision velocity. They were detected at the end of the drift tube by a rotatable detector. The Rydberg atoms were field ionised and detected by a secondary electron multiplier.

Employing a similar experimental technique, Yang *et al.* studied the reactions H + HD ($v = 0, j = 0$) and H + D_2 ($v = 0, j = 0$) [37] [38] [39]. Using a specific LAB detection angle corresponding to backwards scattering, the HD ($v = 0, j = 2$) product cross-section was measured at nineteen energies between 0.4 and 1 eV. In comparison with quantum scattering theory it was concluded that the oscillations in cross section were due to a quantum bottleneck opening up at different collision energies [40].

1.5.2 Early experiments: Ion-molecule reaction

Since the 1960s many experimental and theoretical methods have been developed to study hydrogen ion-molecule collisions [10]. There have been measurements for both cross-sections and rate coefficients. In general, low temperatures are achieved by cryogenic cooling or by supersonic expansions.[41]

1.5.2.1 Swarm techniques

Much kinetic and thermodynamic data has been obtained for ion-molecule reactions by studying flowing afterglow (FA) and selected-ion flow tube (SIFT) techniques. Adams and Smith [42] used a variable-temperature selected-ion flow tube (VT-SIFT). SIFT uses a mass analysed beam of ions injected into a carrier gas; this also allows for the study of isotope exchange in ion-neutral reactions. The standard VT-SIFT was limited to liquid nitrogen temperatures (80 K). In 1983 Bohringer and Arnold developed a drift tube apparatus that was cooled with liquid helium [43]. In this experiment temperatures as low as 20 K have been obtained [41]. These experiments involving cryogenic cooling have the inherent disadvantage that condensation of the target or buffer gas restricts its range of applicability. The use of supersonic expansions allows for the study of reactions at low temperatures and avoids this problem. An example of the use of supersonic expansion is the CRESU (Cinetique de Reaction en Ecoulements Supersoniques Uniformes) technique [44]. In this experiment ions are injected into the core of several centimetre thick supersonic flow of He containing a small amount of the neutral molecules as reactants. Kinetic data at temperatures as low as 8 K have

been obtained [45]. The development of the free jet reactor by Smith in 1998, has provided the possibility to reach temperatures below 3 K [46].

1.5.2.2 Beam methods

The only beam method where ion beams with a laboratory kinetic energy of a few meV can be prepared with sufficient intensity is the guided ion beam (GIB) method [47] [48]. In an ion beam gas cell experiment a beam of ions is guided into a scattering chamber filled with the target gas, the ions emerging from the chamber are detected by mass spectrometry [49]. The scattering cell can be replaced with crossed or merged supersonic beams [50] [51].

Crossed beam experiments typically used proton beams, generated using an ion accelerator, crossed with a D_2 beam: the product ions were recorded by mass spectrometry. In a guided beam experiment, electric fields guide an ion beam into a scattering chamber containing a low pressure of D_2 gas, the variation from the ion beam gas cell experiment lies in the detection method, the product ions are drawn out of the scattering chamber and into the detector by electric fields.

1.5.2.3 Ion traps

A variety of ion-traps have been used since the 1960s for studying ion-molecule reactions. It is possible to confine ions for a long time using stable electric or magnetic fields, and thermal conditions can be obtained using a buffer gas. The most common techniques used in chemistry are the ion cyclotron resonance apparatus and the Paul trap [41]. In order to cool ions in radio frequency ion traps to low temperatures, electrode structures with wide field-free regions are necessary. Traps consisting of stacks of ring electrodes have been used successfully; in several laboratories a linear 22-pole trap [52] has been implemented for this purpose. The ion confinement region is encapsulated by walls cooled by a closed cycle refrigeration system. The nominal temperature can be varied between $T = 10$ and 300 K. The translational and internal degrees of freedom of the ions are coupled to the cold environment by inelastic collisions with helium or hydrogen as buffer gas.

Primary ions are prepared in an external ion source, whereby they are mass selected and formed to a very slow beam. Injection and extraction of ions occurs *via* pulsed entrance and exit electrodes closing the linear mulitpole in the axial direction. In the absence of a target gas the mean-decay time is determined by reactions with background gas, the pressure of which is estimated to be below 10^{-11} mbar at 10 K.

1.5.2.4 Results

Figure 6 shows a selection of the $D^+ + H_2$ measured rate coefficients with different techniques. The experimental measurements from the beam experiments are cross sections that have been converted into effective rate coefficients for comparison.
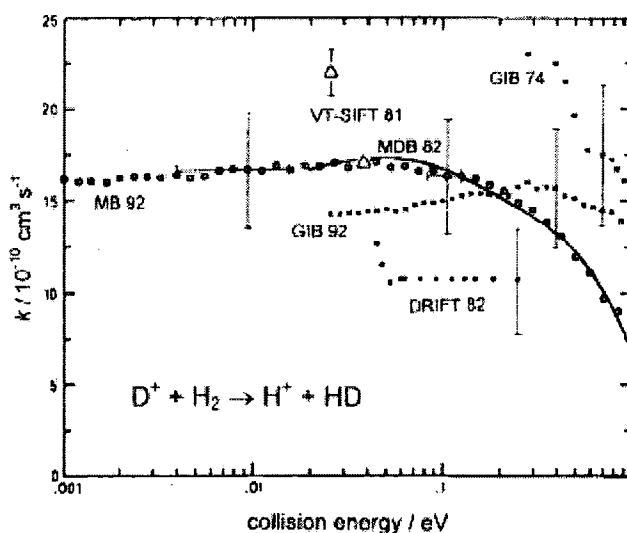
Figure 6: Energy dependence of the rate coefficients for $D^+ + H_2 \rightarrow H^+ + HD$ measured with different instruments, taken from [41]. GIB 74: [47], VT-SIFT: [53], DRIFT 82: [54], GIB 92 and MB 92: [55]. The line shows a rate coefficient calculated by Gerlich [55].

However, the analysis and modelling of the processes requires not only total cross sections or rate coefficients, but also state-selective cross sections to satisfy the demands of the increasingly sophisticated chemical models.

1.5.3 Recent experiments: Rydberg atom scattering

To date, two groups have studied reactive scattering crossed-beam experiments of Rydberg hydrogen atoms with molecular deuterium (reaction shown in Equation 9). Wrede *et al.* were the first to investigate this reaction by adapting the experiment previously employed to probe the neutral reaction described in *section 1.4.1* [17]:

$$H^* + D_2 \rightarrow D^* + HD$$
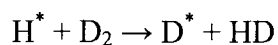
Equation 9

The neutral experimental technique was altered such that the Rydberg excitation laser was moved from the scattering region, where it excited the product atoms, to the path of the incoming H atoms in order to excite the reactant hydrogen atoms [2]. The experiment worked by comparing the results from the two different laser positions i.e. excitation before and after the collision. When the excitation took place prior to the collisions, a much stronger signal of product D^* was observed see Figure 7.
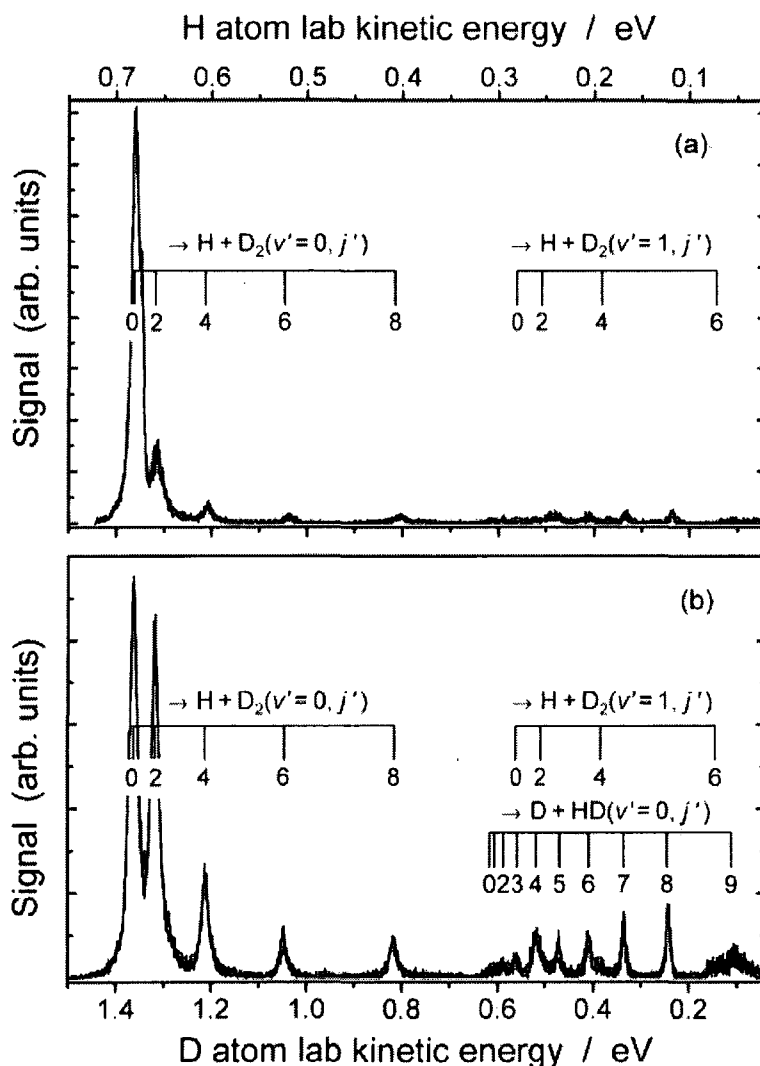
Figure 7: Kinetic energy spectra of detected H*/D* Rydberg atoms a) Rydberg excitation after scattering and b) Rydberg excitation before collision [2].

This method produced kinetic energy spectra for six lab angles between 7.5° and 50°, with a collision energy of 0.53 eV. The spectra displayed full rotational resolution, and therefore, it was possible to compare the rotational populations at these angles with an expected distribution. The peaks were found to be largely statistically populated. Additionally, a measurement was made of the total angular distribution with respect to the lab scattering angle, between 7.5° and 143° as depicted in Figure 8. This data showed a reasonable amount of random scatter, and so it was not sufficient to produce differential cross sections, or to convert the other results to the centre of mass frame. It appeared from the data that there was a

significant amount of backwards scattering but comparatively little forward scattering.
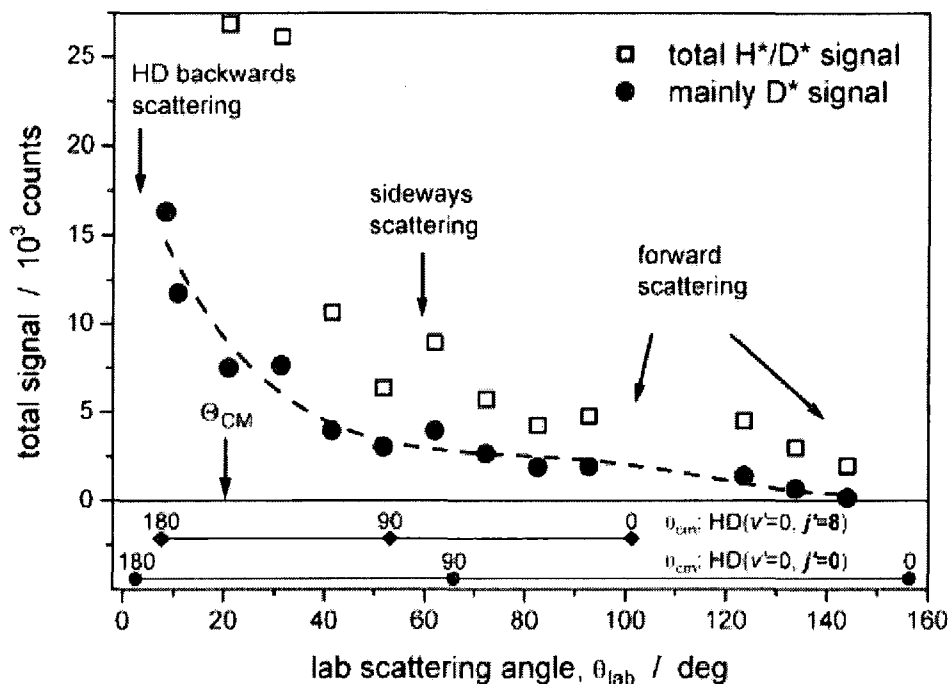
Figure 8: Total H* and D* signal from H* + D$_2$ ($v = 0$, $j = 0$) collisions as a function of lab scattering angle. The correspondence between D* laboratory angles and product HD centre-of-mass scattering angles is depicted in the lower panel for fast ($j= 8$) and slow ($j = 0$) products [2].

The second investigation employed a similar experimental set-up to that used in the time-of-flight study in the previous experiment [2]. This experiment also used a similar collision energy of 0.526 eV and obtained state resolved kinetic energy at a variety of lab scattering angles [56], one of which, (5°) was compared with results from a previous study by Gerlich [57], on the ion molecule reaction, which used a single scattering angle of 5°. The experiments showed good agreement with the exception of the $j' = 4$ peak; this peak was found to be due to the overlapping of the reactive product of HD ($j' = 4$) with the inelastic products of D$_2$ ($v = 0$, $j = 10$) as well as D$_2$ ($v = 1$, $j = 2$) as shown by * in Figure 9.
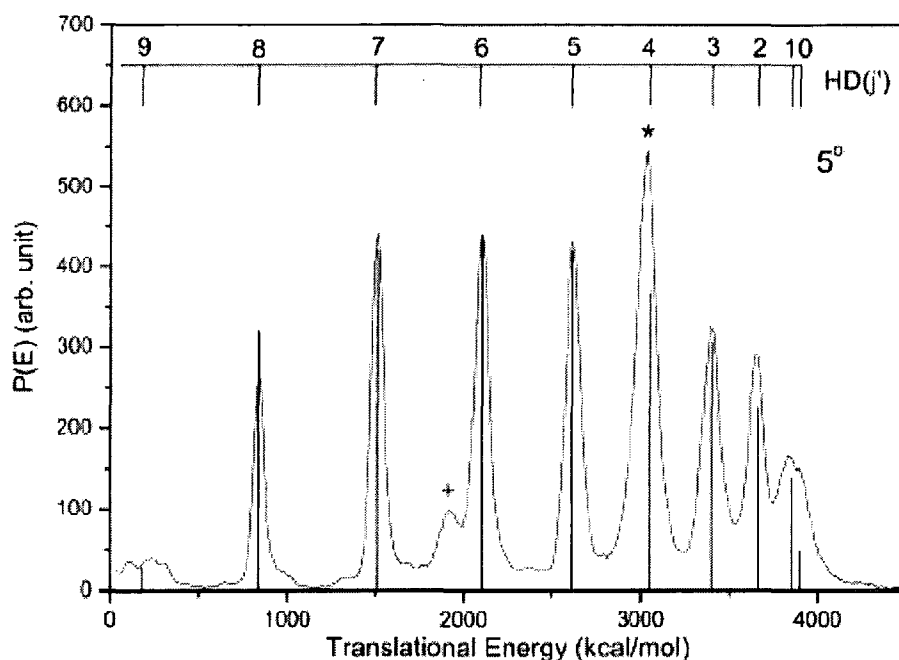
Figure 9: Translational energy distributions of the $H^* + D_2 \rightarrow D^* + HD(v = 0, j')$ reaction at the lab angle of 5°. The sticks are the partially rotationally resolved studies of the ion molecule reaction also at a lab scattering angle of 5° [56].

In addition to this work, quasi-classical theoretical calculations for the ion-molecule reaction were carried out to facilitate a more complete comparison to the Rydberg atom reaction [58] as shown in Figure 10. These comparisons supported the free electron model argument, showing that the Rydberg atom scattering proceeds though the ion-molecule mechanism. The angular product distributions exhibit characteristic forwards-backwards peaks in both the calculations and experiment. However, a difference occurs in the appearance of a higher level of forward-backwards asymmetry of the differential cross section in the experimental measurement.
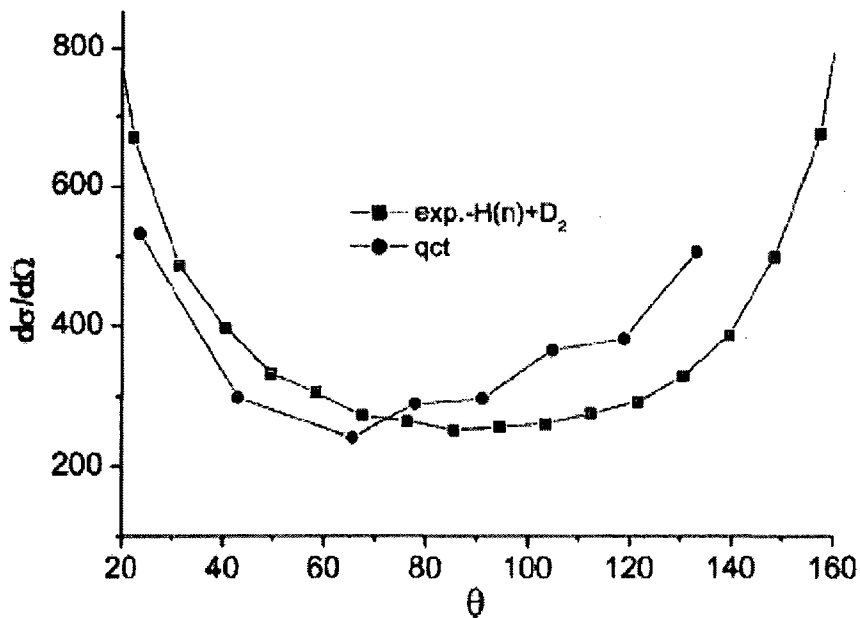
Figure 10: The total differential cross section for scattering angles obtained from the experiment and quasi-classical theoretical calculations. The label on the figure is wrong, and the ■ refers to QCT.

Recently this higher degree of forwards-backwards asymmetry has been assessed and is thought to be due to the difference in the Rydberg atom-molecule and ion-molecule reaction [59]. The ionic core-Rydberg electron coupling may not be negligible in the experiment, which means when comparing the Rydberg atom-molecule reactions to the ion-molecule experiment, this effect must be taken into account. Four mechanisms (relaxation or ionisation phenomena) by which the principal quantum number, n, may change and possibly fall bellow the detection threshold ($n \approx 20$) were outlined. It was found that at least part of the asymmetry found in the measured differential cross section could be due to some angle dependent attenuation of the signal detected on the experiments.

1.6 Theoretical studies

1.6.1 The potential energy surface

In order to carry out theoretical studies the potential energy surface of the system is required. Recently, Gonzales-Lezana *et al.* have produced a potential energy surface (PES) for the $H^+ + D_2$ reaction [60].

The important features of the PES are the deep potential well of about 4.0 eV with no barrier to entry, and the crossing between the energy curves of the electronic states correlating to infinitely separated $H^+ + H_2$ and $H_2^+ + H$ at about 1.6 eV above the H_2 well [61]. Alternative potential energy surfaces are available [62] [63].
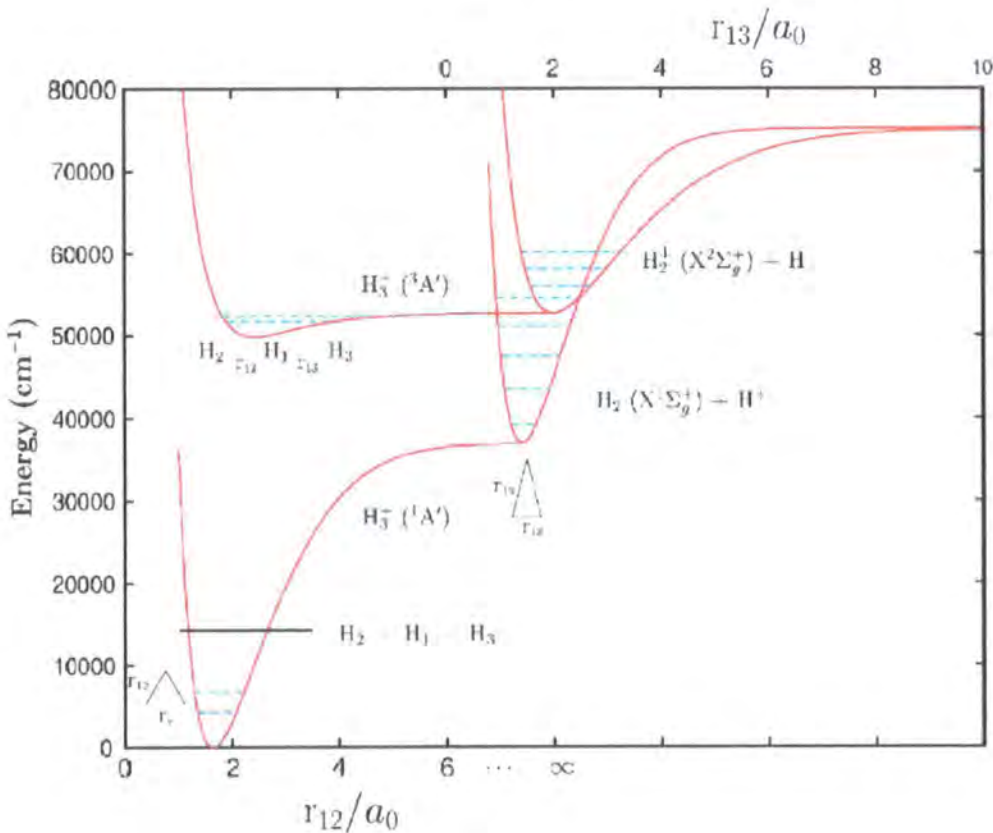
Figure 11: Energy diagram of the electronic energy levels of the H_3^+ system [60].

1.6.2 Quasi-classical trajectories

The first theoretical investigations on the dynamics of reactive collisions were carried out during the 1930s by classical trajectory calculations [64] [65]. Since the 1960s quasi-classical trajectory, QCT, calculations have developed rapidly. The prefix 'quasi' comes from the assignment of quantum states to the rotational angular momentum and rovibrational energy of reactants and products [66]. QCT calculations have been traditionally employed for studying this reaction. QCT uses classical (Newton) mechanics to calculate the motion of the nuclei during a collision by following the trajectories for each particle. The forces required to solve Newton's equations are provided by quantum mechanically calculated potential energy surfaces. The trajectories are started with positions and momenta corresponding to quantum states. After the products have separated, their motions are analysed, and as classical mechanics does not include quantisation, the continuous quantum numbers determined from the calculation are typically rounded to the nearest integer.

This model is computationally "cheap" compared with quantum studies. Typical quantum effects such as tunnelling, non-adiabatic transitions, interference phenomena, resonance features, or zero-point energy constraints are not described by classical mechanics. In reactions whereby these effects do not play a large role in the overall dynamics and kinetics of the chemical reactions, QCT provides a good agreement with more computationally demanding techniques. Whilst QCT does not provide the most detailed calculations and predictions it can provide the general aspects of a reaction.

1.6.3 Statistical Mechanics

Insertion reactions are more difficult to study with quantum mechanics than abstraction reactions due to the deep potential well; all of the bound and low-lying resonance states of the collision complex provide a greater challenge for the computational models. Rackham *et al.* suggest that an exact quantum mechanical method may not always be necessary [67]. They report that if the resonances are

sufficiently long lived, a simple statistical treatment of their formation and decay into reactant and product channels may be enough to provide satisfactory conclusions [68]. The method treats the formation and subsequent fragmentation of the intermediate species separately. The state-to-state reaction probability for the complex is calculated, as the product of the individual capture probability for the complex to be formed from the initial state and the fraction of collision complexes which decay to the final state. Rackham *et al.* [68], have found that a statistical treatment of the reactions N (^{2}D) + H_2 and O (^{1}D) + H_2 gives good agreement with the state-to-state integral cross sections calculated by Honvault and Launay [69] [70], who used exact time-independent quantum mechanical methods.

1.6.4 Quantum mechanics

For a full description of a reactive collision a quantum mechanical approach is required. Quantum mechanical calculations solve the Schrodinger equation for the motion of the nuclei and as such they are more mathematically and numerically intensive. This leads to the calculations being computationally more "expensive" and as a result they provide a complete picture for a given reaction, in the sense that they contain all quantum effects that are not included in QCT and statistical calculations. It was hoped that the experiment in this study would produce data of a level that could be used to asses the quality of the different methods.

In recent work Gonzales *et al.* have used a variety of methods to perform calculations on the H^+ + H_2 ion molecule reaction [71] [72]. The calculations used the potential energy surface from Aguado *et al.* [62]. They compared state-to-state differential cross sections from QCT, SQM and two quantum mechanical methods. These were the time independent exact quantum (TI EQM) and quantum wavepacket (QWP) methods.

TI EQM are more efficient when only a few collision energies are of interest [71]. The time independent method takes a fixed energy and provides the cross-sections from all reactant channels into all product channels. In contrast the QWP method calculates cross sections for a given reactant channel into all product channels for

all simultaneous energies that are included in the wavepacket. As a result, the most suitable method depends on the system in question; for an experiment at fixed energies with many reactant channels contributing, the TI EQM method would be most suitable. However, most experimental systems start from few reactant channels and are conducted at a range of energies, which would result in the QWP calculations being the most advantageous (although this does depend on the system).

Quantum wave packet calculations for the $H^+ + H_2$ ion-molecule reaction are difficult due to the presence of many long lived resonances which may cause the calculation to become trapped in the potential well and a further difficult arises from the necessity of including many helicity components to obtain converged results [72]. The TI EQM also suffers from the latter and has a technical difficulty with the system as all the bound states must be considered.

$$H^+ + D_2(v=0, j=0) \rightarrow HD(v'=0, j') + D^+$$
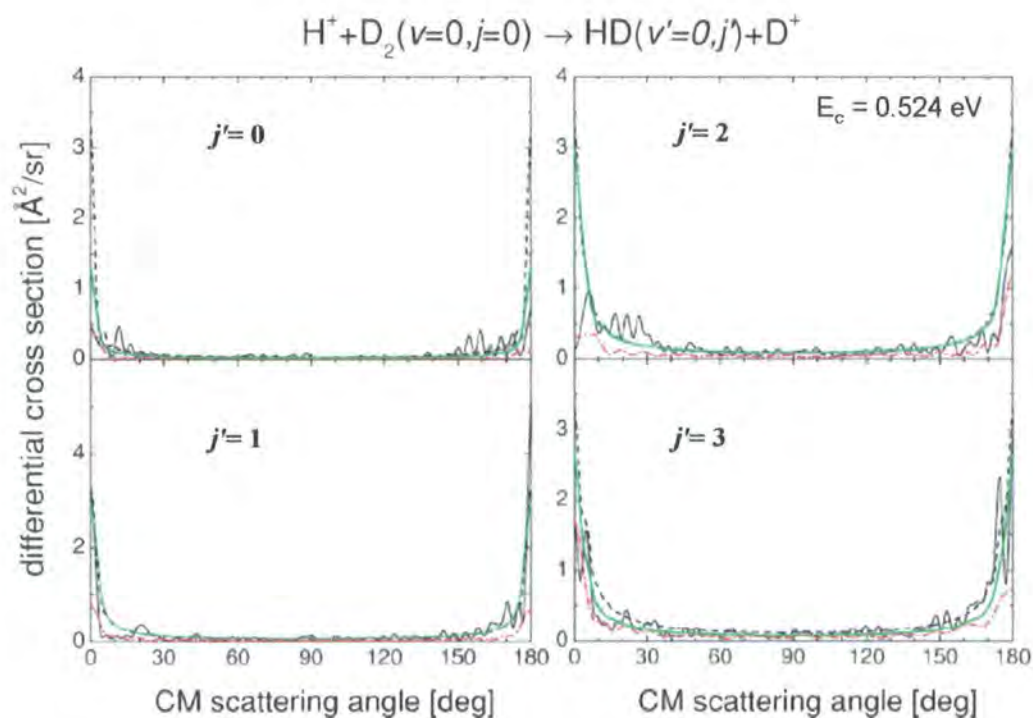
Figure 12: Rotationally state resolved differential cross sections calculated at 0.524 eV collision energy by means of EQM (black line), QWP (green line), QCT (red line) methods and SQM (dashed line) [71].

Carmona *et al.* calculated both the dependence of the product ro-vibrational state distribution on collision energy and the probability of molecules in specific rotational states relaxing with respect to collision energy [71]. The differential cross sections calculated using the different methods are shown in Figure 12.

All calculation show a bias towards forwards-backwards scattering with little sideways scatter. On close inspection the different methods show varying features, SQM shows symmetric forwards-backwards scattering. The other methods show features of forwards-backwards asymmetry. The TI EQM shows a series of oscillations that are not observed in the QWP. This is a feature that requires confirmation by experimental observations. If these oscillations are sensitive to small energy changes, they may be averaged out over the energy spread of the experiment, as mimicked by QWP result. Experimental results will also provide an indication as to whether the computationally less demanding methods such as SQM provide sufficient accuracy for comparison of theory with experiment.

The QCT calculations have been compared to previous experimental studies [71], by Wrede *et al.* [2] and Song *et al.* [58] but to date experimental results of high enough clarity have not been available to test the EQM calculations. The previous experiments have produced state resolution but have only supplied limited angular resolution. This study will employ ion imaging (see *section 2.3*) which has the potential to provide full angular resolution.

Chapter 2: Experimental Techniques

2.1 Chemical reaction dynamics

A single chemical event may be defined as a collision in which the species involved change their chemical identity through the cleavage and formation of chemical bonds. These collisions must conserve energy and momentum, as a consequence the final result of a chemical reaction is determined completely by the forces and energetics involved in the reactive collision. There are many factors that determine the outcome of a reactive collision from the chemical identity and structure of the reactants, to their relative orientation and velocity, and their electronic, vibrational and rotational states. The holy grail of chemical reaction dynamics is the measurement of flux-velocity contour maps for quantum state-selected products from photofragmentation, inelastic and reactive collision processes.

The dynamics of chemical reactions can be probed in detail by experiments that are sensitive to both reactant and product internal state energy distributions and velocities. A key progression in the field has been through the development of crossed molecular beam scattering experiments and the recent development of ion imaging, introduced in 1987 by Chandler and Houston [73]. This provides an attractive alternative detection method to traditional methods.

In this chapter I will give an overview of both traditional crossed molecular beam studies and ion imaging as these are the two key techniques that have been used in this study.

2.2 Molecular beam studies

The products of the reactive collisions of interest must be detected before the information they hold is lost through secondary collisions. These single-collision conditions are produced by the use of low pressures, which ensure that the time it takes the products to reach the detector is much shorter than the average time between collisions.

2.2.1 Early developments

The study of single collisions between neutral atoms and molecules has developed through the use of molecular beams. Prior to 1954, neutral collisions had been studied to a far lesser extent than collisions involving ions or electrons. Work by Bull and Moon started off the field of crossed-beam reactive scattering [74]. For the first time they showed that it was possible to obtain intense beams of heavy atoms (Cs) or molecules (CCl$_4$), moving at known and roughly equal speeds. They demonstrated that it was possible to study the collisions made by crossing one beam of atoms or molecules with a second, by observing the times of arrival of the products of such collisions at a suitable detector (in this case an anode).

The concept developed further by Taylor and Datz, with the invention of the hot-wire surface ionisation detector [75]. This invention has been described as being the birth of experimental reaction dynamics [76]. For the first time this experiment demonstrated the feasibility of studying chemical reactions with molecular beams, by fulfilling the primary requirement: detecting the reaction products with adequate sensitivity and reproducibility[77].

There was a great expansion of work in this field following the discovery of Taylor and Datz, this has become known as the "early alkali age" [76]. Several groups were pursuing reactive scattering studies by the 1960s, and in this time product angular and translational energy distributions were measured for a large variety of alkali atom reactions [78]. The technique was limited to alkali atoms, for which surface ionisation provides a uniquely sensitive and specific detector. The low ionisation potential of alkali atoms makes it possible to use surface ionisation.

In these reactions ionic bonding is dominant whereas covalent bonding is dominant in most chemical reactions and as such the detection system was not sufficiently sensitive to measure such reactions.

The community was revolutionised by a new generation of crossed-beam machine built by Lee *et al.* [79], which provided an opportunity to tackle more important reactions of interest to the chemistry community. Prior to this work attempts had been made to study reactive scattering of reactions such as $D + H_2$ and $H + D_2$, where products were detected using electron bombardment ionisation [80] [81].

By the late 1960s the "universal" detector used in molecular beam spectroscopy was electron bombardment ionisation with mass analysis [82] [83] [84]. However, the interfering back ground was high and the dynamical features of interest could not be determined despite long acquisition times [81] [80]. Lee *et al.* used differential pumping of the source and detection region to significantly reduce the interfering background in the electron bombardment region and avoided creating background in the ionisation region.
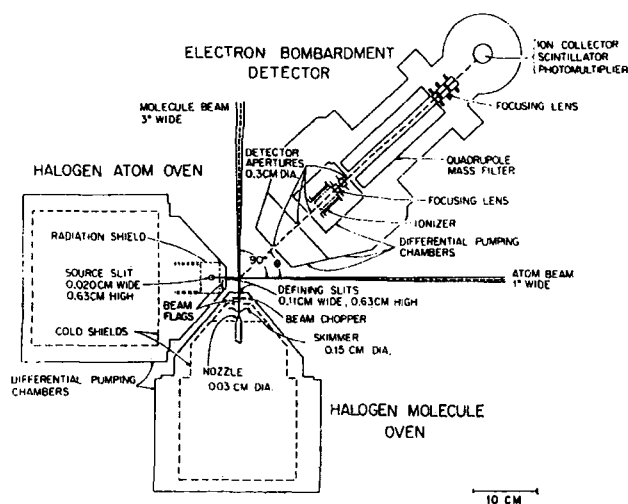
Figure 13: Top view of apparatus used by Lee *et al.* [79] showing differential pumping for detector and source chambers. Also shows the beam geometry.

In 1974 Schultz *et al.* introduced the laser induced fluorescence, LIF, technique to interrogate the product internal state distribution [85] [86], further widening the scope of chemical dynamics [87]. In the 1980s, activity of the field peaked and experimental techniques became more sophisticated. Neumark *et al.* used crossed

molecular beams for studies of F + H_2 (D_2, HD) [88]. The vibrationally state-resolved differential cross section for F + H_2 was the most detailed experimental study in reaction dynamics of its time. There were advances in the detection methods used; besides LIF, coherent anti-Stokes Ramen spectroscopy was used by Gerrity and Valenentini to determine quantum state distributions for the product state distributions for the HD product from H + D_2 [89]. Similar measurements were performed by two further groups using different detection methods. Marinero *et al.* used multiphoton ionisation [90] and Dahv *et al.* used resonance-enhanced multiphoton ionization (REMPI) [91].

An overview of molecular beam studies relevant to this study was provided in *section 1.4* where more recent studies such as Rydberg atom tagging and TOF spectroscopy have been detailed; experiments such as these have vastly improved the ability of exploring chemical reactivity in the gas phase. The Nobel prize in Chemistry was awarded to the leaders in this field in 1986, Herschbach [92], Polanyi [93] and Lee [94] for their inclusive experimental and interpretive work on the dynamics of elementary gas-phase reactions. This perhaps symbolises the success of this research area.

2.3 Ion imaging

Ion Imaging techniques allow the spatial distribution of a product species to be visualised directly by yielding the entire three-dimensional angular and velocity distribution of a photolysis or reaction product in a single digital snap shot. Qualitatively it provides a direct visualisation method into the core of a chemical process.

2.3.1 Early experiments

In 1955 Wiley and McLaren introduced the time-of-flight (TOF) mass spectrometer [95]. This technique uses electron impact in the source region to produce ions. The ratio between the fields of the source and acceleration region causes the ions to all arrive at the detector at the same time for a specific charge-

to-mass ratio (where $TOF \propto \sqrt{mass}$). The set up is shown in Figure 14. While the ions are being formed, the backing plate and first grid have the same voltage. At all times the second accelerating region, d, has an electric field, while region D, the drift tube, is field free. A positive pulse is applied to the backing plate, which determines the start time, producing the electric field E_s; this accelerates the ions from the source to the detector. The velocity of the ions in the flight tube is a function of their charge-to-mass ratio, and upon reaching the detector the ions have been separated into bunches corresponding to this ratio. If only singly charged ions are present, the lightest group reaches the detector first and is followed by groups of progressively heavier mass.
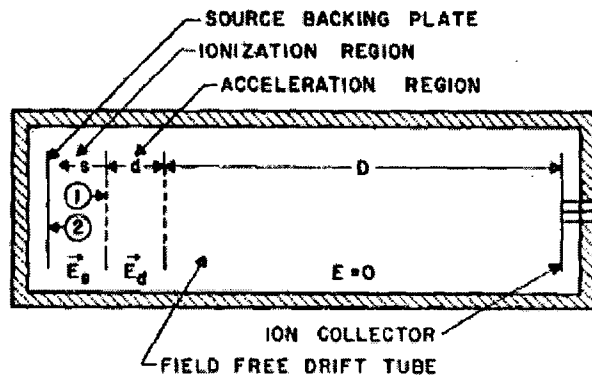
Figure 14: Time-Of-Flight mass spectrometer [95].

2.2.2 Ion Imaging

The inspiration for the development of the modern ion-imaging technique was provided by Solomon's photolysis mapping experiments in 1967 [96]. This was the first experiment in which the spatial distributions of reaction products were imaged directly. The images in the experiment were seen in a photolysis cell, a glass hemisphere coated on the inside with a thin film of tellurium see Figure 15. Polarised light from a mercury lamp was used to photolyse IBr samples within the cell; after hours of exposure to the light an anisotropic lightening of the tellurium coating was observed due to etching by the halogen atom photofragmentation. This experiment provided information about the direction of the scattered products. An angular pattern with respect to the polarisation of the light was

obtained. In contrast to more recent crossed beam experiments which have a rotatable detector, here all angles are measured at once.
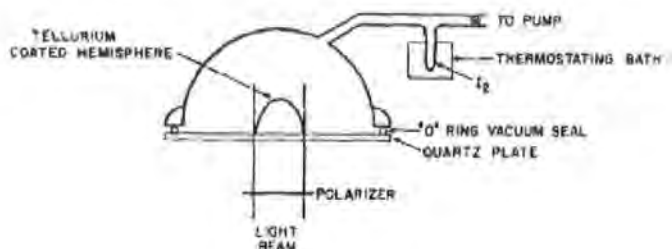
Figure 15: Photolysis Apparatus [96].

The first illustration of the use of ion imaging methods to study a molecular photodissociation process was by Chandler and Houston in 1986 [73]. This pioneering investigation is the foundation of the state of the art imaging techniques used today.
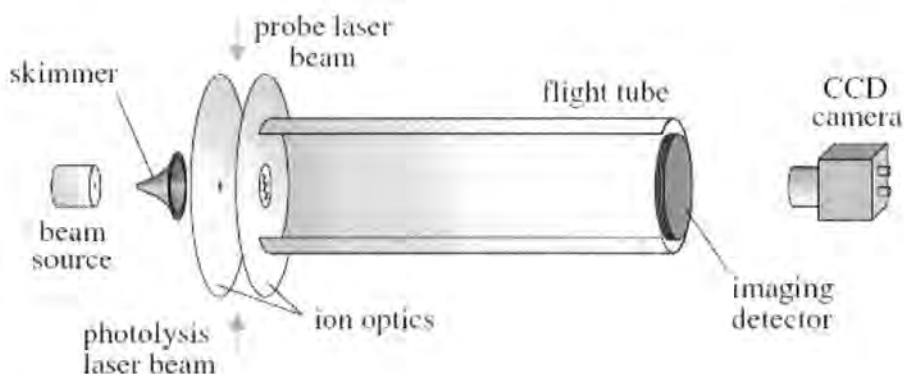
Figure 16: Typical experimental set-up for ion imaging experiments [97].

This typically involves passing a skimmed molecular beam through a small hole of a repeller plate (corresponding to the backing plate in the Wiley McLaren set-up as in Figure 14) in an ion optics assembly where upon it is intersected by a photolysis beam (photodissociation) or a molecular beam (molecular dynamics). The resulting molecule is then ionised with a probe laser beam. The second plate, the extractor, is used along side the repeller to maintain the electric field between the pair and direct the ions formed along a flight tube towards the detector. Unlike the Solomon experiment, where the image was directly seen in the sphere, the

cloud of charged particles (a set of expanding nested spheres) is collapsed in one-dimension along the time-of-flight axis for each mass formed. This "pancaking" implies a minimum spread in time of flight of the cloud, so that mass selectivity and homogeneous detection sensitivity for all particles in the cloud is achieved.

The detector consists of a pair of microchannel plates, MCPs, coupled to a phosphor screen. An ion striking the front face of the MCPs gives rise to a burst of electrons at the back face, as these electrons strike the phosphor screen they produce a flash of light. The pattern of ions striking the MCPs is transformed by this process into an image on the phosphor screen, which may be captured by a CCD camera, digitised and sent to a computer for processing and analysis.

The ion imaging technique extracts all information (kinetic energy and angular distributions) from the spatial appearance of the two-dimensional image, giving direct information on the dynamics of the photodissociation event. This is in contrast to Wiley's conventional time-of-flight method; here kinetic energy release information is contained in the temporal structure in the arrival period of electrons or ions of a specific mass. The image obtained by Chandler and Houston is shown in Figure 17. There is a fixed time delay between the dissociation and probe laser to allow for expansion of the ion cloud. The distribution of photofragments is obtained, by re-constructing the three-dimensional "ion cloud" that gave rise to the two–dimensional image (as described below).
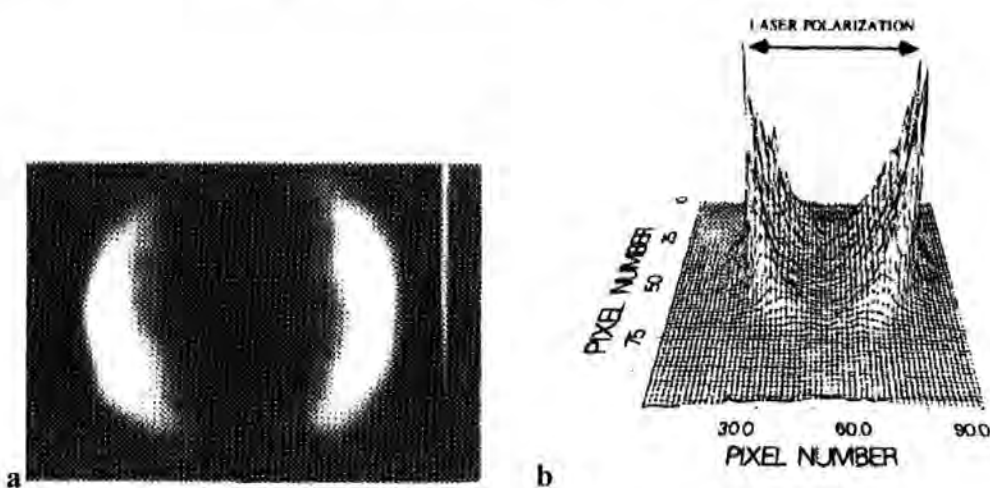
Figure 17: CH_3 ($v = 0$) fragments produced from the photolysis of CH_3I with 266 nm laser light. (a) Grey scale image (white being highest intensity), (b) reconstructed intensity plot of

51

the data of (a). A faint outer ring and an intense inner ring are seen, corresponding to the two possible dissociation channels [73].

There are two main problems with this ion imaging set up:

- **Blurring of the image**. The molecular beam and the photolysis laser beam create the photofragment not at a single point in space but within a finite area.

- **Distorted image**. The set-up used placed grids in the apertures of the electrodes to maintain homogeneous fields in the source region, as used in the Whiley McLaren set-up. The grids distort the image and often the grid pattern is visible on the image. See Figure 18.
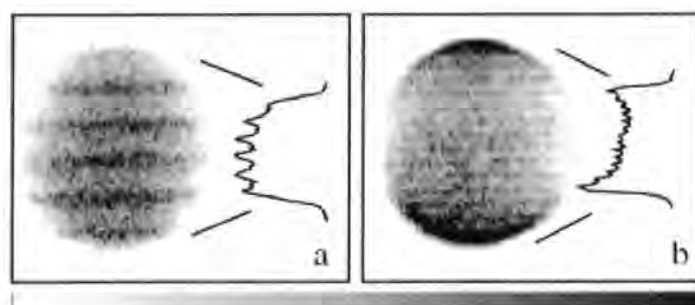
Figure 18: Grid distortions of CH_3^+ images from CH_3I photodissociation at 266 nm using (a) a high transition grid and (b) a fine mesh grid. Shown below the figure is a linear gray scale for the images where larger signal sizes are increasingly darker [98].

2.2.3 Velocity mapping

It was not until 10 years later when Eppink and Parker (1997) [98] made a discovery that solved both of the problems outlined above. They simply removed the grids and used the plates as focusing electrodes. Not only are grid distortions avoided, but the resulting open electrostatic lenses may be tuned such that particles with the same initial velocity vector are mapped onto the same point of the detector irrespective of their initial distance from the ion lens axis. This "velocity-mapping" acts as though there is an ideal point source of photofragments being imaged, leading to substantially improved resolution.

By making use of open electrodes the equipotential surfaces are bent and can be adjusted simply by changing the extractor voltage. The electrode configuration thus acts as an electrostatic lens and provides the possibility of focusing the image sharply on the image detector plane. In this sense the term focusing refers to mapping all charged particles that have the same initial velocity vector onto the same point in the focal plane. This overcomes the need for a point source of ion creation. The lens can also be used to magnify the resulting ion image by varying its focal point, although this means it is necessary to calibrate the lens to determine the magnification factor. This magnification increases the kinetic energy resolution of the method, as the spatial separation of the rings appearing on the detector is increased.
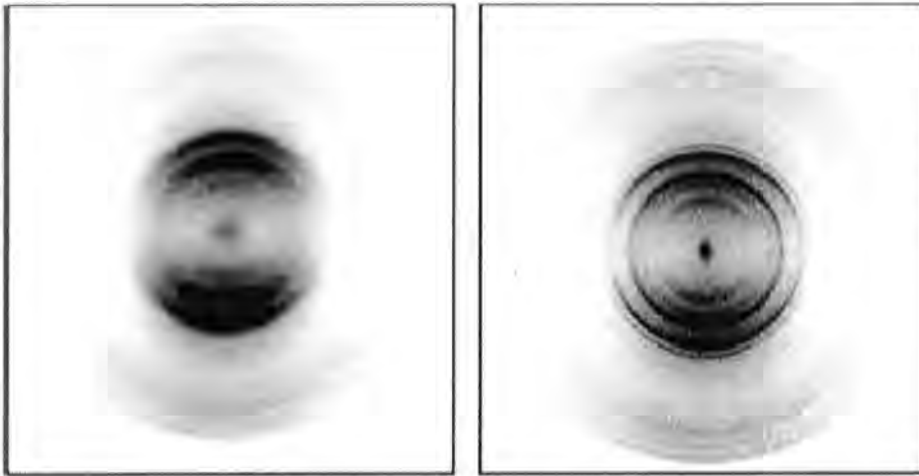
Figure 19: O^+ ion images after O_2 $3d\pi(^3\Sigma_{1g}^-)(v = 2, N = 2) \leftarrow X^3\Sigma_g^-$ Rydberg excitation around 225nm. (left) O^+ ion image measured with fine mesh grid; (right) the same with imaging lens. Intensity scale are the same as shown in Figure 18 [98].

The lens characteristics that were found experimentally by Eppink and Parker were also simulated using a three-dimensional ion trajectory simulation package (Simion 6.0). Figure 20 shows a schematic diagram of the imaging lens used, the ion trajectories can be seen with the equipotential surfaces, the voltage settings on the repeller and extractor are indicated. The trajectories shown originate from three points on the line shaped ion source, eight trajectories are displayed from each, with 1 eV kinetic energy with 45 degree elevation angle difference. The simulation demonstrates the deblurring function of the lens; at the focal plane those

trajectories with the same initial ejection angle but different initial positions are mapped on top of each other. To achieve mass resolution, the extraction field (corresponding to the acceleration field in the Wiley McLaren system) is coupled to a field-free drift region that prolongs the flight time of the ions towards the detector. In addition to this the drift region allows sufficient time for the ion cloud to expand in diameter, limited by detector parameters, achieving better speed resolution.
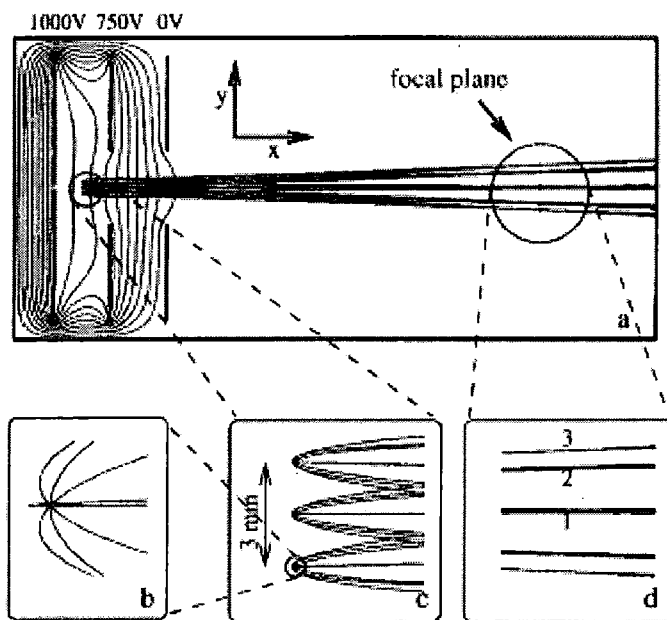
Figure 20: Simulated ion trajectories and equipotential surfaces of the ion lens set at a short focal length. (a) Shows the total view while (b) - (d) show magnified details. (a) The laser propagates along the y direction, causing a line source (c), from which three extremal points are chosen. From each point eight ions with 1eV kinetic energy are ejected with 45° angle spacing (b), thus simulating a spherical expansion. At the focusing plane (d) ion trajectories of the same ejection angle but different start positions come together, where 1, 2 and 3 correspond to ejection angles 0/180° (x direction), 45/135° and 90° (y direction), respectively [98].

A physical constraint of the ion imaging technique is the size of the image on the detector. A small image can be increased by extending the time-of-flight path, which is not always practical, or lowering the potentials of the ion optics, which can lead to field distortions for example by stray fields. An alternative method of using an Einzel lens was introduced to the field in 2001 by Offerhaus *et al.* [99].

This was an electrostatic lens that magnifies the images of an existing velocity map imaging apparatus up to a factor of 20.
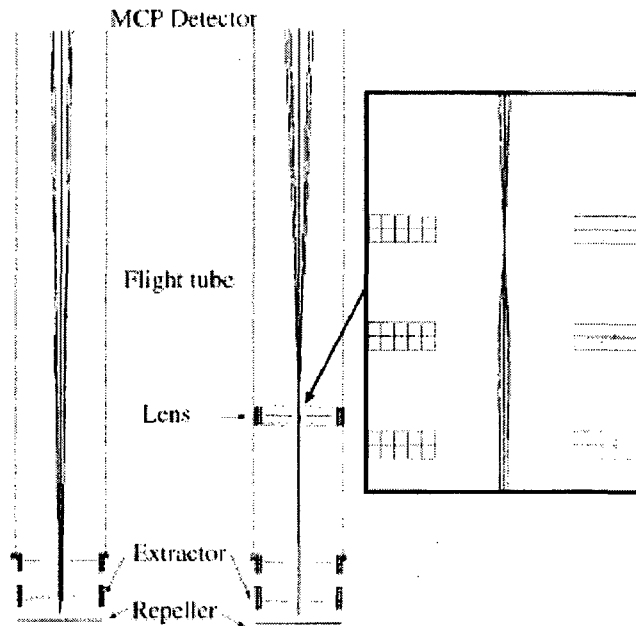
Figure 21: Simion simulation left without and right with a lens. The different trajectories are for different starting angles, increasing in steps of 45°. A high field in the interaction region is present on the right; this causes the velocity map to be small. The image is then magnified by the extra lens [99].

2.2.4 Image reconstruction

The three-dimensional scattering distribution is recovered from the two-dimensional projection measured experimentally using a direct mathematical transformation known as Abel inversion. In the Abel inversion the 2D centre slice of the cylindrical symmetric velocity distribution is reconstructed from the 2D crushed image measured on the detector. However, inherent noise in an experiment is amplified on the centre line of a reconstructed image because of a singularity in the mathematical transformation along that line. If the three-dimensional distribution has no axis of cylindrical symmetry or the axis of cylindrical symmetry is not parallel to the face of the detector, the Abel inversion may no longer be used. Forward simulation or basis set fitting methods must be employed instead [97].

2.2.5 Slice imaging

The most recent breakthrough in the ion imaging community is the introduction of Slicing. Kitsopoulos *et al.* [100] used delayed pulsed extraction of the ions following photodissociation. The delayed pulse extraction causes a sufficient velocity spread in the ion cloud towards the detector such that the time width of the ion packet at the detector is in the order of 500 ns. By using a narrow detector time gate (< 40 ns) it was possible to image the centre slice of the ion packet. The result is equivalent to that obtained by the conventional inverse Abel transformation; however it eliminates the artificial noise produced by this transformation.
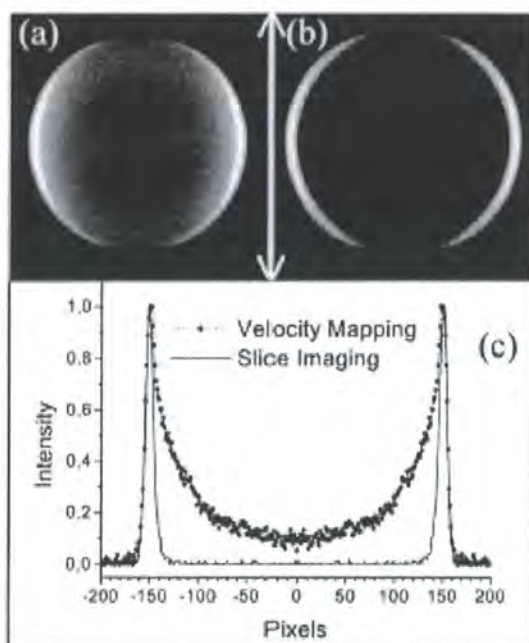
Figure 22: Comparison between conventional ion imaging and slice imaging. (a) a typical ^{35}Cl photofragment obtained under velocity mapping conditions. (b) Image obtained using the slice imaging technique. The arrow indicates the direction of the polarization axis of the photodissociation and ionization lasers. (c) Comparison of intensity profiles for cuts along the equator of the two images above [100].

The drawback to this technique is that a fine mesh grid is introduced into the ion optics assembly to create a field-free expansion region for the nascent fragments produced during the dissociation step. This leads to an inherent blurring of the observed image.

Townsend *et al.* [101] revolutionised this slicing with their Direct Current Slice Imaging. They eliminated the use of grids and pulsed electric fields by using a multi-lens velocity mapping assembly at low voltages, they were able to stretch the ion cloud in the acceleration region owing to the kinetic energy release in the fragments. By applying a narrow time gate (~40 ns) to a detector they were able to slice and record the central section of the distribution.
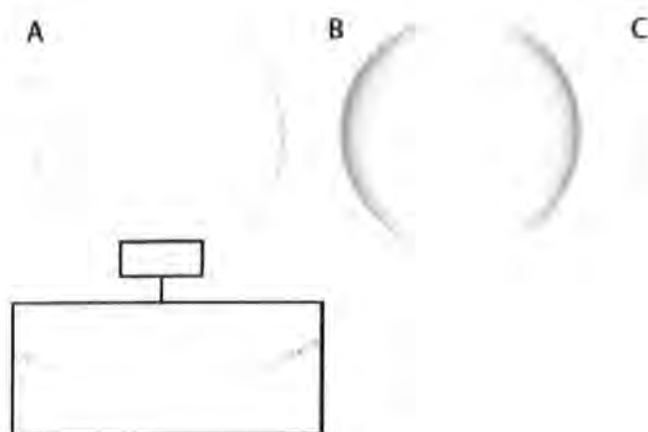
Figure 23: Images of ^{35}Cl ($^2P_{3/2}$) from Cl_2 photodissociation at 355 nm. (a) dc sliced image. (b) Unsliced image. (c) Reconstruction of the unsliced image [101].

The down fall of direct current slice imaging is that it can not be used for very light fragments as the short TOF does not allow for sufficient stretching of the ion cloud to a size suitable for a time slice to be used. The ion cloud can be stretched further by changing the potential of the lens electrodes, however this has the counter effect of reducing the resolution of the lens.

2.2.6 Ion counting

Once the focusing of the product ion cloud onto the detector has been optimized, the burst of electrons striking the phosphor will light up more than one pixel on the CCD camera. Each ion impact creates a light flash which typically has a Gaussian distribution in both coordinates.

In 1998 Chang *et al.* presented a novel ion-counting method which significantly improved the spatial resolution and detection sensitivity of the two-dimensional product image [102]. The method made use of real-time digital image processing to retrieve and determine the local maximum of the light flash from each ion hitting the micro channel plate assembly. The most intense pixel from each strike is located and a new image is generated in which these pixels take the value of one and all others are set to zero. In the resulting summed image the pixels' value translate directly into the total number of ions detected at that pixel position.
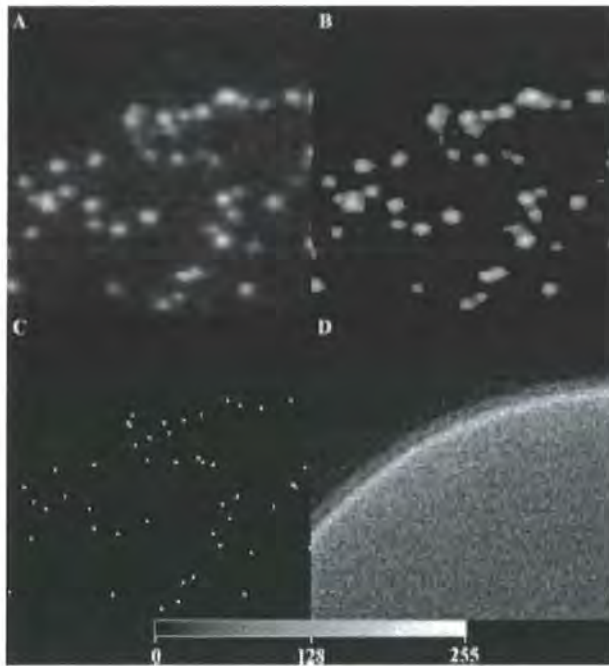
Figure 24: Data shown at various stages of analysis. (a) Raw data. (b) Threshold data. (c) Data following local maxima location. (d) Accumulated data. The frame corresponding to panel A has roughly 200 ions. The accumulated signal corresponding to panel D is the sum of 18000 laser shots [102].

The technique was improved upon by Li *et al.* [103], who overcame the problem whereby it was not clear which pixel had the highest intensity for a given impact (see Figure 25b). For each light flash all the illuminated pixels were analysed, this allowed for the determination of a weighted centre (centre-of-gravity) to an accuracy that is greater than one pixel. This technique can achieve "mega-pixel" ion images, with up to a factor of ten improvement in resolution over conventional approaches, using an inexpensive standard video camera (640 × 480).

a   b
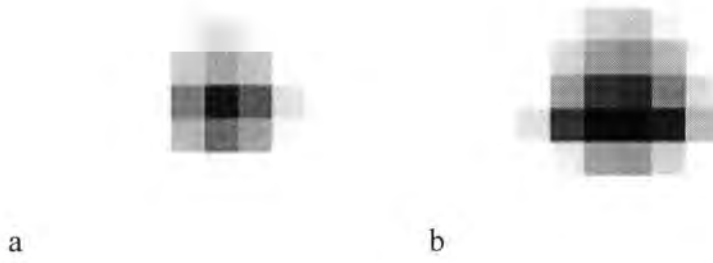
Figure 25: Ion spot morphology: (a) Gausian like and (b) Centre-of-gravity over more than one pixel [103].

Chapter 3:   Aims and Objectives

3.1   Introduction

The main goal of this project has been the reactive scattering of hydrogen Rydberg atoms with deuterium molecules, the aims of which are detailed below in *section 3.2*. The first eight months of this three year project were spent working on a running cavity ring-down spectroscopy experiment led by S. J. Greaves. This experiment provided an excellent opportunity to learn laser and high vacuum techniques. An overview of the cavity ring-down project is provided in the final chapter of this thesis (*Chapter 7*).

3.2   Reactive scattering experiment

The overall scope of this project is to develop a state-of-the-art, high-resolution experiment to study the dynamics of bimolecular reactions of electronically highly excited atoms and molecules. The aim is to measure the outcome of these reactions in great detail and obtain quantum state resolved angular distributions of the products. Such high-quality data could prove a stringent test for theoretical predictions.

The first study to be undertaken with the new experiment will set out to investigate the prototype reaction of highly excited hydrogen Rydberg atoms with D_2 molecules. For this reaction the particular aims are:

- Extend on previous work by Wrede *et al.* [2] and achieve full angular resolved differential cross sections.
- To experimentally measure state-to-state differential cross sections in sufficient detail so as to provide a test of those theoretically calculated very recent by Carmona-Novillo *et al.* [71].
- To examine the scattering as a function of Rydberg state.

- To measure the corresponding photoelectron spectra in order to determine the Rydberg excitation of the product atoms after the reaction.

The objectives of this Ph.D. to achieve the aims above are:

- To finalise remaining parts of the design of the apparatus, namely the ion optics assembly.

- To mount and set up the experiment.

- Develop a technique for the production of pure dry HI gas, the precursor for the experiment.

- Perform calibration checks and test measurements of a well known photo dissociation process of HI at 266 nm, to establish the velocity mapping conditions and the resolution achievable with the ion optics.

- Test and optimise the conditions of use for the pulsed field ionisation of Rydberg hydrogen atoms.

- Perform Rydberg scans to obtain field-free conditions in the extraction region for laser excitation.

- The main goal of the project is to study the reactive scattering of highly excited Rydberg hydrogen atoms with D_2 molecules in order to extend greatly and to quantify the findings of the preliminary study by Wrede *et al.* [2]. Product state resolved angular distributions for the $H^* + D_2$ reaction will be measured and state-to-state differential cross sections extracted in order to characterise the scattering process in detail.

Chapter 4:   Experimental

4.1   Introduction

This section outlines the experimental procedure; the following section (*4.2*) will give details and specifications of the techniques and equipment. A schematic diagram of the reactive scattering experiment can be seen in Figure 26.
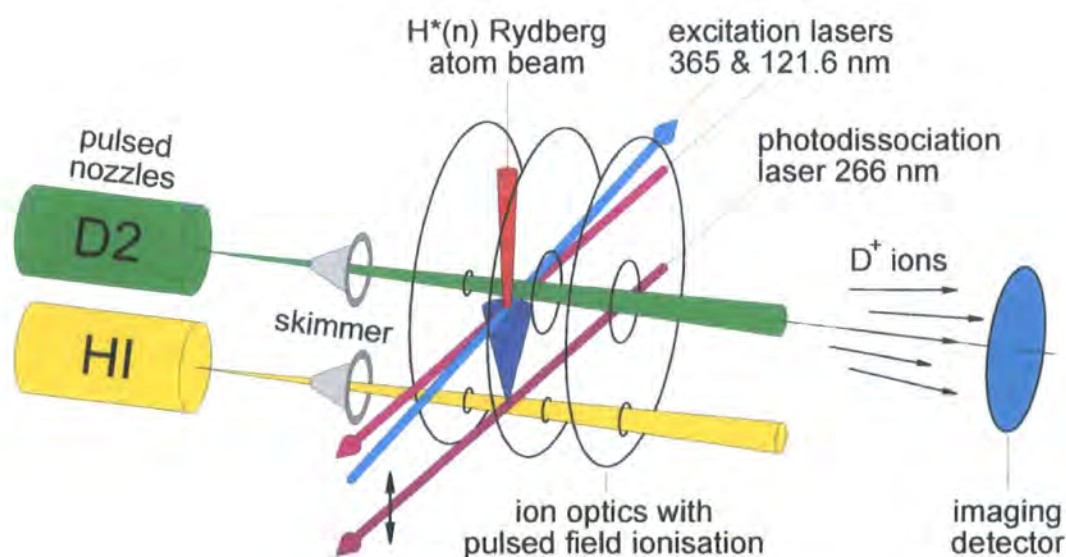
Figure 26: Schematic diagram of the experimental set-up.

The experiment consisted of four main stages: the production of hydrogen atoms from HI, the excitation of these hydrogen atoms into Rydberg levels, the collision of the H* with a molecular beam of D_2 and the detection of the reactive scattering products using the ion-imaging system.

A supersonic molecular beam of HI entered the chamber through a pulsed nozzle and was formed by a skimmer. This beam passed through the first plate of the ion optics (repeller) before being photodissociated by 266 nm light.

$$HI + h\nu \rightarrow H\ (^2S) + I\ (^2P_{3/2})$$

$$\rightarrow H\ (^2S) + I\ (^2P_{1/2})$$
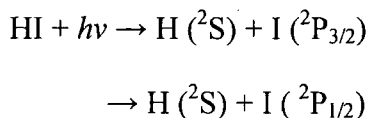
Equation 10

Due to the extreme mass ratio of the photodissociation products, the bulk of the available kinetic energy ($\geq 99\%$) was carried away by the lighter H atom. Since electronic excitation is the only available degree of freedom for the I atom there are only a limited number of pathways open for HI photolysis, resulting in a simple, well defined velocity distribution of the fragments. The absorption into the A band of HI yields iodine atoms in the ground ($^2P_{3/2}$) or excited ($^2P_{1/2}$) spin-orbit state, referred to as I and I* respectively. The polarisation of the 266 nm laser light was chosen to direct the slow H atoms, corresponding to the formation of iodine in its $^2P_{1/2}$ spin orbit excited state, vertically and towards the pulsed, skimmed molecular beam of D_2 that propagated parallel to and 30 mm above the HI molecular beam.

Before the nascent H atoms reached the D_2 beam, the excitation lasers intercepted the H cloud. The H atoms were excited into a high lying Rydberg state by two photon excitation *via* the H (n=2) state using 121.6 and 365.8 nm laser light.
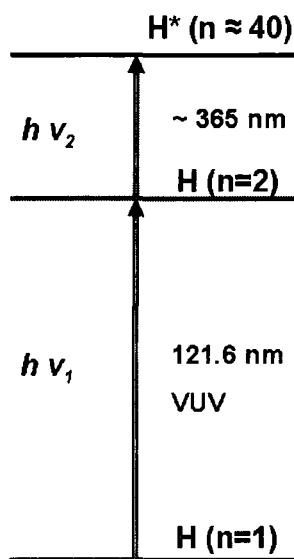
Figure 27: Energy levels in Rydberg excitation.

The small excitation volume defined by the overlap of the H atom cloud and laser beams collimated the resulting H* cloud. This led to a well defined scattering volume within the D_2 molecular beam.

The D_2 molecular beam was formed by a supersonic expansion from a liquid nitrogen cooled pulsed nozzle through a skimmer, producing a molecular beam of ortho-D_2 molecules in their rovibrational ground state ($v = 0, j = 0$). The collision of the D_2 and H* took place in the centre of the extraction region of the ion optics.

H* (n) + D_2 ($v = 0, j = 0$) → H* (n') + D_2 (v', j') (elastic/inelastic collision)

→ HD (v', j') + D* (n') (reactive collision)
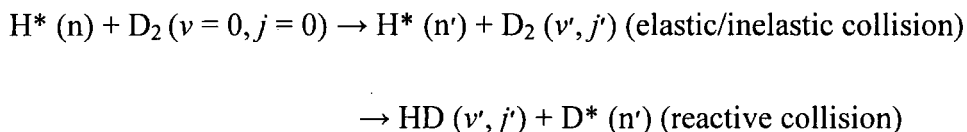
Equation 11

After the collision the product Rydberg atom needed to be ionised. In the case of high Rydberg states, the electric field of the ion optics is sufficient for field ionisation, which means that the electric field had to be pulsed in order not to ionise the reactant H* atoms before the collisions.

The ions were then accelerated by the electric fields of the ion optics out of the scattering volume and finally impacted on the ion imaging detector at the end of the time-of-flight region. Time-gating on the detector enabled H^+ and D^+ ions to be distinguished from their different time-of-flight.

4.2 Experimental Set-up

4.2.1 The Vacuum System

The vacuum chamber was a custom built cuboid made from 20 mm thick stainless steel, with outside dimensions of 780 × 336 × 336 mm (Kurt J. Lesker). The chamber, shown in Figure 28, was divided into three sections: the reaction chamber; and two differentially pumped source chambers. It had five 200 ISO-F ports to give access to the reaction chamber around the experimental centre and

one to give access to the source chambers from the end face. It also had two 160 ISO-F ports to give access to the source chambers from the side faces.

The drift tube was mounted off the ion optics flange (100 CF) and connected the reaction chamber to the detection chamber. It was a 100 CF tee, with the free port extended by a 100 CF nipple, that housed a fast ionisation gauge (FIG) (FIG-1, Beam Dynamics) used to monitor the molecular beam. The 100 CF flange on which it was mounted had a 16 CF and a 40 CF port for mounting the FIG *via* a push pull positioner and electrical feed-throughs.

The drift tube was connected to the detector cross (100 CF cross) that was terminated by the detector. A 100 CF gate valve allowed the detector to be isolated from the main chamber during maintenance.
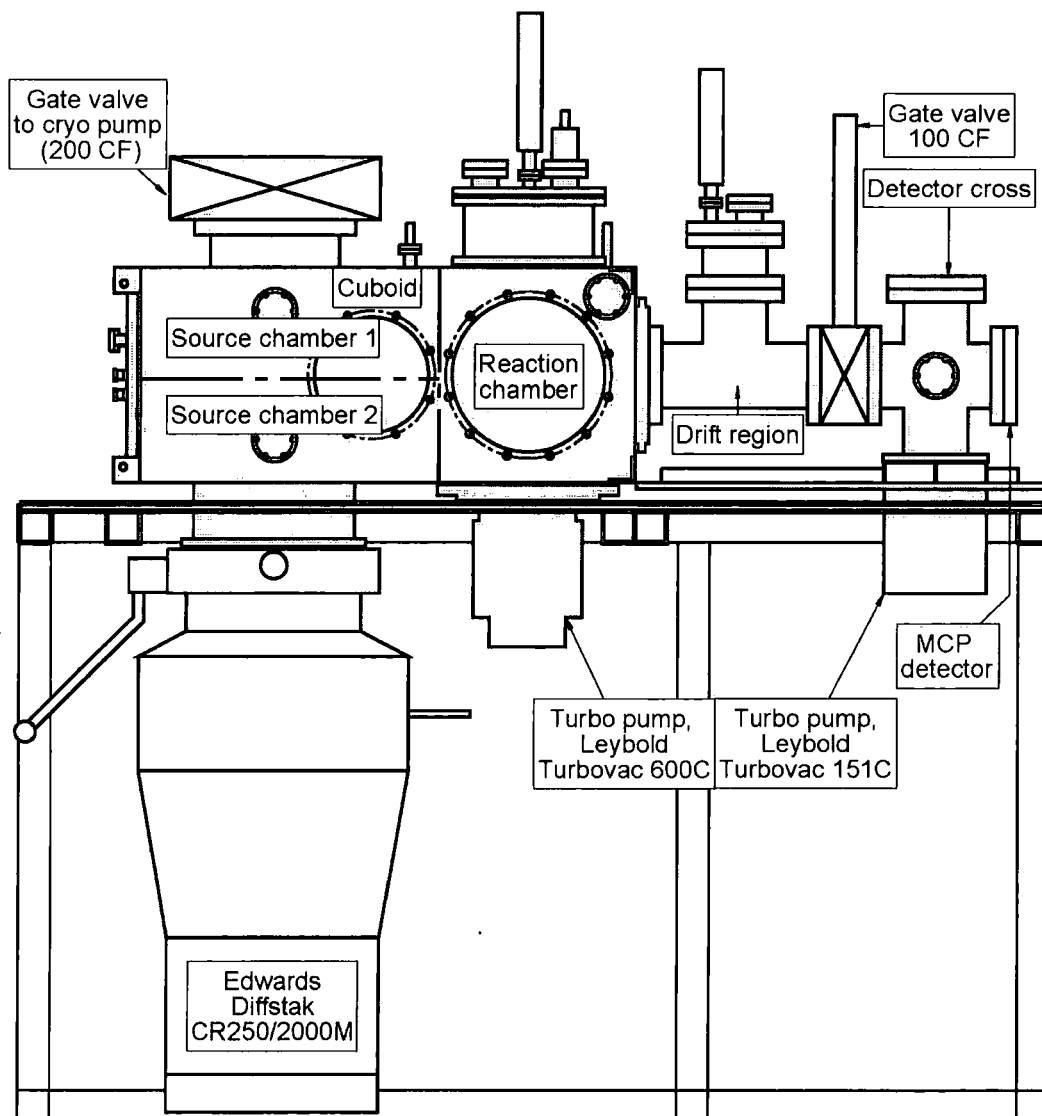
Figure 28: Schematic diagram of the vacuum system.

Within the main chamber, source chamber 1 was evacuated with a cryo pump (Leybold-Heraeus RPK1500, pumping speed: H_2 2000 l s^{-1} with compressor unit RW2) which could be isolated *via* a 200 CF gate valve.

Source chamber 2 was evacuated with a cryo cooled diffusion pump (Edwards Diffstak CR 250/2000M, pumping speed: N_2 1700 l s^{-1}; H_2 3000 l s^{-1}). Cryo cooling was not used since high vacuum was achieved without it. This diffusion pump was backed by a rotary pump (Leybold Trivac D40B, pumping speed: 40 m^3 h^{-1}) with an aluminium oxide adsorption trap.

The reaction chamber was evacuated by a turbo molecular pump (Leybold Turbovac 600C, pumping speed: N_2 560 l s^{-1}). This was mounted *via* a vibration absorber (Leybold) to insulate the turbo molecular pump from vibrations caused by the cryo pump. The turbo molecular pump was backed by a rotary pump (Leybold Trivac D25B, pumping speed: 25.7 $m^3 h^{-1}$) with adsorption trap.

The detector cross was evacuated by a turbo molecular pump (Leybold Turbovac 151 C, pumping speed: N_2 145 l s^{-1}) that was backed by a rotary pump (Leybold Trivac D16B, pumping speed: 16.5 $m^3 h^{-1}$) with adsorption trap.

During down time the diffusion and cryo pumps were closed and the source chambers pumped by the turbo molecular pump of the reaction chamber *via* a bypass (40 CF hose).

The pressure in the four chambers (see Table 2) was monitored using Bayard-Alpert ionisation gauges (source chamber 1: Leybold (IE 413) using an Ionivac controller (IM 510); Source chamber 2, reaction chamber and detector cross: Kurt J. Lesker (G8130) gauges with multi gauge controller). All backing pressures were measured with convection gauges (K. J. Lesker) connected to the multi-gauge controller.

Table 2: Standard pressures without load.

Chamber	Pump	Pressure - no load / mbar
Source 1	Cryo	2×10^{-8}
Source 2	Diffusion	$\leq 1 \times 10^{-7}$
Reaction	Turbo (600C)	$\leq 1 \times 10^{-8}$ cryo shield $\leq 4 \times 10^{-8}$ without cryo shield
Detection	Turbo (151C)	2×10^{-8}

4.2.2 Molecular Beams

Two molecular beams were used in the experiment. The beams were produced though a gas expansion from a high pressure region through the small orifice of a pulsed nozzle into the vacuum chamber. As the molecules accelerate into the vacuum they undergo a large number of two body and many body collisions. Translational cooling equalises the speed of the molecules in the beam and internal motions are cooled through inelastic collisions. Each beam passed through a skimmer resulting in collimated beams.
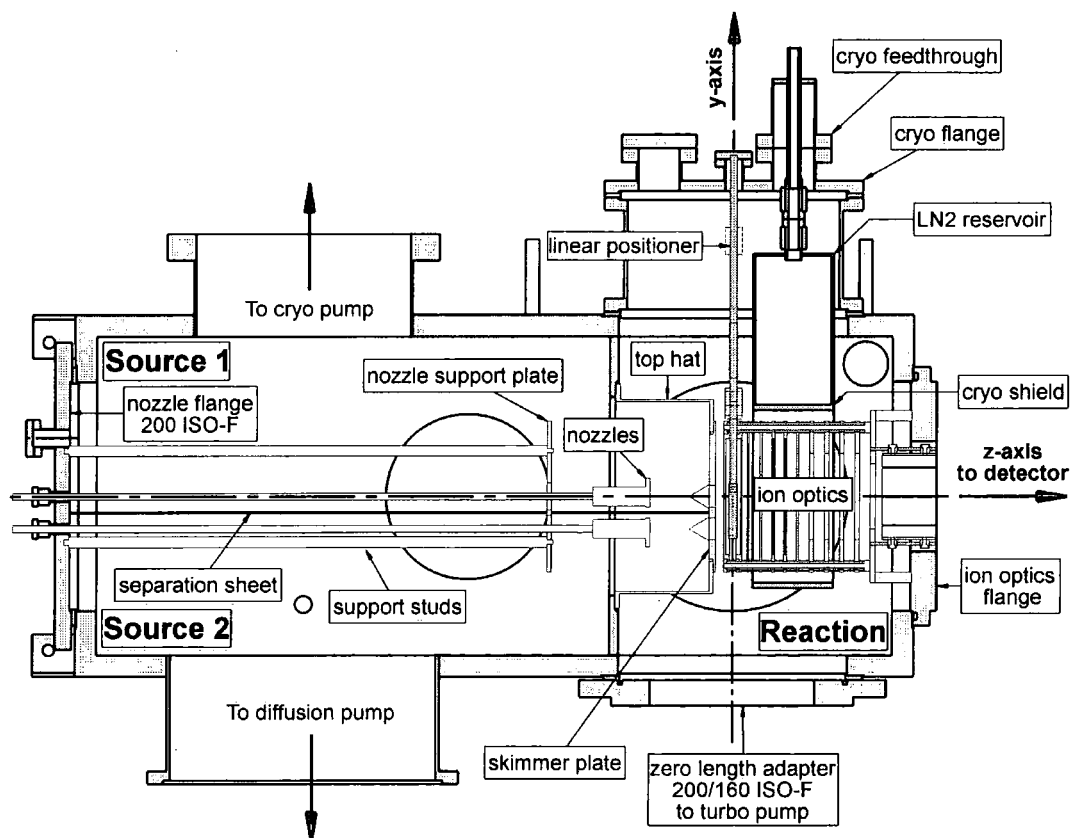
Figure 29: Vertical cut through vacuum chamber.

Each nozzle was centred in front of its skimmer (Beam Dynamics, Model 2, skimmer orifice: D_2 1.0 mm; HI 0.5 mm) by guiding rods mounted on the skimmer plate (not shown in Figure 29). The skimmers were centred in counter sunks on the skimmer plate that were in turn centred onto the top hat. The top hat was aligned on the z axis of the experiment (towards the detector, see Figure 29) using a HeNe

beam through centred irises on the end flanges, such that the upper skimmer was centred on the horizontal z axis. The lower skimmer was 30 mm below by design. Unfortunately, the vertical alignment of the two skimmer orifices was not perfect but with deviations of less than 1° with respect to the vertical y-axis. The skimmer plate could be removed from the top hat for skimmer change and remounted into the same position.

The two pulsed nozzles (Parker Instruments, General valve Series 9, orifice diameter: 0.5 mm with IOTA ONE pulse driver) were individually mounted onto the nozzle flange. They were connected at the end of 1/4″ stainless steel pipes for gas delivery. An o-ring sealed feed through (Cajon, Ultra-Torr fitting) allowed the pipe, and hence the nozzle, to be moved horizontally (along the z-axis). This enabled the adjustment of the distance between the nozzle and the skimmer, providing control of the molecular beam size. The nozzles could be pulled back onto the support plate (stainless steel) and the entire system could be pulled out as a single unit for maintenance. Within the main chamber, rails have been installed to support the weight of the unit. Metal sheets were used to divide the two differentially pumped source chambers.

Monitoring the temporal profile of the molecular beam in situ was achieved using a retractable fast ionization gauge (FIG) (Beam Dynamics INC., FIG-1) with a fast amplifier (response time of 3 μs). The FIG was mounted in the T-section between the cuboid and the detection chamber, 30 cm downstream from the lasers. A push-pull translation stage allows the FIG to be lowered into each beam. Typical emission currents of the FIG were 5 mA. The ion signal was recorded with a digital oscilloscope (LeCroy, Waverunner LT-584).

4.2.2.1 HI Molecular Beam

The H atoms originated from the photodissociation of HI gas in a molecular beam, as detailed in the introduction to this chapter. Unlike D_2, used in the second nozzle, HI gas is not commercially available. The following section details the technique developed for producing pure, anhydrous HI and the formation of the molecular beam.

Production of HI

The method used for producing the gas has been adapted from that detailed by Dillon and Young [104].

5 ml of concentrated hydriodic acid (sp. gr. 1.7, Acros Organics), was added dropwise to 100 g of phosphorus pentoxide (Laboratory reagent grade, Fisher Scientific) in a 0.5 litre round bottom flask. As liquid nitrogen is used to trap the HI, the apparatus was flushed with He (BOC gases) prior to the experiment to remove air. The He pressure was set to provide a steady flow of He using a silicon oil bubbler at the end of the gas flow line. The round bottom flask was fitted with a pressure release valve.

The evolved hydrogen iodide contained traces of iodine, water and phosphine and was therefore purified. The HI was passed through a column containing 25 g of phosphorous pentoxide on a coarse glass sinter, removing water vapour produced in the reaction. The residual gas flowed through a trap maintained at 213 K by a cooling bath of methanol and dry ice, to remove iodine contamination. The HI was collected in a second cold trap maintained at 77 K by liquid nitrogen. The corrosive nature of HI demanded that all components of the apparatus were made from glass with Teflon seals.

Once the HI has been frozen into the trap, it was connected to an all glass vacuum line that was attached to the HI nozzle. The vacuum line (evacuated by a rotary pump: Varian, pumping speed: DS202: 8 m^3h^{-1}) was used for gas storage, purification and mixing. HI rapidly decomposes when exposed to light so the vacuum line and gas delivery pipe to the nozzle were blackened using black insulation tape. The HI was stored in a bulb on the vacuum line and regularly cleaned by freeze-thaw cycles to remove H_2 and I_2.

HI Nozzle

The HI nozzle was typically operated with a backing pressure of 1 bar of pure HI. This resulted in a pressure typically lower than 1×10^{-5} mbar (ion gauge reading not corrected for HI gas) in source chamber 2. An example of a HI beam temporal profile can be seen in Figure 30. This presented pulse has a very short full-width half-maximum of about 110 µs; typically this would vary between 200 and 300 µs on a day-to-day basis depending on the deterioration of the PTFE poppet and I_2 accumulation in the nozzle. A high intensity short pulse indicates a good gas expansion. The FIG was used to monitor the pulse. The nozzle (General valve, series 9) was a solenoid controlled valve. Within the valve the poppet was housed in an armature which was held in position by two counteracting springs and moved by the magnetic force when a current passed through the coil. The tension on these springs could be adjusted in situ by twisting the gas delivery pipe to which the nozzle was connected. This resulted in a tightening of the valve and thus the opening characteristics of the nozzle. The gas pulse profile could also be optimised by adjusting the opening times of the nozzle on the IOTA ONE driver (typically between 200-300 µs). The nozzle was positioned typically 16 mm in front of the skimmer (minimum nozzle to skimmer distance).
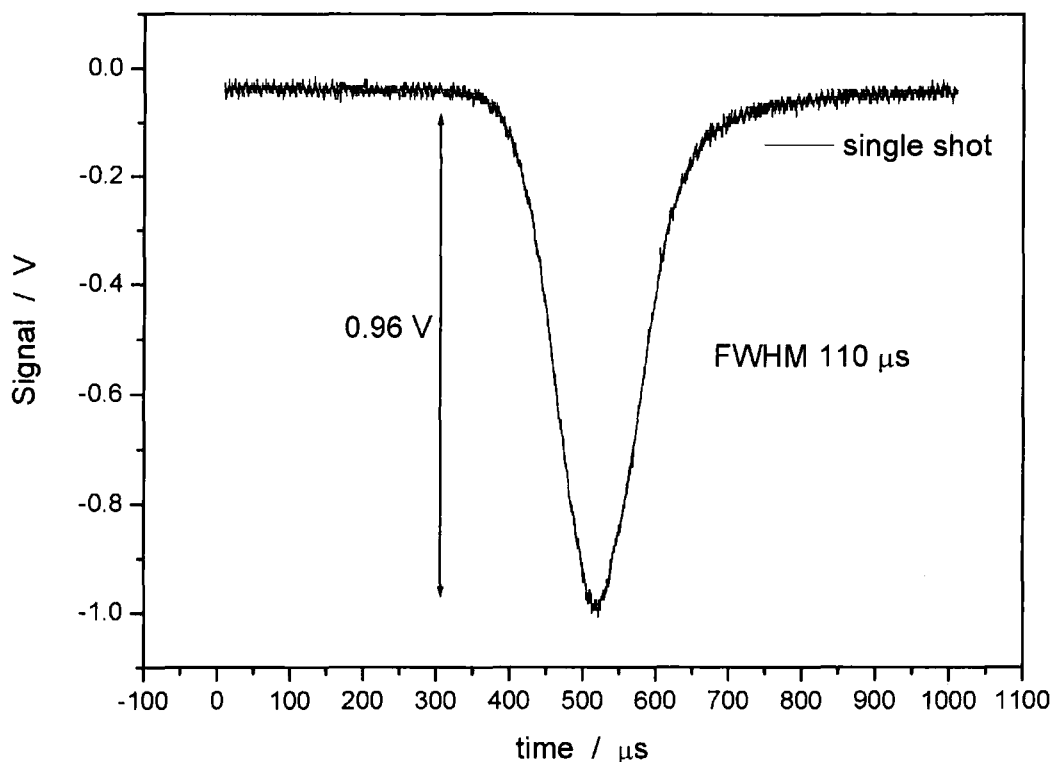
Figure 30: Temporal profile of a typical optimised pulse of pure HI at 1 bar backing pressure. FIG current: 5mAmps.

4.2.2.2 D₂ Molecular Beam

Previous experiments have shown that in order to achieve good resolution in the overall reactive scattering experiment it is necessary to minimise the uncertainties introduced by the velocity spread and the rotational distribution of the D_2 molecules [17].

A suitable molecular beam was produced by converting commercially available D_2 (BOC, purity: 99.8) into ortho-D_2 through a catalytic conversion. This ortho-D_2 was used along with a modified nozzle that was suitable for running at liquid nitrogen temperatures. This low temperature resulted in reduced numbers of rotational quantum states populated in the beam as discussed in the following section.

Conversion of D_2

The D nucleus is a Bose particle as it has a nuclear spin $I = 1$ and as such the overall wavefunction must be symmetric under the exchange of two identical bosons. The total wavefunction, ψ, for a molecule with identical nuclei (D_2) can be separated as

$$\psi = \psi_e \, \psi_v \, \psi_r \, \psi_{ns}$$

where ψ_e, ψ_v, and ψ_r, are the electronic, vibrational and rotational wavefunction and ψ_{ns} is the nuclear spin wavefunction. Both ground state ψ_e and ψ_v are symmetric with respect to nuclear exchange so only ψ_r and ψ_{ns} are considered. Since $I = 1$ for D, ψ, and therefore $\psi_r \, \psi_{ns}$ must be symmetric with respect to nuclear exchange.

For even values of the rotational quantum number j, ψ_r is symmetric with respect to exchange and for odd values of j, ψ_r is antisymmetric to exchange. For $I = 1$, M_I can have values of $+1$, 0, -1 so there are nine possible forms of ψ_{ns} for the molecule as a whole; six of the nuclear spin wavefunctions are seen to be symmetric to nuclear exchange and three are seen to be antisymmetric. In order that $\psi_r\psi_{ns}$ is always symmetric for D_2 the symmetric ψ_{ns} are associated with even J states and the antisymmetric ψ_{ns} with odd J states.

Interchange between states with ψ_{ns} symmetric and antisymmetric is forbidden. There are no electric dipole or multipole transitions between the ortho and para systems and it is not possible to convert by elastic/inelastic collisions. Thus, D_2 can be regarded as consisting of two distinct forms, with any property depending on the rotations varying between the two species, for example the specific heats and thermal conductivity. These forms are

- para D_2 with $I_{tot} = 1$, $M_{Itot} = -1, 0, 1$;
- ortho D_2 with $I_{tot} = 2, 0$, $M_{Itot} = -2, -1, 0, 1, 2, 0$

At thermal equilibrium D_2 gas is a mixture consisting of 2/3 ortho-D_2 ($I_{tot} = 2, 0$) in even rotational levels and 1/3 para-D_2 ($I_{tot} = 1$) in odd rotational levels and is

called normal-D_2 (n-D_2) . In order to change this, the nuclear spin and rotation must be changed simultaneously although the required change in nuclear spin is forbidden. In the presence of an inhomogeneous magnetic field that varies across the size of the molecule the symmetry can be broken. This will exert a torque allowing the nuclear spins to re-orientate. In this way ortho-D_2 was prepared prior to the experiment.

A small sample cylinder (volume = 7 cm^3), filled with catalyst, (Houdricat, Houdry, Division of Air Products and Chem., No. 197-CP) was mounted on the second stage of the cryo pump refrigerator. Normal-D_2 was frozen onto the catalyst at temperature lower than 16 K (estimated value due to the calibration of the temperature sensitive resistor no longer being valid). The cryo pump was then switched off and the catalyst allowed to warm up, releasing the converted D_2. The gas was stored in an aluminium lecture bottle (1 litre) to prevent back conversion induced by magnetic moments from steel surfaces. All steel pipes along the gas flow path from the catalyst to the storage cylinder and the nozzle, were coated with Teflon as another preventative measure. The catalyst had a capacity of about 5 bar litres.

D_2 Nozzle

The standard nozzle (General valve, series 9) has an o-ring to seal the passage between the coil assembly and the body of the valve. The o-ring is designed to work at room temperature and does not seal at the typical operating temperature of 95K. Instead, a seal was made using epoxy glue (Torr Seal from Varian). A valve that seals effectively in the closed position and opens reliably at room temperature will not perform at liquid nitrogen temperature. The standard nozzle allowed for the tension on the springs to be adjusted in situ by tightening the valve to produce optimum performance. The optimum spring tension varied with temperature. Therefore, prior to mounting, the nozzle was tightened such that it opened fully when immersed in liquid nitrogen and was over tight at room temperature. The epoxy glue was then applied, locking the nozzle into this position and stopping any gas from leaking. It was possible to remove this seal by heating to 120°C, at which point the epoxy softened slightly and could be chipped off.

The sealed nozzle was mounted onto a hollow copper block (to act as a reservoir) that had an orifice in the centre for the gas pulse to pass. The copper block was connected to a liquid nitrogen dewar *via* liquid nitrogen feed-throughs on the nozzle flange and flexible hoses. Gravity pushed the liquid nitrogen in the dewar to the copper block where the heat load boiled off some liquid nitrogen forcing the excess through the return pipe and back into the dewar. Both the copper block and nozzle base had a thermocouple attached to monitor the temperature. The typical operating temperature of the nozzle body was 95 K.

The D_2 nozzle was operated with a backing pressure of up to 8 bar ortho-D_2. The nozzle controller was used to adjust the opening duration (typically between 95-120 µs) to obtain an intense, short pulse on the FIG, optimum settings changed with the age of the poppet. This resulted in a pressure of between 4×10^{-6} and 1×10^{-5} mbar in source chamber 1 (not corrected for D_2). The beam was formed by a skimmer with an orifice of 1 mm. The nozzle was typically positioned 22 mm behind the skimmer. The temporal profile of the D_2 beam can be seen below.
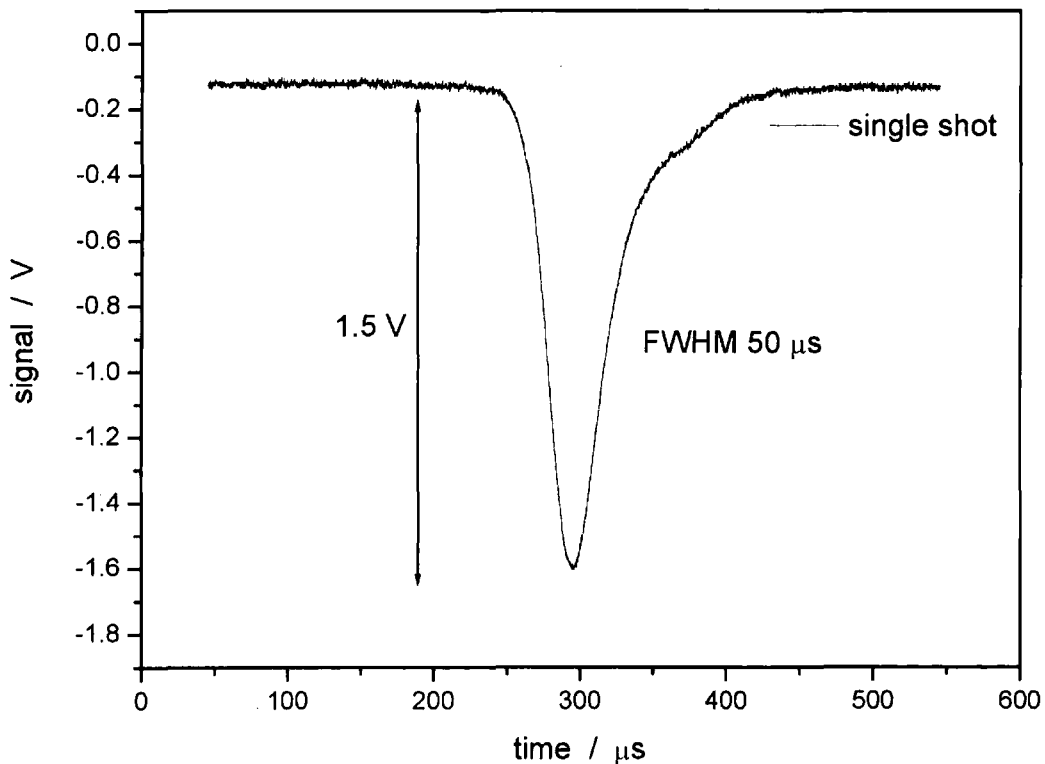
Figure 31: Temporal profile of a typical optimised pulse of o-D_2 at 5 bar backing pressure. Temperature of nozzle 95 K. FIG current: 5mAmps.

4.2.3 The Laser system

The laser system set-up can be seen in Figure 32. A Nd:YAG (Continuum Powerlite Precision II, model 8010, pulse length 5 ns, Q-switched with a repetition rate of 10 Hz) was used to pump all three dye lasers and is shown as Nd:YAG 2 in Figure 32. The beam paths from Nd:YAG 2 through all three lasers were of equal length by design, such that the pulses coincided at the centre of the experiment.
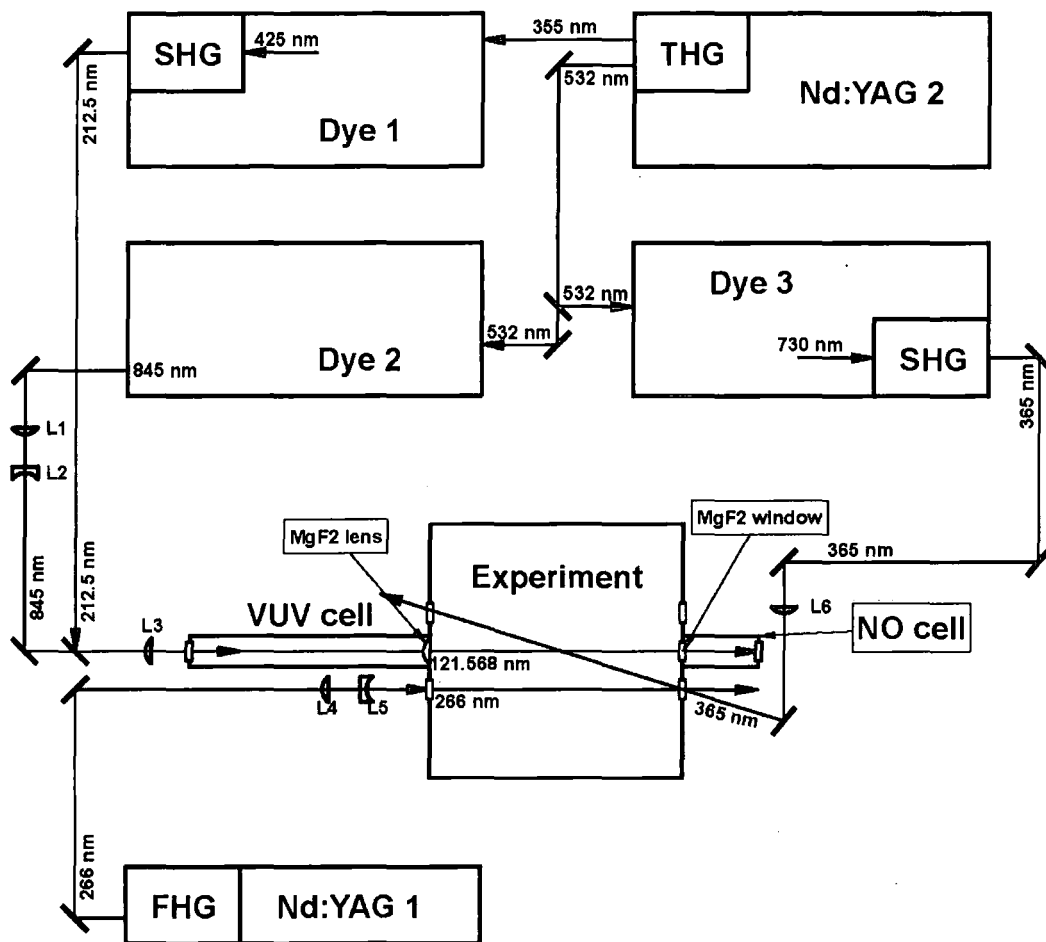
Figure 32: Schematic of laser set-up.

Second and third harmonic generation (SHG and THG in Figure 32) of 1064 nm radiation produced 532 nm and 355 nm light respectively. The 532 nm light was used to pump dye lasers 2 and 3 by passing through a 50% beam splitter (Photonics Solutions), whereas the 355 nm laser was used solely for dye laser 1.

The harmonic generation of Nd:YAG 2 was tuned to produce twice as much 532 nm (~240 mJ) as 355 nm radiation (120 mJ).

The laser flanges on both sides of the chamber had baffles mounted on the inside of all the laser ports. These baffles comprised of a series of 3 annuli (with opening of 4 mm diameter) to reduce the scattered light in the chamber arising from scattered light originating from reflections from the windows.

4.2.3.1 The Dissociation Laser

The HI was dissociated at 266 nm using the fourth harmonic of a Nd:YAG (1) laser (Continuum, Surelight I-10, pulse length 5 ns, repetition rate 10 Hz). The beam was steered to the chamber through a series of 266 nm dichroic mirrors (Photonics Solutions). The dissociation laser ran between the repeller and stabiliser plates of the ion optics, 30 mm below and perpendicular in direction to the D_2 beam (Figure 36). The 266 nm beam passed through a half wave plate (Photonics Solutions) to ensure vertical polarisation of the light. This resulted in the slow H atoms being directed vertically towards the D_2 beam, and the fast horizontally. Typical powers used for the photodissociation were of the order 2-4 mJ, measured after the exit window and diverging lens, using a pyro detector (Sirah, PEM8). The power of the 266 nm light and hence the amount of H atoms produced was controlled using either a combination of half wave plate and polariser or just the half wave plate and the Q-switch delay of the NdYAG(1).

4.2.3.2 The Rydberg Laser

The formation of the Rydberg-H atom is a two-photon excitation

$$H (1s) + VUV (121.6 nm) \rightarrow H (2p)$$

$$H (2p) + UV (365 nm) \rightarrow H^* (n \approx 40)$$
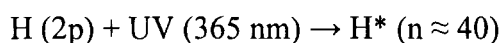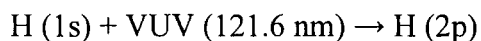
Equation 12

VUV Cell

The VUV (Lyman-α) radiation was generated using resonant four-wave difference frequency mixing. This involved combining two photons of 212 nm light with one photon of 845 nm light in the presence of krypton, a negatively dispersive non-linear medium. A conversion cell (VUV cell) developed for a previous experiment was incorporated for the mixing of the two gases [17] as shown in Figure 33. The entrance window to the cell was an anti-reflex coated UV grade quartz window. The generated VUV light passed through a MgF_2 lens (f = +120 mm at Lyman-α) as it entered the reaction chamber. This positioned the focus at the point where a retractable pinhole was located for alignment. Figure 33 shows this focal point. A UV grade quartz lens (f = +500mm) was used to couple the light into the VUV cell.
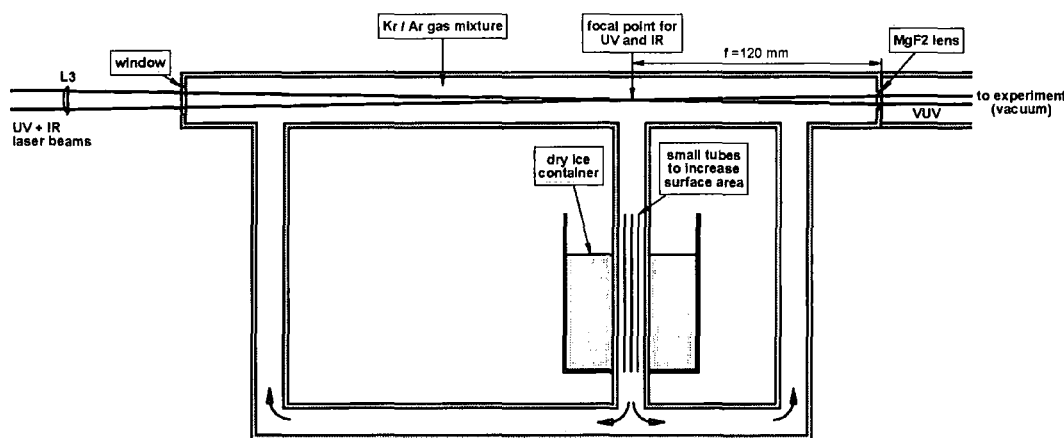
Figure 33: Schematic of the VUV conversion cell.

The Krypton (99.9990% purity, BOC gas) was the optically active medium that was mixed with Argon (99.9995% purity, BOC gas) in order to match the speed of light of all frequencies (phase matching). This phase matching enhances the conversion efficiency by several orders of magnitude [105].

The cell was evacuated using a rotary pump (Leybold, Trivac D4B, pumping speed: 4 m^3h^{-1}). It was also connected to the reaction chamber through an all metal right angled valve and a flexible bellows (DN35 CF) and could therefore be pumped *via* the turbo molecular pump to high vacuum (1 × 10^7 mbar). It was

important to thoroughly clean the VUV cell as Lyman-α light is absorbed by water. The cell was heated and pumped through the main chamber overnight to achieve this. The VUV cell was filled with krypton typically to 100 mbar. Argon was then added to bring the total pressure to typically 420 mbar. The pressure was measured using a piezo pressure transducer (Haenni systems ZED 503, accurate to 1 mbar).

The cell had a cold trap that was filled with dry ice. Firstly, this freezes out impurities from the gas (mainly water), and secondly this generates convection currents which cause the gases to flow through the cell. The two sides of the cell were different lengths, by design, in order to facilitate the mixing of the two gases.

UV and IR Production

The 212 nm radiation was produced by dye-laser 1 (Lambda-Physik FL2002, dye: Excalite 428 in dioxane: oscillator/ preamp 0.15 g dm^{-3}; pre-amplifier 0.05 g dm^{-3}) with a β-barium borate (BBO) crystal for second harmonic generation. The dye laser was upgraded with stepper motors and software (Sirah). A typical power reading for the 212 nm radiation was 1 mJ measured after three 212 nm dichroic mirrors.

The 845 nm radiation was produced by dye laser 2 (Quanta Ray PDL1, dye: Styryl-9 in DMSO: oscillator 0.13 g dm^{-3}, amplifier bypassed). This dye laser was also upgraded with stepper motor and software (Sirah). Both dye lasers were pumped by Nd:YAG 2. A maximum power reading for the 845 nm radiation was 1.3 mJ, measured directly from the dye laser output; the minimum power required was approximately 0.5 mJ, this allowed for degradation of the dye.

This combination resulted in around 1×10^{12} VUV photons per pulse, measured with the NO cell.

The 212 nm light was steered to the chamber by four dichroic mirrors which helped to eliminate any remaining 425 nm light (dye laser fundamental). The IR beam was directed by four IR coated mirrors (Thorlabs)

The IR beam did not have the same focal length as the UV beam. A UV grade IR anti reflex coated, quartz lens telescope (lens 1 (+160 mm) and 2 (-100 mm) in Figure 32) was used to change the divergence of the beam. The overlap of both foci was achieved within the VUV cell controlled by the retractable pin hole.

NO Cell

An NO ionisation cell was used to determine the number of VUV photons produced. It consisted of a sealed chamber containing NO gas (1% NO in He mixture) and two electrodes between which a voltage was maintained by an external circuit. When a photon enters the chamber, through the MgF_2 window, it may ionise one gas molecule. The ions and electrons are attracted to the oppositely charged electrodes; their presence causes a momentary drop in the voltage, which is recorded by the external circuit. The observed change in voltage helps to identify the radiation because it depends on the degree of ionisation.
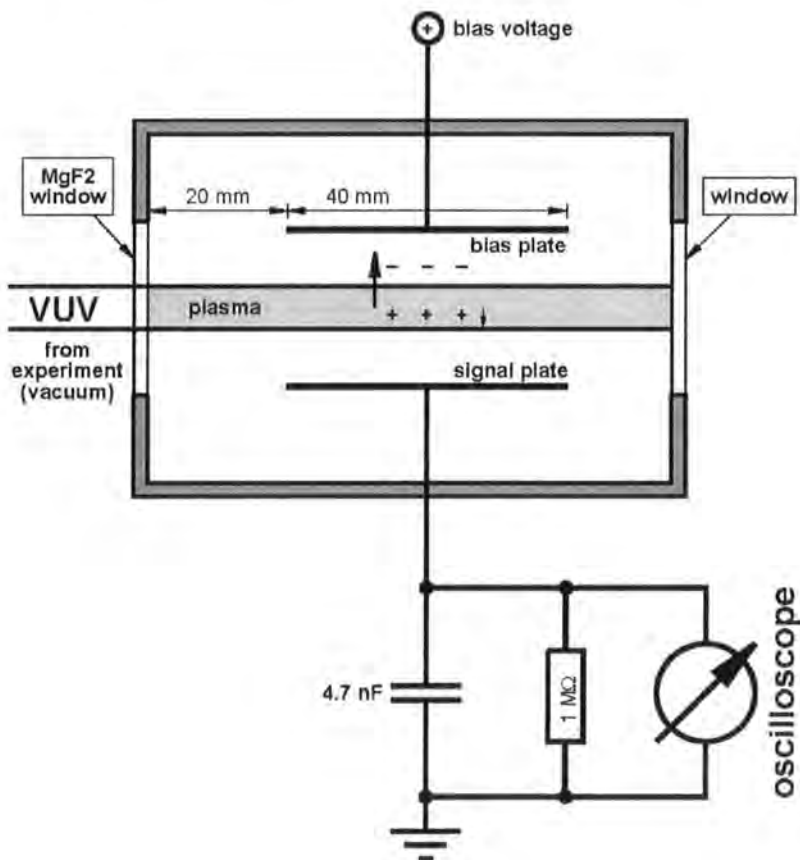
Figure 34: Schematic diagram of the ionisation cell.

Typical operating conditions of the NO cell were 0.15 mbar of 1 % NO in He mixture. The operating conditions of the NO cell were characterised with Anna Heath [106].

4.2.3.3 The UV laser for Rydberg excitation

Excitation from the H(2p) level into a high lying Rydberg level ($n \approx 40$) was achieved using pulsed UV radiation from dye laser 3 (Sirah, Cobra-Stretch, dye: Pridine-2 in Ethanol: oscillator 0.25 gdm^{-3}; amplifier 0.083 gdm^{-3}; with a KD*P non-linear crystal for second harmonic generation and Pellin-Broca wavelength separator), this was pumped by the second harmonic of Nd:YAG (2) laser. The light was delivered to the chamber through a series of 355 nm dichroic mirrors and a prism. The entrance and exit windows were UV grade quartz windows (Comar). Typical laser power was of the order 2.4 mJ, measured after the exit window and diverging lens.

4.2.3.4 Laser Alignment

A motorised 150 mm linear positioner (Kurt J. Lesker) was mounted on the top reaction chamber flange to position a series of pin holes at the centre of the experiment. Focusing both lasers through the pin hole ensured that the overlap of the Rydberg and VUV lasers were at the same point relative to the dissociation laser beam. The positioner was fully retractable after laser alignment (see Figure 29).

The beams were aligned through the pinholes which defined their position relative to each other. The size of the laser beams was set by comparing the intensity passing through the pin hole with the intensity of the full beam. The lenses for each beam entering the experiment were set such that the beam diameters were approximately 0.4 mm (FWHM) at the experiment centre.

4.2.4 Ion Imaging and Detecting

4.2.4.1 Ion Optics Design

The ion imaging detection system was designed using Simion (Simion 3D, version 7.00), a simulation program that models ion optics with electrostatic and/or magnetic potentials and calculates the trajectories of ions in the fields. The system was based upon a recent state-of-the-art ion optics design by Townsend *et al.*, who made use of many electrodes to allow greater control and flexibility over the focusing conditions than the simpler traditional three electrode systems [101]. The system developed for this experiment also had the feature of using a stabilising electrode, placed between the repeller and extractor to create a homogeneous field in the source region. Wrede *et al.* found that optimum focusing was achieved when the field in the ionisation region was homogeneous [107]. The stabilising electrode ensures that field distortions created by the ion lens do not penetrate into the ionisation region; this can be seen by the straight potential lines within the source region in Figure 35.
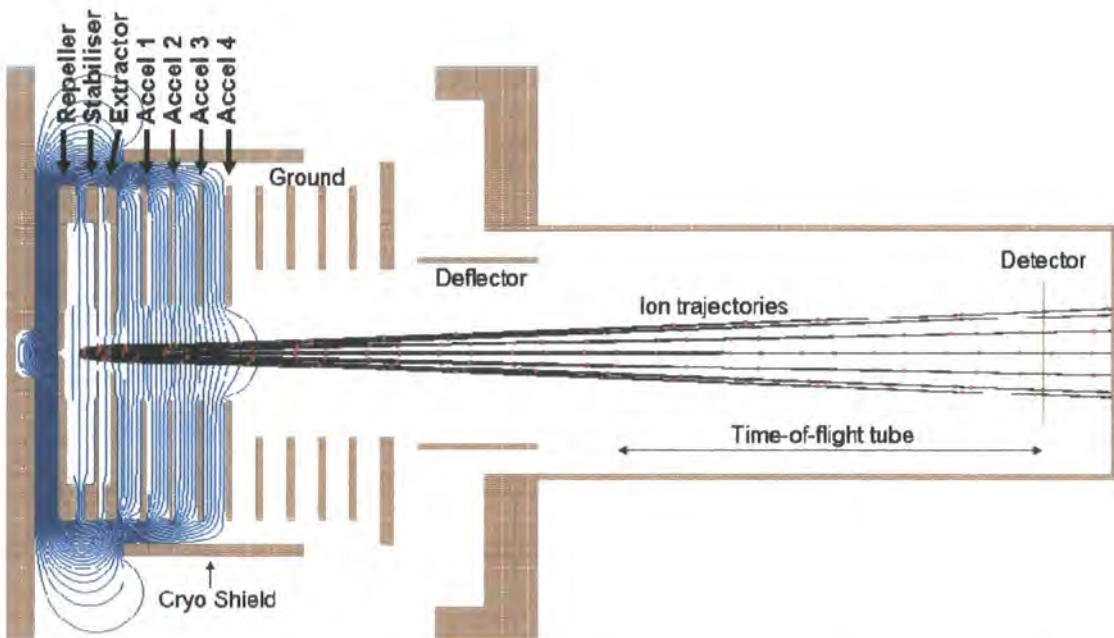
Figure 35: Simulation showing optimum voltages for velocity mapping where: V_{rep} = 5000 V, V_{stab} = 4340 V, V_{ext} = 3975 V, V_{acc1} =2990 V, V_{acc2} = 1990V, V_{acc3} = 995 V, V_{acc4} = 0 V.

Simion was used to optimise the geometry of the electrodes. The program feature of Simion was used to find the optimum voltages required to obtain velocity mapping onto the detector for a given geometry. This was an iterative procedure; for a given geometry the program was used to find optimum voltages for velocity mapping, the extent to which focusing on the detector was achieved was assessed, and then systematic changes to the geometry were made and the process repeated to find the optimum geometry and optimised velocity mapping. The best focusing conditions obtained are reported in Figure 35.

The final geometry of the electrodes is shown in Figure 36 and Figure 37. The ion optics assembly was made up of eleven stainless steel electrodes which are 140 mm in diameter. They were mounted on four stainless steel studs. The studs were centred relative to the time-of-flight axis (z-axis) in counter sunks on the support plate, that was itself mounted onto the 200 ISO-F ion optics flange (see Figure 29). The flange had four high voltage (5 kV) feed-throughs for the ion optics and a 10-pin feed-through for the deflector (*see later*). The whole system could be removed from the reaction chamber for maintenance as a single unit.
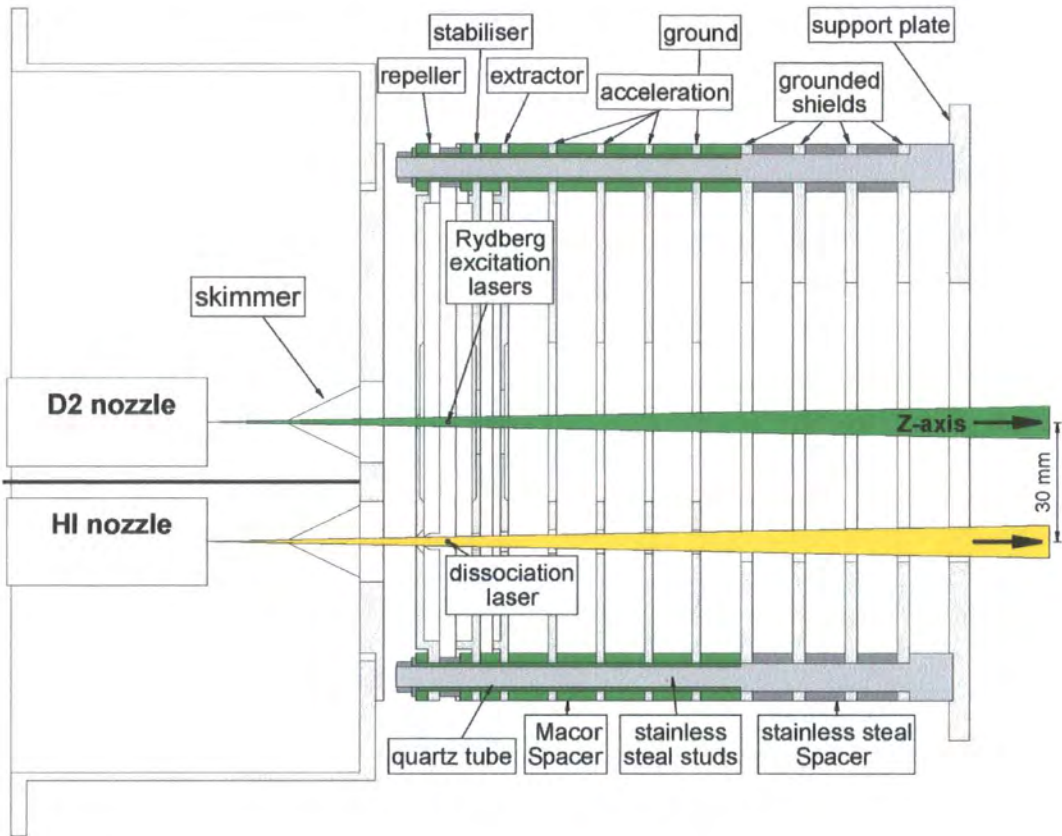
Figure 36: Schematic diagram of the ion optics system and molecular beams.
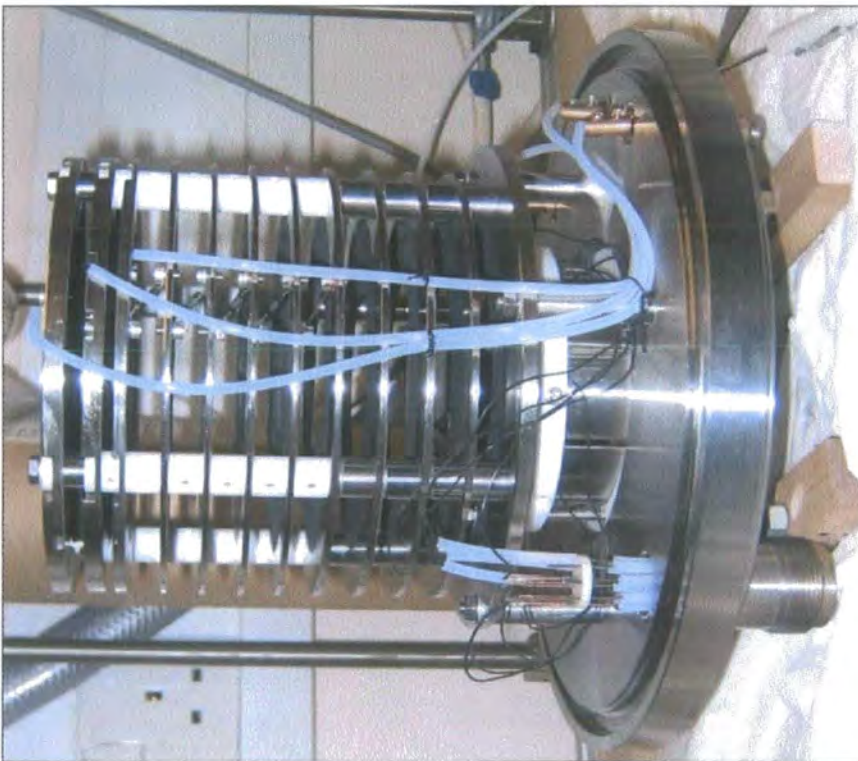
Figure 37: Photo of the ion optics.

The electrodes were insulated from the studs *via* precision quartz tubes slipped over the studs, ensuring the electrodes were centred with respect to the flange. The electrodes were positioned along the studs by cylindrical spacers, manufactured to the same length, to ensure they were parallel to each other. All the electrodes were coated in a thin even layer of graphite to provide good and even surface conductivity. The acceleration electrodes were connected by a resistor chain (2 MΩ) as can be seen in the photo in Figure 37.

The first seven electrodes had two apertures that allowed the two molecular beams to pass into the ion optics. The remaining grounded electrodes had a larger hole that allowed both beams to pass through. The HI molecular beam was prevented from impacting onto the detector by an annulus placed in the drift tube, the annulus allowed for the expanding ion cloud to pass though while blocking the HI beam. The region between the repeller and the extractor is known as the extraction region. The reaction volume, the overlap of the H* and the D_2 beams, is situated between the repeller and the stabiliser. The dissociation and excitation laser beams were aligned perpendicular to the z-axis and run through the spacing between the repeller and stabiliser electrodes. During Rydberg excitation the repeller voltage was lowered to give a minimum field at the centre as depicted in Figure 38 (see *section 6.2)*. After the collision the cloud of Rydberg atoms expanded. After the short expansion the repeller was pulsed to the potential required for velocity mapping. This created a field of around 400 V/cm (Simion estimation), which should be sufficient to field ionise the Rydberg atoms (see *section 6.3*). The potentials in the field excitation region and the potentials for velocity mapping (high field) are shown in Figure 38.
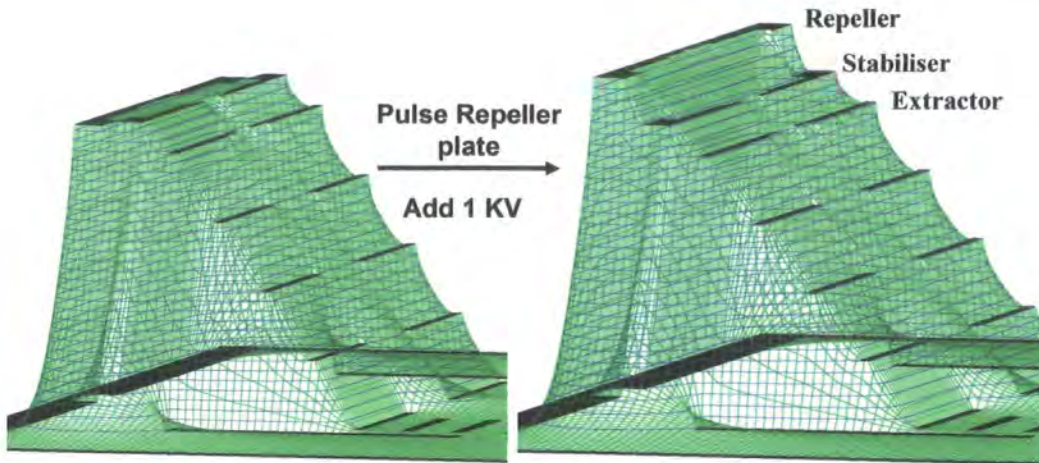
Figure 38: Ion optics simulation from Simion; the electrodes are shown in black, the equipotential lines are shown in green.

The next four electrodes produced the acceleration field. As the ion cloud moved into the acceleration region the ions' velocity component towards the detector was compressed such that the ion cloud impacted onto the detector in a pancaking fashion. It is the difference between the extraction and acceleration fields that creates the lens at the extractor orifice, allowing for velocity mapping. The voltages on the electrodes could be scaled to change the size of the image on the detector, while the voltage ratio between the plates remained constant. The final four, closely spaced electrodes are held at ground potential. They prevented external fields from distorting the ion imaging field as the ions passed through the main body of the chamber.

The centre-of-mass velocity of the $H^* + D_2$ collision complex, with a collision energy of 0.53 eV in this experiment, had a vertical component of 2200 m/s. Thus, the ion cloud would experience this effect and would impact high on the detector. A deflector, a stainless steel tube cut into eight segments, could be used to compensate for this. The deflector was 50 mm long with an inner diameter of 76 mm, it was mounted downstream of the ion optics. The voltage of each segment could be controlled independently, in order to create a near homogeneous deflection field in any direction. A deflection field in the order of 10 V/cm was sufficient to counteract the centre-of-mass velocity and steer the ion cloud onto the central axis of the detector.
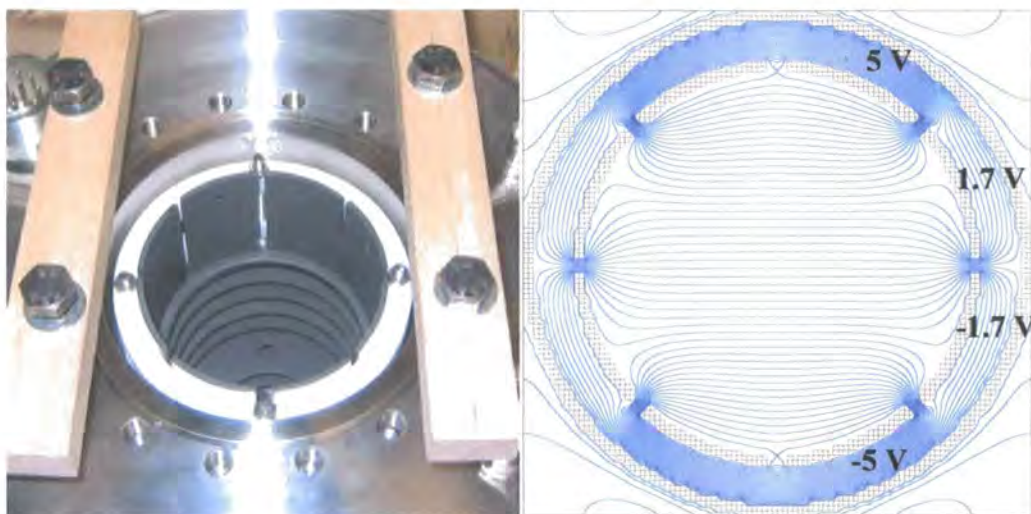
Figure 39: Left: photo of mounted deflector. Right: Simion simulation showing field lines (in blue) created when potential is applied to plates (in brown), the deflector is shown mounted through the ion optics flange (outer circle shown in Simion simulation).

The ion cloud then passed through the flight tube before hitting the detector. The nominal drift path (ionisation volume to detector) was 735 mm.

A cryo shield was used for extra pumping of the reaction chamber to reduce background ions created by short wavelength, intense laser radiation. The cryo shield (nickel tube) was sintered to a two litre stainless steel tank suspended from a liquid feed through from the top flange of the reaction chamber. The ion optics were mounted through the centre of the cryo shield as can be seen in Figure 29.

4.2.4.2   Ion optics power supply

The ion optics were biased using a custom made high voltage supply (Photek Ion Slicer BPS5). This consisted of 4 independent high voltage supply modules capable of supplying up to + 5 kV. The front panel control had a fifth display which provided remote control and monitoring of the repeller plate pulser unit bias voltage, detailed below.

The pulsing of the repeller plate, demonstrated in Figure 38, was achieved with the pulse unit supplied with the system. The pulser was triggered on the rising edge of a TTL pulse. The pulse output had variable amplitude up to + 1000 V and a

maximum repetition rate of 1000 Hz, which was limited internally. Examples of the pulse output are shown in Figure 40.
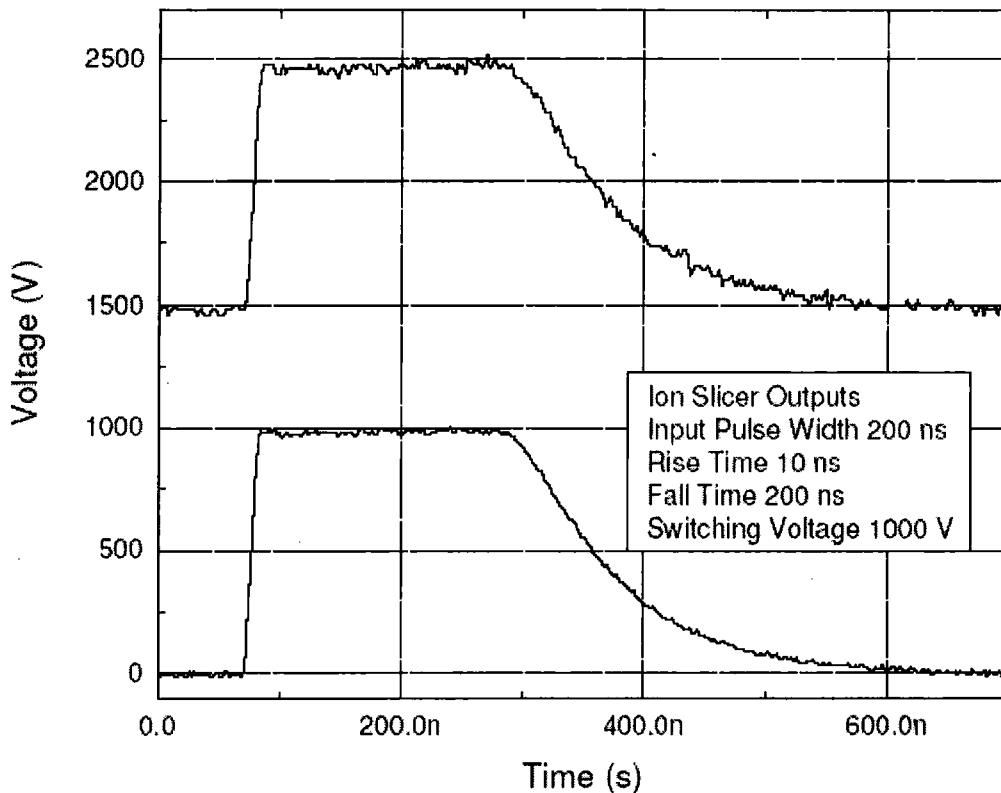
Figure 40: Example of the pulse output with and without an offset, measured by Photek.

The pulse width was set by the trigger width. The trigger width was approximately equal to the flat top of the output pulse. The minimum output width was 100 ns. Photek specified a rise time of $\leq$ 10 ns (10%-90%). This was also measured in situ (see *section 6.1*).

The pulsed voltage is added to the constant (baseline) voltage of the repeller high voltage output of the ion optics high voltage supply.

The pulser had an insertion delay of 75 ns between the trigger and the pulse output, in addition to any delays generated by the connecting cables. In the laboratory this was measured to be 88 ns.

The deflector was powered using an eight channel voltage supply built by the Chemistry Department electronics workshop. It consisted of four pairs of positive

and negative channels each of which was individually adjustable from 0 to $\pm$ 60 V. This design ensured that the centre of the deflector could be held on ground potential.

4.2.4.3 Detector

The detection system comprised of a vacuum compatible detector incorporating two microchannel plates with a 50:1 (length over diameter) ratio, custom manufactured by Photek Ltd. under the Photek reference number S06-135.

The image quality detector consisted of dual MCPs (0.8 mm thick) in chevron configuration with O.D. 40 mm (outer diameter) in front of a P20 phosphor on a glass substrate. The whole device was mounted on a 152 mm O.D. conflat flange.
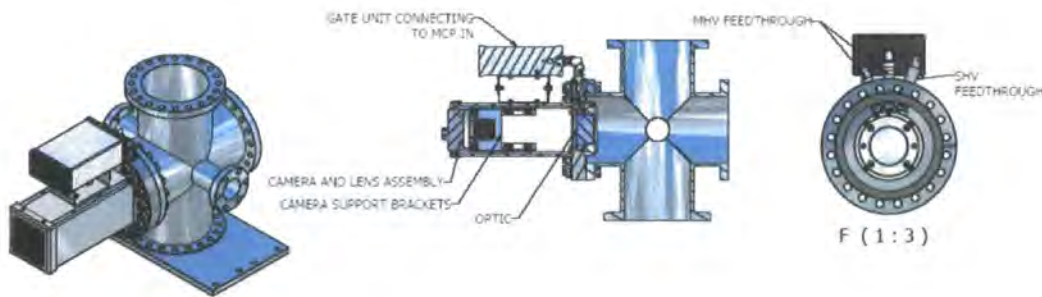
Figure 41: Overview of mounted deflector (image provided by Photek).

The high voltage power supply (Photek, VID BPS3) had 3 independent high voltage supply modules which had inter-linked control functions for maintaining the potential ratio across the MCPs and phosphor screen.

The detector could be used in two modes, a TOF mode and a gated mode. In TOF mode the three bias voltages were constant. The timing signal (created by ions hitting the MCPs at different times) was collected by the conductive coating of the phosphor screen and capacitively coupled to allow monitoring by the oscilloscope. The TOF mode allowed for the measurement of mass spectra. In the gated mode the bias voltage across MCP 2 was split into a constant contribution and a fast, pulsed contribution, fixed at 500 V. Both parts were added *via* a fast high voltage switch. This allowed the detector to be switched on and off to image ions arriving

at the detector at a selected time gate, *i.e.* mass. Pulsing the second MCP rather than the front of MCP1, as is conventional in most ion imaging set-ups, ensured the front plate was grounded and therefore would not distort the image. The gate unit (GM-MCP-2) was triggered by the rising edge of a TTL pulse. The shortest gate pulse was approximately 8 ns (FWHM) and is presented in Figure 42.
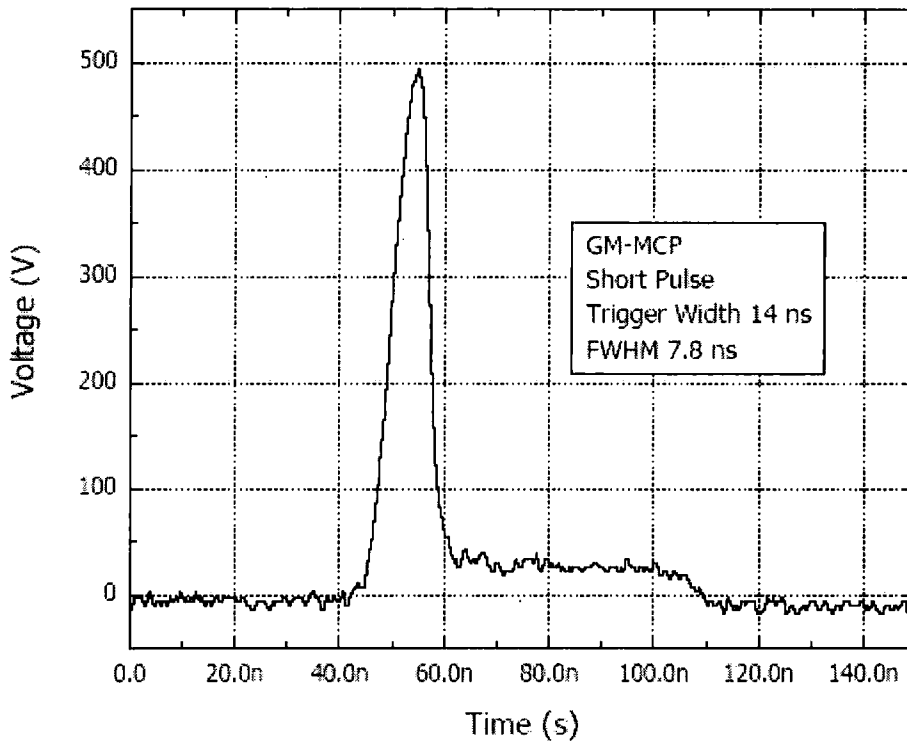
Figure 42: The minimum gate output measured by Photek.

There was a 75 ns insertion delay from the trigger input to the gate output, plus potential delays generated by connecting cables for the trigger input and gate output.

The light from the phosphor screen was detected with a CCD digital camera (Basler, A312f) with a firewire connection to the PC. The camera had low thermal noise and was externally triggered. It had 768 × 576 pixels. The maximum frame rate was 53 frames/second.

The image software provided by Photek (Image32) communicated with the camera to acquire images. The image buffers generated outputs consisting of the (x, y)

coordinates of centroided events, to pixel and sub pixel resolution. A large range of image processing functions were incorporated in the software; these included algebraic operations on images, enhancement, measurement of profiles and ring diameters, etc.

The images could be collected in 2 modes, bright field and event counting. In bright field mode the camera image was seen in real time. The event counting mode was the data collecting mode; here the events were summed and an image was accumulated in a buffer over time. The image was built up by identifying conjoint illuminated pixels. The most intense pixel from each light spot is the pixel to which the single event was assigned. An event was only counted if the intensity was over a user defined threshold. The camera could detect 10000 events per frame and the events were summed then stored to a file on a frame by frame basis. Further analysis used the coordinates from this file. The image software could also provide sub pixel resolution, which has not been used for the images in this study. Here a 5 by 5 grid around each event would also be recorded, and post processing this grid would provide sub pixel resolution as the centre of an event could be identified.

Chapter 5: Test Measurements and Calibration

5.1 Introduction

The complex nature of the full reactive scattering experiment caused the experimental set-up to be a challenging process. It was important to test each stage of the experiment and confirm that all parts were correctly installed and calibrated. This chapter describes the test measurements and results.

5.2 Ion imaging tests

The magnification of the ion lens directly translates pixels into speeds. The aim of this calibration procedure was to obtain ion optics settings that produce optimum velocity mapping and to determine how the speed calibration compares to the Simion simulation.

5.2.1 Photodissociation of HI

5.2.1.1 Introduction

Photodissociation is the fragmentation of a bound molecule through absorption of one or more photons. The electromagnetic energy of the light is converted into internal energy of the molecule and if the transferred energy exceeds the binding energy of the weakest bond, the molecule can irreversibly break apart.

Photodissociation studies are valuable in providing the basic knowledge concerning dissociation channels, the product branching ratio, or even the product state distribution [108]. Information about dissociation processes, such as possible non-adiabatic effects, can be deduced from the angular distribution of final fragments, while investigations of the absorption spectrum will permit the

exploration of repulsive states or those portions of bound states that lie above the dissociation energy [109].

The photodissociation of HI has been extensively studied [108] [110] [111]. When excitation occurs in the first absorption profile, which is assigned to $\sigma^* \leftarrow np\pi$ transitions, HI undergoes a direct bond fission to produce H (^{2}S) and an iodine atom in the spin-orbit excited state I ($^2P_{1/2}$) (I*) or the ground state I ($^2P_{3/2}$) (I) as depicted in Figure 43.
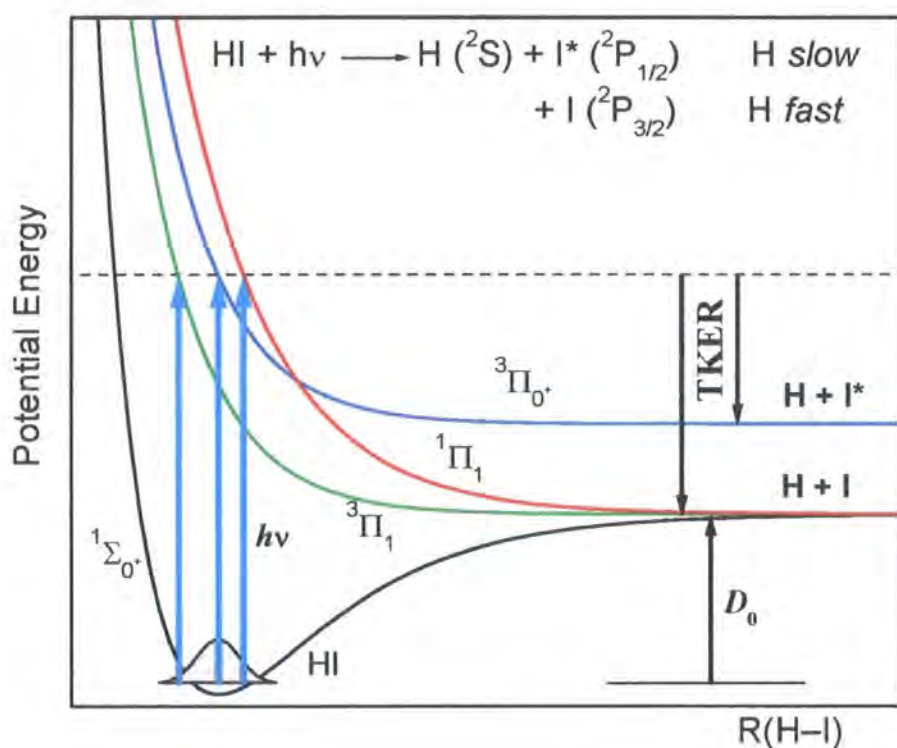
Figure 43: Schematic potential energy curves for HI.

Despite the wealth of experimental measurements, little has changed in the qualitative interpretation of the photodissociation process since Mulliken's work in 1937 [112]. His interpretation was that the A-band absorption was due to contributions from three overlapping continuum transitions into the $a^3\Pi_1$, $A^1\Pi_1$, and $a^3\Pi_{0+}$ states. Among these valence states, the $a^3\Pi_1$ and $A^1\Pi_1$ correlate to I ($^2P_{3/2}$) and the corresponding transitions are polarised perpendicular, $\Delta\Omega = 1$, (where $\Delta\Omega$ is the projection of total electronic angular momentum onto the bond

axis) to the bond axis, whereas the $a^3\Pi_{0+}$ state is correlated with I* ($^2P_{1/2}$) and the corresponding transition dipole is aligned parallel to the H-I bond, where $\Delta\Omega = 0$.

For prompt dissociation of the diatomic molecule following absorption of linearly polarised light, the fragment recoil velocity angular distribution to lowest order is given by [113]

$$I(\theta) \propto \frac{1}{4\pi}\left[1 + \beta P_2(\cos\theta)\right]$$

Equation 13

where θ is the angle between the electric field vector of the laser (ε) and recoil velocity vector, and β is the anisotropy parameter. For a diatomic molecule with axial recoil (dissociation fast compared to rotation) β has extreme values of 2 (parallel transitions) and -1 (perpendicular transitions).
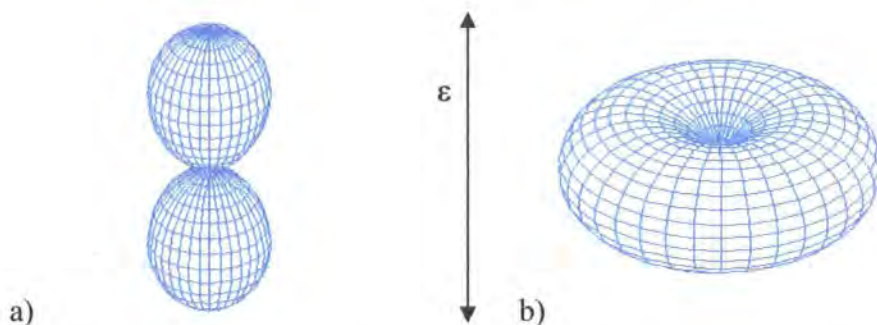
Figure 44: Angular distribution of fragments in the lab frame, a) $\cos^2\theta$ for a β parameter of 2, and b) $\sin^2\theta$ for a β parameter of -1.

The photodissociation of HI is well studied. The velocity and angular distributions are known to great accuracy providing a calibration tool to test the ion optics and the accuracy of the velocity mapping, providing a stringent test of the detection system.

5.2.1.2 Experimental

The experimental set-up closely follows that described in *chapter 4*. For this test measurement the HI molecular beam was moved up to the central axis of the experiment, requiring the modified D_2 nozzle to be replaced by a standard General Valve nozzle. This positioned the HI molecular beam at the centre of the ion optics. The alignment of the 266 nm beam was adjusted such that it entered the chamber along the angled path shown in Figure 45 rather than the lower path used for the main experiment. The laser baffles inside the laser ports had slits that allowed the light to enter at the required angle.
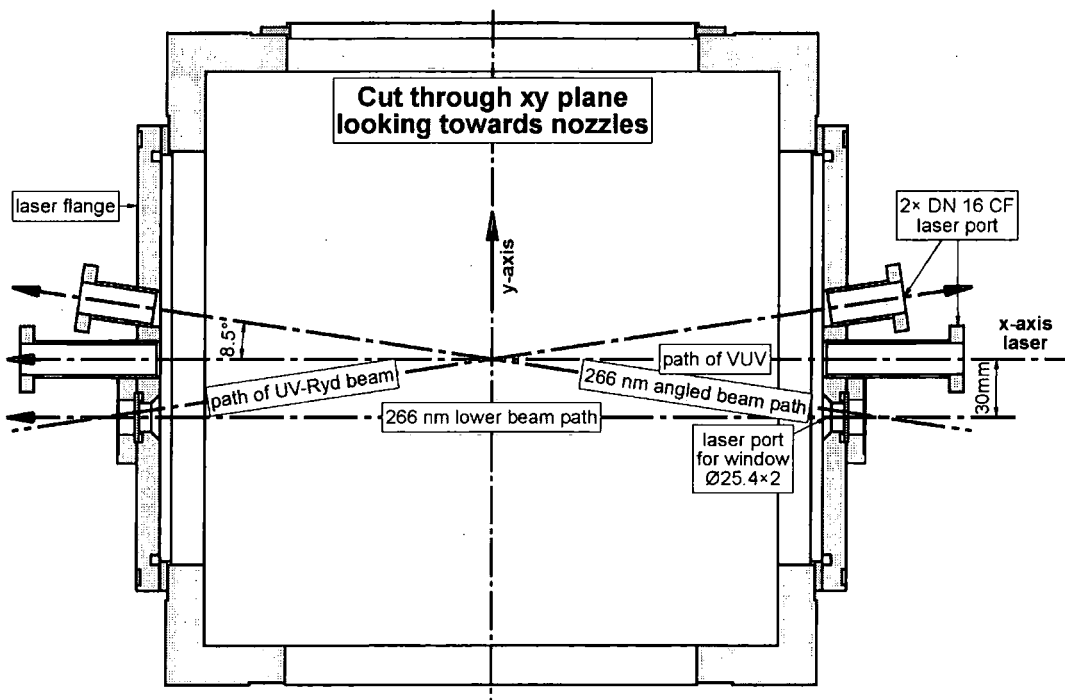
Figure 45: Diagram showing cut through chamber in the xy plane, looking towards the nozzles. The laser paths are shown as arrows.

The standard HI nozzle operated with 6% HI in argon at a backing pressure of 1 bar HI. The beam was collimated by a 1.0 mm skimmer. 266 nm light was used to photodissociate the HI. The H fragments were probed with (1 + 1′) resonant ionisation from the Lyman-α VUV and UV-Rydberg lasers. The Lyman-α VUV wavelength was scanned over the Doppler profile of the H-fragment atom and the UV-Rydberg laser was tuned to maximise ionisation.

5.2.1.3 Fitting program

The image analysis program used in this work was developed by E. Wrede at the University of Bristol [107], and was designed to analyse ion images from photodissociation events. The programme is a useful tool in the analysis of the acquired images allowing them to be processed in a variety of ways.

It is important to define the centre of the images, *i.e.* the position of the velocity origins, as precisely as possible. The analysis programme has an automatic procedure that uses the underlying symmetry of the photodissociation process in comparing, respectively, the upper/lower and left/right halves of each image with respect to a test origin, and minimizes the squared differences with sub-pixel resolution.

The images can be rotated and four-fold symmetrised in order to increase the signal-to-noise ratio. A 2D Gaussian filter can be applied to smooth noise in the images.

The reconstruction of the 3D velocity distributions from the accumulated 2D ion images uses an algorithm based on the filtered back projections by Sato *et al.* [114]. The velocity and angular distributions can be extracted from the reconstructed 3D velocity distributions.

To determine meaningful errors, the total signal of each image (i.e., the number of ion events) is conserved, and the statistical errors (proportional to the square root of the number of counts in an individual pixel) are propagated throughout the whole reconstruction and analysis process.

5.2.1.4 Results

The quality of the images recorded with the detection system is very high. Figure 46 a) shows the raw data collected; the image has been rotated by 8.5°, which is necessary to compensate for the laser set-up used in the photodissociation process. The 266 nm light is vertically polarised parallel to the detector face but it

interacts with the beam at an angle of 8.5°; this results in the image being recorded at such an angle relative to the horizontal axis of the detector.
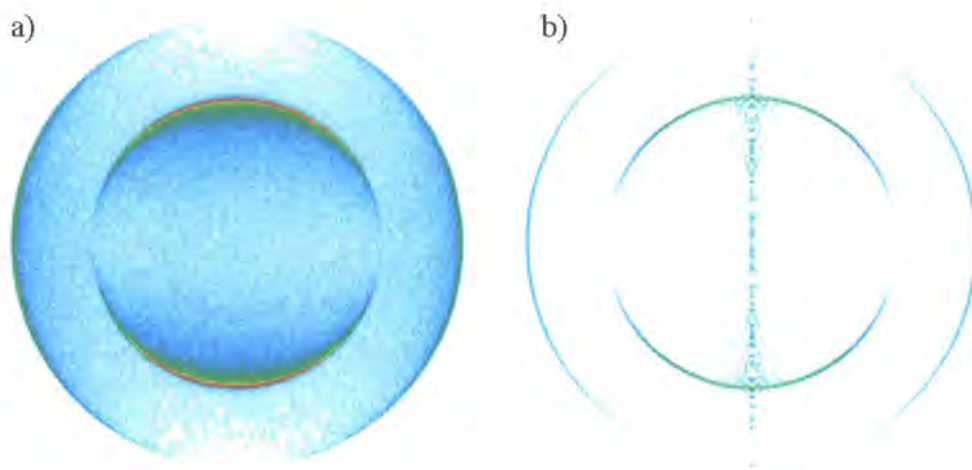
Figure 46: a) Raw ion image, rotated by 8.5° and, b) 2D slice through the reconstructed 3D distribution.

The sharpness of the image corresponds to optimised velocity mapping conditions (see Table 3), where good focusing shows optimum electrode voltage settings. Figure 46 b) shows a 2D slice through the reconstructed image. Analysis on this image can provide detail on how sharp the image is and to what extent good velocity mapping conditions have been achieved. Figure 47 shows the projection onto both the X and the Y axis for the raw image in Figure 46. This illustrates the slope of the rising and falling edges, a more useful illustration of which can be seen in Figure 48, which shows the derivatives of the signal in Figure 47. The width of these peaks is a direct measure of the achieved resolution. In order to determine optimised velocity mapping conditions a series of images were recorded at differing voltage settings; the derivatives of the x and y projections (as in Figure 48) provided a means to conclude which settings provided the sharpest image.
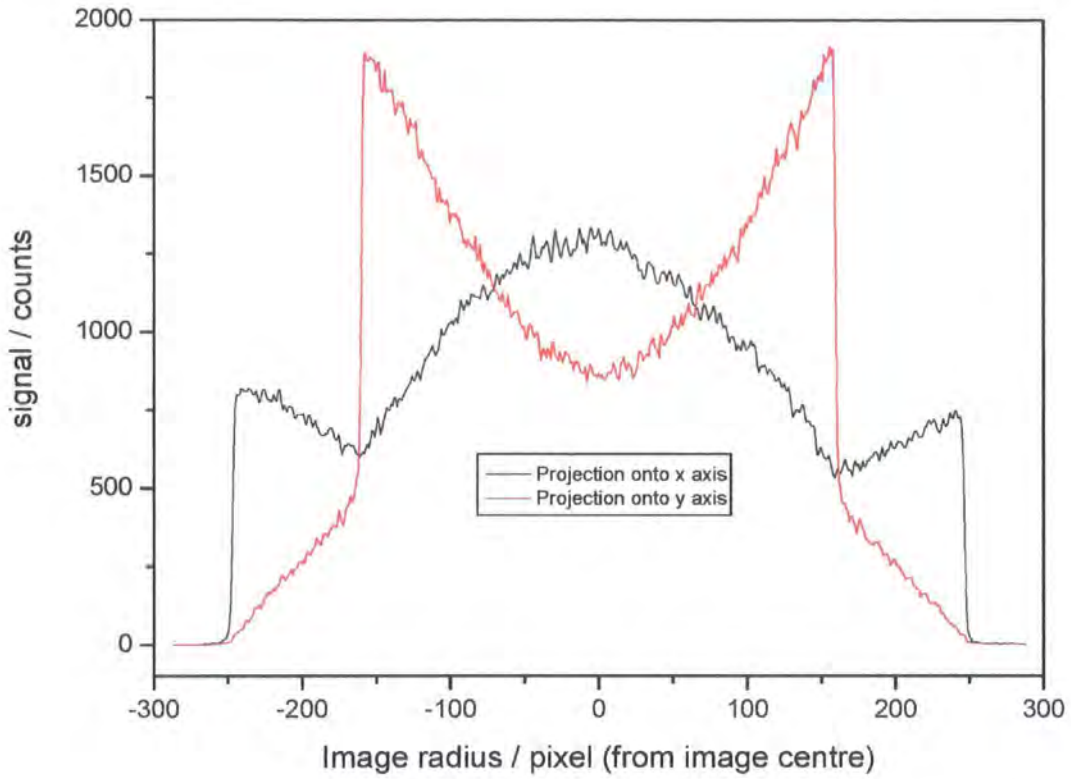
Figure 47: Signal projection on x axis and y axis. Velocity mapping conditions from Table 3.

Table 3: Optimised potentials for velocity mapping.

	Repeller / V	Stabiliser / V	Extractor / V
Experimentally optimised	5000	4320	4139
Simion optimised	5000	4346	3978
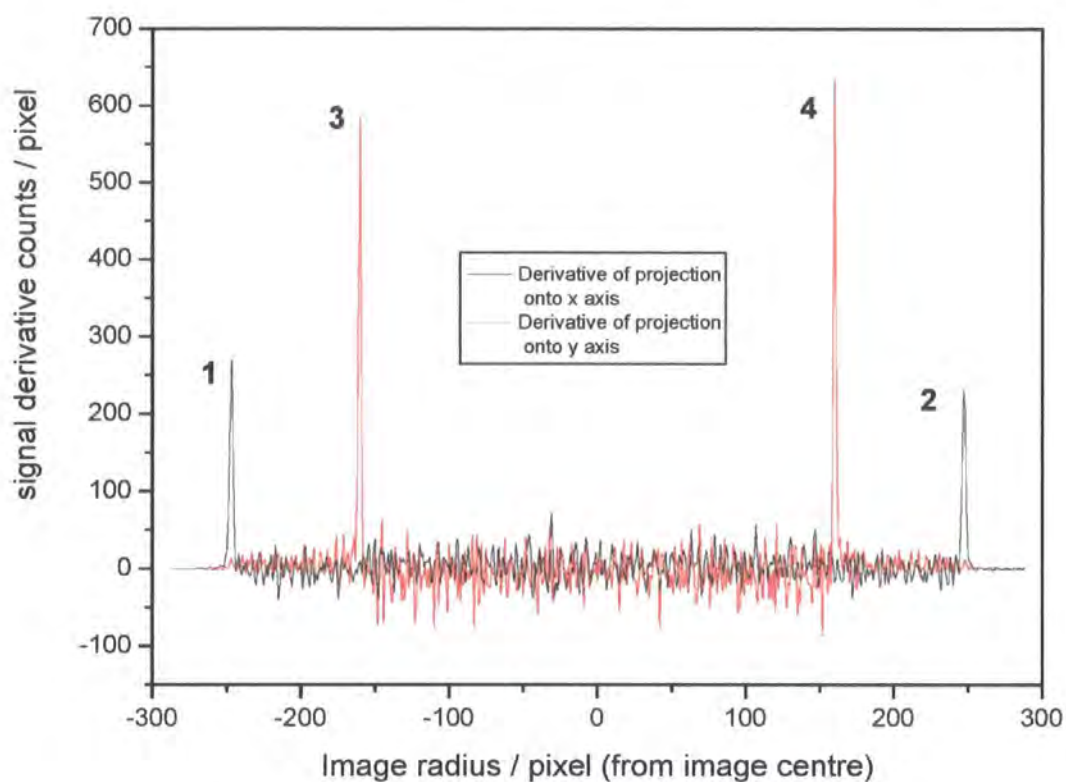
Figure 48: Signal derivatives of projection in Figure 47.

Table 4: Peak width information taken from Figure 48 obtained from a Gaussian fit.

Peak number	1	2	3	4
Width (FWHM) / pixels	2.26 ± 0.07	2.30 ± 0.09	1.85 ± 0.09	1.72 ± 0.08

The peaks of the signal derivatives are very sharp with widths (FWHM) of around 2 pixels. There are factors to be taken into account when considering the maximum sharpness theoretically possible:

- The skimmed molecular beam has a velocity spread perpendicular to the beam velocity, determined by the nozzle and skimmer orifices. For these measurements the nozzle was positioned 38 mm behind the skimmer and 77 mm from the laser. Geometric arguments show the largest spread in speed perpendicular to the beam is 12 m/s for HI in argon, this translates into 0.3 pixels on the detector.

- The rotational distribution of the HI must also be considered. From rotational populations at an estimated upper temperature of 30 K, the velocity spread originating from the rotationally excited HI can be found to account for an estimate of 0.8 pixels.

- The largest contribution to the peak width stems from the finite pixel resolution of the camera. The event counting algorithm assigns an event to the pixel with the highest intensity which results in a resolution of 2 pixels.

These considerations give a good indication that the velocity mapping is well focused.

The outer ring has slightly wider signal peaks. This can be attributed to unavoidable spherical aberrations, which cause the focusing of the ion lens to be better at the centre of the image than out towards the edge. This can be seen in Figure 49 below.
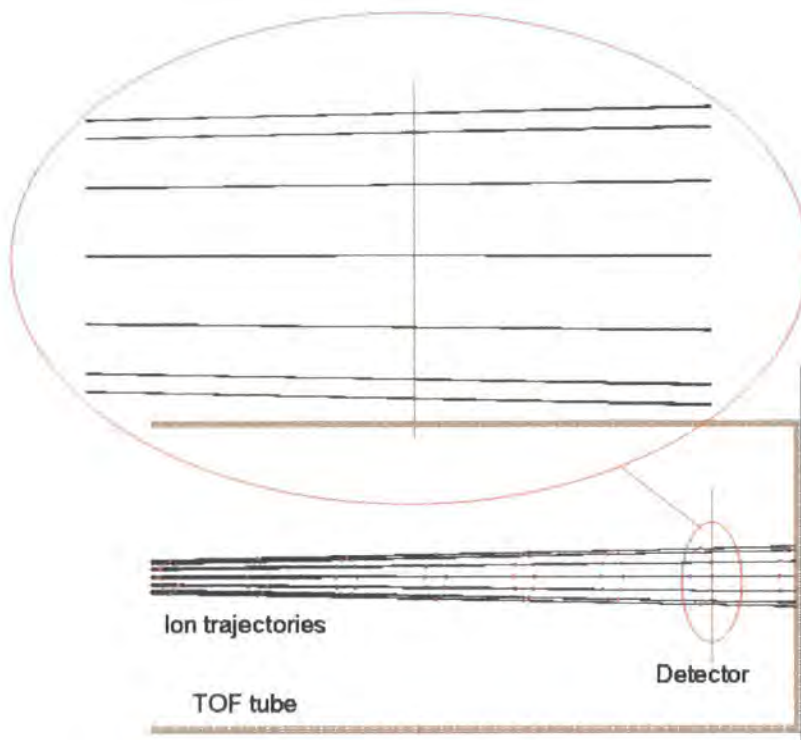
Figure 49: Image from Simion showing ion trajectories in TOF tube. The magnified section shows focusing deteriorating towards the edge of the image due to spherical aberrations.

The velocity distribution and β parameters for the reconstructed image in Figure 46 are shown in Figure 50. The radius of the rings is proportional to velocity. This ratio provides a test on the ion imaging system to ensure the position of the rings corresponds to the known velocity.
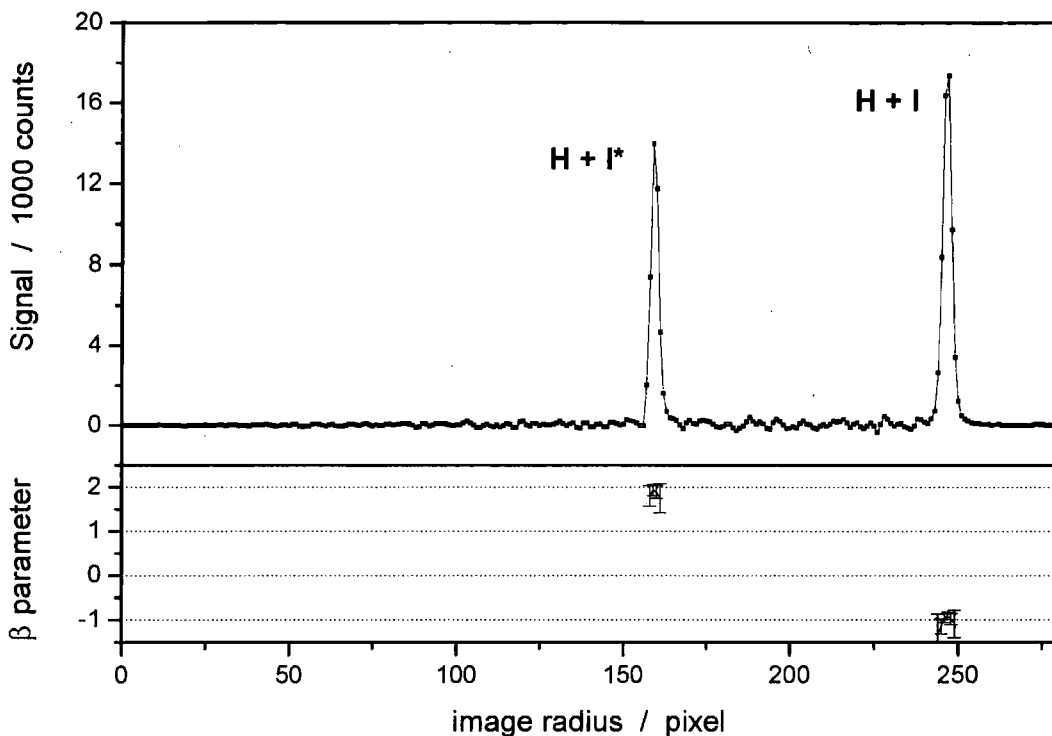
Figure 50: Shows the velocity distribution corresponding to the image in Figure 46. The lower section shows the anisotropy parameter.

Table 5: Shows the details of peaks from Figure 50 obtained from a Gaussian fit.

	H + I*	H + I
Simion (pixels)	162	252
Centre (pixels)	159.3 ± 0.1	246.6 ± 0.1
FWHM (pixel)	2.29 ± 0.03	2.59 ± 0.02
Area (counts)	40720 ± 474	58390 ± 486
	Branching fraction: 0.41 ± 0.01	

The branching fraction, Γ, of the excited I* atom is a fundamental characteristic of the photofragmentation reaction and is defined as

101

$$\Gamma = \frac{\sigma(I^*)}{\sigma(I) + \sigma(I^*)}$$

Equation 14

where σ (I*) and σ (I) denotes the probabilities for dissociation into I* and I atoms at a particular wavelength (266 nm). This is a well studied value and hence provides a further test of the experimental set up.

A branching fraction of 0.41 ± 0.01 has been obtained through this test which is in agreement with the literature [110], as are the β parameters, which have a value of 2 for the parallel transition and -1 for the perpendicular transition.

By increasing the power of the Lyman-α light and reducing the power of 266 nm light, the probability of detecting hydrogen atoms that stem from photodissociation of HI with Lyman-α light increases. This resulted in observing two further rings, which are shown in Figure 51.

a)   b)
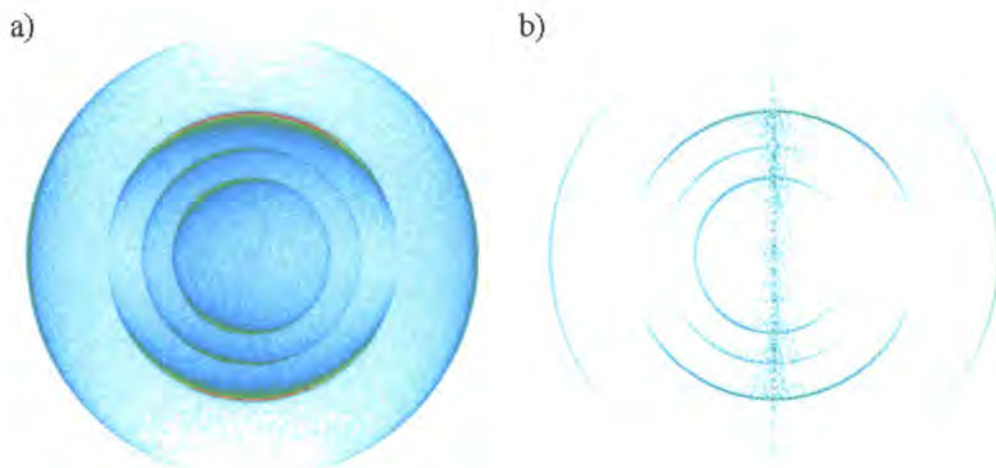
Figure 51: a) Raw ion image, rotated by 8.5° and b) 2D slice through the reconstructed 3D distribution.

A total of four rings are produced from the photodissociation of HI with Lyman-α, however the photodissociation into I ($^2P_{1/2}$) and I ($^2P_{3/2}$) produces rings that are too big to fall on the detector. The relevant energy levels are displayed in Figure 52.
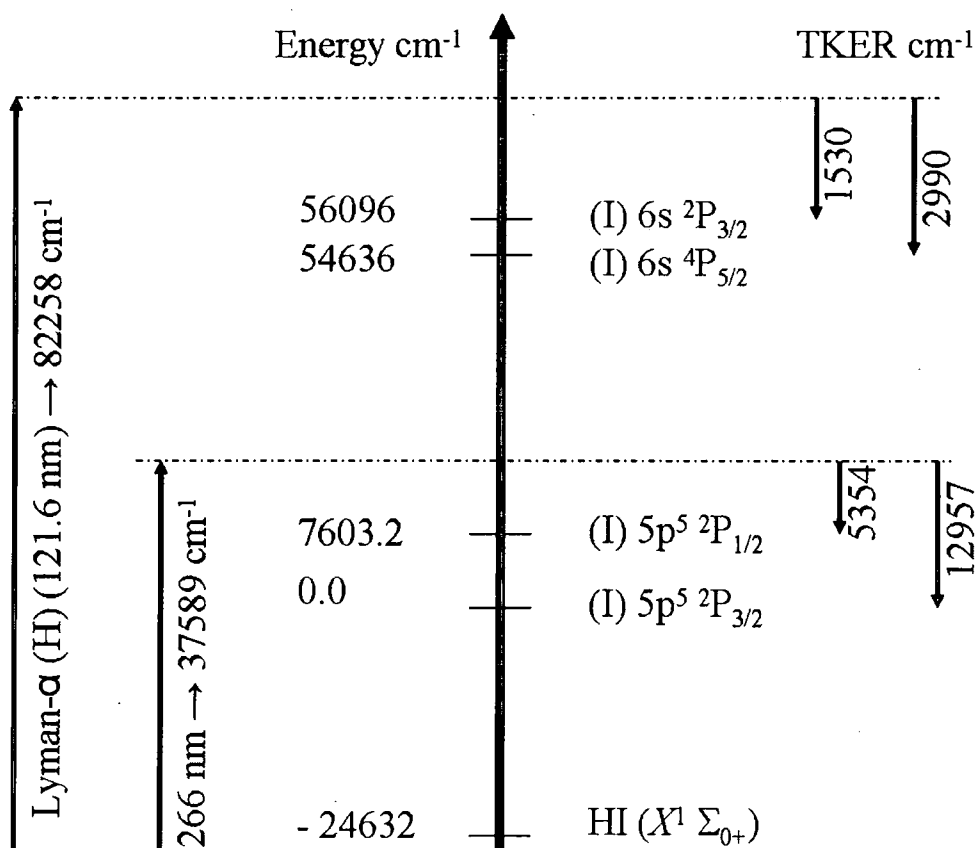
Figure 52: Relevant dissociation energies of HI. Where D_0^0 **is taken from [115], the dissociation energies from [116] and 4th harmonic from [117] (calibrated against a transition in OH). TKER is the total kinetic energy release.**

The calibration procedure was to check the ratio of the velocities of different channels with the total kinetic energy released. The ratio of the position of the peaks (velocity) should correspond to the square root of the kinetic energy ratio of the two channels ($v \propto \sqrt{E_k}$).

$$TKER \times \frac{m_I}{m_{HI}} = E_k(H) = \frac{1}{2}m_H v_H^2$$

$$v_H = \sqrt{\frac{2E_K(H)}{m_H}} = \sqrt{\frac{2\frac{m_I}{m_{HI}}TKER}{m_H}}$$

Equation 15
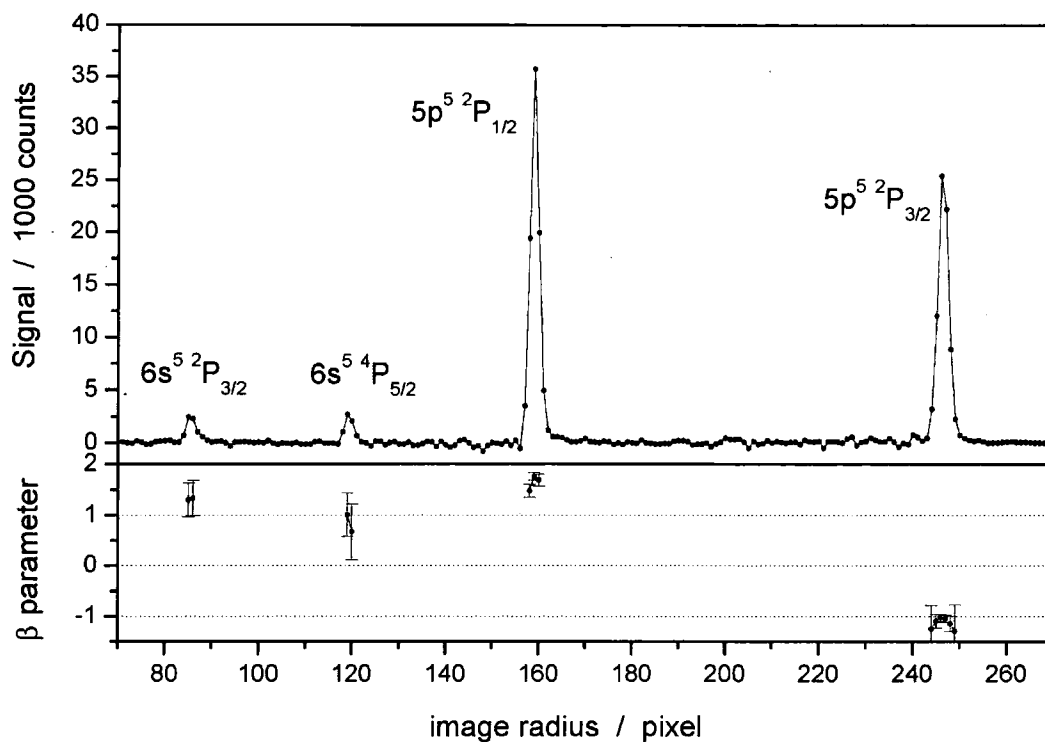
Figure 53: The velocity distribution corresponding to the image in Figure 51. The lower section shows the anisotropy parameter.

Table 6: Details of peak position from Figure 53 obtained from a Gaussian fit and calculated peak positions using the $^2P_{1/2}$ peak as a reference.

Peak	6s ($^2P_{3/2}$)	6s ($^4P_{5/2}$)	$5p^5$ ($^2P_{1/2}$)	$5p^5$ ($^2P_{3/2}$)
Experimental centre point (pixels)	85.50 ± 0.07	119.08 ± 0.05	159.03 ± 0.01	246.39 ± 0.01
Scaling factor	0.534	0.747	1	1.55
Predicted theoretical centre (pixel)	85.00	118.82	**159**	247.35
% Error	0.70%	0.16%	X	0.55%

Table 6 details the position of the peaks taken from Figure 53. The scaling factors have been obtained from the TKER values presented in Figure 52. The sharpest peak ($^2P_{1/2}$) has been used as a reference along with the scaling factors to calculate

where the other 3 peaks should be positioned relative to the $^2P_{1/2}$ peak. The calculated peak positions are in good agreement with the experimentally observed peaks. This gives a good indication that the velocity mapping ion imaging system functions well.

5.2.2 Deflector test

The deflector is required to steer the image onto the centre of the detector. Simion simulations were used in the design of the deflector and it was designed to move the ion cloud in a symmetrical way without causing distortions and blurring; however the simulation does not take into account the possible minor errors in manufacture and installation. The following discusses the tests undertaken to ensure the image remained circular as it was 'deflected'.

Figure 54 shows the raw images collected (which have been rotated by 8.5°), varying the settings on the deflector in order to move the ion cloud vertically on the detector. The final image d) is slightly clipped as the whole image did not fit onto the detector.
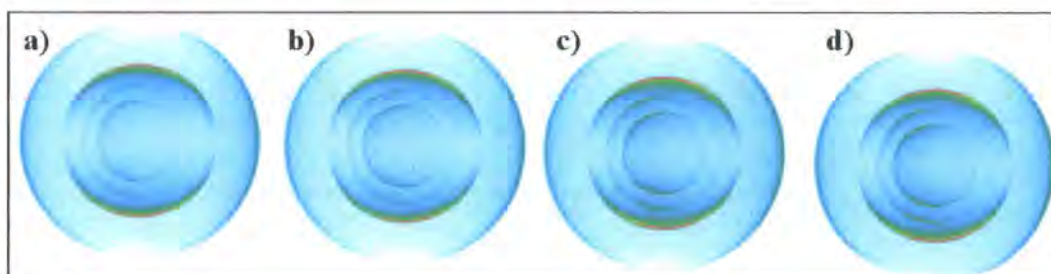
Figure 54: Raw images rotated by 8.5°. Velocity mapping conditions from Table 3. Deflector settings: a) all plates at 0 V. b) Top plates (TP): 10 V, upper middle plates (UM): 3.4 V, lower middle plates (LM): -3.4 V, and bottom plates (BP): -10 V. c) TP: 20 V, UM: 6.8 V, LM: -6.8 V, BP:-20 V. d) TP: 40 V, UM: 13.6 V, LM: -13.6 V, BP:-40 V,

A comparison of image a) and image c) has been made to establish whether the symmetry is maintained when using the deflector. Image a) is a standard image with no voltage applied to the deflector where as for image c) the deflectors top plates were at 40 V, the upper middle plates were at 6.8 V, the lower middle plates were at -6.8 V, and the bottom plates at -40 V.

Figure 55 shows a 2D slice through the reconstructed 3D distribution of the two raw images from Figure 54.

a)   c)   e)
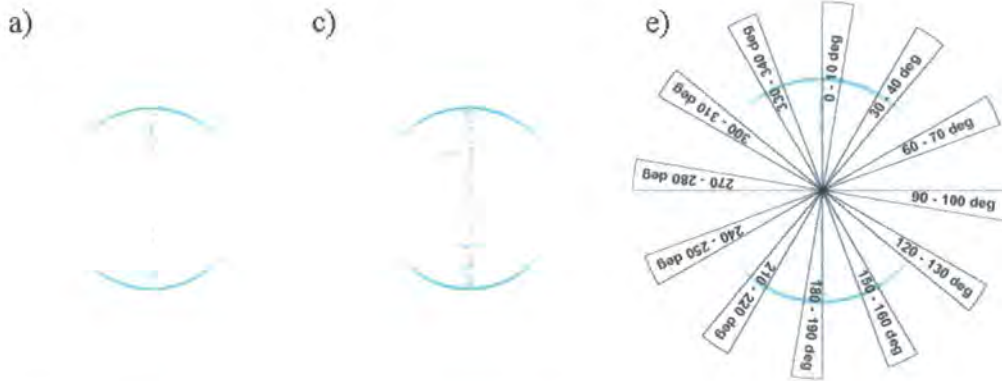
Figure 55: a) and c) 2D slice through the reconstructed 3D distribution corresponding to raw images from Figure 54. e) Sections used for analysis.

The image analysis programme was used to take 10° sections and determine the velocity distribution of that section; if the images were circular all the sections would show the velocity peaks to be at the same place (in pixels). The same analysis was undertaken for both images a) and c) in order to test that the image remained circular after the deflector had been used to move it on the detector. The velocity peaks of the two images should remain constant.

Figure 55 e) shows the sections of each image analysed to produce the velocity distributions shown in Figure 56 and Figure 57.
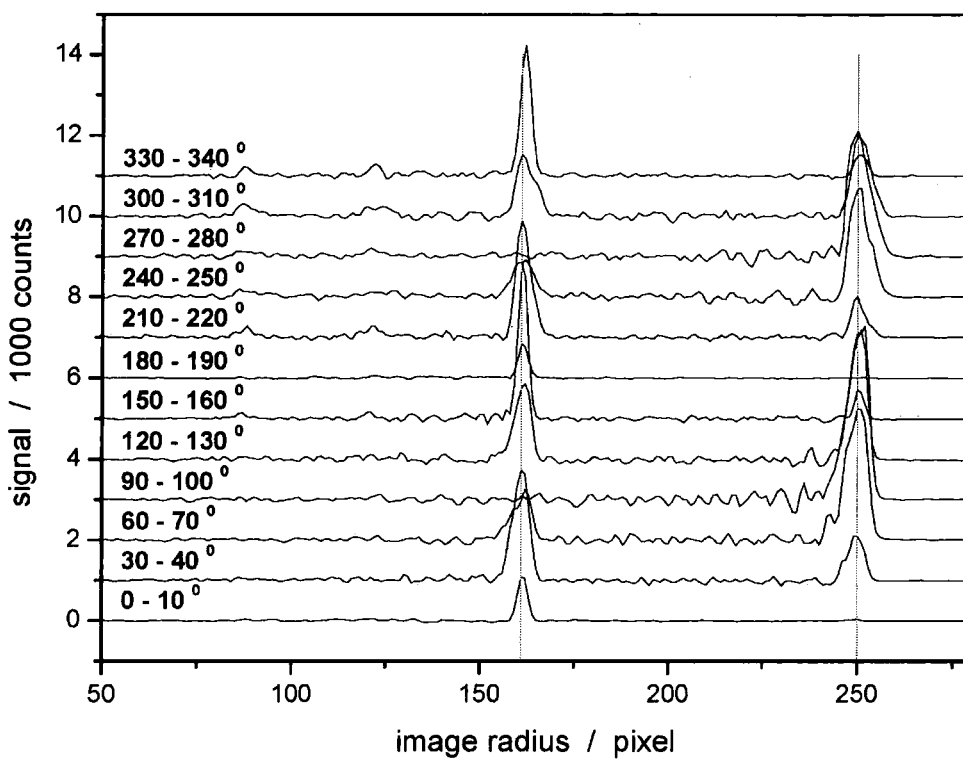
Figure 56: Velocity distributions of angular sections taken from Figure 55 a). The graphs are offset by 1000 counts for ease of viewing.
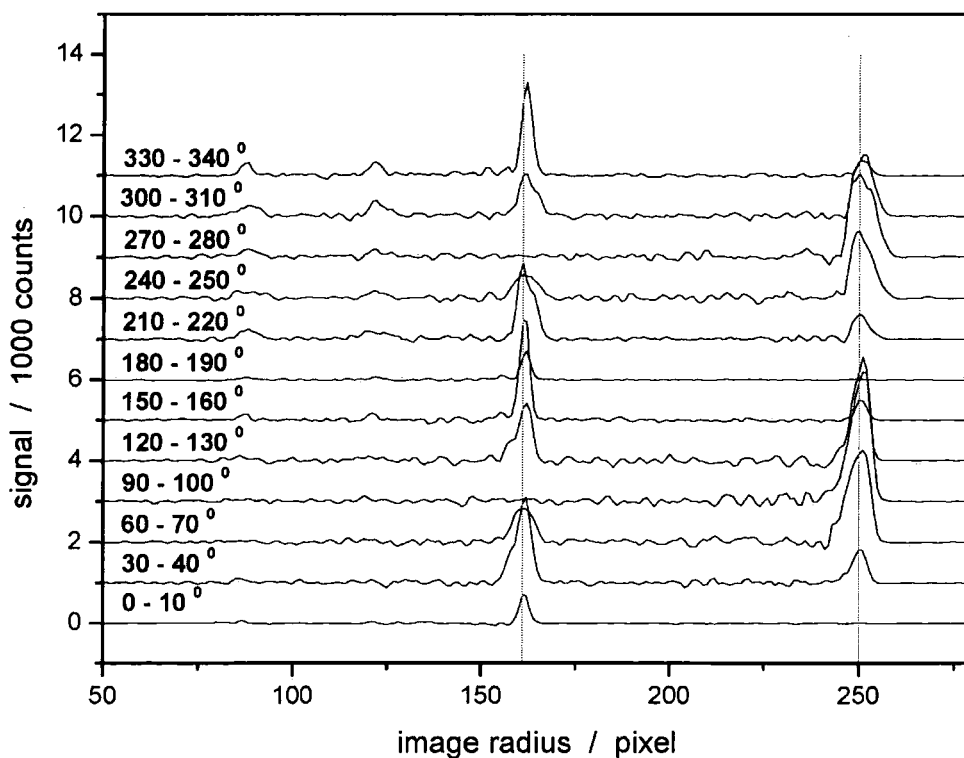
Figure 57: Velocity distributions of angular sections taken from Figure 55 c). The graphs are offset by 1000 counts for ease of viewing.

107

Figure 56 shows the velocity distribution from the various angle sections of Figure 55 a), which is the 2D slice of the 3D reconstruction of Figure 54 a). For this image the deflector was kept at ground potential to provide a control against which an image created by using the deflector could be tested. The graph demonstrates that the image is circular as all the different angular slices have velocity peaks at the same radii, 161 and 250 pixels (shown by grey line).

Figure 57 shows the velocity distribution from the various angle sections of Figure 55 c), which is the 2D slice of the 3D reconstruction of Figure 54 c). For this image the photodissociation signal had been moved vertically (lowered) on the detector using the deflector. Figure 57 shows that the image has remained circular as the peaks for the differing angle slices can be seen at the same position. This shows that the deflector works well and does not distort the image.

5.3 D$_2$ Conversion

5.3.1 (3 + 2) Resonance-enhanced multiphoton ionisation

5.3.1.1 Introduction

Resonance-enhanced multiphoton ionisation, REMPI, is a laser ionisation technique that has been used extensively as a selective ionisation source for mass spectrometry. In the REMPI process, a molecule is excited by a photon, or multiple photons, whose energy is in resonance with an electronic state of the molecule. The excited molecule is then ionised by absorption of additional photons. Resonance ionisation is highly efficient because of the increased lifetime of the intermediate state by as much as 6 orders of magnitude compared with that of non-resonant multiphoton ionisation. Various excitation schemes can be used for REMPI, and these are described by the number of photons used for excitation and ionisation. For example, in the simplest resonance-ionisation scheme one photon is used to excite the molecule and an additional photon to ionise it, this is the (1 + 1) REMPI scheme. In higher-order excitation schemes, two or more photons are involved in the excitation and the ionisation processes.

(3 + 2) REMPI has been used to test the purity of the ortho-D_2 to be used in the reactive scattering experiment. This ortho-D_2 has been converted from normal-D_2 using a catalyst as described in the experimental section.

The (3 + 2) REMPI experiment (shown in Figure 58) uses the three photon excitation into the B state through the transition: $X^1\Sigma_u^+ (v' = 3) \leftarrow B^1\Sigma_g^+(v' = 0)$. Absorption of a fourth photon can produce ionisation, D_2^+ ($X^2\Sigma_g^+$), or cause dissociation into neutral atoms D (1s) + D (2s, 2p). A fifth photon is then required to ionise the excited D (2s, 2p) atom to produce D^+ ions which can be detected. The (3 + 2) signal was more intense than the (3 + 1) and as such this signal was used.
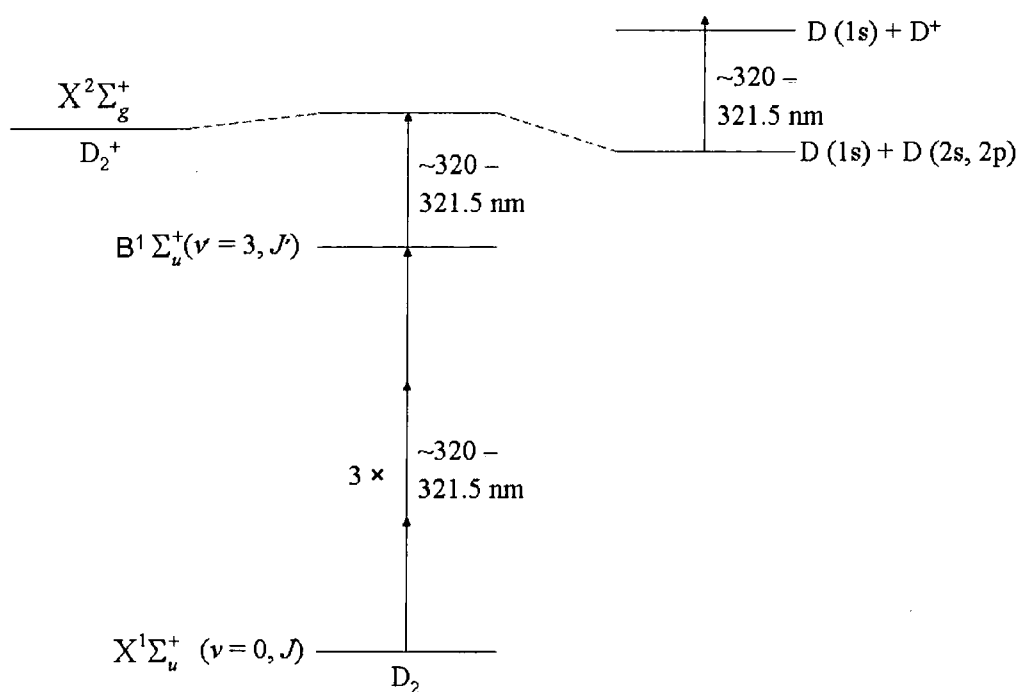
Figure 58: (3 + 2) REMPI process for D_2. Adapted from [117]

5.3.1.2 Experimental

The modified cooled D_2 nozzle was operated with a backing pressure of 3 bar D_2. Both normal and ortho D_2 were tested in order to provide a comparison.

The second harmonic of a Nd:YAG laser (Continuum, Surelight I-10, pulse length 5 ns, repetition rate 10 Hz) was used to pump a dye laser (Sirah, Cobra stretch, dye: DCM in methanol: oscillator and pre amplifier 300 mg/litre, with a KD*P non-linear crystal for second harmonic generation and Pellin-Broca wavelength separator) which is labelled as Dye 3 in the laser set-up schematic in Figure 32. The accessible wavelength range of the doubled light was 301-330 nm.

The D^+ signal was detected using TOF mode of the detection system and only the D^+ signal was integrated.

5.3.1.3 Results

In order to test the conversion into o-D_2, a comparison was made with the spectrum of n-D_2. The n-D_2 REMPI spectrum has lines corresponding to R(0), R(1) and P(1). Long scans provided no evidence of populations with $J > 1$ and as such the spectra presented in Figure 59 only show the region from 320.9 to 321.35 nm. The n-D_2 has a known proportion of 67 % in $j = 0$. The o-D_2 spectrum only has lines corresponding to R(0) and R(1) and so is presented on the same scale. This suggests the cooling system of the molecular beam works well. By fitting Lorentzian curves to the REMPI spectra and comparing the proportions, 94 % of the molecules in the ortho-D_2 beam were measured to be in the ground state ($j = 0$). As 6 % of the molecular beam comprises of molecules with $j = 1$, the average rotational energy can be seen to be 0.21 meV and as such contribution of reactive scattering from D_2 ($j = 1$) will not be a significant error in the experiment.
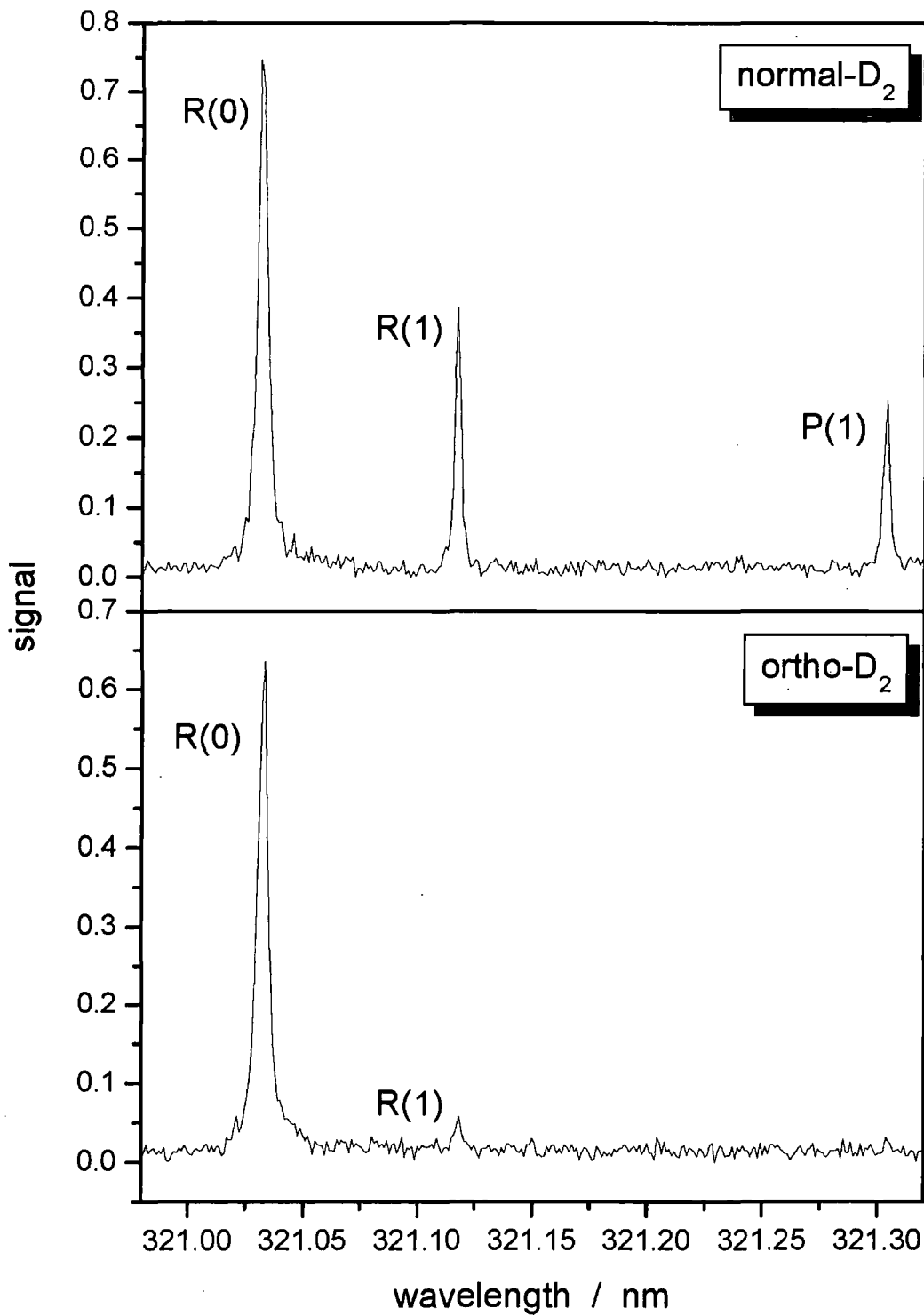
Figure 59: REMPI spectra for normal- (upper) and ortho- (lower) D_2. Recorded using modified cooled nozzle operating at 95 K.

Chapter 6: Results and Analysis

6.1 Introduction

This chapter presents the first results from the reactive scattering experiment. The first step of running the experiment was to achieve field-free conditions in the extraction region of the ion optics. This is required in order to facilitate the efficient creation of Rydberg atoms and to excite Rydberg atoms of a certain quantum number selectively. The highest quantum number that can be selectively excited and distinguished reflects the extent to which field-free conditions are obtained. The results presented in this chapter demonstrate how field free conditions were obtained with the aid of Rydberg scans. In the process of researching the field-free conditions unexpected patterns were observed with non field-free conditions; these results are also presented and discussed. In the final part of this chapter the first reactive scattering ion images obtained are displayed and a comparison is made with simulations.

6.2 Rydberg Scan

6.2.1 Experimental

The experimental set-up is identical to that described in the calibration and test measurements chapter with the HI molecular beam on the central axis of the experiment as shown in Figure 45.

The standard HI nozzle operated with a backing pressure of 1 bar with up to 26% HI in argon. The beam was collimated by a 1.0 mm skimmer. 266 nm light was used to photodissociate the HI. The H fragments were excited with the Lyman-α VUV and UV-Rydberg lasers. The UV-Rydberg wavelength was scanned over the range of 364.9 nm to 366.3 nm and the VUV was tuned to the centre of the Doppler profile for the dissociated H atoms.

During Rydberg excitation the repeller voltage of the ion optics was held at low potential with the aim of producing a field-free region at the excitation point. The cloud of Rydberg atoms expanded for 12 ns after the laser excitation, the repeller was then pulsed to a potential that gave a field required to ionise the Rydberg atom and restore velocity mapping conditions. This field was in the order of 400 V/cm following Simion simulations with the nominal ion optics potentials which should ionise Rydberg atoms in $n = 30$. The pulsed field ionisation is discussed in detail later. The detection system was used in time-of-flight mode and the integrated signal of the H^+ ions was recorded as a function of UV-Rydberg laser wavelength.

6.2.2 Field-free conditions

The Rydberg scan obtained with the ion optics potentials optimised for field-free conditions is displayed in Figure 60. For comparison a scan with non-optimised conditions is shown in Figure 61. In both figures panel b) shows the spectrum of the integrated H^+ signal (Rydberg scan), as the signal was recorded as a function of UV-Rydberg laser wavelength.

While scanning the Rydberg laser wavelength it was observed that the time-of-arrival for H^+ appears shorter with increasing Rydberg principal quantum number and it was possible to see two peaks in some scans. In order to investigate this, the Labview program was adapted to record the time-of-arrival trace at each wavelength. With this data it is possible to produce a contour plot that shows the changing H^+ time-of-arrival with Rydberg laser wavelength. This is shown in panel a) in both Figure 60 and Figure 61.

Figure 60 displays well-defined, sharp individual Rydberg levels, suggesting that optimised 'field-free' conditions were achieved. Whilst these conditions do not provide an absolute field-free environment, the term field-free will be used to describe these optimum conditions. In Figure 61, the Rydberg levels $n = 30$-33 are comparable to those seen in Figure 60 again showing well defined sharp peaks. As the spectrum increases in Rydberg principal quantum level the appearance of a side peak can be observed; in panel b) the integrated signal shows double peaks. These two peaks corresponds to different time-of-arrivals as shown in panel a).

Figure 60 shows well-defined peaks up to a Rydberg level of $n = 49$, where as in Figure 61 these can only be observed up to a maximum value of $n = 39$.
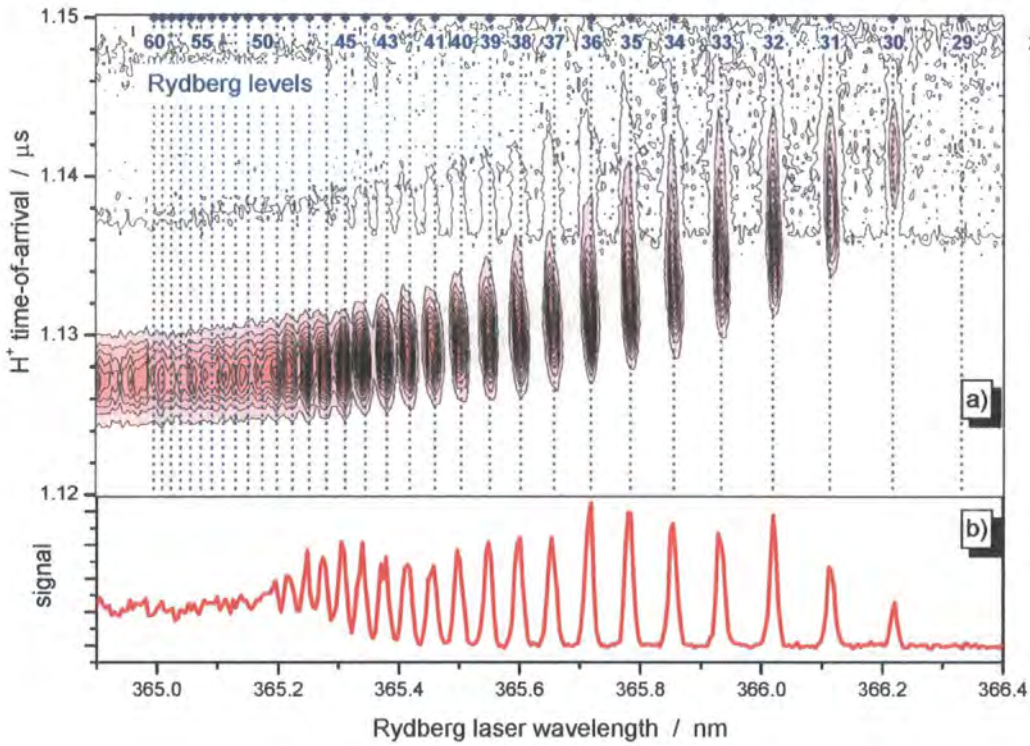
Figure 60: Rydberg scan obtained with conditions: Pulser: 875V, Rep: 3865 V, Stab: 3896 V, Ext 3450 V. The pulser was triggered 12 ns after the laser light. a) contour plot of the H$^+$ time-of-arrival and b) signal as a function of wavelength.
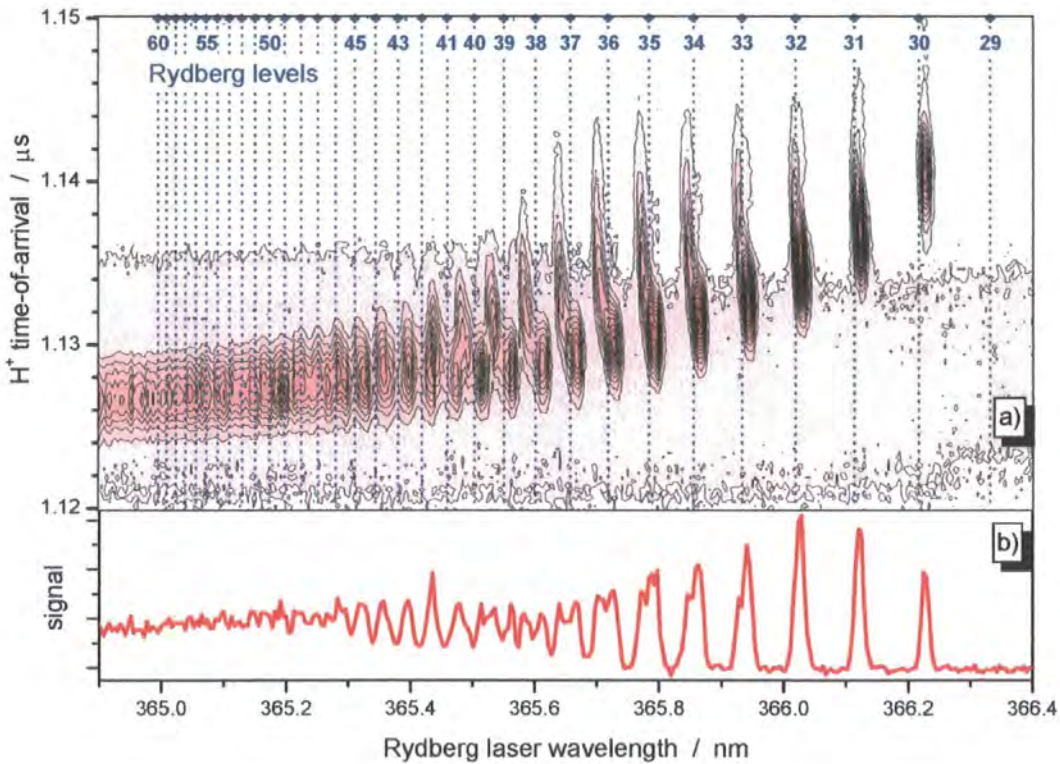
Figure 61: Rydberg scan obtained with conditions: Pulser: 850V, Rep: 3890 V, Stab: 3896 V, Ext 3450 V. a) and b) as in Figure 60.

115

The following trends can be observed in Figure 60 for lower *n*:

- The H⁺ time-of-arrival is later.
- The spread of time-of-arrival is longer.

The aim of the following analysis is to explain these observations by fitting a simulation to Figure 60. A Simion simulation of the pulsed ion imaging was performed in order to investigate how the time dependent rise in the field affects the ion trajectories and their time-of-arrival at the detector.

The pulse rise time from the pulser was measured using a high voltage probe. The high voltage probe was connected *via* a T-piece between the pulser and high voltage feed-through. This allowed the pulse to be recorded as it was used in the experiment. The obtained pulse trace is shown in Figure 62.
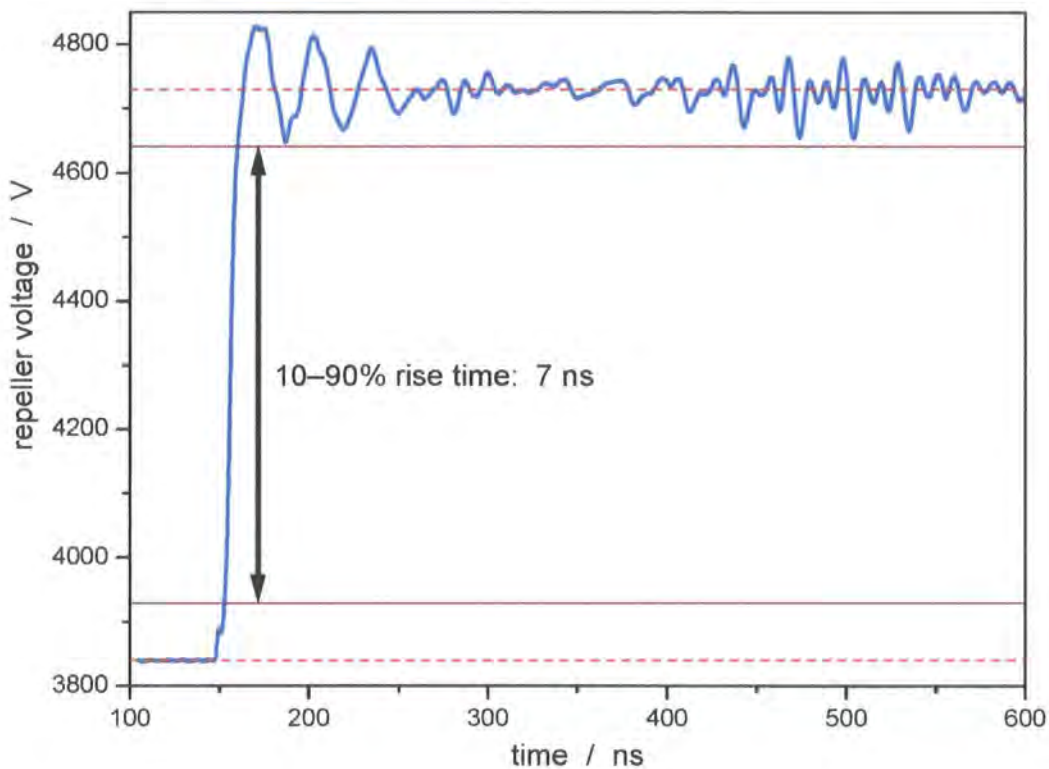
Figure 62: Rise time of pulsed repeller potential measured with high voltage oscilloscope probe. Ion optics settings: Repeller: 4000 V, Pulser: 1000 V.

The pulse trace shows a short 10% to 90% rise time of 7 ns. This exceeds the specifications given by Photek which guaranteed a rise time of ≤ 10 ns.

The recorded pulse in Figure 62 shows a sharp edge and, low amplitude ringing, which dies off after a few hundred nanoseconds. This ringing was not observed in the tests carried out by Photek, (see *section 4.2.4.2*) and so may not necessarily be inherent artefacts of the pulser. It is possible that the effect was caused by the T-piece to connect the oscilloscope probe. However, if the observed ringing is real it is possible that it arises from an imperfect matching of the impedance of the pulser to that of the ion optics.

The user program feature of Simion was applied to model the rise of the repeller potential and the first part of the ringing. This model was then employed to simulate the ion trajectory where the repeller potential changes as a function of time. The simulation is set-up such that neutral atoms fly with an initial speed and direction which mimics the creation of the fast hydrogen atoms produced through the 266 nm photodissociation of HI. With each time step the repeller potential is adjusted according to the simulated pulser function. At a given user defined field the atoms are ionised. The initial trajectories of the neutral atoms being ionised are shown in Figure 63.
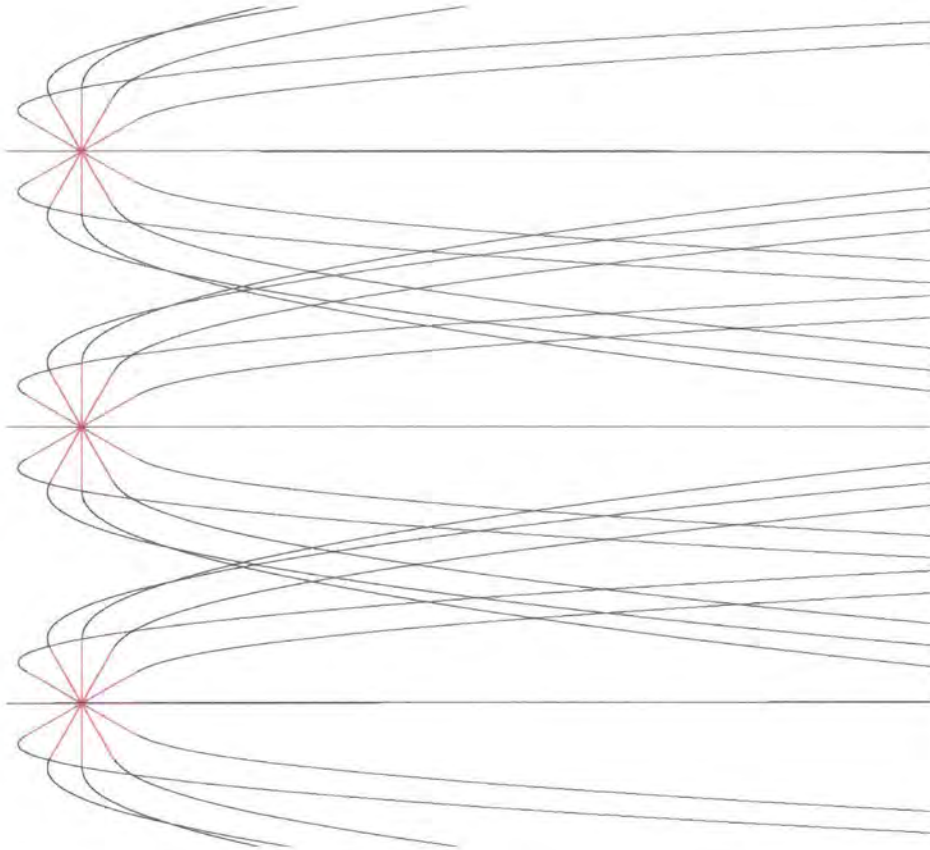
Figure 63: Simion simulation of neutral atoms' (red) trajectories as the pulser voltage rises to a point where they are ionised and the ions' trajectories (black) are determined by the electric field.

As the neutral atoms are not affected by the electric field they fly in straight lines. Once the atoms are ionised, the ions are accelerated by the electric field and as such this defines their trajectories. A time dependent Simion simulation of an atom-ion trajectory is shown below in Figure 64.

The simulation was run with one atom created in the centre of the extraction region, this atom had an initial kinetic energy of 1.5938 eV (fast H atoms from 266 nm photodissociation) and flew in the direction of the detector. Figure 64 shows the time dependence of the simulated rise in the repeller voltage, and the corresponding potential and field experienced by the flying atom/ion.
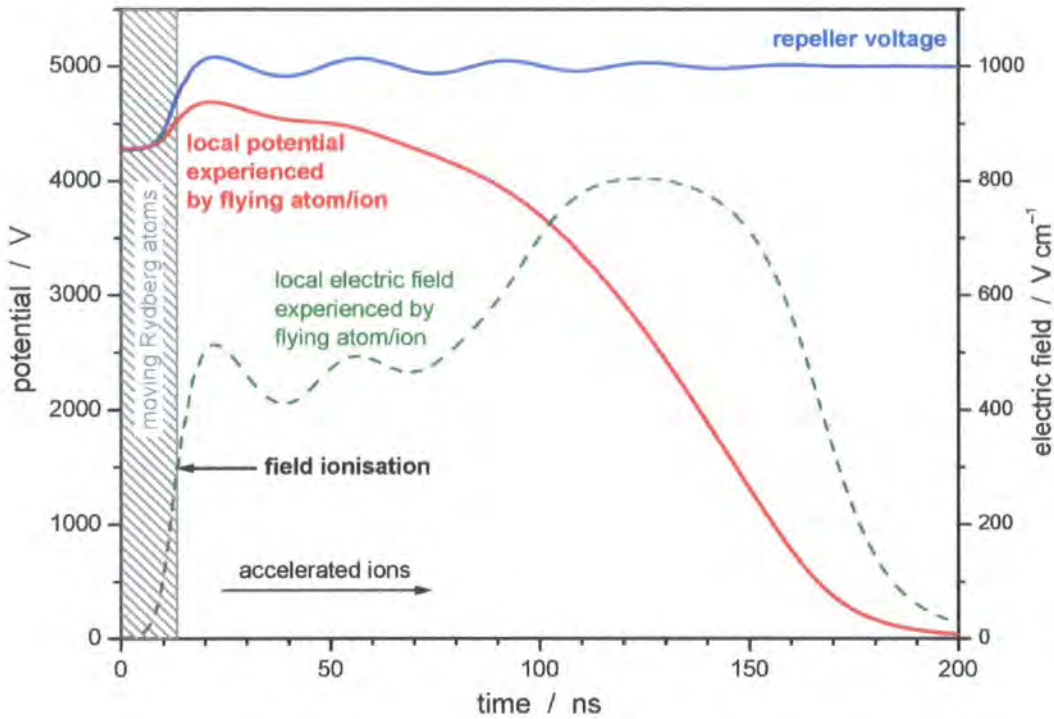
Figure 64: Simion simulation of Rydberg atom trajectory, field ionisation and ion trajectory with time dependent repeller potential.

The rising edge of the repeller potential causes the field to rise to a point at which ionisation occurs: in this simulation this was set to 300 V cm^{-1}. From the point of ionisation the ion is accelerated by the (still rising) extractor field. As the ion enters the acceleration region of the ion optics it experiences a steeper gradient in potential and as such accelerates down the potential hill. After 200 ns the ion has left the ion optics and flies into the drift path.

This simulation leads to the understanding that atoms in higher Rydberg levels will be ionised earlier in time, as they require a lower field to ionise than lower Rydberg levels.

As the repeller voltage increases the potential experienced by the flying atom will increase until a point at which the field is high enough to ionise the atom. As such, an atom in a lower Rydberg level will fly as a neutral atom for longer before being ionised and accelerated by the electric field. This may have a consequence for the velocity mapping conditions as the field continues to rise after ionisation. The

velocity mapping conditions depend on the specific ionisation time and as such this may be an explanation for the spread in arrival times (see Figure 60).

The relationship between the time-of-ionisation and the time-of-arrival at the detector can be found through the Simion simulation. To clarify: the time-of-ionisation is the time between the Rydberg laser pulse and the time at which the field is high enough to ionise an atom, and the time-of-arrival is the time between the Rydberg laser pulse and the ion hitting the detector. Using this relationship it will be possible to calculate a time-of-arrival for a given ionisation field. This will result in a fit to Figure 60 once the ionisation thresholds for each Rydberg level are determined.

There is a discrepancy between the voltages dialled into the ion optics power supply and those actually achieved. As such, in order to use Simion for simulations, corrected voltages were required. Tests using the high voltage oscilloscope probe provided factors that must be taken into account when dialling a voltage into the power supply, in order to accurately determine the applied voltage required; these are presented Table 7. It is assumed that the resistance of the pulser is responsible for the drop in the repeller voltage.

Table 7: Conversion factor to be considered with ion optics voltages (actual plate voltage = factor × dialled in voltage).

Plate	Factor without pulser	Factor with pulser
Repeller	0.995	0.960
Pulser	1.00	0.874
Stabiliser	1.00	1.00
Extractor	1.00	1.00

When the corrected voltages were applied in the simulation, Simion indicated that a field of around 50 V cm^{-1} was present at the source volume. In order to simulate the field-free conditions the repeller and pulser voltages were adjusted. These discrepancies may arise from the position of the laser beams in the experiment, as explained in the experimental section a positioning plate is used to align all of the

120

beams at the same point in the centre of the extraction region. The spindle of the linear feed-through causes the positioning plate to sway slightly as it is driven into position. This may cause the lasers to be up to 1 mm away from their expected position. Simion indicates that a deviation of 1 mm would cause a field change of 30 V cm^{-1} in this region, which is not enough to fully account for the different voltages used in the Rydberg scans. It must be remembered that the actual experimental set-up, while designed from Simion, can not be considered identical, as slight errors will be present from the manufacture and positioning of the ion optics assembly.

The simulation applied the modelled rise of the repeller potential as displayed in Figure 64. In this case, however, the ringing was ignored for simplification. The atoms were held at rest in the source region, the repeller voltage was then raised. For different ionisation thresholds (shown as red lines in Figure 65) the time-of-arrival at the detector was simulated and is shown in Figure 65.
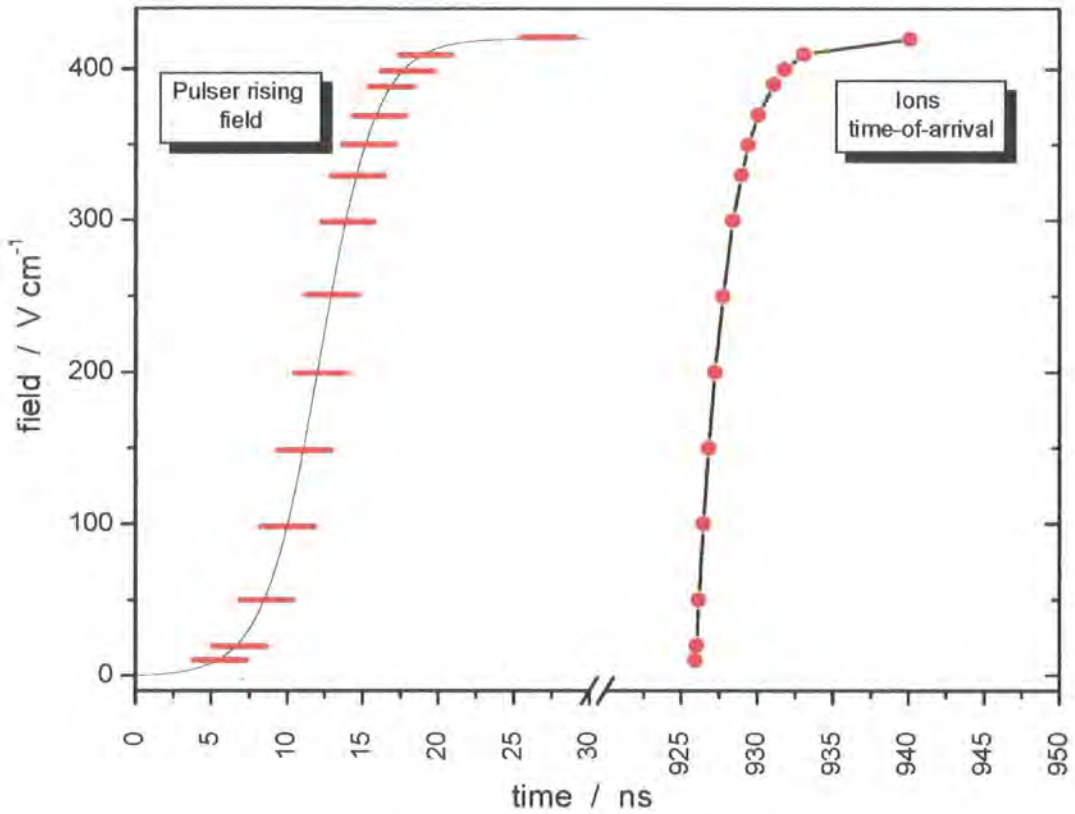
Figure 65: The curve at low times shows the rising edge of the simulated pulsed field, the red lines show the different ionisation thresholds, the red points show corresponding times-of-arrival. The atoms to be ionised were created with zero kinetic energy. Ion optics voltage settings: Pulser: 665V, Rep: 3810 V, Stab: 3896 V, Ext 3450 V.

Figure 65 demonstrates that the effect of ionisation occurring at earlier times (lower field) for higher Rydberg levels does not cause a significant stretch in time-of-arrival, as the ions appear to bunch up rather than spread in time. This can be explained by the acceleration felt by those that are ionised early.

In order to assess whether the rising field causes the spread in time and the increasing time-of-arrival with lower Rydberg levels, it is necessary to invert the time-of-arrival graph in Figure 65, shown in Figure 66. The data from the simulation in Figure 66 shows curves for three sets of ions. The arrival times of these ions correspond to nascent atoms with a kinetic energy of 1.5938 eV directed towards and away from the detector, and also nascent atoms at rest. These three groups of atoms simulate extremes of how the atoms can fly. Curves have been fitted to this data and are shown as the solid lines running though the individual data points.
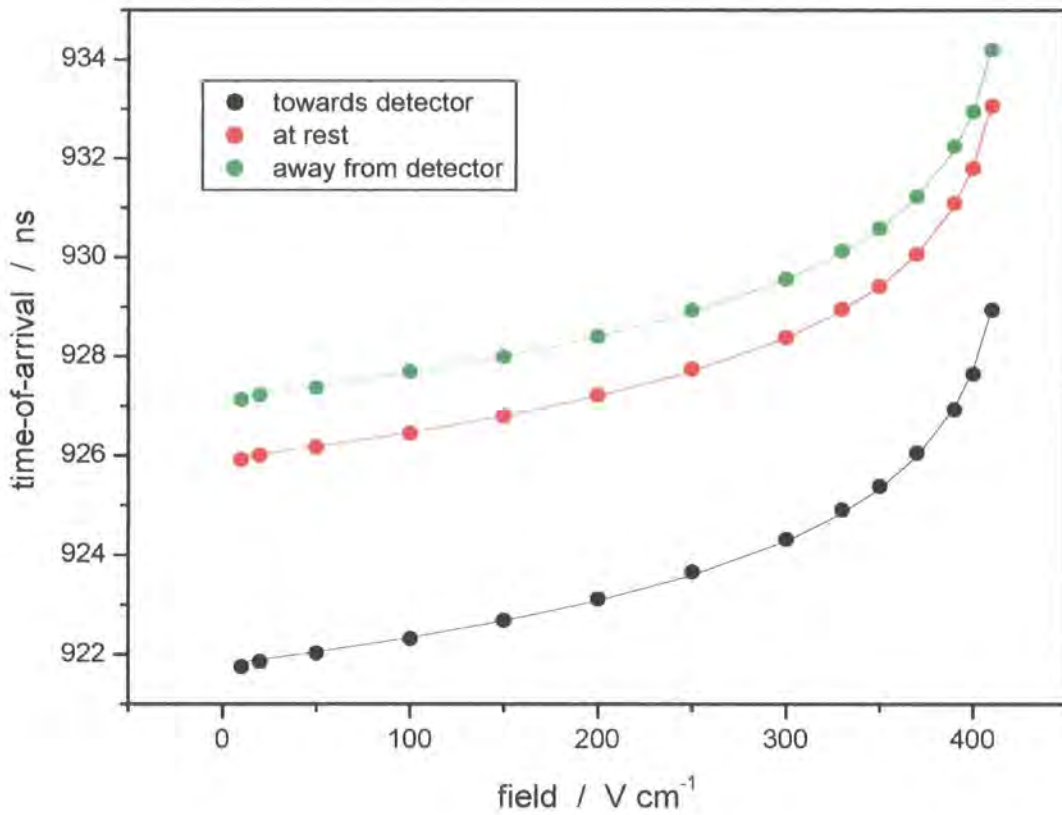
Figure 66: Time-of-arrival as a function of ionisation field for three groups of ions. The three groups are: ions with direction towards, at rest, and away from the detector. A fit has been made to the points (see text).

The curve has the equation:

$$t = dt \times \ln\left(\frac{A_1 - A_2}{f - A_2} - 1\right) + t_0$$

<div align="right">**Equation 16**</div>

where t = time-of-arrival, f = ionisation field and the other parameters have been solved for each curve to fit the points.

The three curves obtained from Figure 66 provide a conversion from a given ionisation field into time-of-arrival at the most extreme atom scattering conditions. This information will provide a fit to the Rydberg scan in Figure 60 once the field at which each Rydberg level will ionise is known. In order to determine the field required to ionise each Rydberg level the Stark effect must be considered.

6.3 The Stark effect

6.3.1 The classical Stark effect

When an atom is placed in an external electric field, perturbations to the energy levels of the system are observed. Figure 67 shows how the potential energy of the electron in the hydrogen atom changes in the presence of an electric field, f, along a line that passes through the nucleus and is parallel to the field direction. The Columbic potential is changed by the addition of the fz term for a field in the z-direction and this raises the electronic potential for $z > 0$ and lowers it for $z < 0$.

a) Field free   b) Homogeneous field
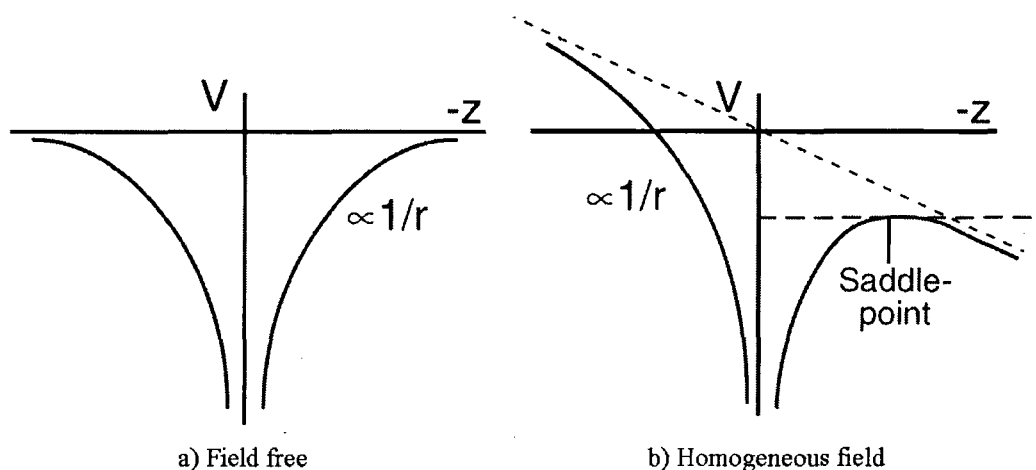
Figure 67: Potential of an electron in a hydrogen atom along the z-axis. a) Field-free and b) with an electric field directed along the z-axis [118].

To avoid confusion in the following treatment the symbols f and ε will denote field and energy respectively, in atomic units and F and E will represent more "user friendly" laboratory units (V cm^{-1} and cm^{-1} respectively). The conversions are: $F = f_0 \times f$ and $E = \varepsilon_0 \times \varepsilon$ where:

$f_0 = 5.14 \times 10^7$ V cm^{-1}/ a.u. and $\varepsilon_0 = 2.19 \times 10^5$ cm^{-1}/ a.u.

For a hydrogen atom in an electric field f in the z direction, the potential of the electron on the z-axis is given by:

$$V = \frac{-1}{|z|} + fz$$

<div align="right">**Equation 17**</div>

where z is the distance from the nucleus. The saddle point in the potential occurs at $z = -f^{-1/2}$, and the potential at this point is given by:

$$V_{sp} = -2f^{1/2}$$

<div align="right">**Equation 18**</div>

Classically, ionisation occurs whenever the energy of a level exceeds V_{sp}. The classical field ionisation threshold is given by:

$$f = \frac{1}{16n^4},$$

<div align="right">**Equation 19**</div>

where n, the principal quantum number can be obtained from the unperturbed energy level:

$$\varepsilon_n = -\frac{1}{2n^2}$$

<div align="right">**Equation 20**</div>

Combining Equation 19 with Equation 20 yields the classical ionisation threshold of a level with enegy E_n at specific field F.

$$E_n = -6.12\sqrt{F} \qquad \text{or} \qquad \varepsilon_n = -2\sqrt{f}$$

<div align="right">**Equation 21**</div>

6.3.2 The static Stark effect

A classical approach of the Stark effect can be used to provide a qualitative insight into the energy level structure of the hydrogen Rydberg levels [119].

The energy levels for a hydrogen atom in an electric field are shown in Figure 68, for principal quantum numbers 8 to 14 where the Stark splitting can be observed. For the states that increase in energy in the field, the lines are referred to as blue shifted Stark states. In these states the electron density is located in the positive z-region away from the saddle point [120]. For the states that decrease in energy in the field, the lines are referred to as red shifted Stark states. Here the electron density is located in the negative z-region towards the saddle point [120].

The hydrogen atom is a special case; in a small field only the linear Stark effect needs to be considered. The quadratic Stark effect is small as hydrogen has a single electron and therefore there can be no coupling to other electrons. As a result Stark levels of the same value of m_l (magnetic quantum number) can cross so that adjoining Stark manifolds intersect without interaction and only the diabatic mode of field ionisation is possible for the hydrogen atom [121].

The curve passing through the Stark manifolds in Figure 68 represents the classical saddle point limit. For a classical approach this can be thought of as the ionisation threshold, see Equation 19.
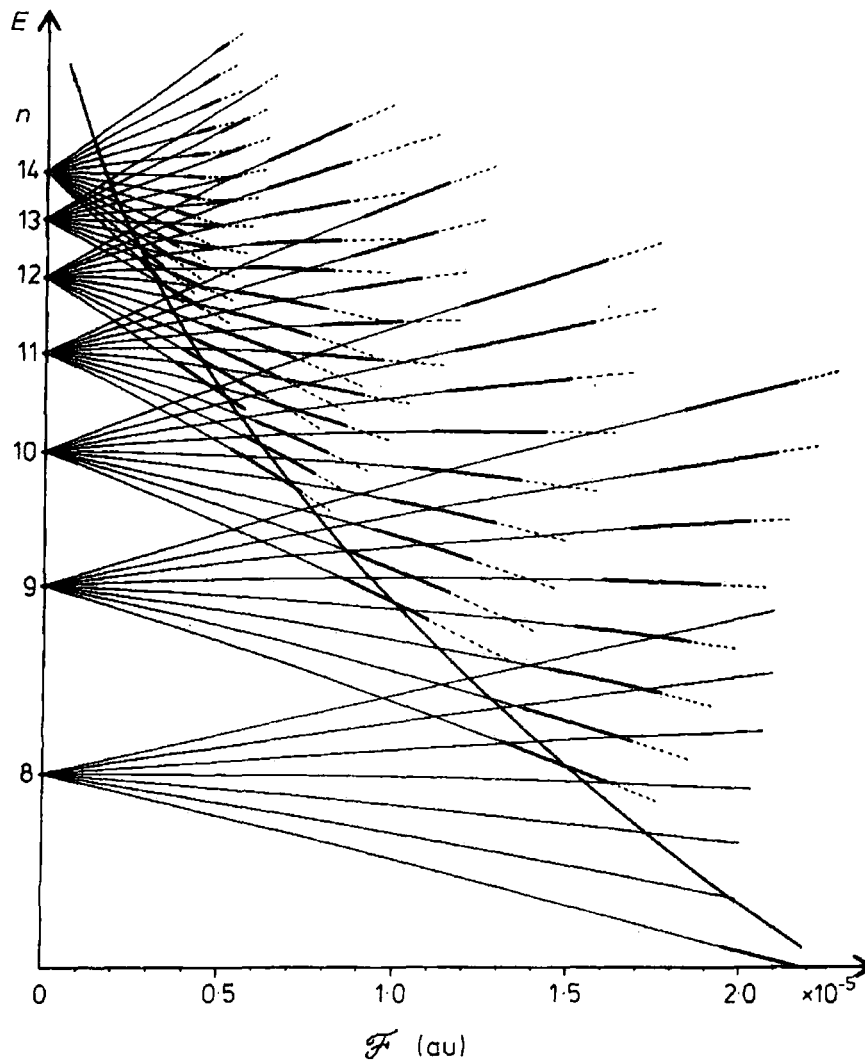
Figure 68: Stark structure for the H atom. The zero field manifolds are characterised by the principal quantum number n, The saddle point limit $\varepsilon_{sp} = -2\sqrt{f}$ shown as a curve [122].

From a classical approach the extreme red and blue Stark energy levels can be described by Equation 22 below (this equation is comparable with Equation 23, which includes the quadratic term):

$$E_n(F) = \frac{-\varepsilon_0}{2n^2} \pm \frac{3}{2}\frac{\varepsilon_0}{f_0} n(n-1)F \qquad \text{or} \qquad \varepsilon_n(f) = \frac{-1}{2n^2} \pm \frac{3}{2} n(n-1)f$$

Equation 22

6.3.3 Time dependent Stark effect

In the case of the Rydberg scan in Figure 60 it is important to understand the time at which the pulser provides a field high enough to ionise the various quantum states. Figure 69 shows the Stark splitting (only the extreme red and blue Stark shifts are shown) for different Rydberg levels as a function of temporal rise of the extraction field at the centre of the extraction region of the ion optics. The classical ionisation threshold is shown as a black curve. This simple purely classical picture is not able to explain the H^+ time of arrival observed in Figure 60.
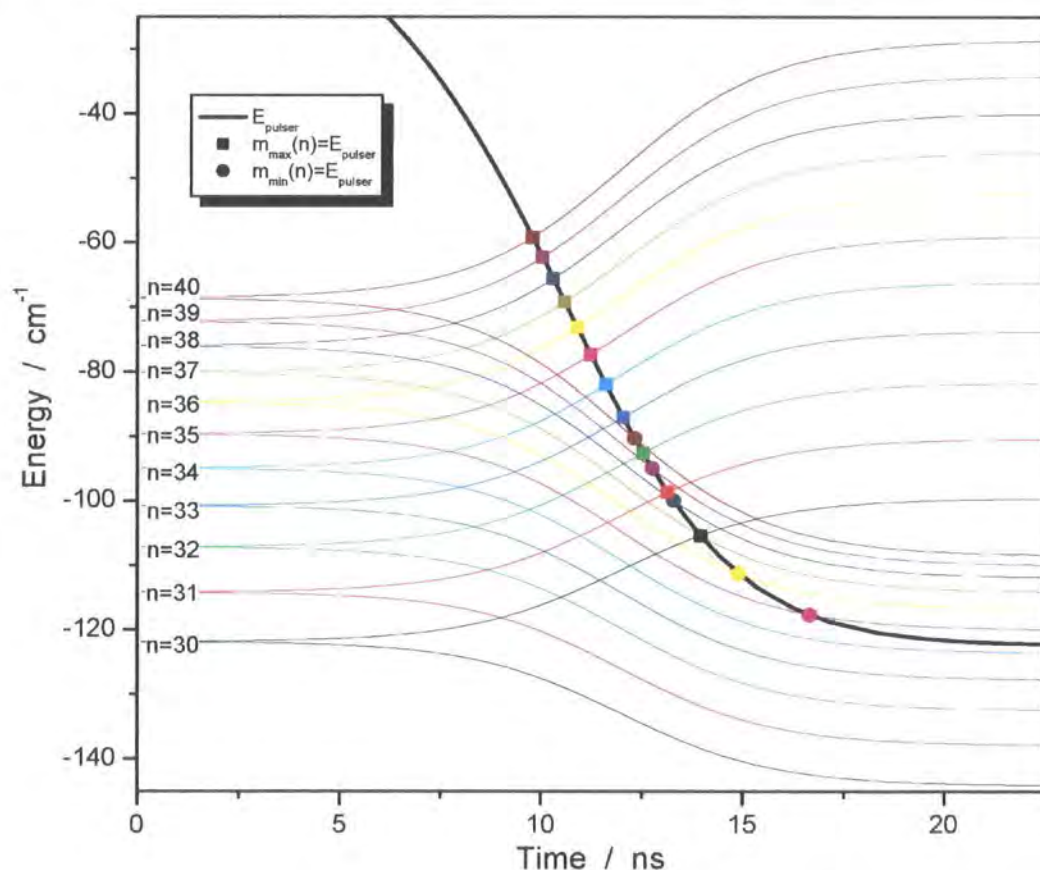
Figure 69: Stark splitting of quantum states between $n = 30-40$ for extreme red and blue Stark states. The classical ionisation threshold is shown as a bold curve. Red Stark state crossing point denoted by ■ and blue Stark state crossing point denoted by ●.

6.3.4 A quantum mechanical approach

The classical view is not appropriate for the blue shifted Stark states as the energy rises and will reach the energy of the classical ionisation threshold at a relatively low field. However, the wavefunction is highly localised away from the region of the saddle point and such a state is metastable with respect to ionisation [123].

In the classical picture the familiar spherical co-ordinates define the radial wavefunctions: n, principal quantum number, l, the azimuthal quantum number associated with the discrete orbital angular momentum values ($l = 0, ..., (n-1)$), and m_l which is known as the magnetic quantum number and results from the space quantisation of the orbital angular momentum ($m_l = 0, ..., \pm l$).

The Schrödinger equation for a hydrogen atom perturbed by a uniform electric field is separable in parabolic coordinates. The resulting wavefunctions are defined by the quantum numbers n, m, n_1 and n_2. Where n is the principal quantum number, m labels the eigenvalues of the L_z component of angular momentum, and n_1 and n_2 are parabolic coordinate quantum numbers where $n_1 = 0, 1, 2, ..., n-1$, and $n_2 = 0, 1, 2, ..., n-1$. The quantum numbers are always linked by the relationship $n + n_1 + n_2 + |m| + 1 = 0$

The energy levels that are obtained are given approximately by the expansion [118]:

$$\varepsilon = -\frac{1}{2n^2} + \frac{3}{2}f(n_1 - n_2)n - \frac{1}{16}n^4\left(17n^2 - 3(n_1 - n_2)^2 - 9m^2 + 19\right)f^2 + O(f^3)$$

Equation 23

At low electric field the linear term dominates the expression. With a maximum field in the order of 400 V cm^{-1} the quadratic term only accounts for approximately 2% of the calculated energy for $n = 36$.

The Stark effect occurs indirectly as a result of the field inducing a dipole moment by perturbing the electronic charge distribution [124]. The dipole may then have a favourable electrostatic interaction with the field, lowering its energy. Starting

129

from unperturbed spherical harmonic orbitals, the n, l, m_l, interaction arises from the differences in the orientation of the electronic charge distribution (orientation of m_l) in the different states with respect to the field direction. The magnitude of the induced dipole is dependent on this orientation.

The Stark diagram in Figure 68 shows several important points. The levels exhibit linear Stark shifts from zero field to a point at which field ionisation occurs at significant rates, shown by broken lines. The red shifted Stark states ionise near the classical ionisation limit, but those that are blue shifted ionise only at higher fields [120]. This arises from the electron probability distribution in the perturbed atom. In the blue Stark state the electron is located in the positive z-region where the potential is high on the side of the atom away from the saddle point. As there is such low probability of the electron ever going near the saddle point, a field far stronger than the classical field is required for ionisation [125]. For the red Stark states the electron is located in the negative z-region where the potential is low, hence the electron is near to the saddle point [125]. This means it will ionise at fields closer to the classical limit.

6.3.5 Pulsed field ionisation

Zero electron kinetic energy (ZEKE) spectroscopy relies upon pulsed field ionisation and therefore there is a wealth of literature available that takes into account the Stark effect [126] [127]. In these examples it seems that a rate of ionisation of 10^9 s^{-1} (per particle) is needed for adequate detection. In rough approximation this rate yields a range of ionisation from $f \approx 1/(9n^4)$ to $f \approx 1/(4n^4)$ in atomic units, for the extreme red and blue members respectively of the n Stark manifold with $m = 0$ [118] [125]. The use of these approximate expressions leads to a critical field of $\sqrt{F} = E_0/4.6$ and $\sqrt{F} = E_0/3.1$, (in "user friendly" units) respectively.

This range of ionisation was used in addition to the classical expression ($1/(16n^4)$ in atomic units leading to $\sqrt{F} = E_0/6.1$ in "user friendly" units), to attempt a fit to Figure 60; however, these ionisation threshold formulas predict that, with a

maximum field in the order of 420 V cm^{-1}, it would not be possible to ionise $n = 35$, even in the extreme red shifted level. The experimental results do not agree with this, the lowest quantum level which appears to be ionised in the Rydberg scan is $n = 30$. The literature employs a rate of 10^9 s^{-1} (per particle); such a rate of ionisation for a single atom would occur within a nanosecond. This appears to be a reasonable estimate for a rate required to detect signal in the ZEKE experiments in the literature; however, in the Rydberg scan (Figure 60) a spread in time of 10 ns can be observed from the time-of-arrival. This leads to a closer approximation of a maximum rate of 10^8 s^{-1} for the Rydberg atoms to be ionised and detected in this experiment.

Using Equation 24 from the original formulas by Damburg and Kolosov [128] [129], the field required to provide this specific ionisation rate, which is estimated to be a measurable level, has been deduced.

$$\Gamma = \frac{(4R)^{2n_2+m+1} e^{-2R/3}}{n^3 n_2!(n_2+m)!}\left(1 - \frac{n^3}{4}(34n_2^2 + 34n_2 m + 46n_2 + 7m^2 + 23m + \tfrac{53}{3})\right)f + O(f^2)$$

where, $R = \dfrac{(-2E_0)^{3/2}}{f}$

Equation 24

where E_0 corresponds to the energy of the Rydberg state (ε in Equation 23)

Using the formulas of Damburg and Kolosov [128] [129], it is possible to estimate that the field needs to rise to a value of $\sqrt{F} = E_0/2.7$ (in wavenumber units) in order for the rate of ionisation of a blue shifted level to increase to 10^8 s^{-1}. For a red shifted Stark state the energy moves down with increasing field, tending to stabilise the state energetically, but the lowering of the ionisation threshold occurs at a greater rate with respect to increasing field. For the most extreme red shifted state the field has to be raised to $\sqrt{F} = E_0/5.0$, in order for the rate to be greater than 10^8 s^{-1}.

The maximum field that was reached with pulsed ion optics was ≈ 420 V cm^{-1} in the extraction region. With this field and a rate of 10^8 s^{-1} (per particle) the calculations predict that the entire Stark manifold will not be ionised. The extreme red shifted state for a given Rydberg level has the lowest ionisation threshold for the entire manifold and as such 420 V cm^{-1} is predicted to be sufficient to ionise the extreme red shifted stark state for Rydberg level $n = 33$. By Rydberg level $n = 36$, 420 V cm^{-1} is sufficient to ionise all the red shifted states and the centre of the manifold, however, it is not until Rydberg level $n = 45$ that the entire Stark manifold can be ionised by 420 Vcm^{-1}. The red and blue shifted extremes and the centre of the stark manifold to be at these conditions are presented in Table 8.

Table 8: Lowest Rydberg level to be ionised at a field of 420 V cm^{-1} for corresponding rate.

Rate s^{-1}	maximum red shifted n	centre of manifold n	maximum blue shifted n
10^8	33	36	45
10^6	32	35	44

Table 8 also includes the lowest Rydberg levels that would ionise with a rate of 10^6. It is possible that a lower rate is required as the detection is very sensitive. However, in order to ionise level $n = 30$, a rate of 10^{-10} s^{-1} would be required, this is not realistic. It is assumed that the equations are a fit to quantum mechanical equations and as such the formulas are only approximate and may not reflect reality.

6.3.6 Rydberg scan analysis

The original purpose of this analysis was to explain the variation in the H$^+$ time-of-arrival from the Rydberg scan shown in Figure 60. To do this the time-of-arrival as a function of ionisation field were determined. The Stark effect analysis has established ionisation thresholds which can be used alongside the link between ionisation field and time-of-arrival, established in *section 6.2.2*, to produce a fit to the Rydberg scan in Figure 60.

A summary of the fitting process is as follows:

- A Rydberg level was selected, of which the energy was known (y-axis).
- For each level the field required to give a rate of ionisation of 10^8 s^{-1} (per particle) was calculated, for the unperturbed level (*i.e.* the centre of the Stark manifold) and for extreme red and blue shifted Stark levels.
- The link between ionisation threshold and time-of-arrival was used to provide the x-axis.

The result of this analysis is shown is shown in Figure 70. the time of arrival curves are overlaid on the contour plot. The green points correspond to H$^+$ ionised from the Rydberg state at the centre of the manifold (*i.e.* where $n_1 = n_2 = \dfrac{n-1}{2}$ and therefore $m = 0, 1.$). The red and blue points correspond to H$^+$ ionised from the Rydberg state at the extreme red and blue shifted levels (*i.e.* extreme red ($n_1 = n - 1$, $n_2 = 0$) and blue ($n_2 = n - 1$, $n_1 = 0$)). The link between ionisation field and time-of-arrival has been made using the conversion curve for nascent atoms at rest; this is the red curve in Figure 66. To guide the eye along the broadening of the time-of-arrival, the dark red and dark blue curves have been included. These curves again depict the extreme red and extreme blue stark shifted levels, however these fits to time-of-arrival have been obtained using nascent atoms with extreme speed towards and away from the detector respectively (black and green curve in Figure 66). These dark line fits show a greater spread than observed in the Rydberg scan. These are extreme conditions and do not account for the majority of detected particles.

The time-of-flights simulated by Simion are significantly shorter than those observed experimentally. In order to fit the simulation to the plot all points were shifted by 201 ns. This is unexplained and may arise from an experimentalist error in the timing settings (longer delay between laser pulse and pulsed field).

This analysis has provided fits to the data that qualitatively explain the shifts in time-of-arrival. The centre and red shifted lines from analysis closely fit the experimental observations. This analysis also suggests that the maximum field

achieved through pulsed ion optics is not sufficient to ionise large parts of the Stark manifold; this may have implications for the reactive scattering experiment.
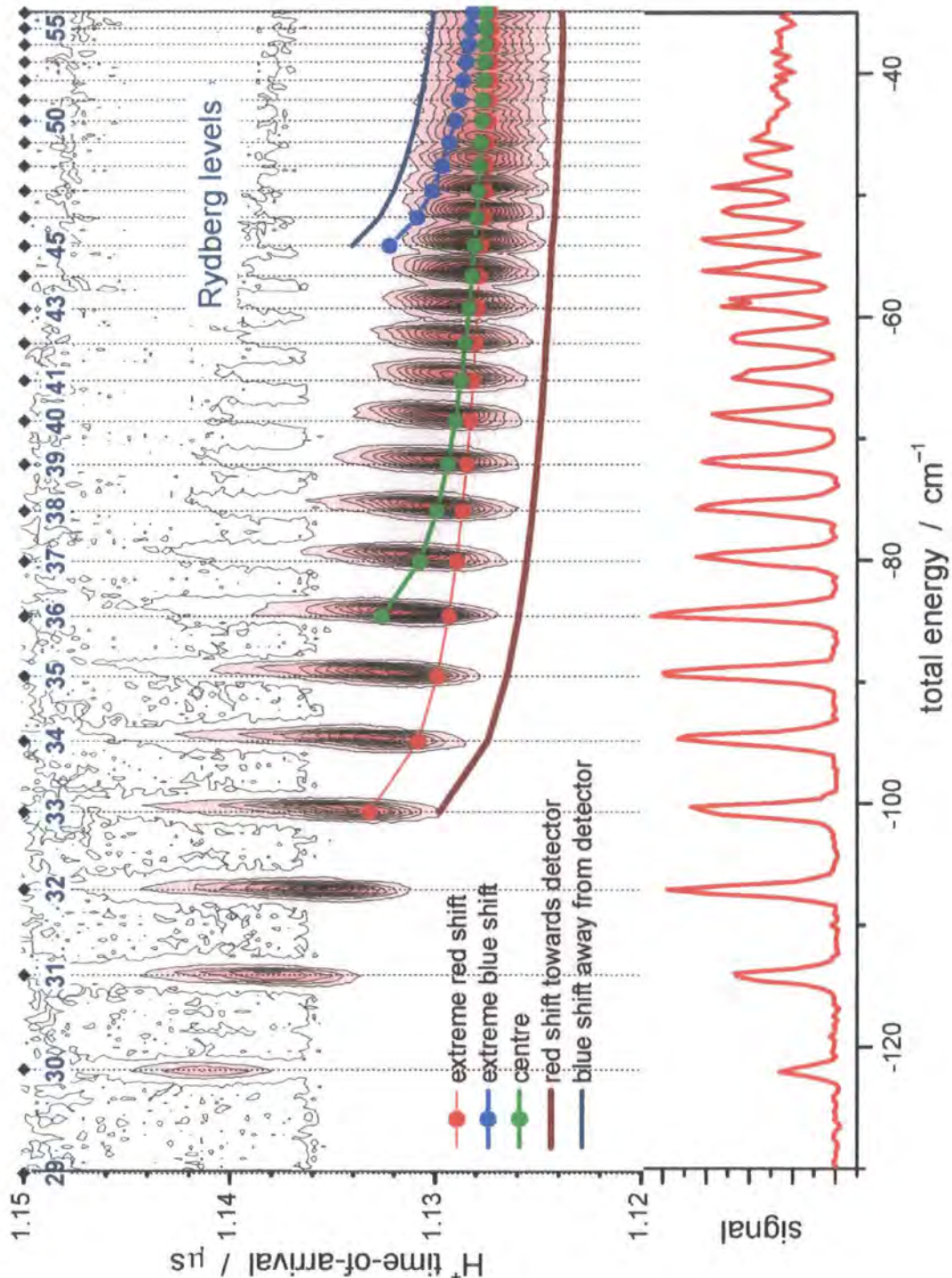
Figure 70: Analysis overlaid onto experimental data from Figure 60. Pointed lines represent analysis including ions created at rest from the extreme red (red points) extreme blue (blue points) and centre (green) of the Stark manifold. The solid lines represent atoms with extreme speed towards (red) and away from (blue) the detector for the extreme red and blue shifted Stark levels.

6.4 Non-field free conditions

This section presents Rydberg scans obtained when non-optimum conditions were used. These conditions provided an initial field in the extraction region of the ion optics. These non field-free conditions produced Rydberg scans whereby the Rydberg levels were not selectively excited to as high a principal quantum number as when field-free conditions were obtained. An example of this is shown in Figure 61 in section *6.6.2*. When comparing the H^+ time-of-arrival of Figure 61 with Figure 60 it can be observed that as the Rydberg level increases the integrated signal peaks in panel b) begin to show side peaks, which corresponds to the later side peaks in the time-of-arrival panel. This appearance of double peaks with different times-of-arrival seems to arise from the small field present in the source volume when non optimised conditions are used. The energy spread of the double peak can be taken from the spectrum shown in Figure 71 . For $n = 38$, the time-of-arrival shows a spread in energy of 2.93 cm^{-1}, as shown by the green arrows in Figure 71. This energy spread is assumed to be the extreme difference in the Stark splitting *i.e.* the extreme red and extreme blue levels of the Stark manifold. From Equation 22 it can be calculated that a field of 16.3 V cm^{-1} would produce a Stark splitting with the required maximum energy spread of 2.93 cm^{-1}, for $n = 38$.

The field conditions in the extraction region vary between Figure 60 and Figure 61. The repeller voltage is 25 V higher for the scan in Figure 61. Using Simion it can be observed that 25 V above the field free repeller voltage provides a field of approximately 16 V cm^{-1} in the source region. This is in good agreement with the energy spread observed from the Rydberg scan which is shown below in Figure 71 and previously in Figure 61. This suggests that the initial field present when the atom is excited is responsible for this spread in energy.

The same field of approximately 16 V cm^{-1} also explains the energy spread for higher n. For $n = 40$, a spread in energy of 3.26 cm^{-1} is observed from Figure 71. this corresponds a field, for extreme Stark splitting, of 16.4 V cm^{-1}. For the level $n = 36$, the field which produces a spread of 3.26 cm^{-1} is calculated to be 18.2 V cm^{-1}, this is a little higher than the estimated extraction field of 16 V cm^{-1}; this is

in agreement with the discussion in *section 6.3*. At lower Rydberg levels the ionisation threshold for higher blue shifted levels is not reached, so the argument breaks down as the full manifold is not observed.
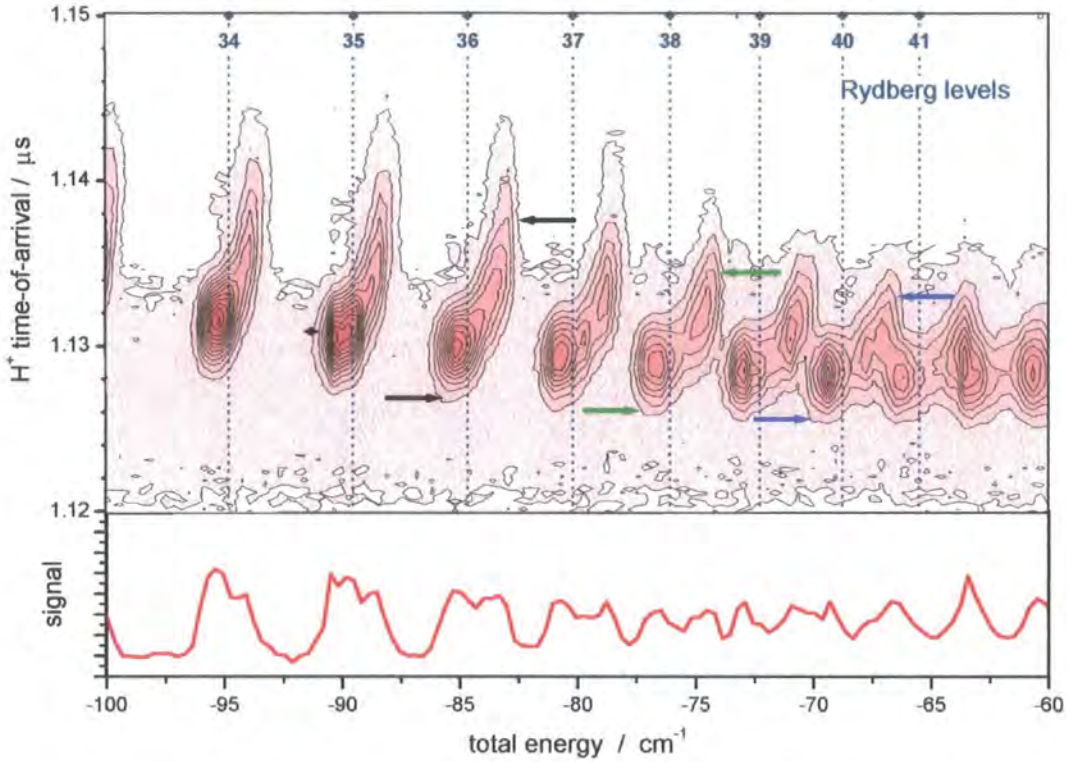
Figure 71: Zoom into Figure 61. Arrows show spread in energy for three different Rydberg levels.

From examining the spreads for different Rydberg levels it can be seen that the energy spread is close and consistent in the order of 16-18 V cm^{-1}. On close inspection the time-of-arrival peaks (especially $n = 38$) seem to show up as double peaks, whereby the blue shifted end appears at later time-of-arrival. The spread in time-of-arrival was discussed in the previous section. The appearance of this double peak may suggest that we are exciting more sublevels towards the red and blue extremes of the Stark manifold rather than at the centre. A possible explanation is that the relative orientation between the polarisation of the Rydberg laser and the electric field in the source region may favour excitation of the extreme red/blue shifted sub levels rather than the centre of the manifold. This was not the aim of the project and as such the effect of the laser polarisation has not been investigated.

The same argument can be applied to the Rydberg scan in Figure 60 to provide an upper limit to the field obtained when using optimised field-free conditions. The slight spread in energy from level $n = 38$ is approximately 0.65 cm^{-1}; this extreme Stark splitting corresponds to field of 3.5 V cm^{-1}.

The Rydberg scan shown in Figure 61 is achieved with near field-free conditions. In the next example the source region was far from field-free. Figure 72 shows a Rydberg scan where the repeller voltage was high, causing a field of ≈ 100 V cm^{-1} in the source region. This time-of-arrival panel shows a second group of ions arriving early in time for high principal quantum numbers.

A field of 100 V cm^{-1} is sufficiently high to ionise the extreme red shifted levels for $n = 46$ and above according to the discussion in *section 6.3*. This suggests at the point of laser excitation there is a field high enough to ionise a proportion of the atoms, which are instantly accelerated by the already present field. As the pulsed field rises the Rydberg atoms with a higher ionisation threshold ionise in the normal fashion and as such, arrive later in time.
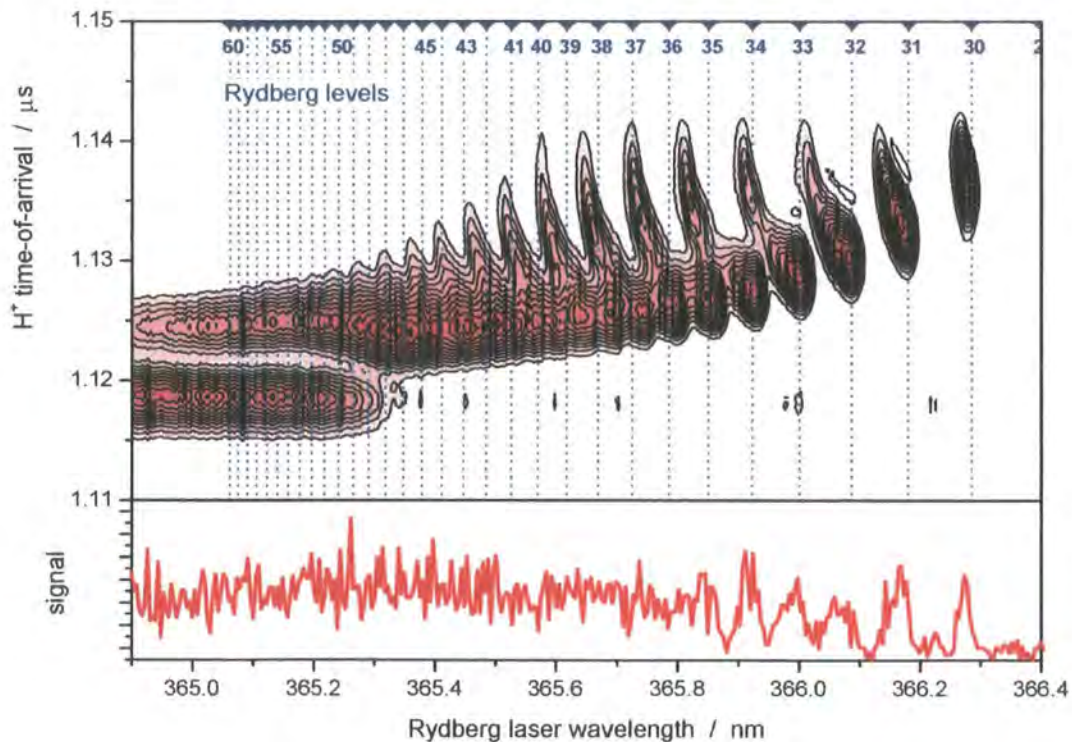
Figure 72: Rydberg scan obtained with conditions: Pulser: 750V, Rep: 3965 V, Stab: 3896 V, Ext 3450 V. The pulser delay was set to 12 ns after laser. The upper panel shows a contour

plot of the H^+ time-of-arrival and the lower panel shows the signal as a function of wavelength.

The Simion simulation shown in Figure 73 displays the fields when the repeller voltage is 125 V above field free conditions, mimicking the conditions under which the Rydberg scan shown in Figure 72 was recorded. The source region between the repeller and stabiliser electrodes shows a steep field gradient. This may be responsible for the acceleration felt by those ions created as a result of the initial field before the rising pulser field.
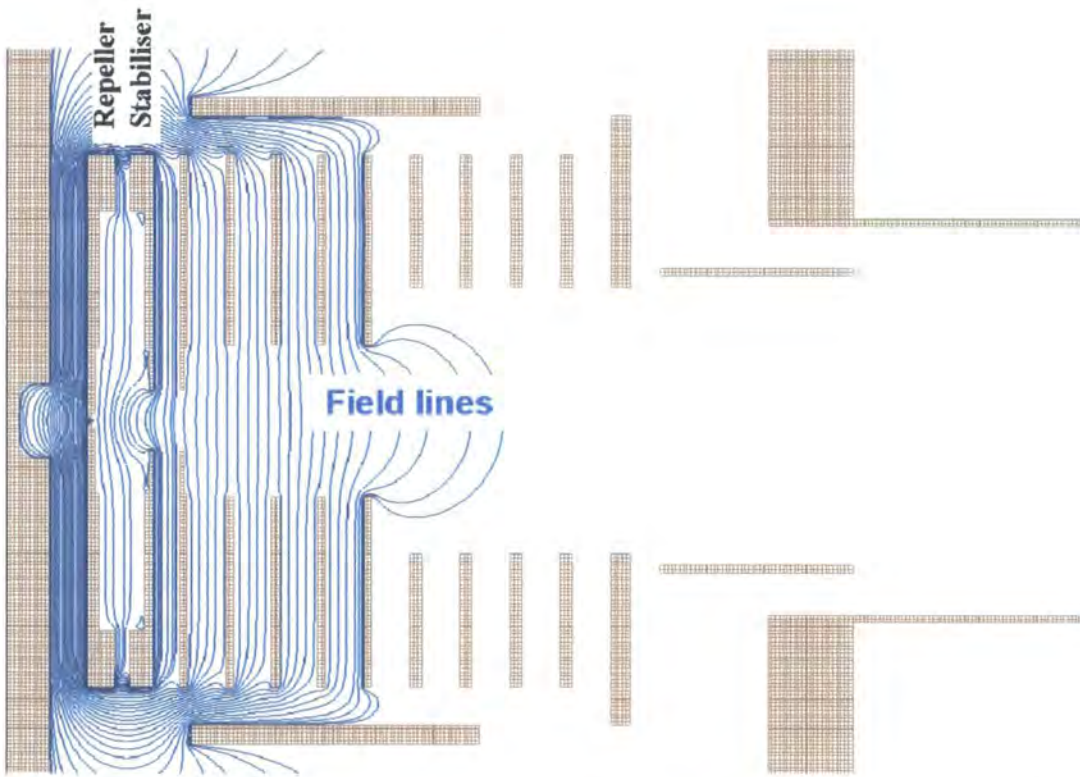
Figure 73: Simion simulation showing electric field for simulated conditions from Figure 71. Where blue lines show field and brown lines represent the chamber walls, electrodes and cryoshield.

In summary, the Rydberg scans together with the time-of-arrival spectra (TOA as a function of Rydberg wavelength) provided a sensitive tool to optimise and define good field-free conditions for Rydberg excitation. The analysis has given an upper limit to the extent to which field free conditions were obtained and as such has shown the limitations for ion imaging of pulsed field ionised Rydberg atoms.

6.5 Reactive H* + D$_2$ scattering

The first reactive scattering ion images from H* + D$_2$ ($v = 0$, $j = 0$) collisions are shown below in Figure 74. These are raw images with no analysis or reconstruction. In the following section the images are compared to the results of simulations performed within the research group [130], and the problems regarding the resolution of the experimental images are discussed.
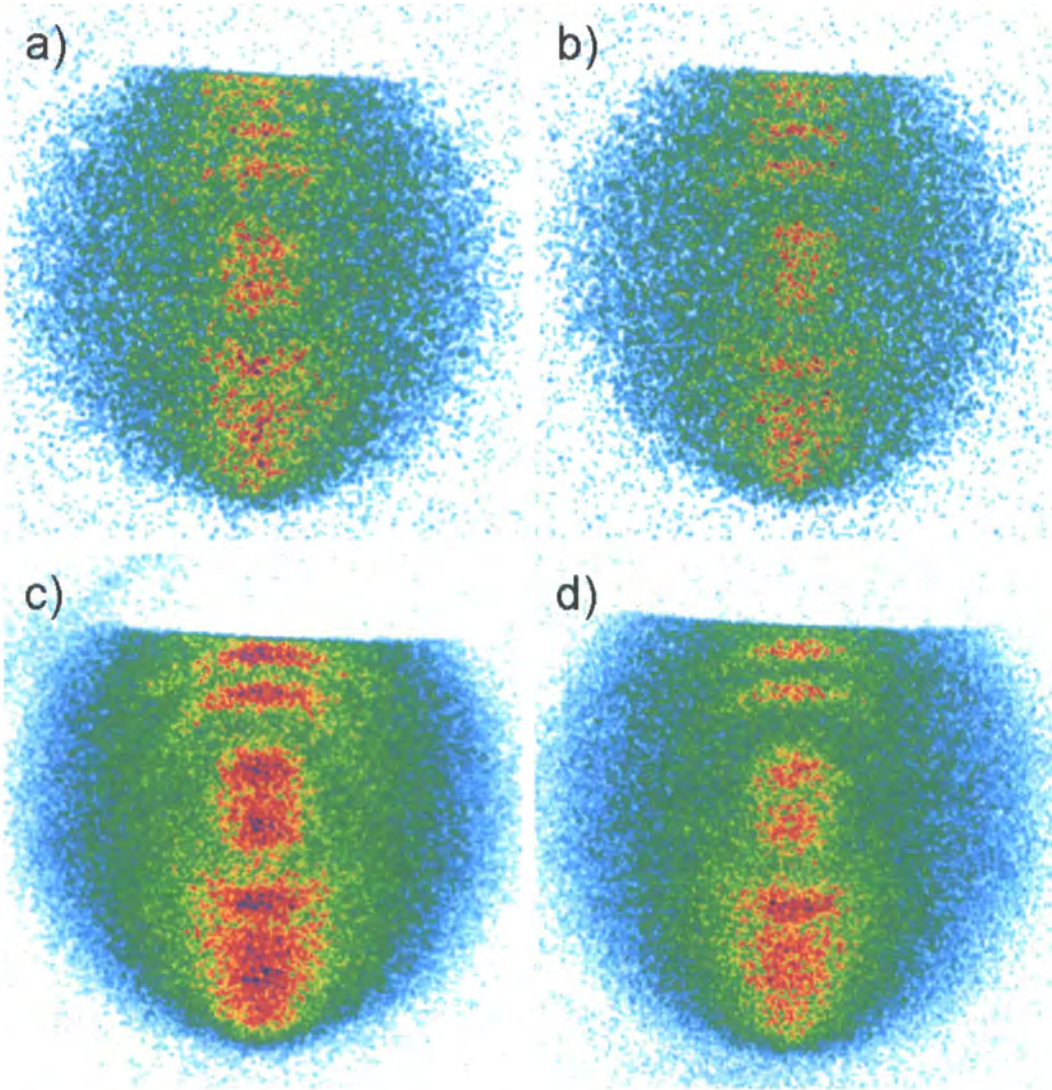
Figure 74: Series of H* + D$_2$ reactive ion images, detecting D$^+$ products. Experimental details are presented in Table 9.

6.5.1 First ion images

The images presented in Figure 74 were recorded using the procedure outlined in the experimental section *(Chapter 4)*. The series of images represent the first reactive signal obtained whilst running the experiment. These images were collected over the course of two days, whilst attempting to optimise velocity mapping and signal-to-noise. An overview of the specific experimental conditions is presented in Table 9.

The hydrogen atoms were excited to Rydberg level $n = 36$; the Rydberg scans showed that this level was well defined and had good signal (Figure 60), at this stage the Stark effect analysis had not been performed and so it was not known that the full Stark manifold would not be ionised at $n = 36$. Figure 74 a) depicts the first reactive ion image signal obtained; this was achieved using the velocity mapping settings optimised in the calibration procedure. The first attempt to optimise the blurred image was through adjusting the voltage of the pulser to produce sharper velocity mapping; as a result a slightly higher resolution of the rings is observed in Figure 74 b). The next step was an attempt to increase signal. The delay between the excitation lasers and the rising pulsed field was increased, in order to allow the expanding cloud of Rydberg hydrogen atoms more time to collide and hence increase signal; the result of this change is displayed in Figure 74 c).

A series of optimisation steps were then performed, all with the aim of higher resolution and better signal. Both the concentration of HI in the molecular beam and the 266 nm power were increased with the aim of creating more hydrogen atoms to collide with the deuterium beam. The VUV power was reduced as it was suspected that the blurring may have been due to space charge effects caused from the ionisation of the large number of remaining reactant H* atoms from the VUV light. The extractor voltage was adjusted to achieve better velocity mapping conditions. The final image obtained from these optimisations is shown as Figure 74 d).

Table 9: Experimental settings for images a-d in Figure 74.

	a)	b)	c)	d)
HI molecular beam	300 mbar HI made up to 1 bar with Ar	300 mbar HI made up to 1 bar with Ar	280 mbar HI, pushed towards nozzle with Ar made up to 1 bar.	900 mbar HI, pushed towards nozzle with Ar.
266 nm power	4 mJ	4 mJ	4 mJ	6 mJ High to reduce space charge effects
Rydberg level	$n = 36$	n = 36	n = 36	n = 36
D2 molecular beam	4 bar	4 bar	8 bar	8 bar
VUV power	high	high	high	lowered power to reduce signal to reduce space charge effects
laser excitation to pulser delay	120 ns	120 ns	200 ns (increased for more signal)	200 ns (increased for more signal)
ion optics settings	Pulser: 870 V, Rep: 3865V, Stab:3890V, Ext: 3450 V	Pulser: 860 V, Rep: 3865V, Stab:3890V, Ext: 3450 V (opt vel map for pulser)	Pulser: 860 V, Rep: 3865V, Stab:3890V, Ext: 3450 V	Pulser: 860 V, Rep: 3865V, Stab:3890V, Ext: 3430 V (opt vel map for ext)
number of frames	8290	7999	14281	40689
number of counts	49629	41815	195616	172276

Time gating on the detector enables H^+ and D^+ to be distinguished by their differing time-of-flight. In order to obtain significant D^+ signal, a large number of primary Rydberg hydrogen atoms was required; these atoms were also field ionised and accelerated towards the detector. Although the detector was set to D^+ signal, in the off state (voltage across MCP 2 = 450 V, rather than 950 V for the on state) this voltage was not low enough to block the electrons produced from the large number of H^+ ions hitting the detector from reaching the phosphor screen (see Newton diagram in Figure 75). As a result this large signal at the top of the image had to be blocked such that it did not cause damage to the detector. This was achieved by lowering the gate valve that separates the reaction chamber from the drift tube. The gate valve is not a sharp edge so in order to fully block the hydrogen signal some of the reactive signal was lost. The lack of signal due to the gate valve can be seen at the top of the images in Figure 74.

The images in Figure 74 indicate that the main signal is on the centre line with little sideways scatter, partial quantum state resolution is seen around the top of the image, with a decrease in definition towards the bottom of the image. There is not sufficient resolution to distinguish whether the top and bottom of the images are symmetric. Although there are fewer counts in images a and b, the position of the gate valve blocking the primary hydrogen signal is a little higher and as such it is possible to see slightly more reactive scattering.

The Newton diagram in Figure 75 can be used to relate the laboratory and centre of mass (CM) coordinates in order to determine the relationship between initial and final velocities. The Newton diagram in the detection plane is shown along with a scale labelling the quantum levels corresponding to the individual rings. The diagram for the scattering plane details the viewpoint of the reactant molecules whereby v_{D_2} and v_{H*} represent the velocities of the reactants in the lab frame and the corresponding centre-of-mass velocities u_{D_2} and u_{H*} lie along the relative velocity axis.
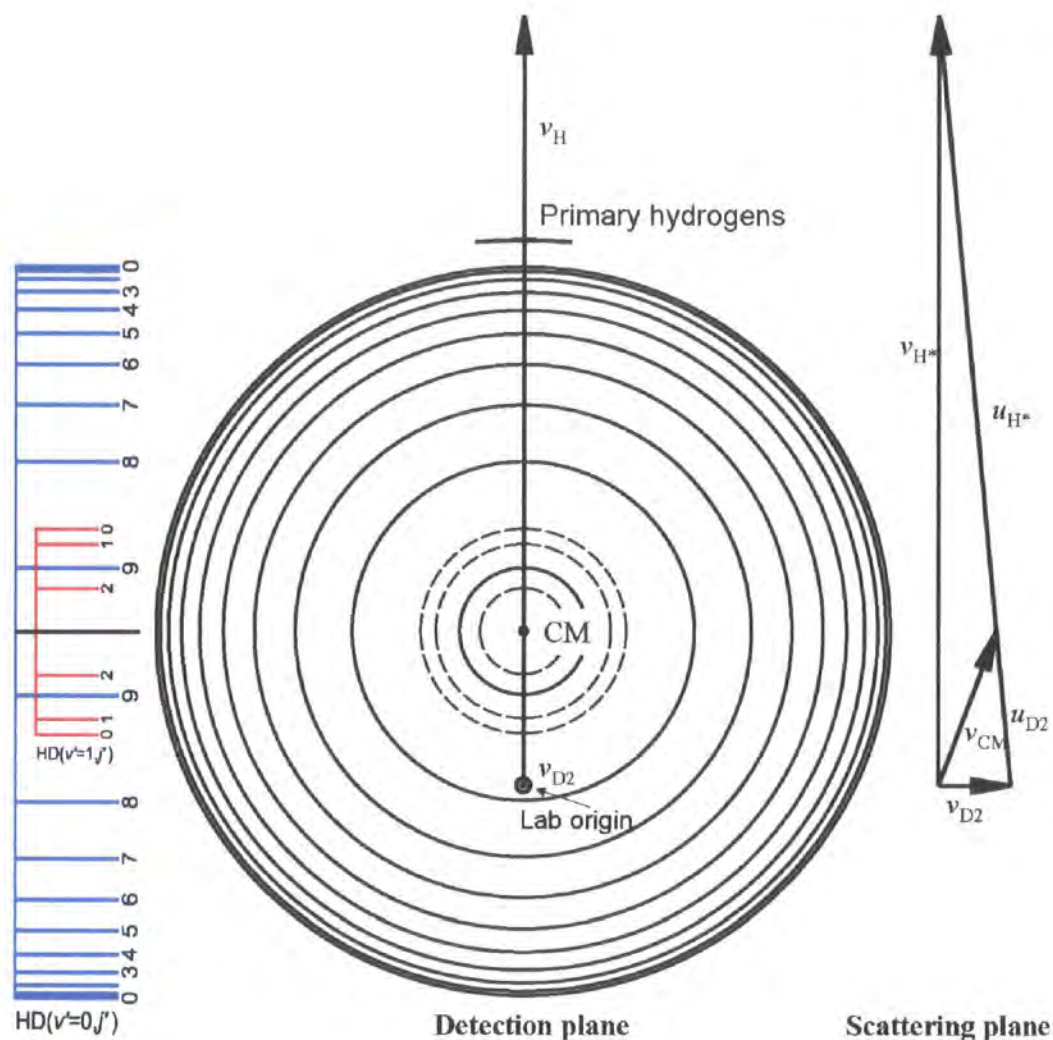
Figure 75: Newton diagram,

The Newton diagram in Figure 76 explains the appearance of the recorded images displayed in Figure 74. After the reaction both products fly away from the centre-of-mass in opposite directions, u'_{HD} and u'_{D*}. Traditionally the scattering angle, θ, is defined as the angle between the incoming atom, H*, and the outgoing molecule, HD. However, in the experiment the atomic product D* is detected, therefore the signal at the bottom of the image is due to backwards scattered D*. This corresponds to the outgoing molecule, HD, being forward scattered and vice versa for signal at the top of the image.

Forwards scattered D*
Backwards scattered HD

$\approx$

u_{D2}

HD $(v = 0, j')$

Sideways scattering

u'_{HD}

θ_{HD}

θ_{D*}

CM

u'_{D*}

Sideways scattering

u_{H*}

$\approx$

Backwards scattered D*
Forwards scattered HD
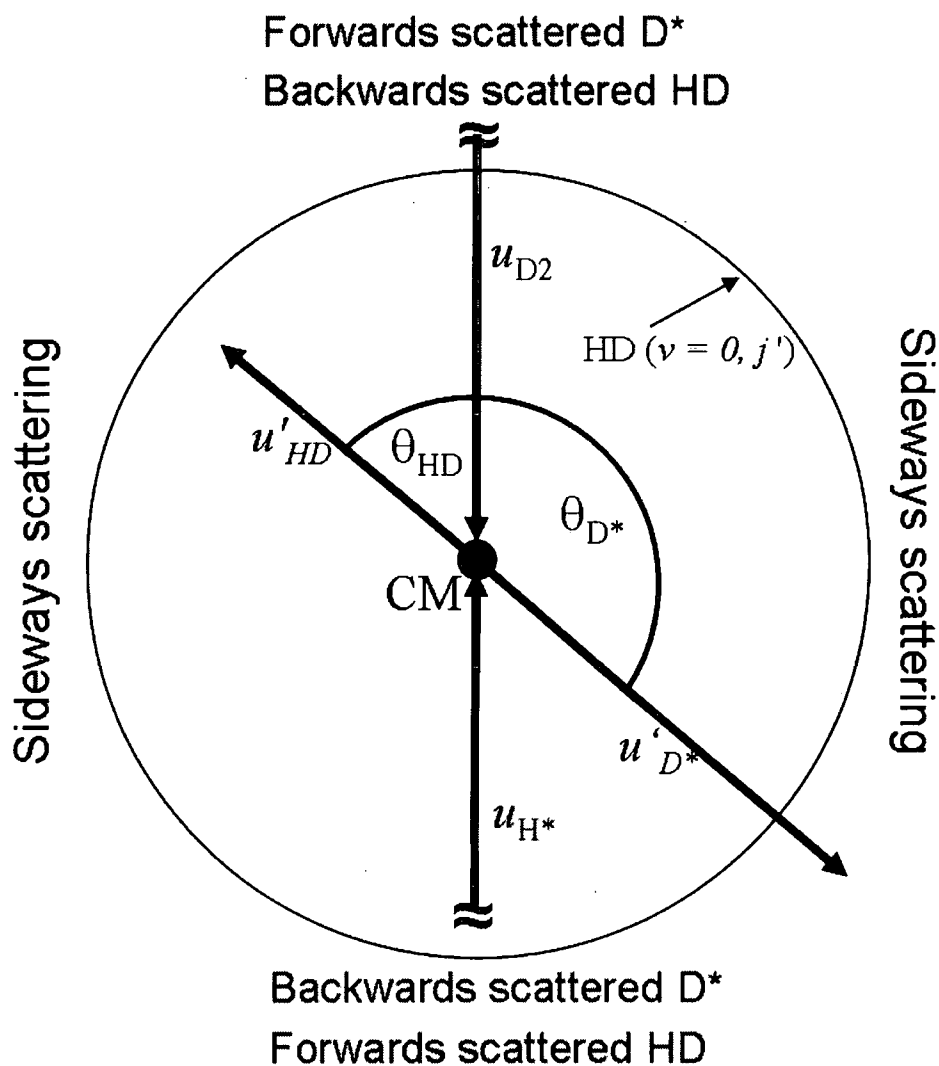
Figure 76: Schematic Newton diagram, depicting direction of scatter for reactive products.

The resolution of the images does not show clearly whether the forwards-backwards scattering is symmetric. A symmetric distribution would occur as a result of a long lived intermediate (H_3^+). If the lifetime of the intermediate is longer than its rotational period then the complex can undergo more than one rotation before it breaks-up into products. This leads to an isotropic distribution of the recoil directions of the products. However, this level of detail can not be extracted from the images.

6.5.2 Ion image simulations

A Monte Carlo simulation has been performed by Trottier in order to investigate how the geometry of the experiment affects the ultimate energy resolution that could be achieved with this experiment [130]. This simulation can be broken down into two parts: firstly sampling all the possible collisions (positions and directions); and secondly, for each of these collisions sampling the possible outcomes (product quantum state and scattering angle). The simulation follows the trajectory of the reactants until the point of collision as follows:

- The trajectory of the HI molecule from the nozzle orifice to the dissociation point.

- The trajectory of the H atom from dissociation point to collision point in the D_2 beam.

- The probability for excitation into the Rydberg state is evaluated for the hydrogen atom on its flight through the space- and time-dependent excitation laser beams.

- The trajectory of the D_2 molecule from the nozzle orifice to the collision point.

- The velocity of the product D^* is used to simulate idealised reconstructed ion images (2D slice through the 3D velocity distribution).

The parameters for the simulation are:

- The size, density profiles and velocity spreads of the skimmed molecular beams.

- The pulse intensities (beam and temporal profiles) and spectral line widths of the laser beams, which define the time and space dependent laser intensities.

- Angular distribution of the HI photodissociation.

- Timing between dissociation and excitation lasers.

The crucial step is to accurately simulate the Rydberg excitation of the hydrogen atom. This two step excitation is explained by a three level model which describes the relative populations of the 1s, 2p, and 36d levels by factoring the Einstein coefficients and the laser field intensity experienced by each atom as it travels in and out of the excitation lasers paths.

For the second part of the simulation all of the parameters outlined above are collectively used as a weighting factor associated with the Newton diagram for each collision. This ensemble of pre-collision Newton diagrams is used to sample the possible outcomes (for each product quantum state and scattering angle). A theoretical differential cross section for each product quantum state is used as an additional weighting factor to build up the idealised ion image (2D slice) as a 2D histogram *via* the velocity component of the D* product atom. It is important to note that the simulation does not take into account the pulsed field ionisation and the ion trajectories through the ion optics, thus there is no allowance made for non field-free Rydberg excitation conditions and imperfect velocity mapping.

In an initial test the simulation was run with a uniform differential cross section and scattering restricted into the plane parallel to the detector in order to create the idealised 2D slice. The image produced displays full resolution of HD rotational levels. Upon close inspection of the simulated image, blurring of the rings can be observed towards the sides of the image and the resolution is not uniform up/down. This can be seen in the simulation shown in Figure 77.
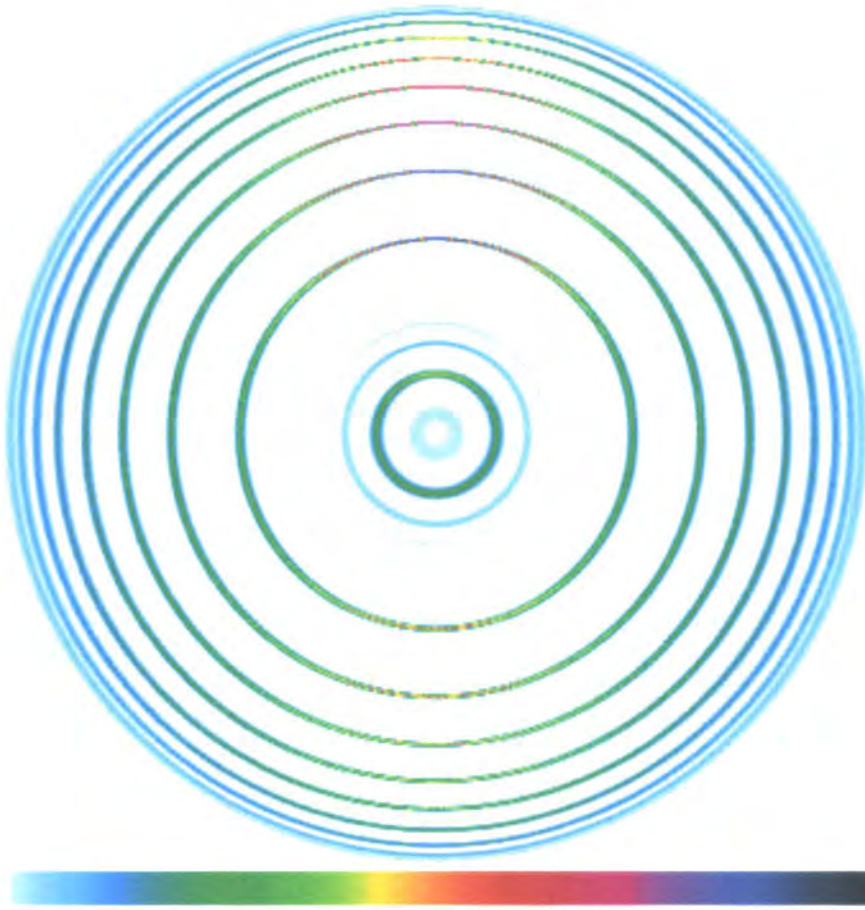
Figure 77: Simulated ion image, using a uniform differential cross section and uniform scattering in the plane of the detector. The bar depicts the colour scale used in the image.

The lower resolution towards the sides of the image can be explained by the vertical spread of relative velocity along the laser axis determined by the path of the hydrogen atom; this is caused by the finite size of the molecular beam as depicted in Figure 78.
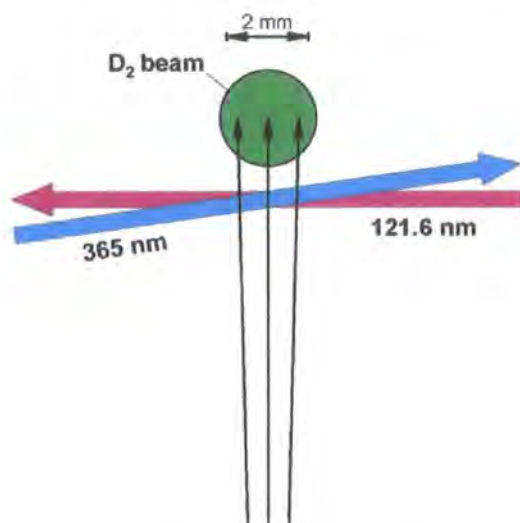
Figure 78: Schematic diagram of the angular spread of the hydrogen atoms (represented by the arrows) corresponding to collisions within the D$_2$ beam, view from detector towards nozzle.

The up/down asymmetry in resolution can be explained with the aid of the diagram in Figure 79. Panel a) shows the plane of the molecular beams: in 1 the hydrogen atom (blue circle) collides with a D$_2$ molecule in the centre of the molecular beam; in 2, (pink circle) it collides above the centre; and in 3 (green circle) the collision occurs below the centre. Panel b) shows the corresponding Newton diagrams for two product quantum states (schematic features are exaggerated). The coloured rings refer to the three different collisions depicted in panel a). When the H* collides above the centre of the D$_2$ beam the velocity components of the D$_2$ (v_{D_2}) and centre of mass (v_{CM}) are tilted upwards, this results in a reduction of the relative velocity corresponding to a smaller product D* velocity (smaller ring diameter). The opposite is true when the H* collides below the beam centre, v_{D_2} and v_{CM} are tilted downwards and the ring diameter is larger. The combined effect of tilting the centre of mass and the size of the rings lead to a reduced velocity spread for the D* atom flying upwards compared to a larger spread for the D* atom flying downwards.
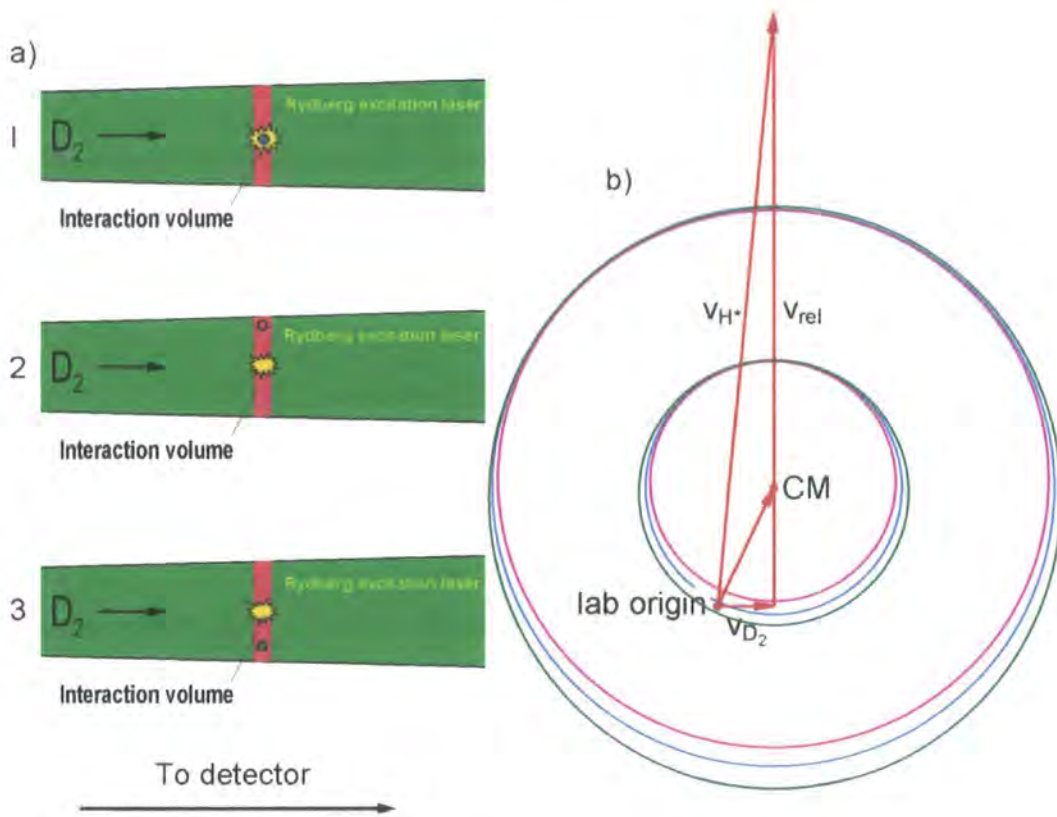
Figure 79: a) Hydrogen atoms colliding with different parts of the D_2 beam shown in the plane of the D_2 beam. b) Newton diagram corresponding to the three collison points. The direction of velocity of the D_2, H^* and centre of mass (CM) are shown by the red arrows and the corresponding relative velocity is labelled V_{rel}.

This effect can be observed in Figure 77, where the outer two rings $j' = 0$ and $j' = 1$, can be resolved up/down but can not be resolved left/right.

6.5.3   Simulation with theoretical differential cross section

Idealised ion images were simulated using two theoretical differential cross sections from Carmona-Novillo *et al.* [71] which have recently been used for a comparison with previous experimental work by Wrede *et al.* [2]. These were the statistical quantum method (SQM) and the time independent exact quantum method (EQM). The simulated images obtained from these differential cross sections suggested that it may be possible to achieve resolution high enough to observe the theoretically predicted features of the differential cross sections. Figure 80 displays the simulated idealised reconstructed ion image (2D slice) and

the full simulated images (*i.e.* the projection of the full 3D spheres collapsed onto the detector). The image shows that using the exact quantum method differential cross section the simulated images have high enough energy and angular resolution to observe the fine detail oscillations in the angular dependance arising from interference effects, which, for example, the statistical quantum method differential cross sections does not include and as such these oscillations observed in b) and d) can not be seen in a) and c) from Figure 80. An experimental image of this resolution would allow for a stringent test to the theoretically calculated differential cross sections.
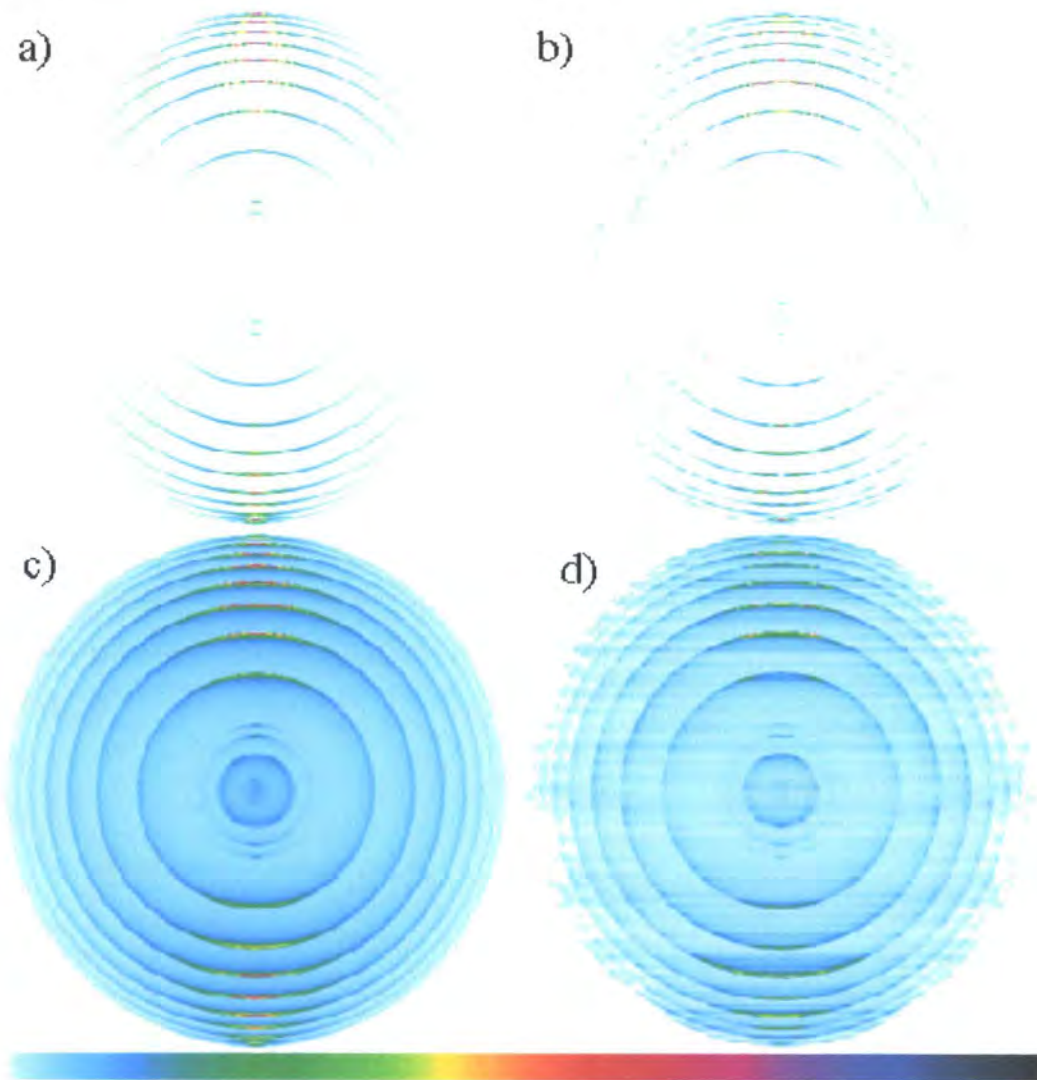
Figure 80: a) simulated 2D slice from a statistical quantum method and b) simulated 2D slice from from an exact quantum method. c) and d) are simulated full images (not sliced) using SQM and EQM respectively. The bar depicts the colour scale used in the images.

The actual resolution obtained for these first ion images is of a lower quality than the simulated images, this is discussed in greater detail in the following section. Whilst the images cannot be compared quantitatively, qualitative similarity can be observed; this is demonstrated in Figure 81 and Figure 82. In Figure 81 the experimental ion image (Figure 74 cropped for ease of viewing) is shown in comparison to a scale indicating the predicted sizes of the rings corresponding to the product quantum states, taken from the Newton diagrams. Figure 82 shows a comparison of the experimental image and the simulated image. In this case the simulated image is the projection of the full 3D sphere onto the detector (i.e. mimicking the experiment), which allows for comparison with the raw ion image. Both Figure 81 and Figure 82 show a qualitative likeness to the simulation.
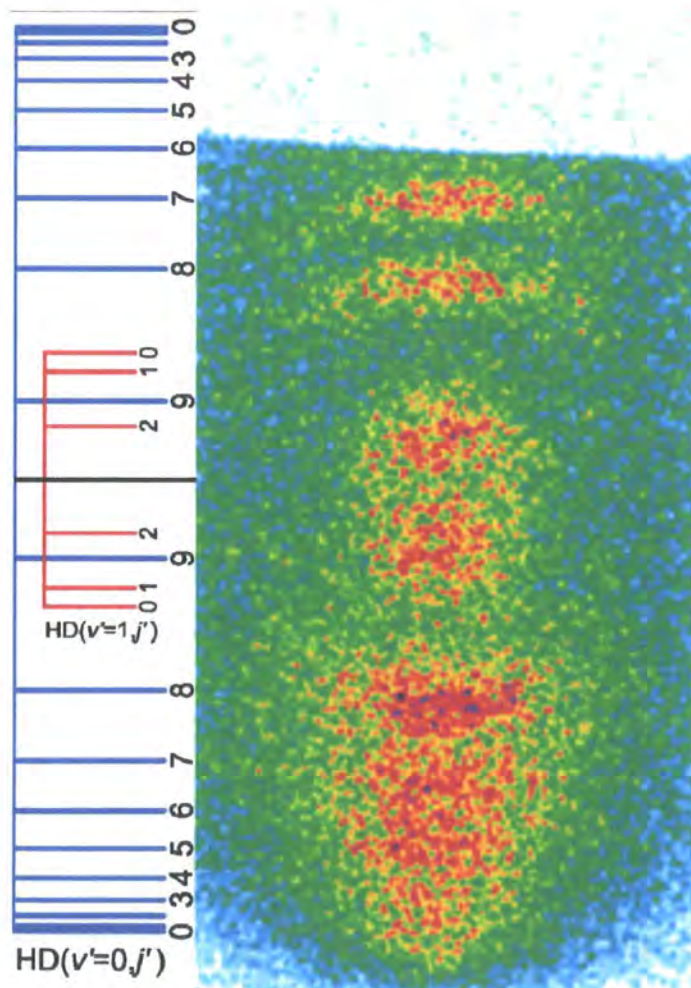
Figure 81: Quantum state assignment using the central section of the experimental ion image from Figure 74. The predicted ring size scale is taken from the Newton diagram.
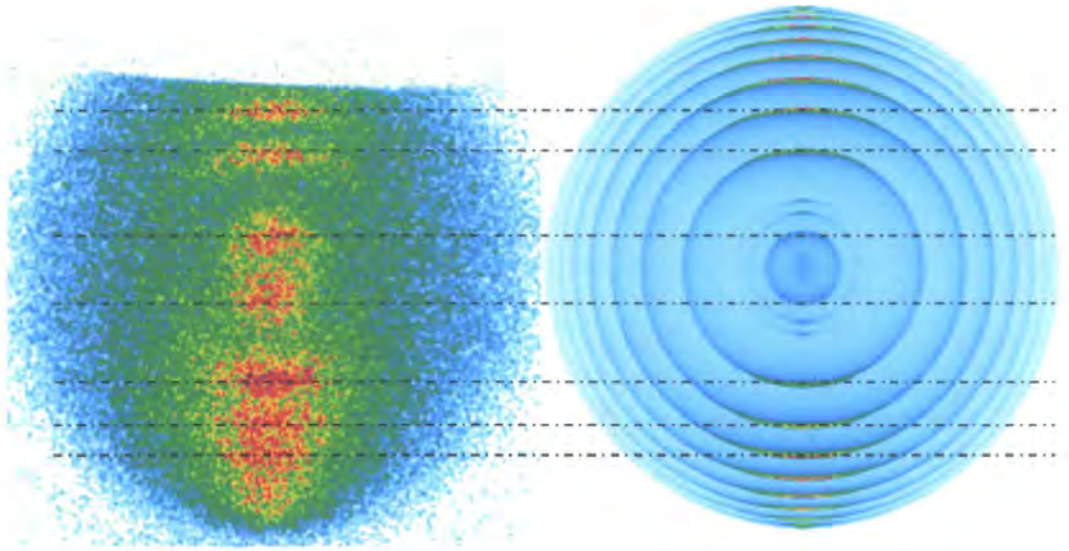
Figure 82: a) The raw experimental ion image from Figure 74. b) A simulated full image (not sliced) using the SQM DCSs.

6.5.4 Analysis of image

The experimental ion image does not achieve the resolution displayed by the simulation. The simulation does not take into account the effects from the ion optics i.e. the possibility of non field-free excitation and the pulsed field ionisation such as imperfect velocity mapping. These issues are potentially the largest sources of error in the experiment. In *section 6.3* the effect of Stark splitting in the field was analysed for hydrogen atoms; the same argument can be applied to the case of deuterium. It was found that at a quantum level of $n = 36$, the ionisation threshold of the blue shifted Stark states was higher than the maximum ionisation field produced by the ion optics and that only the red shifted levels had a sufficiently low ionisation threshold. The Stark effect was also observed to cause a spread in the ions' time-of-arrival at the detector, as the rising field caused different levels of the Stark manifold to ionise at different times. This may affect the velocity mapping and introduce blurring into the resulting image.

It must also be considered that the simulated ion image is not a direct comparison to that obtained experimentally. The simulation places the excitation step 3 mm below the centre of the D_2 beam, which is the design for the experiment. However, for practical reasons the image in Figure 74 was obtained with the excitation lasers

in the centre of the molecular beam. Additionally, the amount of signal obtained in the experiment was lower than estimated in comparison to previous experiments carried out by Wrede *et al.* [2]. This short-fall could be attributed to the fact that only a proportion of the Stark manifold is ionised. In order to boost signal in the experiment a delay of 200 ns, from the laser excitation to the pulser, was required to allow for more collisions before ionisation. Whilst this did result in more signal, the scattered D^* atom cloud expanded for 200 ns, which corresponds to a possible source region up to 2 mm thick in the molecular beam. The imperfections of the velocity mapping conditions may result in blurring from such a large source volume.

Recently, Hayes and Skodje reported that the Rydberg level of the product atom is likely to change during the reactive collision [59]. The redistribution for each collision is complex and can result in higher and lower Rydberg levels. This study helped to explain differences between experimental results and quasi classical theoretical differential cross sections by Yang and co-workers [131]. These studies imply that a direct comparison with the current experiment cannot be made due to the experimental differences. This affect would cause a further complication to the pulsed field ionisation; it is possible that the change would result in low n states or in blue shifted states that would have undetectably high ionisation thresholds.

A test was performed to investigate the extent to which the existence of different Rydberg levels would alter the ion image. The experimental method used in the calibration process (detailed in chapter 4) was employed. In this method the HI molecular beam was on the central nozzle rather than on the lower nozzle. Photodissociation of HI was used as a source of hydrogen atoms on the central axis of the experiment. In a series of measurements the hydrogen atoms were excited to a variety of Rydberg levels prior to the pulsed field ionisation restoring the velocity mapping conditions. Figure 83 shows a zoom into the slow hydrogen channel of the photodissociation images, whereby the hydrogen atoms were excited to three different Rydberg levels. The images indicate that the diameter of the ring does change, although the velocity of the H^* is constant across the three images. The difference in the diameter arises from the time dependent rise of the

field as discussed in *section 6.3.5*. This indicates that a difference in the image is observed for differing Rydberg levels. This effect could contribute to the observed blurring due to a distribution of D*(n') Rydberg states.

Figure 83 shows a difference of 10 pixels in the measurement of the diameters of the ring between $n = 32$ and $n = 42$. Close inspection of Figure 81 determines that the ring due to $j' = 8$ in the upper section of the image is spread over 10 pixels, it is therfore conceivable that this effect may be a contribution towards the blurring in the image.

The first images from the $H^+ + D_2$ reaction have been presented in this chapter. Whilst the images are of low resolution they have been compared to theoretical predictions. They show a qualitative agreement with the SQM method, but the poor resolution does not allow detailed comparison between the alternative methods.
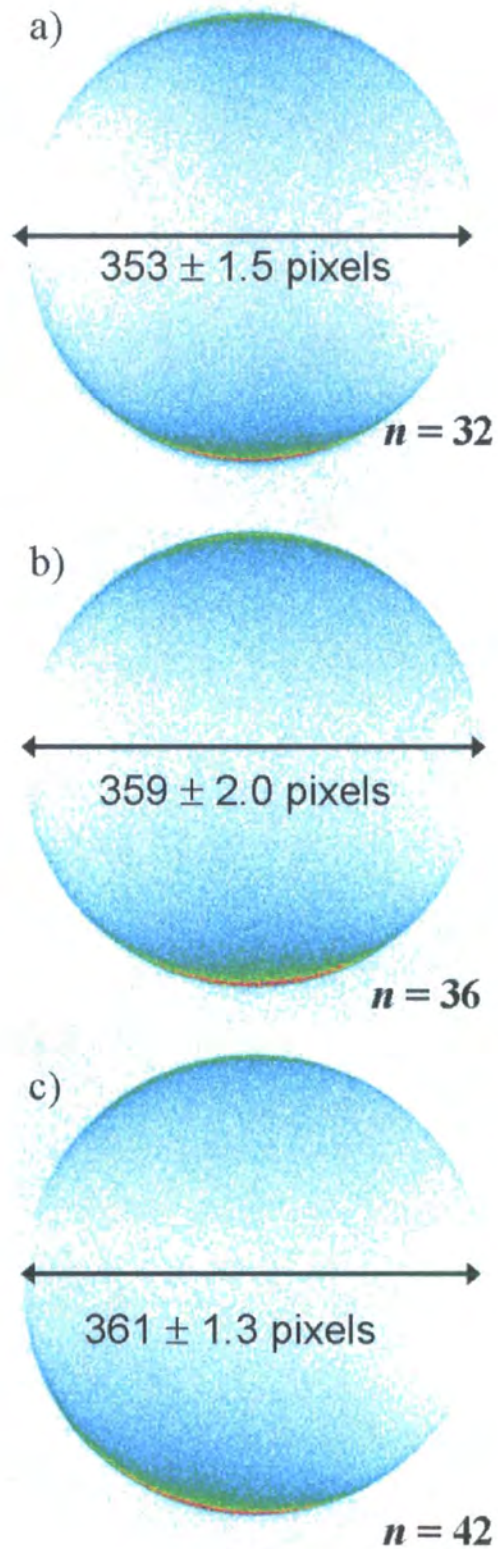
Figure 83: Slow channel of photdissociation of HI with 266 nm light. Photodissociation products are excited to three different Rydberg levels and then pulsed field ionised.

Chapter 7: Conclusions and Future work

7.1 Conclusion

The objective of this project was the development of a state-of-the art experiment to study the reaction dynamics of highly excited hydrogen Rydberg atoms with D_2 molecules and to test the extent to which the free electron model, which predicts that the Rydberg electron acts as a spectator while the ionic reaction takes place, holds, *i.e.* to test the similarity to the ion-molecule reaction $H^+ + D_2 \rightarrow HD + D^+$. The experimental set-up has been completed throughout the course of this Ph.D. This has involved the construction of the vacuum chamber and design and installation of the necessary accessories.

The development of the ion optics was completed with the aid of Simion where ideal velocity mapping conditions were estimated. The electrodes have been installed and tested, an overview of which was provided in *Chapter 5*. One of the first goals during the development of the experiment was to establish the velocity mapping conditions and investigate the resolution possibilities of the ion optics using the photodissociation of HI. Images of high resolution were produced and velocity mapping conditions were achieved. A reliable method for producing the dry, pure HI gas has been implemented. The convenient and economical technique developed results in sufficient HI for around two weeks of measurements from one batch produced.

The novel technique of pulsed field ionisation followed by ion imaging has been developed and tested. The high voltage switch used to pulse the extraction field of the ion optics has been found to alter the high voltage settings required for velocity mapping. Rydberg scans were used to obtain optimised near field-free conditions in the extraction region for the state selective excitation into Rydberg levels. In *sections 6.2* and *6.3* the appearance of the Rydberg scans was analysed and it can be concluded that the Stark effect causes a broadening in the time-of-arrival at the

detector of the field ionised H* atoms and also the entire Stark manifold of a specific Rydberg level may not be ionised.

The main goal of this project was to study the H^* + D_2 reaction. It was hoped that the images obtained would be of high enough quality to extract state-to-state differential cross sections and provide a stringent test on recent theoretical calculations and predictions on the ion-molecule reaction H^+ + D_2 [71]. To date only a few low-resolution reactive scattering ion images have been recorded. It was hoped that once signal had been obtained the multitude of experimental conditions could be optimised to increase signal and improve resolution. However, a series of unforeseen problems and equipment failure resulted in no further images being produced in the time scale of this project. It is hoped that these first experimental images will act as "prototypes" and the study will be continued to achieve images with the desired resolution. It is this close interplay between experiment and theory that is needed to aid the understanding of elementary chemical reactions [132].

Whilst the main goal of this project has not been fully realised, there have been important and worthwhile outcomes. A novel technique of pulsed field ionisation has been established for the ion imaging of hydrogen Rydberg atoms. This technique has been tested and the limitations in applying the technique have been discovered.

7.2 Future work

7.2.1 Improvement of resolution

During the preparation of this thesis experimental work was continued by other members of the group. However, due to time constraints and problems with equipment it was not possible to reproduce reactive scattering signal. One of the suspected reasons is the modified D_2 nozzle. The nozzle used to record the images presented in this thesis began to leak and was replaced. Producing a reliable nozzle that works well at liquid nitrogen temperatures has been found to be "hit and miss"; we suspect that the new nozzle was not working as well as its predecessor. The pulse amplitude measured by the FIG could not be directly compared to previous measurements as the amplifier for the FIG had been replaced. In the two days of measurements that produced the images in this thesis, significant damage was caused to the optics on the 266 nm beam path; the window entering the chamber was almost fully drilled through. This caused the measurements that followed to be undertaken with more caution *i.e.* less 266 nm power. There were other technical problems with the pulser which resulted in experiment down time and the overall project came to an end before any further measurements could be attempted.

It is hoped that images of far higher quality will be produced when the experiment is resurrected in the future, such that a meaningful comparison can be made with theoretical studies. Short term goals for optimisation would firstly use a new D_2 nozzle in an aim to boost the initial signal obtained. It has become apparent that the 266nm power needs to be high in order to produce sufficient hydrogen atoms available to collide with the D_2 molecules to produce measurable signal. It may be essential to sacrifice a few laser optics along the way, in order to use the desired high power.

7.2.2 Technical improvements

The images produced suffered from lost signal arising from the gate valve being used as a block for the primary H signal. An idea arose in the course of the project whereby a few modifications to the deflector (used to steer the signal to the centre of the detector) would allow for it to be "pulsed" such that the voltage could be high when the earlier hydrogen atoms pass through, deflecting them higher than the detector face, and not affecting the paths of the D_2. Initial calculations using Simion suggest that this is a feasible idea.

During the tests of the pulser and the analysis using the Stark effect an idea arose to exploit the effect observed. The pulsed field ionisation produced different time-of-arrivals for different Rydberg levels; if this fast rising field was slowed down, it may be possible to set the detector gate on specific Rydberg levels and directly measure the scattering into a specific Rydberg state.

$$H^* \ (n) + D_2 \rightarrow D^* \ (n') + HD$$
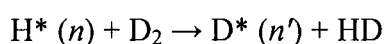
Equation 25

7.2.3 Variation of H* + D_2 scattering

A simple change to the experiment would be to change the polarisation of the 266 nm light; this could result in directing the fast hydrogen photodissocated products towards the deuterium beam. This would alter the collision energy of the reaction to approximately 1.28 eV.

It would perhaps be more interesting to reach collision energies above 1.85 eV as this would allow investigation of the dynamics of another potential surface of the reactive charge transfer pathway (see Figure 11). This is theoretically more challenging as non-adiabatic coupling between 2 surfaces needs to be considered.

This idea could be applied to the current reaction by colliding a neutral hydrogen atom with a Rydberg deuterium molecule; by detecting mass 1, 2, 3 or 4 (see reaction in Equation 26) this could provide access to all four channels:

$$H + D_2 \rightarrow H + D_2^* \quad \text{(inelastic)}$$

$$\rightarrow HD^* + D \quad \text{(reactive)}$$

$$\rightarrow H^* + D_2 \quad \text{(charge transfer)}$$

$$\rightarrow HD + D^* \quad \text{(charge transfer)}$$
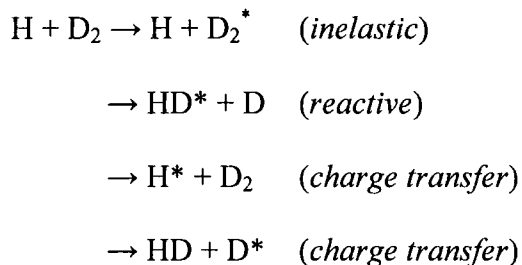
Equation 26

7.2.4 Study of alternative systems

A natural progression of this study would be to investigate alternative ion molecule reactions, using the hydrogen Rydberg atom with a variety of alternative molecules using the pulsed field ionisation with ion imaging technique. The study of $H^* + O_2$ would give an insight into important atmospheric chemistry.

A second interesting idea would be to use an alternative Rydberg atom in a collision with hydrogen or deuterium molecules. One such example would be a Rydberg oxygen atom. Lin *et al.* have reported a technique whereby oxygen Rydberg atoms are produced *via* double-resonance two-photon excitation of the photodissociated product of NO_2 [133]. Other desirable atoms would include N^* and C^*.

Chapter 8: Cavity Ring-Down Spectroscopy of 1, 4-bis(phenylethynyl)benzene, (BPEB)

8.1 Introduction

This final chapter details an overview of work done in the lab in the first eight months of this three year project. This work was not the primary aim of my Ph.D. and was a running experiment developed by S. J. Greaves [134] [135]. My contribution towards this project was based around experimental technique in order to obtain optimum experimental conditions and define the laser calibration procedure in what was already a running experiment. This provided an excellent opportunity to learn skills and understand the working of lasers, molecular beams and vacuum techniques.

8.2 Molecular wires and switches

Miniaturisation of micro electronics is presently a significant topical issue concerning many industrial areas of science. The decreasing size of devices since the invention of transistors in 1947 [136], has allowed the incorporation of more components per chip, faster operation, higher performance and lower power consumption. Over the last three decades vast improvements and reductions in cost have been observed in computers and electronics [137]. Eventually this trend will end as conventional fabrication methods of silicon chips are reaching their limits [138], with the production of components around 100 nm in size. The next step is to produce components 10 times smaller [139].

Alternative materials and operating principles for communication of data in electronic circuits and optical networks is currently a growing area of science. Organic molecules are promising candidates for the realisation of future digital processors [140]. Their attractive features are the miniaturised dimensions and the high degree of control on molecular design possible in chemical synthesis. It is

161

plausible that organic synthesis will lead to nanostructures with engineered properties and specific functions.

A family of organic molecules, referred to as molecular switches, can adjust their structural and electronic properties when stimulated with chemical, electrical, or optical inputs [141]. These transformations are often reversible; the chemical system returns to the original state when the input signal is turned off, thus, fabricating logical circuits at a single molecule scale.

Organic compounds with aromatic groups that are linearly conjugated through acetylene linkages have become a source of great interest in the field of molecular wires [142]. Attention has been paid to a variety of compounds including, simple organic and metallo-organic chromophores [143], complex nanometre-scale molecular architectures [144], and high molecular weight conducting polymers such as poly(phenyleneethynylenes) [145].

8.2.1 Poly(phenyleneethynylenes)

Poly(phenyleneethynylenes) (Figure 84) typically have linearly conjugated structures which allows for efficient electronic communication [145]. These molecules have been studied as a possibility for molecular wires, switches and diodes [146].
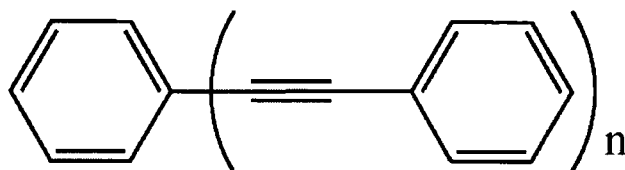
Figure 84: Poly(phenyleneethynylenes)

The triple bond in the molecules has a cylindrical symmetry, that is able to maintain conjugation between adjacent phenyl groups depending upon the relative orientation of their aromatic planes [147]. The alkyne-aryl single bonds in the molecules allow for relatively free rotation about the axis [148]. The barrier to rotation is estimated to be less than 1 Kcal/mol ($\approx$ 4 kJ mol^{-1}) [145]. This free

twisting of the molecule causes the extent of π conjugation to be dependent on the orientation of the planar aromatic moieties [149].

Experiments have been conducted that indicate these molecules and their derivatives exhibit bistable conductance states (memory), controlled switching under an applied electric field and negative differential resistance (NDR) [150], NDR entails an initial increase in the conductance of the molecule with an applied voltage, followed by a fall in conductance upon addition of further current. By varying the conjugation of the molecules the HOMO-LUMO gap will be affected accordingly. This gives the potential for these molecules to have applications in photo- and electroluminescence devices [151].

8.2.2 Tolane

Research using fluorescence spectroscopy into tolane, (diphenylacetylene) a Poly(phenyleneethynylene) where n=1 (Figure 84), has shown that the conductivity of the molecule is dependent upon the relative twist angle of the benzene rings [152]. The ground and excited state twisting potentials were obtained *via* fluorescence studies, and showed that the S1 and S2 excited states are very similar in energy. It is generally accepted that this is not the case for longer Poly(phenyleneethynylenes) where the S1 and S2 excited states have shown a greater energy difference. This has been related to the change in structure of Tolane by the benzene rings, the higher states have a linear structure with the lower states showing a weakened acetylene link in a bent structure [153].

By fully understanding the effect of the twisting on the π conjugation it may be possible to develop a molecule that will act as an effective switch that can be controlled.

8.2.3 1, 4-Bis(phenylethynyl)benzene, (BPEB)

The poly(phenyleneethynylene) where n=2, is commonly known as BPEB (Figure 85). Unlike tolane BPEB does not show a great change in structural orientation in its excited states [148]. This allows for a comparison between the higher oligomers of poly(phenyleneethynylenes) and allows for BPEB to be used as a model compound to study this group of materials.
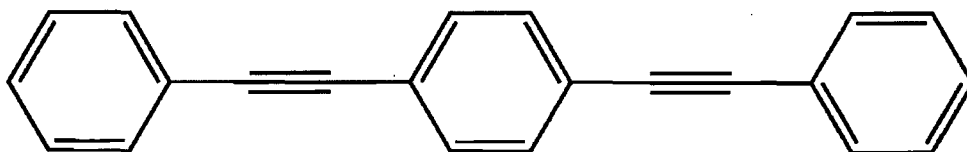
Figure 85: 4-Bis(phenylethynyl)benzene, (BPEB)

8.2.4 BPEB as a model molecular wire/switch

To date BPEB has been used as the backbone in many switching studies [154]. It has been shown that when inserted into self assembled monolayer's (SAM) of dodecanethiol films, stochastic (random) conductance switching is observed [141]. Whereby it appears that the twisting of the rings from a planar geometry affects the conjugation that in turn affects the conductivity. One of the more interesting properties of BPEB is that it does not display NDR, which is closely linked with switching. This has caused BPEB to be of great use when studying this behaviour and trying to determine the mechanism behind NDR in this family of molecules [145].

Theoretical switching studies have looked at the twisting of the central ring. The lumped inertia technique was used to calculate the vibrational frequency of the torsion of tolane and found it to be equivalent to 16 cm^{-1}, with the experimental value known to be 17 cm^{-1} [155]. The values for the torsional frequency in BPEB have been calculated to be 13.2 and 19.4 cm^{-1}. Frontier orbital studies have been used to understand the twisting. By comparing the molecular orbitals it can be seen that for the planar geometry the π orbitals are delocalised across the whole molecule (Figure 86). However when the central ring is twisted the alignment of

164

the ring π orbitals is destroyed and the orbitals are isolated on the central rings as shown by Figure 87 [148]. It has been predicted that there is a 500 times change in conductance on rotation of the middle ring from planar to perpendicular orientation in BPEB [145].
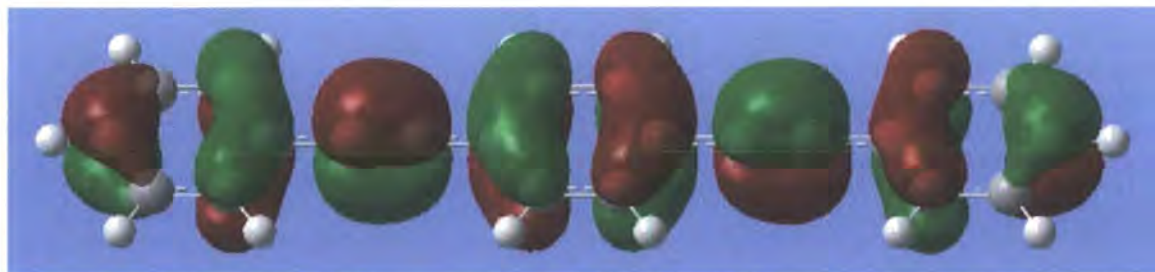
Figure 86: π orbitals fully delocalised in HOMO of BPEB in planar orientation [135].
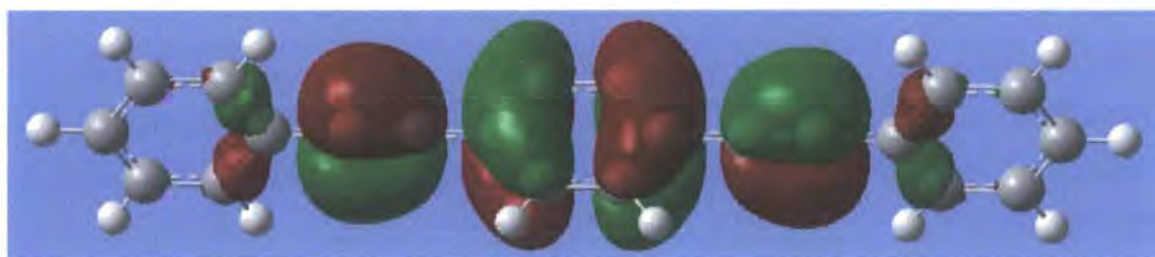
Figure 87: π orbitals isolated on individual rings in HOMO of BPEB with central ring twisted by 90° [135].

BPEB has been studied spectroscopically using solution based techniques [147] [148]. These techniques have provided a valuable insight into the character of the excited BPEB; however, to date, information on the torsional motion of the molecule in either the ground or excited state has not been fully obtained. BPEB has 102 normal mode vibrations and so produces broad featureless absorption spectra. The challenge of studying the torsional motion of BPEB has been approached using a molecular beam to reduce spectral congestion by cooling the internal motions of the molecule. This study investigated the torsional transitions within the $\pi^* \leftarrow \pi$ electronic transition [134]. A highly sensitive absorption technique was required to measure these transitions as molecular beams have very low concentrations.

8.3 Molecular spectroscopy

The study of molecular absorption and emission of radiation is of great importance in basic and applied science. Many laser-based spectroscopic techniques are used, such as laser induced fluorescence (LIF) [156], resonance enhanced multiphoton ionisation (REMPI) [157], degenerate four-wave mixing (DFWM) [158] and photoacoustic spectroscopy [156]. These methods all use a secondary effect following the laser excitation of the sample. The great advantage of cavity ring-down spectroscopy (CRDS) is that it is a highly sensitive application of absorption spectroscopy (direct absorption spectroscopy) [159]. Where other absorption methods fall down due to background fluctuations in light, CRDS has the advantage of large pathlengths. Measuring the rate of decay of a laser pulse in an optical cavity, allows ultra sensitive quantitative absorption measurements. This sensitivity provides an ideal tool for studying weak absorptions resulting from low concentrations, forbidden transitions and short life times [160].

8.3.1 Absorption Spectroscopy

Conventional absorption spectroscopy involves the absorption of light by a sample and is described using the Beer-Lambert Law[156]:

$$I = I_0 \exp[-\sigma C l]$$

Equation 27

Where I_0 and I are the intensities of light entering and leaving the sample respectively. σ is the absorption cross section of the sample at a value of wavelength of the light. C is the number density of the absorber and l is the sample path length.

When employing broad-band light sources, the light leaving the sample needs to be dispersed through a monochromator. If monochromatic light is used an absorption spectrum is simply obtained from the transmitted intensity as a function of wavelength [161]. The main problem with laser absorption spectroscopy is that

the change in intensity of the light as it passes through the sample can be very small compared with the initial laser intensity. So the sensitivity is generally limited by fluctuations in I_0 [159].

8.3.2 Development of CRDS

The transmission of a light pulse through an optical cavity has been studied in depth. The fundamental concept behind CRDS can be traced back to the early 1980's, where Herbelin *et al.* demonstrated a novel method which accurately measured the average reflectivity of a pair of coated mirrors in a cavity to 0.01% [162]. This showed the high reflectance of their mirrors by intensity modulating a continuous wave light beam and measuring the phase shift introduced by the optical cavity.

This was followed by the work of Anderson *et al.* in 1984 [163], in which the reflectivity of a pair of mirrors was determined to an accuracy of 0.0005%. This was achieved by measuring the decay of the light in the cavity and then calculating the ring-down time, rather than using the phase-shift. This decay was measured by switching off the continuous wave light source when the intercavity field was greater than a threshold value. The intensity decay of light in the cavity was then recorded. This method did however encounter problems with mode matching *i.e.* the length of the cavity must be an integral number of half wavelengths of the light.

In 1988 O'Keefe and Deacon overcame these problems by using a pulsed laser [159]. This meant that the laser no longer needed to be switched off to observe the decay, leading to a simple cavity loss experimental design. This technique is very sensitive and was used to observe weak absorptions in trace samples. O'Keefe and Deacon measured the absorption spectra for the doubly forbidden $b^1\Sigma_g^+ \leftarrow X^3\Sigma_g^-$ transition of gaseous O_2.

To date this same method of cavity ring-down is used. Over time modifications have increased the sensitivity of the technique and furthered its applications.

8.3.3 Pulsed Cavity Ring-Down Spectroscopy

8.3.3.1 Principle

In a typical experiment a light pulse is coupled into a non-confocal optical cavity, which consists of two identical high reflectivity plano-concave mirrors. The light coupled into the cavity is reflected back and forth between the mirrors. At each mirror a fraction of light is leaked out of the cavity. This leakage is measured and the intensity of the light in the cavity can be seen to decay as a function of time.

8.3.3.2 Experimental set-up

A schematic diagram of the set-up is shown in Figure 88. The components involved are a pulsed laser source, an optical cavity and a photo-detection system. The ring-down cavity consists of an absorption cell formed by the two high reflectivity mirrors [164].
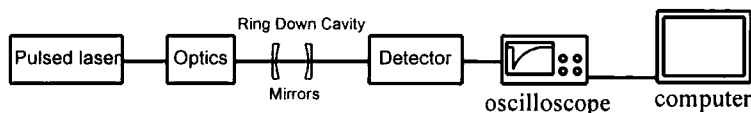
Figure 88: Schematic diagram of the experimental set-up for cavity ring-down spectroscopy.

These mirrors act as the windows of the chamber. They have specific coatings corresponding to suitability over the wavelength required. The maximum reflectivity is typically between 99.95-99.999%. With optimal alignment of the mirrors the laser pulse can be trapped in the cavity by ensuring it retro-reflects back and forth between the mirrors. In the few microseconds that the pulse is stored in the cavity it will do thousands of round trips. The light intensity in the cavity decays by a percentage on each round trip due to the cavity decay losses [156].

The pulsed laser system is required to be tuneable. The type of laser used is dependent upon the wavelength region being observed. Pulsed dye lasers are very commonly used, covering the near UV to near IR spectral range [164].

168

The light decaying from the cavity is detected by, for example, a photomultiplier tube or amplified photodiode to the rear of the output mirror. The light decay consists of a series of intensity peaks characterised by the pulse train shown in Figure 89. The distance between each peak is equal to one round trip in the cavity. Due to the slow time response of the detector the pulse train may not be observed but instead a smooth decay curve may be seen as is superimposed on Figure 89 [156].
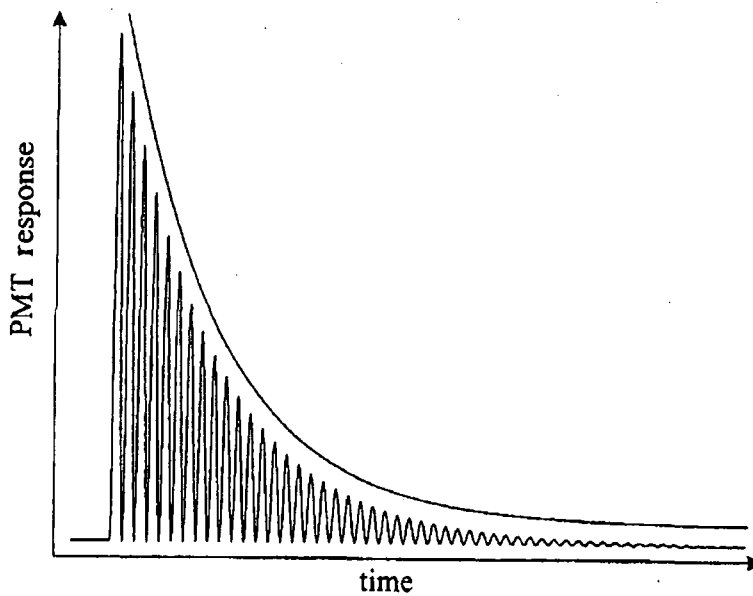
Figure 89: Schematic diagram of expected pulse train and exponential envelope obtained [156].

The signal from the detector is then amplified, digitised and sent to a computer, whereupon the digital trace is fitted to a first order exponential function in order to determine the decay time constant for each laser pulse. An important feature is that by measuring the decay time rather than the absolute intensity, shot-to-shot inconsistencies are not detected.

8.3.4 Absorption spectra

The decay of light in the cavity can be used to obtain the absorption spectrum of a sample. In an empty cavity with mirrors of reflectivity, R, the exponential decay of light exiting the cavity can be calculated as a function of time, t:

$$I(t) = I_0 \exp\left(-\frac{t}{\tau}\right)$$

Equation 28

Where τ is the cavity ring-down time and is equal to the time for the intensity to decay to $1/e$ of its original value. I_0 and $I(t)$ are the intensity of the laser pulse initially and at time t respectively [156]. The cavity ring-down time can be calculated as follows:

$$\tau = \frac{1}{(c(1-R))}$$

Equation 29

Where l is the cavity length, c is the speed of light and $(1-R)$ is the cavity losses due to transmission through the mirrors. This cavity loss also includes the losses due to scattering and diffraction. However these factors are usually much smaller and so can be ignored, making the approximation based on R reasonable. The cavity ring-down time that is determined is therefore strongly dependent on the reflectivity of the mirrors [165] [166].

When a sample is present in the cavity and the wavelength of the light matches one of its transitions the decay of light from the cavity will increase due to sample absorption [156]. This exponential decay will be given by:

$$I(t) = I_0 \exp(-(t/\tau) - \alpha ct)$$

Equation 30

Where α is the molecular absorption coefficient and c is the speed of light. The pathlength, l, over which the absorption is measured is equal to ct, thus the decay rate can be rewritten as:

$$1/\tau' = 1/\tau + c\alpha$$

<div align="right">**Equation 31**</div>

Where τ' is the ring-down time when a sample is present in the cavity. To obtain the absorption spectrum of a sample the molecular absorption coefficient, α, must be determined from the ring-down time at each wavelength of light.

8.3.5 Obtaining a spectrum

To obtain a spectrum the ring-down time of the empty cavity must first be known. This is either taken from the baseline level between peaks in a discrete spectrum or from a mirror scan of the empty cavity in a non-discrete spectrum. The light leaking from the cavity will decay with an exponential time profile according to:

$$I(t) = I_0 \exp(-t/\tau)$$

<div align="right">**Equation 32**</div>

Where $\tau = \dfrac{1}{c|LnR|} \approx \dfrac{1}{(1-R)}$ in the empty cavity and n is the number of round trips.

When a sample gas is present within the cavity the light decay is more rapid. If the wavelength of the light within the cavity matches that of an absorption of sample gas then the light is absorbed by the sample gas, hence the overall light decay is speeded up. For absorption conditions corresponding to Beer-Lambert law behaviour the decay of the light intensity will still be exponential with time dependence given by Equation 30.

The wavelength of the laser is scanned and the light decay detected. This gives the absorption coefficient for each laser wavelength, producing a spectrum.

8.3.6 Cavity mode effects

In order for light to be coupled into the cavity its frequency must match a cavity mode [167]. This requires the cavity length to match an integral number of half-wavelengths of the laser light. The frequency spacing of the longitudinal modes of the cavity, the free spectral range (FSR), needs to be narrower than the width of the spectral features. If this is not the case absorptions will be absent from the spectra. The FSR of the cavity, Δv, is dependent on the round trip time, t_r, of the light within the cavity:

$$\Delta v = \frac{1}{t_r} = \frac{c}{2l}$$

Equation 33

In an ideal case a single Lorentzian cavity mode would be excited, which would result in an exponential decay of the light intensity within the cavity. This is preferentially the lowest order transverse cavity mode (TEM_{00}). The beam entering the cavity has to have a Gaussian profile in order to exclusively excite the TEM_{00} mode and hence achieve a good exponential decay.

Non exponential decay may be caused by: i) multi mode excitation of higher order transverse modes, unless the losses per round trip are the same; and ii) transverse mode beating, which is the interference between modes with different frequencies and different decay rates [156]. These problems would result in inaccuracies in the ring-down time and absorption coefficients

To reduce the occurrence of non-exponential decay the transverse mode beatings are minimised by suppressing the higher order TEM modes, this is achieved by spatially matching the input laser beam to the TEM mode of the cavity. To achieve this, a Gaussian beam must be coupled into the cavity. The Gaussian beam can be obtained using a telescope and pinhole arrangement. The cavity needs to be aligned so that the laser couples to the beam waist of the cavity, *via* a coupling lens, following a parallel path. Several decay curves are usually obtained for each

wavelength and then averaged, which results in a decay curve generally unaffected by mode beating [168].

8.3.7 Sensitivity

The sensitivity of cavity ring-down spectroscopy is dependent upon many experimental conditions the main factor being the reflectivity of the mirrors. Higher reflectivity results in longer ring-down times, which in turn results in a greater ability to measure small changes in ring-down time [168]. Over time the mirrors can become contaminated with dirt or the sample, this reduces their reflectivity, however this can be minimised by a flow of a buffer gas. Other factors that must be taken into consideration are the quality of the optical components, the resolution of the detector electronics and the noise from the laser system and detector.

8.3.8 Applications

As this is a sensitive and general technique it is inevitable that it will have a large range of analytical applications. O'Keefe and Deacon were the first to apply the technique to environmental studies in atmospheric monitoring of trace gases. This has led to use as a detector in hostile environments such as plasmas and combustion [169]. An impressive application is that of Stanford, whereby radicals are probed (non-invasive) during diamond growth [166] [170].

Kinetic reaction studies have also made use of cavity ring-down spectroscopy [171]. It can be used for rate-constant determination and to obtain information on the mechanisms involved in the reactions studied by observing concentrations and lifetimes of radicals.

Cavity ring-down spectroscopy has been applied to a variety of molecular spectroscopic applications [156]. Due to its high sensitivity and the fact that it is a direct absorption technique it has been of great use in both vibrational and electronic spectroscopy.

As the technique becomes more widely used potential applications on a greater scale evolve. The agricultural use of ethylene for fruit ripening and medical breath testing applications are interesting examples of potentially large volume, but very low cost, instrumentation markets for ultra-trace-gas detection [172]. It is important to note that these schemes are still a long way from being both affordable and widely used.

8.4 Experimental

The overview of the experimental setup is shown in Figure 90. It consists of a pulsed dye laser system, the ring-down cavity, signal detection and processing electronics.

The second harmonic of a Nd:YAG laser (Continuum, Surelight I-10, pulse length 5 ns, repetition rate 10 Hz) was used to pump a dye laser (Sirah, Cobra stretch, dye: DCM in methanol: oscillator and pre-amplifier 300 mg/litre, amplifier bypassed, with a KD*P non-linear crystal for second harmonic generation and Pellin-Broca wave length separator). The accessible wavelength range of the doubled light was 301-330 nm with the pulse energy limited to ≤ 0.4 mJ at 320 nm by reducing the Nd:YAG pump power to avoid overload of the detector.
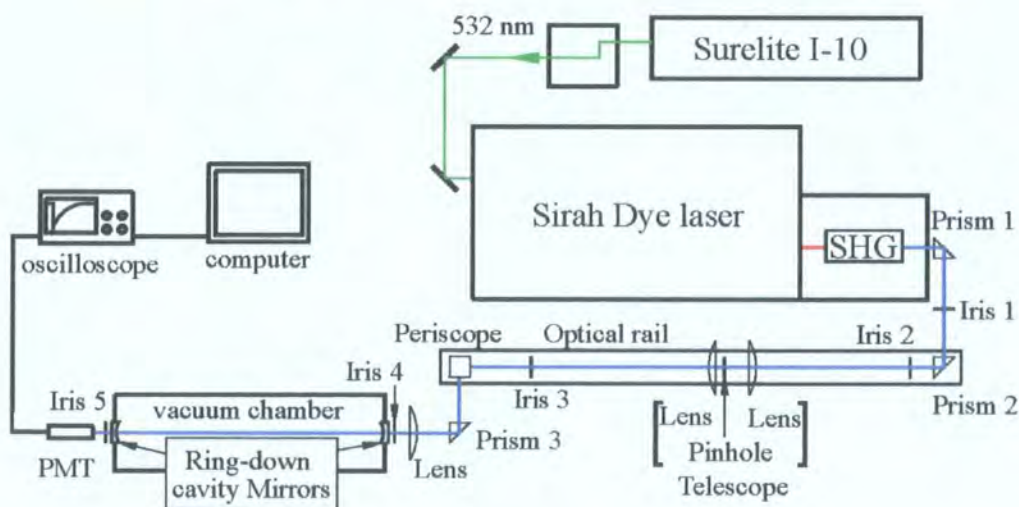
Figure 90: Schematic experimental set-up.

To ensure that the light entering the cavity had a Gaussian profile, the beam first passed through a spatial filter. This consisted of a lens (plano convex, 100mm), a pinhole (diameter 100 μm) and a second lens (plano convex, 50 mm). The height of the laser beam was lowered using a periscope to bring the beam in line with the cavity. The laser light was coupled into the TEM_{00} mode in order to minimise mode beating *via* a lens (focal length 750 mm for 550 nm light) mounted in an x-y adjustable lens holder. This was directly in front of the cavity, and the distance between the lens and first mirror was optimised for coupling the light into the cavity [135].

The ring-down cavity comprised of a stainless steel 6-way cross vacuum chamber (Boc Edwards 100/80 ISO-KF) between 2 mirrors with reflectivity of $\geq 99.9\%$ between 330 and 340 nm (Layertec, plano concave, R = 1 mm), and a diameter of 7.75 mm separated by approximately 77 cm.
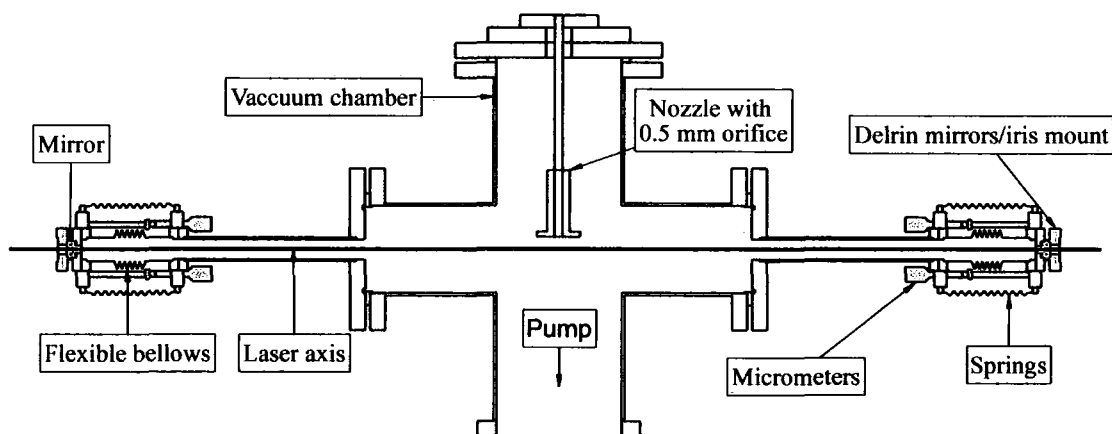
Figure 91: Cross section of vacuum chamber.

On the horizontal axis the cavity had extension tubes (80 ISO-K, DN16CF), ending with the mounted cavity mirrors. The mirrors were centred onto a CF 16 flange *via* a delrin mount which also centred irises to aid alignment. The mirror mount was fixed to flexible knife-edge bellows. The mirrors were finely adjusted *via* micrometer screws (Thorlabs), which were set-up to mimic kinematic optical mounts.

The chamber was evacuated to approximately 1×10^{-7} mbar by a diffusion pump (Boc Edwards CR1100/300, 230 ls^{-1}), backed by a rotary pump (Varian DS 202, 8.3 m^3 per hour). The diffusion pump was mounted on the lower section of the vertical axis (100 ISO-K). The pressure in the chamber was monitored using a Bayard-Alpert ionization gauge (Laybold, Ionivac ITR90).

The molecular beam was generated by a pulsed, unskimmed, nozzle (Parker Instrumentation, General Valve Series 9, 0.5 mm orifice, with IOTA ONE pulse driver) using argon as the carrier gas. The nozzle was operated between 4 and 5 bar; this produced a gas pulse approximately 200 µs in length.

A retractable fast ionisation gauge (Beam Dynamics Inc., FIG-1) was mounted on a linearfeed through in the horizontal section of the cavity, perpendicular to Figure 91. It was necessary to prevent the FIG from overloading as the nozzle was in close proximity (27-30 mm), therefore a shielding plate with a 1mm slit was mounted on the upper side of the FIG.

The chamber pressure was maintained below 5×10^{-4} mbar. The nozzle was mounted in the upper section of the vertical axis. In order to achieve good overlap of the molecular beam and laser, the nozzle was mounted so as to allow vertical adjustment of its position using an o-ring sealed feed through (Cajon, Ultra-Torr fitting). The horizontal adjustment was optimised by changing the position of the stage upon which the nozzle was mounted.

An oven was used to seed the Ar pulse with BPEB vapour. The argon gas pulse from the nozzle passed through the channel of the sample oven (see Figure 92). As the pulse passed through the oven BPEB vapour was caught in the exit channel and seeded into the pulse, which expanded and cooled after leaving the oven.
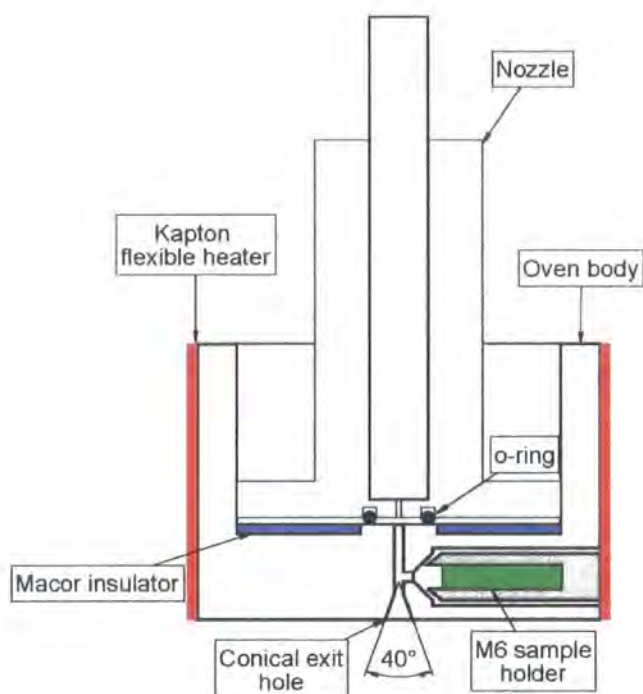
Figure 92: Cross section of the oven.

The sample oven is a copper cylinder with a central 1 mm diameter (exit) channel directly mounted to the nozzle, perpendicular to this was a second 1 mm diameter channel which leads to an M6 tapped bore in the side of the oven, this houses a hollow M6 screw used to hold the sample. A ceramic disk (Macor) reduces the thermal load on the nozzle from the oven, which is heated by a flexible heater (Omegalux, Kapton flexible heater). In order to prevent the sample channel from blocking, the oven had to be heated slowly over a period of two hours. A stable temperature of 145°C to 155°C was required to sublime sufficient BPEB to record spectra. The signal-to-noise ratio could be improved by increasing the temperature of the oven to over 160°C. This resulted in seeding the molecular beam with a higher concentration of BPEB. However this did mean that the BPEB was used at a greater rate, therefore the temperature could not be so high, in order to ensure the sample was not exhausted during the run. Lower temperatures (145°C to 155°C) resulted in a reduced, but maintainable, signal for typically a full day. A 3 mm deep 40° cone at the exit of the oven was used to spatially focus the beam expansion and enhance cooling, as suggested by Hillenkamp *et al.* [173]. The

angular distribution of the molecular beam was approximately 20° (FWHM), calculated from the size of BPEB deposits on the FIG shield.

The timing of the nozzle opening and laser firing to achieve overlap was obtained using a delay box (University of Bielefeld, Physics Department). Nozzle adjustment and monitoring of the molecular beam made it possible to produce a short intense pulse (FWHM of approximately 200 µs) and obtain the correct timing.

The transmitted light through the output mirror of the cavity was detected by a photomultiplier tube (Hamamatsu PMT: Model R 1463: Quantum efficiency: maximum 20% at 350 nm, 6% at 600 nm). In order to stop other light from reaching the detector it was mounted in a black Delrin cylinder. The PMT was coupled (50 Ω coupling) to a digitising oscilloscope (LeCroy, Waverunner LT584). This was then connected to a PC *via* a GPIB card (National Instruments). This allowed real time data transfer at the laser repetition rate (10 Hz). The PC ran a customised version of Lab VIEW (National Instruments) program, developed at the University of Bristol and adapted for current use.

8.5 Calibration

8.5.1 Introduction

It was necessary to calibrate the wavelength of the dye laser and to ensure that the calibration did not vary during a scan. In order to do this a room temperature iodine spectrum was acquired with the dye laser over the range 632-641 nm, (this range is doubled for use with BPEB). The spectrum was then compared to that from a simulation in order to asses the error inherent with the dye laser. The WI2 simulation package, developed by C. M Western of the University of Bristol [174], uses spectroscopic constants to simulate the iodine spectrum from the electronic transitions over the required wavelength range, thus allowing for comparison between the experimental and simulated spectra.

8.5.2 Experimental set-up

A variety of experimental set-ups were attempted to calibrate the laser. Problems with the noise level of the spectrum and computational analysis were overcome by using a set-up similar to that of the cavity ring-down experiment. The laser light was steered through irises, a telescope and a lens before entering the cavity. The six-way cross was replaced by a simpler metal tube. Iodine was placed in the cell with mirrors at each end mounted on the bellow arrangement as detailed in *section 8.4*. The mirrors used were highly reflective fused-silica, plano-concave mirrors (Layertec) with radius of curvature of 1 mm. The manufacturer specified their reflectivity as $\geq$ 99.98%, over the wavelength range 590-650 nm, with optimum reflectivity at 620 nm. The cell was evacuated using a rotary pump (Varian DS 202, pumping speed: 8.3 m^3 per hour). Flexible heaters (Omegalux) were wrapped around the cell and used to raise the temperature of the cell to 80-100 °C to produce iodine vapour. The PMT was used to detect the light escaping the cavity and set-up as detailed in experimental section.

8.5.3 Results

The WI2 simulation package has parameters that require alteration. These are the temperature and the Lorentzian and Gaussian contributions to the shape of the absorption peaks. This optimisation produced a simulation that fitted the experimental data very closely (Figure 93 and Figure 94).

The comparison shown in Figure 93 indicates that the dye laser calibration gives relative line positions to within $\pm$ 0.05 cm^{-1} and absolute line positions to between -0.15 and -0.31 cm^{-1}. This is within the stated calibration limits of the laser.
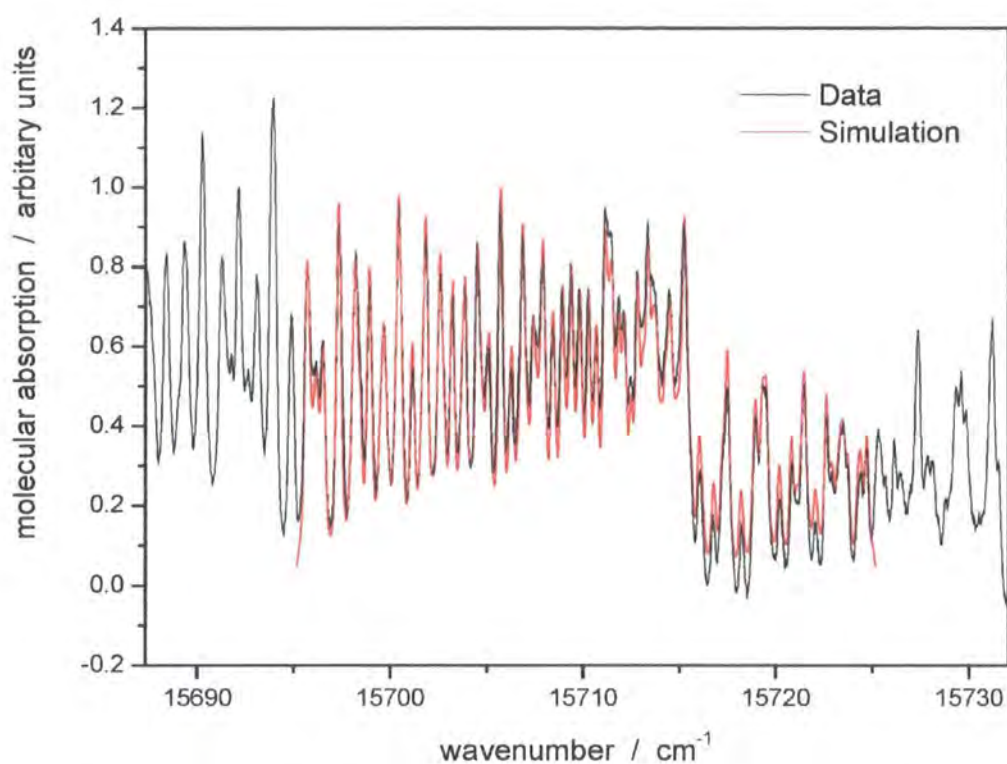
Figure 93: Comparison between simulation (red) and experimental (black) spectra of I_2. Close fit achieved using parameters: Offset: 0, Gaussian: 0.29, Lorentzian: 0, scaling factor:3, base: 0.06.
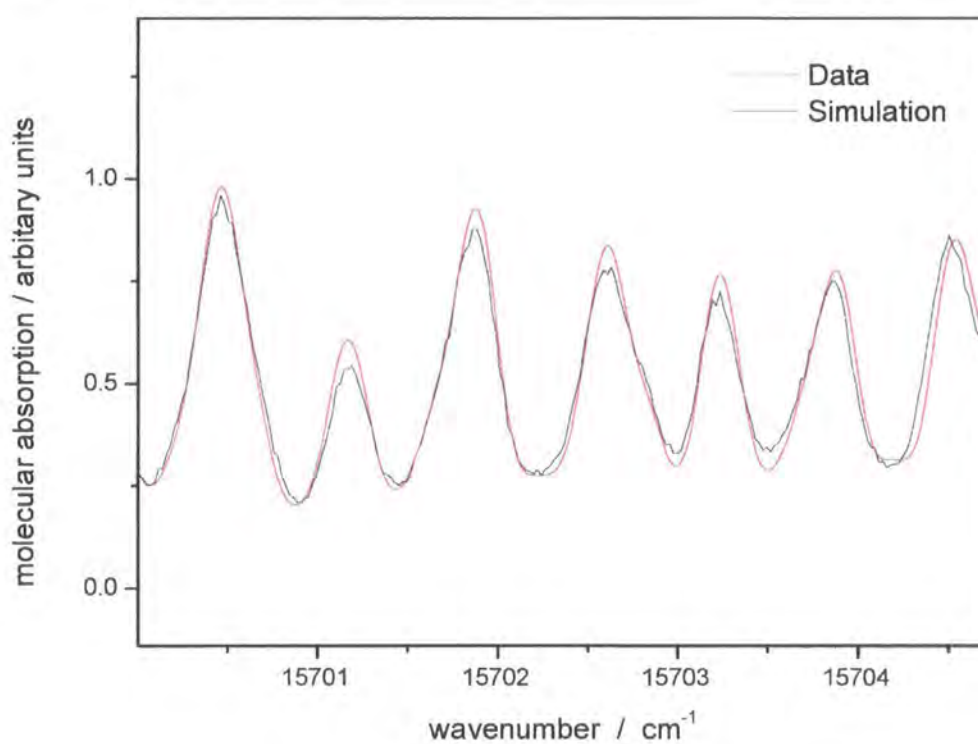
Figure 94: Shows overlap of individual peaks between simulation (red) and experimental (black).

8.6 Results

8.6.1 Obtaining a spectrum of BPEB

In order to obtain good quality reproducible spectra the necessary experimental conditions were optimised. The optimum required oven temperature was chosen as a balance between good signal to noise and the length of time a sample lasted. The maximum carrier gas backing pressure and therefore minimum beam temperature was limited by the pumping speed of the diffusion pump. A reduced cooling effect was seen when the pressure in the chamber was greater than 1×10^{-3} mbar.

Another important factor was the nozzle: a long-term temperature drift during the experiment would cause the nozzle to detune. The Teflon poppet within the nozzle was vital for producing a good quality pulse. A sharp stable pulse of FWHM $\cong 200$ µs was obtained with a good poppet, however experimental conditions could remain the same and an alternative poppet would produce broadened and variable 'hot' spectra. The unreliable poppets tended to deform greatly when used.

The optimum conditions were determined to be: oven temperature 145-155 °C; backing pressure 4-5 bar Ar; and a pulse length with FWHM $\cong 200$ µs. Figure 95 shows a comparison between 'hot' and 'cold' raw ring-down spectra. The peak heights indicate the torsional temperature, whilst the FWHM of the peaks correlates to the rotational temperature and the temperature of additionally excited vibrations. The spectra were reproducible, however, the peak height and shape varied from spectrum to spectrum due to variation in beam temperatures.
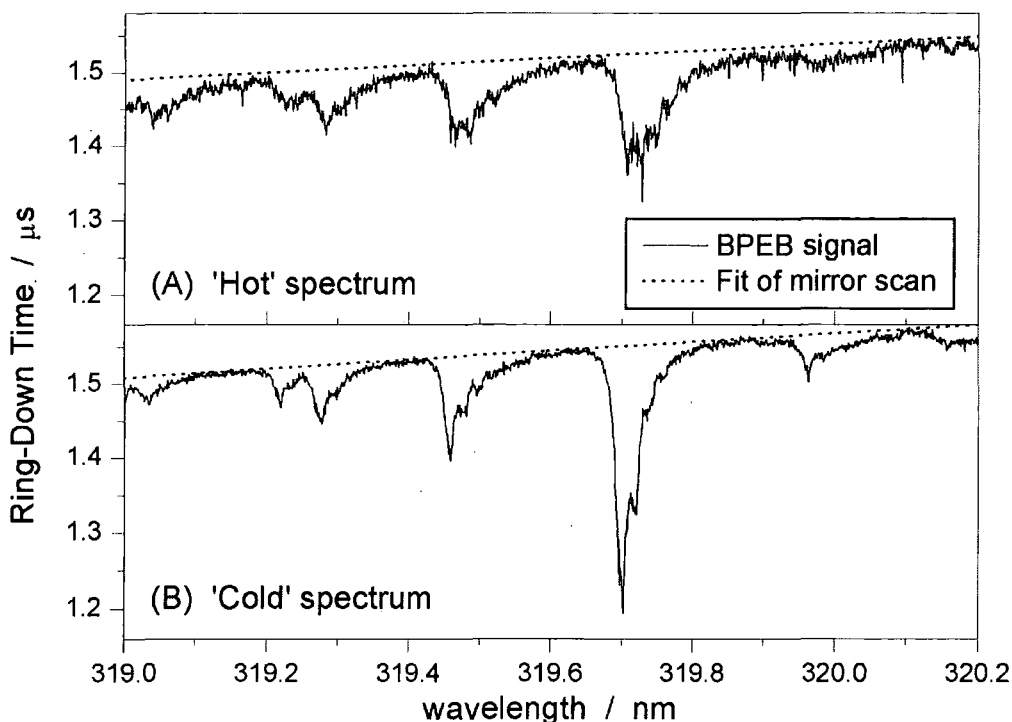
Figure 95: BPEB spectra of optimised and poor conditions; the dashed lines show the mirror scans taken with the nozzle mis-timed.

The spectra were recorded between wavelengths of 316-320.5 nm (Figure 96); at lower wavelengths the ring-down time was shorter and any transitions were indistinguishable from the noise. Higher wavelengths were studied, however, no further transitions were observed.

Different BPEB samples were used throughout the data collection, the spectra were reproducible and no features due to impurities were observed within the limits of experimental stability.
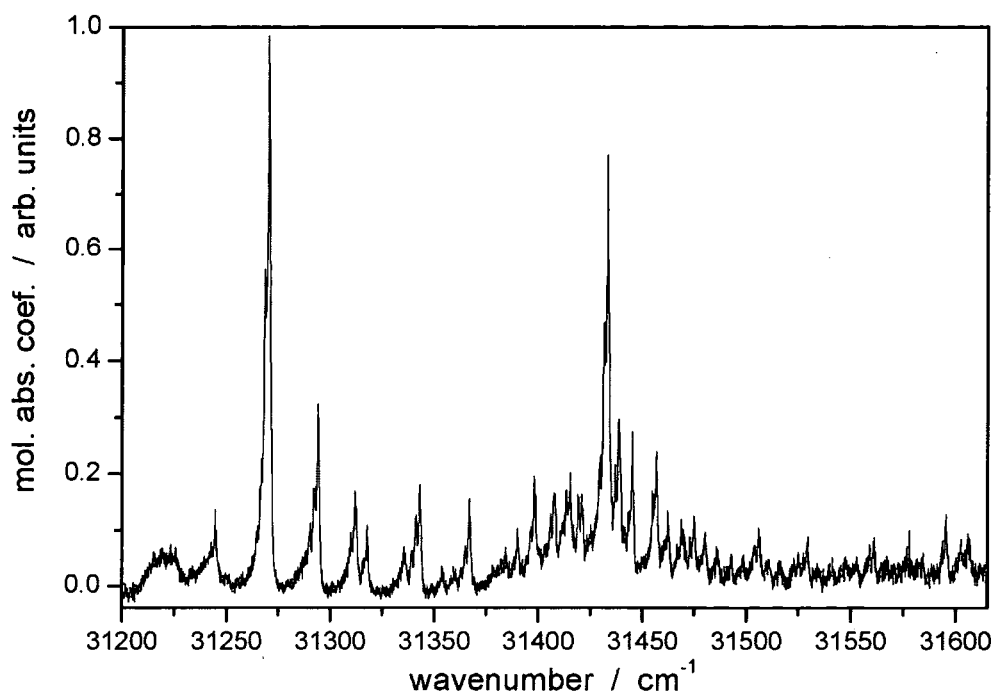
Figure 96: BPEB spectrum showing the full range covered by the experiment.

8.7 Discussion

8.7.1 Normal mode analysis

The first step in assigning the torsional transitions in the spectra was to work out which transitions are expected to be present, that is to say how BPEB twists. A technique produced by Zheng *et al.* [155] was designed for efficient and accurate prediction of the frequencies of the low frequency torsional twisting modes of poly(phenyleneethynylene). This method was used by S. J. Greaves in the analysis outlined in this section [135]. This method, known as 'lumped–inertia', simplifies the vibrational analysis by modelling each component ring as a rigid body with inertia equal to that of the ring and its attached hydrogens and any substituents present. The twisting modes are described as relative rotations of these lumped-inertias about the principal axis of BPEB, with adjacent inertias interacting with force constants, k.

This procedure reduces the higher frequency modes from the vibrational analysis. In doing so it reduces the vibration analysis from one of $3N - 6$ normal modes, where N is the number of atoms in the molecule, to $n - 1$ torsional modes, where n is the number of rings in the polyphenyl chain.

For a 3-ring linear oligomer, when all long-range coupling is considered, the equations of torsional motion (corresponding to the twist modes) are given in terms of the angular positions of each lumped inertia

$$\Rightarrow I_1\ddot{\theta}_1 = k^{(1)}(\theta_2-\theta_1)+k^{(2)}(\theta_3-\theta_1)$$

$(j = 1)$ **Equation 34**

$$\Rightarrow I_2\ddot{\theta}_2 = k^{(1)}(\theta_1-2\theta_2+\theta_3)$$

$(j = 2)$ **Equation 35**

$$\Rightarrow I_3\ddot{\theta}_3 = k^{(1)}(\theta_2-\theta_3)+k^{(2)}(\theta_1-\theta_3)$$

$(j = 3)$ **Equation 36**

Symbolically

$$\ddot{\vec{\theta}} = M\vec{\theta}$$

Equation 37

where θ_j is the angular trajectory of the j-th phenyl ring relative to its position at equilibrium and I_j is the moment of inertia of the j-th phenyl ring about the twist axis. $k^{(l)}$ is the torsional force constant between the target ring and its l-th nearest neighbour and M is a 3×3 matrix, as 3 rings are present in the molecule.

$$M = \frac{1}{I}\begin{bmatrix} -(k^{(1)}+k^{(2)}) & k^{(1)} & k^{(2)} \\ k^{(1)} & -2k^{(1)} & k^{(1)} \\ k^{(2)} & k^{(1)} & -(k_1+k_2) \end{bmatrix}$$

Equation 38

The solution to the symbolic equation above can be written in the form

$$\vec{\theta} = \vec{C}e^{i\omega t}$$

Equation 39

where $\vec{C}$ is a vector of coefficients, $i = (-1)^{1/2}$, t is time, and ω is a vibrational angular frequency. It follows that:

$$M\vec{C} = -\omega^2 \vec{C}$$

Equation 40

By solving this eigenvalue problem the eigenvalues, $-\omega^2$, and eigenvectors are obtained in terms of force constants $k^{(1)}$, $k^{(2)}$ and moment of inertia I_j.

Table 10: Eigenvalues and eigenvectors.

Name	Eigenvalue $-\omega^2$	Eigenvectors C_1	C_2	C_3
Rotation	0	1	1	1
Anti-symmetric	$-\dfrac{k^{(1)} + 2k^{(2)}}{I_{outer}}$	-1	0	1
Symmetric	$-\dfrac{k^{(1)}(2I_{outer} + I_{inner})}{I_{inner}I_{outer}}$	1	$-\dfrac{2I_{outer}}{I_{inner}}$	1

Where I_{outer} is the moment of inertia of the outer most phenyl rings and I_{inner} that of the central ring. $k^{(1)}$ is the force constant between a ring and its nearest neighbour and $k^{(2)}$ that of a ring and its next nearest neighbour.

The eigenvalue of zero corresponds to free rotation of the entire molecule around its axis. The motion of the rings in the anti-symmetric and symmetric modes are shown in Figure 97 and Figure 98 .
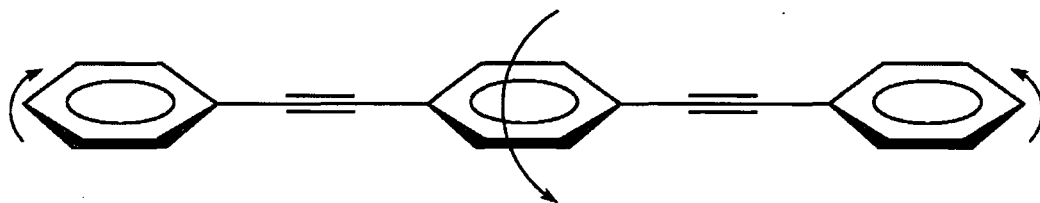
Figure 97: Symmetric normal mode twist of BPEB.

Figure 98: Anti-symmetric normal mode twist of BPEB.

8.6.2 Comparison with Deuterated BPEB

A method of distinguishing the torsional transitions is to compare the spectrum with that of an equivalent molecule with isotopic substitution. The molecule used for this was 1, 4-bis(phenylethynyl)-2,3,5,6-tetradeuterobenzene, BPEB with the hydrogens on the central ring replaced by deuteriums (DBPEB). As deuterium has a higher mass than hydrogen all of the transitions involving the central ring will be affected and will change position in the spectra. Figure 99 shows the comparison of a BPEB spectrum with a DBPEB spectrum.
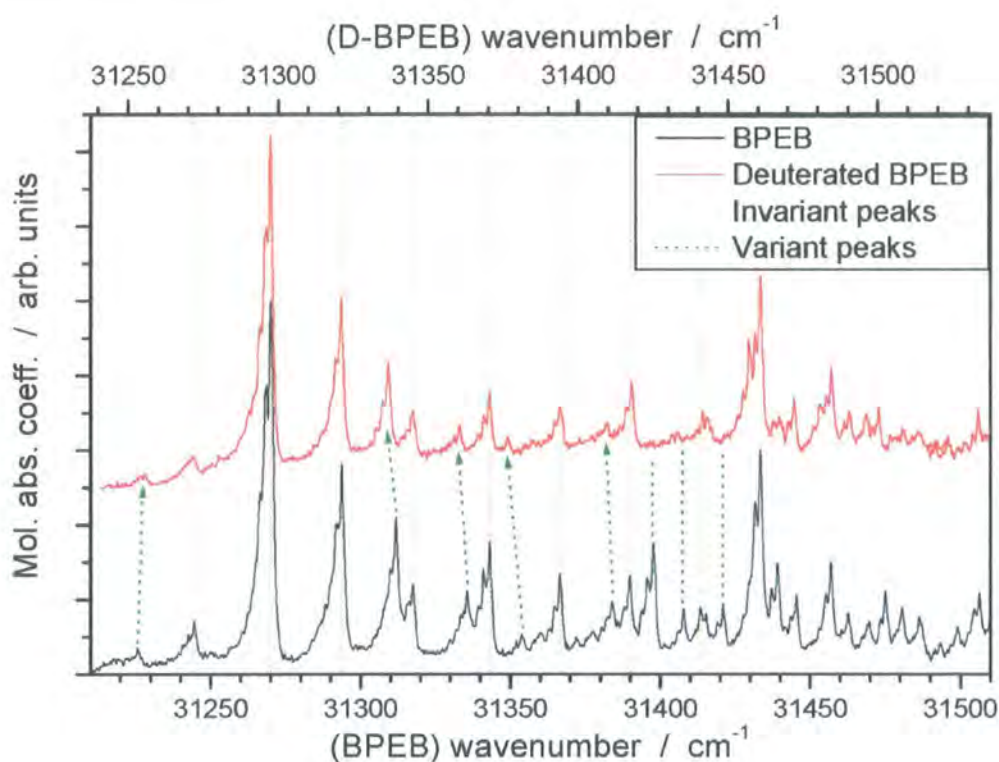
Figure 99: Spectra of BPEB and DBEP, the DBPEB has been shifted on the x-axis so that the band heads of both spectra line up and has been shifted on the y-axis for ease of comparison.

8.8.3 Assigning spectra

The largest peak in the spectra can automatically be assigned as the $00 \leftarrow 00$ band, $v_s' v_{as}' \leftarrow v_s'' v_{as}''$, where v is the torsional quantum number (the subscript corresponds to symmetric and antisymmetric torsions in the ground and excited state). The $00 \leftarrow 00$ band has the highest population and the greatest Franck-Condon factor, giving it the largest line strength. It is not possible to assign all the peaks using combination differences, as this would require knowledge of the ground state and excited state potential. The comparison of the spectra due to BPEB and DBPEB allows for the peaks related to the symmetric twist to be separated from those due to the anti-symmetric.

The difference between the symmetric and anti-symmetric modes is the motion of the central ring, which only moves in the symmetric twist (Figure 100). When the hydrogens on this central ring are replaced by deuterium, only the bands arising

from the twisting of the middle ring will appear altered. All the peaks due to the symmetric twist will move in the spectra of DBPEB compared with BPEB, and those due to the anti-symmetric twist will remain in the same position as this twist remains unaltered.
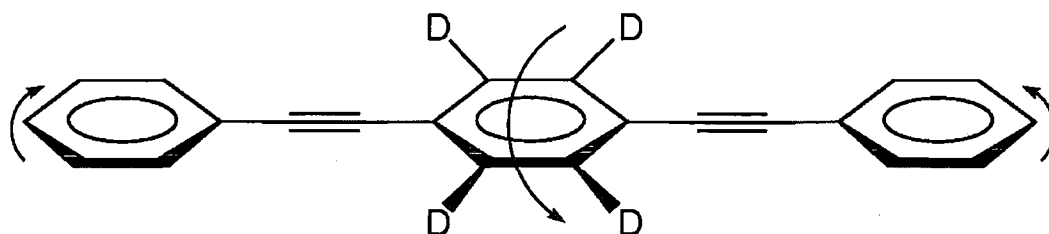
Figure 100: Symmetric twist of DBPEB.

A comparison of the two spectra can be seen in Figure 99. The green lines show which peaks have moved, *i.e.* which peaks are due to the symmetric twist, and the yellow lines show those due to the anti-symmetric twists. The two hot bands to the left of the $00 \leftarrow 00$ band were assumed to correspond to the $0 \leftarrow 2$ transitions, the separation from the $0 \leftarrow 0$ and $0 \leftarrow 2$ bands corresponds to the harmonic vibrational constant, $2\nu_e$, for each twisting mode (Figure 101).
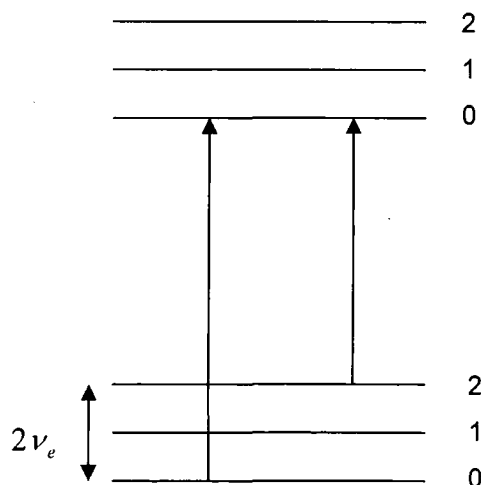
Figure 101: Separation from the $0 \leftarrow 0$ and $0 \leftarrow 2$ bands corresponds to $2\nu_e$.

By assigning these bands, an approximation of the ground state potential can be determined. The value for ν_e can be used to calculate the force constant for a nearest neighbour ring twist as detailed below. These values can then be input into

a simulation programme in order to simulate the spectra and so gain the full assignment of the spectra.

8.7.4 Simulation program

The simulation program (developed by Dr E. Wrede) was developed from a simple periodic potential:

$$V(\theta) = \frac{1}{2}V_{max}(1 - \cos 2\theta)$$

Equation 41

Where V_{max} is the torsional barrier height and θ is the ring to ring angle. The force constant comes from the harmonic potential $V(\theta) = \frac{1}{2}k\theta^2$ and can be related to V_{max} through the second coefficient of the Taylor expansion of the simple periodic potential.

$$V(\theta) = \frac{1}{2}V_{max}(2\theta^2) = V_{max}\theta^2$$

Equation 42

V_{max} can be calculated from the force constant governing the interaction from

$$V_{max} = \frac{1}{2}k$$

Equation 43

using the value for v_e obtained from the experimental spectra, the force constant k, for a nearest neighbour twist can be calculated using:

$$v_e = \frac{1}{2\pi}\sqrt{\frac{k}{I_{red}}}$$

Equation 44

the ground state potential is determined by the relative position of the two hot bands $(2 \leftarrow 0)$ with respect to the $00 \leftarrow 00$ origin.

The analysis treats the symmetric twist and anti-symmetric twists independently, thus in order to determine the energy of the potential they must be combined:

$$E(\upsilon_{as}, \upsilon_s) = h\upsilon_e^{as}\left(\upsilon_{as} + \frac{1}{2}\right) + h\upsilon_e^s\left(\upsilon_s + \frac{1}{2}\right)$$

Equation 45

The excited state energy levels are more widely spaced than those of the ground state. In the ground state of BPEB the bonding can be assumed to have alkyne character. However, in the excited state it has more double bond character. This acts to hinder the twisting, hence increasing the torsional potential. The excited state potentials were assumed to have barrier heights about eight times those of the ground state as was found with tolane [155].
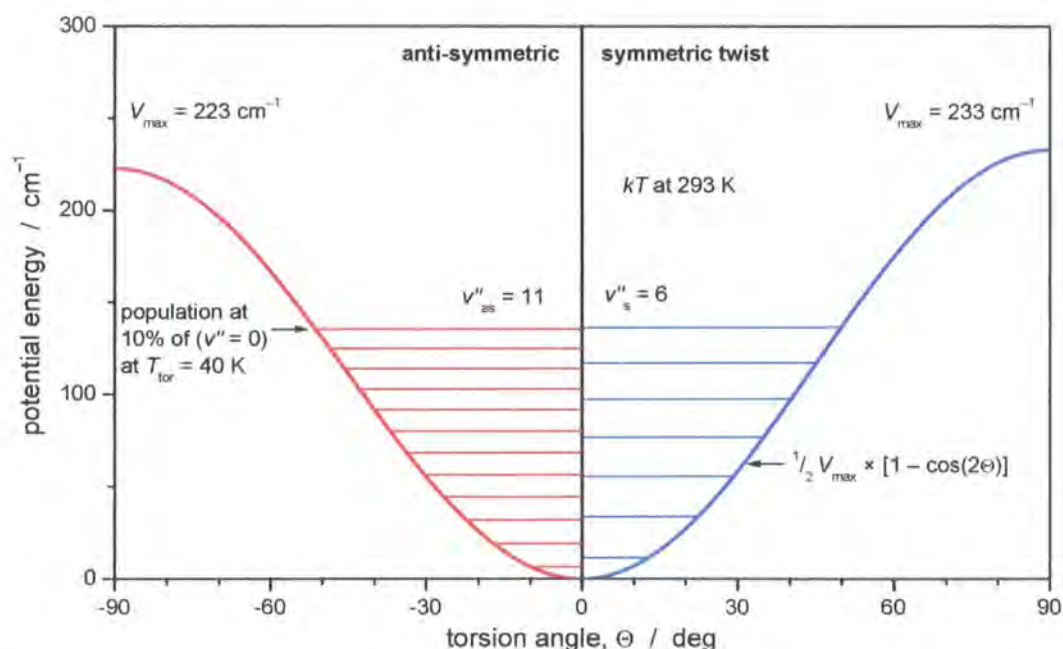
Figure 102: Potential curve of ground state BPEB showing barrier height and energy levels.

The values of V_{max} obtained were 222.8 cm^{-1} for the anti-symmetric and 232.7 cm^{-1} for the symmetric twist. V_{max} does not represent the actual barrier height as the spectrum is only sensitive to the lower third of the potential, it does

however, give the shape of this part of the potential. The difference between the anti-symmetric and symmetric shapes occurs as the anti-symmetric twist has an additional force constant ($k^{(2)}$) from the interaction of next nearest neighbour.

The simulation was optimised by varying the scaling factors of the upper states and the torsional temperature. These values created a simulation that was a good fit to the experimental data for the first part of the spectra. It was necessary to add an additional torsional progression, which can be seen in Figure 103 as black horizontal ladders. These progressions may be due to other lower frequency vibrational modes but this is not certain.

A comparison of experimental (black lines) and simulated (red lines) spectra for BPEB and DBPEB is displayed in Figure 103. An offset has been added to the experimental spectra to aid comparison
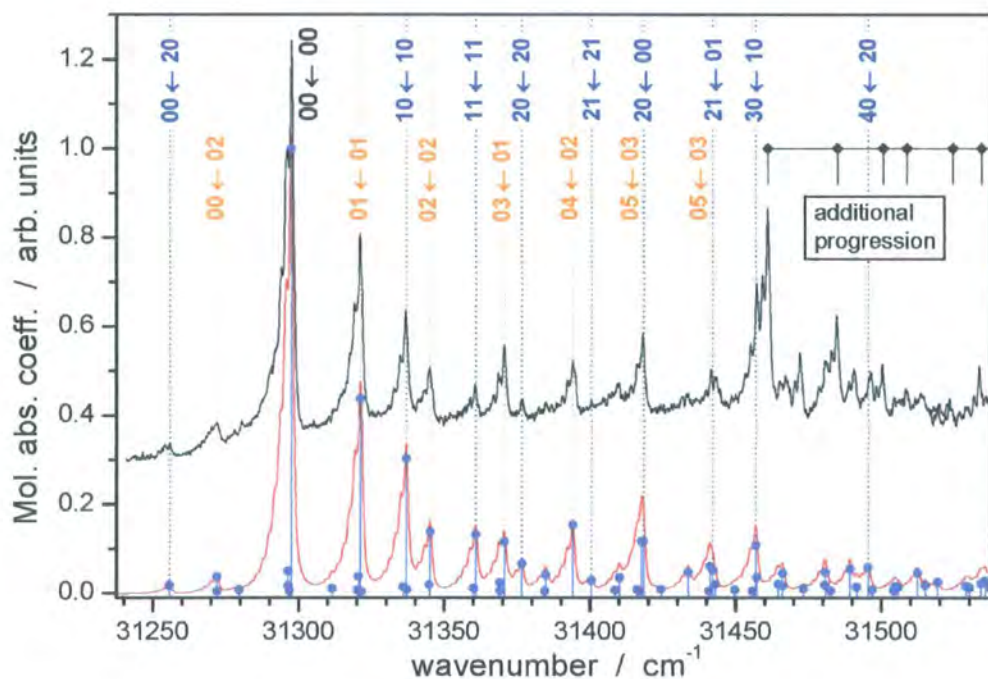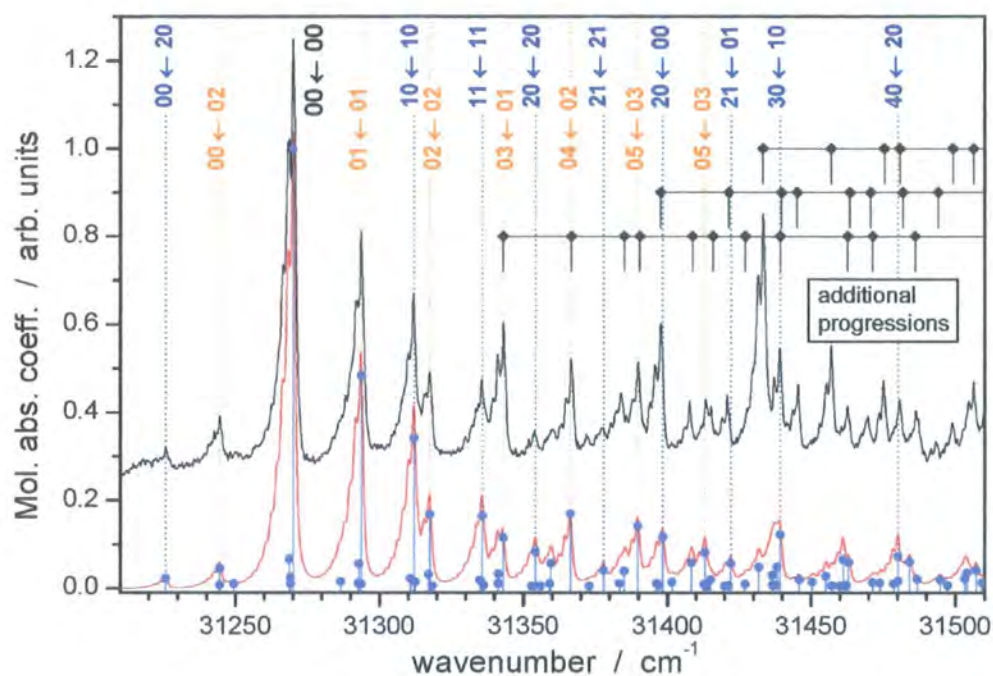
Figure 103: Upper: experimental and simulated spectra of BPEB. Lower: experimental and simulate spectra of DBPEB. The transitions of the main torsional progression are shown as vertical sticks with intensities shown by points. The most intense progressions are labeled in blue and orange ($\nu_s' \nu_{as}' \leftarrow \nu_s'' \nu_{as}''$), where orange are pure anti-symmetric transitions and blue are transitions with symmetric contributions. The locations of additional torsional

progressions originating from other vibrational modes are shown with combs starting at position of the 00 ← 00 transition.

8.8 Conclusion

Cavity ring-down spectroscopy has been used to study BPEB and DBPEB. High-resolution absorption spectra of jet-cooled BPEB and DBPEB have been obtained. The individual torsional transitions within the $\pi^* \leftarrow \pi$ electrical transition have been identified. Spectral lines resulting from the symmetric twisting mode were identified by isotopic substitution of the hydrogens on the central ring (DBPEB).

A simple periodic potential was used in order to simulate both the BPEB and the DBPEB spectra. In order to completely simulate the spectra it was necessary to add extra torsional progressions possibly resulting from low frequency vibrational modes. The simulation produced had excellent overlap with the experimental findings and provided full analysis of the spectrum.

The torsional potential barrier height has been found to be 220-235 cm^{-1}. However, the recorded spectra are only sensitive to the bottom third of the potential. Therefore this value does not represent the true height, but does define the shape of the lower section of the potential.

This torsional barrier height is just above kT at room temperature (207 cm^{-1}). As such, a proportion of the BPEB molecules in the sample will have sufficient energy to overcome the barrier leading to hindered rotation of the rings. The shallow torsional ground state potential results in most molecules reaching twist angles that will severely disrupt the conjugation along the molecule and hence affect the conductivity. As such, BPEB does not work as a molecular wire at room temperature.

8.9 Future work

A logical progression of this work would be to test the validity of the model using isotopic substitution, for example perfluoronated BPEB. This could be used to study the effect of electron withdrawing groups on the torsional motions of the molecule.

Another possible development would be to study BPEB with bulky substituents such as the one in the Figure 104. This would enable investigations into how the steric interactions affect the torsional motions. This molecule is of particular interest because it may have implications for the design of molecular switches due to the fact that the ground state corresponds to the geometry whereby the outer rings are twisted at 90° compared to the inner ring. The ground state potential minimum corresponds to the excited state maximum which means that the excited state minimum is the planar geometry [175]. As, such this molecule would be an ideal candidate for investigating molecular switching.
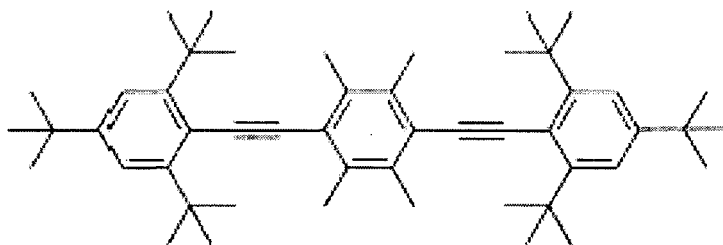
Figure 104: 1, 4-bis(2,4,6-tritertbutylphenylethynyl)-2,3,5,6-tetramethylbenzene

Bibliography

1. F. J. Aoiz, L. Banares, and V. J. Herrero, *Int. Rev. Phys. Chem.*, 2005. **24**, 119.

2. E. Wrede, L. Schnieder, K. Seekamp-Schnieder, B. Niederjohann, and K. H. Welge, *Phys. Chem. Chem. Phys.*, 2005. **7**, 1577.

3. B. J. McCall and T. Oka, *Science*, 2000. **287**, 1941.

4. T. R. Geballe and T. Oka, *Nature*, 1996. **384**, 334.

5. B. J. McCall, T. R. Geballe, K. H. Hinkle, and T. Oka, *Science*, 1998. **279**, 1910.

6. T. Oka, T. R. Geballe, M. Goto, T. Usuda, and B. J. McCall, *Astrophys. J.*, 2005. **632**, 882.

7. S. Miller, N. Achilleos, G. E. Ballester, T. R. Geballe, R. D. Joseph, R. Prange, D. Rego, T. Stallard, J. Tennyson, L. M. Trafton, and J. Hunter Waite Jr, *Phil. Trans. R. Soc. Lond. A.*, 2000. **385**, 2485.

8. E. Herbst and W. Klemperer, *Astrophys. J.*, 1973. **185**, 505.

9. J. E. P. Connerney, R. Baron, T. Satoh, and T. Owen, *Science*, 1993. **262**, 1035.

10. J. G. Wang and P. C. Stancil, *Phys. Scr.*, 2002. **T96**, 72.

11. A. Dalgarno, J. Weisheit, and J. Black, *Astrophysical Letters*, 1973. **14**, 77.

12. P. C. Stancil, S. Lepp, and A. Dalgarno, *Astrophys. J.*, 1998. **509**, 1.

13. B. R. Strazisar, C. Lin, and H. F. Davis, *Phys. Rev. Lett.*, 2001. **86**, 3997.

14. S. Badiei and L. Holmlid, *Mon. Not. R. Astron. Soc.*, 2002. **333**, 360.

15. F. Claeyssens, R. J. Lade, K. N. Rosser, and M. N. R. Ashfold, *J. App. Phys.*, 2001. **89**, 697.

16. M. Matsuzawa, *Rydberg States of Atoms and Molecules*, ed. R. F. Stebbings and F. D. Dunning. 1983: Cambridge University Press.

17.   L. Schnieder, K. Seekamp-Rahn, E. Wrede, and K. H. Welge, *J. Chem. Phys.*, 1997. **107**, 6175.

18.   S. P. Renwick, F. Deng, H. Martinez, and T. J. Morgan, *Phys. Rev. A.*, 1993. **47**, 1907.

19.   E. Fermi, *Nuovo Cimeno*, 1934. **11**, 157.

20.   E. Amaldi and E. Segre, *Nuovo Cimeno*, 1934. **11**, 145.

21.   P. M. Dehmer and W. A. Chupka, *J. Phys. Chem.*, 1995. **99**, 1686.

22.   F. B. Dunning and R. F. Stebbings, *Rydberg States of Atoms and Molecules*, ed. R. F. Stebbings and F. B. Dunning. 1983: Cambridge University Press.

23.   P. M. Koch, *Phys. Rev. Lett.*, 1979. **43**, 432.

24.   L. J. Wang, M. King, and T. J. Morgan, *J. Phys. B: Atom. Molec. Phys.*, 1986. **19**, L623.

25.   F. B. Dunning, *J. Phys. B: At. Mol. Opt. Phys.*, 1995. **28**, 1645.

26.   C. A. Kocher and A. J. Smith, *Phys. Rev. Lett.*, 1977. **39**, 1516.

27.   J. Boulmer, G. Baran, F. Devos, and J. F. Delpech, *Phys. Rev. Lett.*, 1980. **44**, 1122.

28.   A. Pesnelle, C. Ronge, M. Perdrix, and G. Watel, *Phys. Rev. A.*, 1986. **34**, 5146.

29.   A. Pesnelle, C. Ronge, M. Perdrix, and G. Watel, *Phys. Rev. A.*, 1990. **42**, 273.

30.   M. Brouard, *Reaction Dynamics*. Oxford Chemistry Primers, ed. R. G. Crompton. 1998: Oxford University Press.

31.   J. Geddes, H. F. Krause, and W. L. Fite, *J. Chem. Phys.*, 1972. **56**, 3298.

32.   R. Gotting, H. R. Mayne, and J. P. Toennies, *J. Chem. Phys.*, 1986. **85**, 6396.

33.   S. A. Buntin, C. Giese, and W. R. Gentry, *J. Chem. Phys.*, 1987. **87**, 1443.

34.   E. Wrede and L. Schnieder, *J. Chem. Phys.*, 1997. **107**, 786.

35.   E. Wrede, L. Schnieder, K. H. Welge, F. J. Aoiz, L. Banares, J. F. Castillo, B. Martinez-Haya, and V. J. Herrero, *J. Chem. Phys.*, 1999. **110**, 9971.

36. L. Banares, F. J. Aoiz, V. J. Herrero, M. J. D'Mello, B. Niederjohann, K. Seekamp-Rahn, E. Wrede, and L. Schnieder, *J. Chem. Phys.*, 1998. **108**, 6160.

37. D. Dai, C. C. Wang, S. A. Harich, X. Wang, X. Yang, S. D. Chao, and R. T. Skodje, *Science*, 2003. **300**, 1730.

38. S. D. Chao, S. A. Harich, D. X. Dai, C. C. Wang, X. Yang, and R. T. Skodje, *J. Chem. Phys.*, 2002. **117**, 8341.

39. S. A. Harich, D. Dai, C. C. Wang, X. Yang, S. D. Chao, and R. T. Skodje, *Nature*, 2002. **419**, 281.

40. R. T. Skodje and X. Yang, *Int. Rev. Phys. Chem.*, 2004. **23**, 253.

41. D. Gerlich and S. Schlemmer, *Planet. Space Sci.*, 2002. **50**, 1287.

42. D. Smith and N. G. Adams, *Adv. At. Mol. Phys.*, 1988. **24**, 1.

43. H. Bohringer, W. Glebe, and F. Arnold, *J. Phys. B: At. Mol. Phys.*, 1983. **16**, 2619.

44. B. R. Rowe, J. B. Marquette, G. Dupeyrat, and E. E Ferguson, *Chem. Phys. Lett.*, 1985. **113**, 403.

45. I. W. M. Smith and B. R. Rowe, *Acc. Chem. Res.*, 2000. **33**, 261.

46. M. A. Smith, *Int. Rev. Phys. Chem.*, 1998. **17**, 35.

47. G. Ochs and E. Teloy, *J. Chem. Phys.*, 1974. **61**, 4930.

48. E. Teloy and D. Gerlich, *Chem. Phys.* , 1974. **4**, 417.

49. J. R. Krenos and R. Wolfgang, *J. Chem. Phys.*, 1970. **52**, 5961.

50. J. R. Krenos, R. K. Preston, R. Wolfgang, and J. C. Tully, *J. Chem. Phys.*, 1974. **60**, 1634.

51. K. L. Wendell and P. K. Rol, *J. Chem. Phys.*, 1974. **61**, 2059.

52. D. Gerlich, E. Herbst, and E. Roueff, *Planet. Space Sci.*, 2002. **50**, 1275.

53. M. J. Henchman, N. G. Adams, and D. Smith, *J. Chem. Phys.*, 1981. **75**, 1201.

54. H. Villinger, M. J. Henchman, and W. Linderger, *J. Chem. Phys.*, 1982. **76**, 1590.

55. D. Gerlich, *Inhomogeneous Electrical Radio Frequency Fields: A Versatile Tool for the Study of Processes with Slow Ions" in: State-Selected and State-to-State Ion-Molecule Reaction Dynamics.* Advances in Chemical Physics Series, LXXXII, ed. C. Y. Ng. and M. Baer. 1992: J. Wiley & Sons.

56. D. Dai, C. C. Wang, G. Wu, S. A. Harich, H. Song, M. Hayes, R. T. Skodje, X. Wang, D. Gerlich, and X. Yang, *Phys. Rev. Lett.*, 2005. **95**, 013201.

57. D. Gerlich, *Ph.D. thesis.* 1977, University of Freiburg.

58. H. Song, D. Dai, G. Wu, C.C. Wang, S. A. Harich, M. Hayes, X. Wang, D. Gerlich, X. Yang, and R. T. Skodje, *J. Chem. Phys.*, 2005. **123**, 074314.

59. M. Y. Hayes and R. T. Skodje, *J. Chem. Phys.*, 2007. **126**, 104306.

60. T. Gonzales-Lezana, A. Aguado, M. Paniagua, and O. Roncero, *J. Chem. Phys.*, 2005. **123**, 194309.

61. R-F. Lu, T-S. Chu, and K-L. Han, *J. Phys. Chem. A.*, 2005. **109**, 6683.

62. A. Aguado, O. Roncero, C. Tablero, C. Sanz, and M. Paniagua, *J. Chem. Phys.*, 2000. **112**, 1240.

63. W. Kutzelnigg and R. Jaquet, *Phil. Trans. R. Soc. Lond. A.*, 2006. **364**, 2855.

64. H. Eyring and M. Polanyi, *Phys. Chem. Abt.*, 1931. **12**, 279.

65. J. O. Hirschfelder, H. Eyring, and B. Topley, *J. Chem. Phys.*, 1936. **4**, 178.

66. F. J. Aoiz, L. Banares, and V. J. Herrero, *J. Chem. Soc., Faraday Trans.*, 1998. **94**, 2483.

67. E. J. Rackham, T. Gonzales-Lezana, and D. E. Manolopoulos, *J. Chem. Phys.*, 2003. **119**, 12859.

68. E. J. Rackham, F. Huarte-Larranaga, and D. D. Manolopoulos, *Chem. Phys. Lett.*, 2001. **343**, 356.

69. P. Honvault and J-M. Launay, *J. Chem. Phys.*, 1999. **111**, 6665.

70. P. Honvault and J-M. Launay, *J. Chem. Phys.*, 2001. **114**, 1057.

71. E. Carmona-Novillo, T. Gonzales-Lezana, O. Roncero, P. Honvault, J-M. Launay, N. Bulut, F.J. Aoiz, L. Banares, A. Trottier, and E. Wrede, *J. Chem. Phys.*, 2008. **128**, 014304.

72.   T. Gonzales-Lezana, O. Roncero, P. Honvault, J-M. Launay, N. Bulut, F. J. Aoiz, and L. Banares, *J. Chem. Phys.*, 2006. **125**, 094314.

73.   D. W. Chandler and P. L. Houston, *J. Chem. Phys.*, 1987. **87**, 1445.

74.   T. H. Bull and P. B. Moon, *Discuss. Faraday. Soc.*, 1954. **17**, 54.

75.   E. H. Taylor and S. Datz, *J. Chem. Phys.*, 1955. **23**, 1711.

76.   A. Casavecchia, *Rep. Prog. Phys.*, 2000. **63**, 355.

77.   W. H. Rodebush and W. F. Henry, *Phys. Rev.*, 1932. **39**, 386.

78.   J. H. Birely and D. R. Herschbach, *J. Chem. Phys.*, 1965. **44**, 1690.

79.   Y. T. Lee, J. D. McDonald, P. R. LeBreton, and D. R. Herschbach, *Rev. Sci. Instrum.*, 1969. **40**, 1402.

80.   S. Datz and E. H. Taylor, *J. Chem. Phys.*, 1963. **39**, 1896.

81.   W. L. Fite and R. T. Brackmann, *J. Chem. Phys.*, 1965. **42**, 4057.

82.   G. Wessel and H. Lew, *Phys. Rev.*, 1953. **92**, 641.

83.   G. O. Brink, *Rev. Sci. Instrum.*, 1966. **37**, 857.

84.   J. H. Birely and D. R. Herschbach, *J. Chem. Phys.*, 1966. **44**, 1690.

85.   A. Schultz, H. W. Cruse, and R. N. Zare, *J. Chem. Phys.*, 1972. **57**, 1354.

86.   R. N. Zare and P. J. Dagdigian, *Science*, 1974. **185**, 739.

87.   K. Liu, *J. Chem. Phys.*, 2006. **125**, 132307.

88.   D. M. Neumark, A. M. Wodtke, G. N. Robinson, C. C. Hayden, K. Shobatake, R. K. Sparks, T. P. Schafer, and T. T. Lee, *J. Chem. Phys.*, 1984. **82**, 3067.

89.   D. P. Gerrity and J. J. Valentini, *J. Chem. Phys.*, 1983. **79**, 5202.

90.   E. E. Marinero, C. T. Rettner, and R. N. Zare, *J. Chem. Phys.*, 1984. **80**, 4142.

91.   A. V. Dahv, D. E. Adelman, and R. N. Zare, *J. Chem. Phys.*, 1990. **94**, 1069.

92.   D. R. Herschbach, *Chem. Scr.*, 1987. **27**, 327.

93.   J. C. Polanyi, *Chem. Scr.*, 1987. **27**, 228.

94.   Y. T. Lee, *Science*, 1987. **236**, 793.

95.   W. C. Wiley and McLaren, *Rev. Sci. Instrum.*, 1955. **26**, 1150.

96.   J. Solomon, *J. Chem. Phys.*, 1967. **47**, 889.

97.   C. Vallance, *Phil. Trans. R. Soc. Lond. A.*, 2004. **362**, 2591.

98.   A. T. B. Eppink and D. H. Parker, *Rev. Sci. Instrum.*, 1997. **68**, 3477.

99.   H. L. Offerhaus, C. Nicole, F. Lepine, C. Bordas, F. Rosca-Pruna, and M. J. J. Vrakking, *Rev. Sci. Instrum.*, 2001. **72**, 3245.

100.   C. R. Gebhardt, T. P. Rakitzis, P. C. Smartzis, V. Ladopouloud, and T. N. Kitsopoulous, *Rev. Sci. Instrum.*, 2001. **72**, 3848.

101.   D. Townsend, M. P. Minitti, and A. G. Suits, *Rev. Sci. Instrum.*, 2002. **74**, 2530.

102.   B. Chang, R. C. Hoetzlein, J. A. Geiser, and P. L. Houston, *Rev. Sci. Instrum.*, 1998. **69**, 1665.

103.   W. Li, S. D. Chambreau, S. A. Lahankar, and A. G. Suits, *Rev. Sci. Instrum.*, 2005. **76**, 3106.

104.   R. T. Dillon and W. G. Young, *J. Am. Chem. Soc.*, 1929. **51**, 2389.

105.   R. Lipson, *An introduction to Laser Spectroscopy.* 2nd ed, ed. Andrews and Demidov. 2002, New York: Kluwer Academic/Plenum Publishers.

106.   A. Heath, *4th Year Project Report.* 2006, Durham University.

107.   E. Wrede, S. Laubach, S. Schulenburg, A. Brown, R. E. Wouters, A. J. Orr-Ewing, and M. N. R. Ashfold, *J. Chem. Phys.*, 2001. **114**, 2629.

108.   D. Zhang, A. Abdel-hafiez, and B. Zhang, *Chem. Phys.*, 2007. **342**, 119.

109.   A. B. Aleksey, H-P. Liebermann, D. B. Kokh, and R. J. Buenker, *J. Chem. Phys.*, 2000. **113**, 6174.

110.   P. M. Regan, D. Ascenzi, C. Clementi, M. N. R. Ashfold, and A. J. Orr-Ewing, *Chem. Phys. Lett.*, 1999. **315**, 187.

111.   N. Balakrishnan, A. B. Alekseyev, and R. J. Buenker, *Chem. Phys. Lett.*, 2001. **341**, 594.

112.   R. S. Mulliken, *Phys. Rev.*, 1936. **51**, 310.

113. R. N. Zare, *Photo. Chem.*, 1972. **4**, 1.

114. Y. Sato, Y. Matsumi, M. Kawasaki, K. Tsukiyama, and R. Bersohn, *J. Chem. Phys.*, 1995. **99**, 16307.

115. K. P. Huber and G. Herzberg, *Electronic spectra and electroin structure of polyatomic molecules*. Vol. 4. 1979: Van Nostrand Reinhold Company.

116. C. Moore, *Atomic energy levels*. Nat. Stand. Ref. Data: Ser. Bur. Stand. Vol. 35. 1971, US.

117. E. Wrede, *Ph.D. Thesis*. 1998, Universitata Bielefeld.

118. T. P. Softley, *Int. Rev. Phys. Chem.*, 2004. **23**, 1.

119. A. Hooker, C. H. Greene, and W. Clark, *Phys. Rev. A.*, 1996. **55**, 4609.

120. T. F. Gallagher, *Rydberg Atoms*. Cambridge Monographs on Atomic, Molecular, and Chemical Physics 3, ed. A. Dalgarno, et al. 1994: Cambridge University Press.

121. W. A. Chupka, *J. Chem. Phys.*, 1993. **98**, 4520.

122. E. Luc-Koenig and A. Bachelier, *J. Phys. B: Atom. Molec. Phys.*, 1980. **13**, 1743.

123. J. O. Hirschfelder and L. A. Curtiss, *J. Chem. Phys.*, 1971. **55**, 1395.

124. T. P. Softley, *Atomic Spectra*. Oxford Chemistry Primers, ed. R. G. Compton. 1999: Oxford University Press Inc.

125. P. Pillet, H. B. van Linden van Heuvell, W. W. Smith, R. Kachru, N. H. Tran, and T. F. Gallagher, *Phys. Rev. A.*, 1984. **30**, 280.

126. C. E. Dessent, S. R. Haines, and K. Muller-Dethlefs, *Chem. Phys. Lett.*, 1999. **315**, 103.

127. H-J. Dietrich, K. Muller-Dethlefs, and L.Y. Baranov, *Phys. Rev. Lett.*, 1996. **76**, 3530.

128. R. J. Damburg and V. V. Kolosov, *J. Phys. B: Atom. Molec. Phys.*, 1978. **11**, 1921.

129. R. J. Damburg and V. V. Kolosov, *J. Phys. B: Atom. Molec. Phys.*, 1979. **12**, 2637.

130. A. Trottier. 2006.

131. C. C. Wang, G. R. Wu, S. A. Harich, H. Song, M. Y. Hayes, R. T. Skodje, X. Y. Wang, D. Gerlich, and X. Yang, *Phys. Rev. Lett.*, 2005. **95**, 013201.

132. R. N. Zare, *Science*, 2006. **311**, 1383.

133. C. Lin, M. F. Witinski, and F. Davis, *J. Chem. Phys.*, 2003. **119**, 251.

134. S. J. Greaves, E. L. Flynn, E. L. Futcher, E. Wrede, D. P. Lydon, P. J. Low, S. R. Rutter, and A. Beeby, *J. Phys. Chem. A,*, 2006. **110**, 2114.

135. S. J. Greaves, *Ph. D Thesis*. 2005, University of Durham.

136. W. Shockly and G. L. Person, *Phys. Rev.*, 1948. **74**, 232.

137. G. E. Moore, *Electronics*, 1965. **38**, 1.

138. X. Zhao, Y. Xia, and G. M. Whitesides, *J. Mater. Chem.*, 1997. **7**, 1069.

139. A. Zehe and J. G. Robles Martinez, *Journal of Molecular Structure*, 2004. **709**, 215.

140. S. Kohler, J. Lehmann, and P. Hanggi, *Supperlattices and Microstructures*, 2003. **34**, 419.

141. Z. J. Donhauser, B. A. Mantooth, K. F. Kelly, L. A. Bumm, J. D. Monnell, J. J. Stapleton, A. M. Price, D. L. Allara, J. M. Tour, and P. S. Weiss, *Science*, 2001. **292**, 2303.

142. U. H. F. Bunz, *Chem. Rev.*, 2000. **100**, 1605.

143. K. D. Ley and K. S. Schanze, *Coord. Chem. Rev.*, 1998. **171**, 287.

144. J. S. Moore, *Acc. Chem. Res.*, 1997. **30**, 420.

145. M. Levitus, K. Schmieder, H. Ricks, K. D. Shimizu, U. H. F. Bunz, and M. A. Garcia-Garibay, *J. Am. Chem. Sco.*, 2001. **123**, 4259.

146. R. J. Magyar, S. Tretiak, Y. Gao, H. L. Wang, and A. P. Shreve, *Chem. Phys. Lett.*, 2005. **401**, 149.

147. A. Beeby, K. S. Findley, P. J. Low, T. B. Marder, P. Matousek, A. W. Parker, S. R. Rutter, and M. Towrie, *Chem. Comm.*, 2003. **19**, 2406.

148. A. Beeby, K. S. Findley, P. J. Low, and T. B. Marder, *J. Am. Chem. Sco.*, 2002. **124**, 8280.

149. J. Tomfohr and O. F. Sankey, *J. Chem. Phys.*, 2004. **120**, 1542.

150. J. Cornil, J. L. Karzazi, and J. L. Bredas, *J. Am. Chem. Sco.*, 2002. **124**, 3516.

151. L. Zhao, I. F. Perepichka, F. Turksoy, A. S. Batsanov, A. Beeby, K. S. Findley, and M. R. Bryce, *New Journal of Chemistry*, 2004. **8**, 912.

152. K. Okuyama, H. Takahumi, and N. Mikami, *J. Phys. Chem.*, 1984. **88**, 1711.

153. K. Okuyama, M. C. R. Cockett, and K. Kimura, *J. Chem. Phys.*, 1992. **97**, 1649.

154. P. F. H. Schwab, M. D. Levin, and J. Michl, *Chem. Rev.*, 1999. **99**, 1863.

155. X. Zheng, N. Vedova-Brook, and K. Sohlberg, *J. Phys. Chem. A.*, 2004. **108**, 2499.

156. M. D. Wheeler, S. M. Newman, A. J. Orr-Ewing, and M. R. Ashfold, *J. Chem. Soc. Farad. Trans.*, 1998. **94**, 337.

157. M. N. R. Ashfold, S. G. Clement, J. D. Howe, and C. M. Western, *J. Chem. Soc., Faraday Trans.*, 1993. **89**, 1153.

158. M. D. Wheeler, I.R. Lambert, and M. N. R. Ashfold, *Chem. Phys. Lett.*, 1994. **229**, 285.

159. A. O'Keffe and D. A. G. Deacon, *Rev. Sci. Instrum.*, 1988. **59**, 2544.

160. K. J. Schulz and W. R. Simpson, *Chem. Phys. Lett.*, 1988. **297**, 523.

161. P. W. Atkins, *Physical Chemistry*. 6th ed. Oxford University Press. 1999.

162. J. M. Herbelin, J. A. McKay, M. A. Uenten, R. H. Urevig, D. J. Spenser, and D. J. Bernard, *Appl. Opt.*, 1980. **19**, 144.

163. D. Z. Anderson, J. C. Frisch, and C. S. Masser, *Appl. Opt.*, 1984. **23**, 1238.

164. G. Berden, R. Peeters, and G. Meijer, *Int. Rev. Phys. Chem.*, 2000. **19**, 565.

165. P. Zalicki and R. N. Zare, *J. Chem. Phys.*, 1995. **102**, 2708.

166. P. Zalicki, Y. Ma, R. N. Zare, E. H. Wahl, J. R. Dadamio, T. G. Wowano, and C. H. Kruger, *Chem. Phys. Lett.*, 1995. **234**, 269.

167. D. H. Lee, Y. Yoon, B. Kim, Y. L. Lee, Y. S. Yoo, and J. W. Hahn, *App. Phys. B.*, 2002. **74**, 435.

168. J. J. Scherer, J. B. Paul, A. O'Keffe, and R. J. Saykally, *Chem. Rev.*, 1997. **97**, 25.

169. A. O'Keffe and O. Lee, *Am. Lab.*, 1989. **21**, 19.

170. M. N. R. Ashfold, P. W. May, C. A. Rego, and N. M. Everitt, *Chem. Soc. Rev.*, 1994. **23**, 21.

171. T. Yu and M. C. Lin, *J. Am. Chem. Sco.*, 1993. **115**, 4371.

172. B. G. Fidric, R. A. Provencal, S. M. Tan, E. R. Crosson, A. A. Kachanov, and B. A. Paldus, *Optics and Photonics News*, 2003. **14**, 24.

173. M. Hillenkamp, S. Keinan, and U. Even, *J. Chem. Phys.*, 2003. **118**, 8699.

174. C. M. Western, *WI2 Simulation Package*, Private Communication.

175. A. Beeby, *Private communication.*